Universitat Autònoma de Barcelona

A New Synthetic Method for Nanoscale Metal-Organic Frameworks and their Application as Contrast Agents for Magnetic Resonance Imaging

Arnau Carné Sánchez

Doctoral Thesis

Doctorat en Química

Supervisors

Prof. Dr. Daniel Maspoch and Dr. Inhar Imaz

Tutor
Dr. Félix Busqué Sánchez

Catalan Institute of Nanoscience and Nanotechnology
Departament de Química- Facultat de Ciències

2014

Memòria presentada per aspirar al Grau de Doctor per Arnau Carné Sánchez

Vist i plau

Prof. Dr. Daniel Maspoch

Investigador ICREA

Supramolecular Nanochemistry and Materials Group

Institut Català de Nanociència i Nanotecnologia

Dr. Inhar Imaz

Investigador Ramón y Cajal

Supramolecular Nanochemistry and Materials Group

Institut Català de Nanociència i Nanotecnologia

Dr. Félix Busqué Sánchez

Professor Agregat

Departament de Química

Universitat Autònoma de Barcelona (UAB)

Bellaterra, 24 de juliol de 2014

Table of contents

Abstract

The present Thesis has been dedicated to the synthesis of nanoscale Metal-Organic Frameworks (NMOFs) and the study of their potential application as Contrast Agents (CAs). Accordingly, two main lines of work can be distinguished through the lecture of this Thesis: i) the development of a novel synthetic methodology to synthesise NMOFs; and ii) the synthesis of new NMOFs that meet the specific requirements for their use as CAs.

In the first Chapter, we review the evolution of the field of MOFs, from their antecedents that made their discovery possible to their current applications and prospects. We pay special attention to the current methodologies to synthesise MOFs at the nanoscale, and the advent of new applications resulting from their small size.

Chapter 3 describes the validation of the Spray-Drying (SD) technique as a new methodology to synthesise NMOFs and their related hollow superstructures. The impact of the main experimental parameters on the synthesis of NMOFs is given as well as the different modes of operations that the SD technique offers for their synthesis. The versatility of the technique has allowed us to synthesise a wide panel of NMOFs belonging to the most representative subfamilies.

In Chapter 4 the possibilities of combining NMOFs with other functional species using the SD technique to synthesise MOF-based composites is explained. We show how the MOF-based hollow superstructures can be used to encapsulate different materials, including NaCl crystals, dyes and FeOx inorganic nanoparticles (INPs). Furthermore, we also prove that NMOFs can also be easily encapsulated within functional matrices, such as polymers, by SD. Finally, we demonstrate that the unique capabilities of the SD to create MOF-based composites can be exploited to further expand the applications of NMOFs.

In the second axis of this Thesis, Chapter 5 describes the synthesis of a new generation of NMOFs with CA properties. The strategy consists on using heterocyclic ligands currently employed in the synthesis of molecular CAs, which possess high chelating capabilities towards Gd(III) ions. The macrocyclic ligand DOTP is used to assemble a porous, heterometallic MOF. This MOF is miniaturizable down to the nanoscale to form stable colloids; is stable in physiological saline solution and cell culture media; and is not cytotoxic. It shows interesting relaxometric properties with a r_1 at high field (500 MHz) of 5 $mM^{-1} \cdot s^{-1}$ and a maximum in r_1 of 15 $mM^{-1} \cdot s^{-1}$ at 40 MHz, which remains constant over a wide pH range and increases with temperature.

Resum

La present Tesis ha estat dedicada a la síntesis de materials Metal·lorgànics a la nanoescala (NMOFs, fent servir l'acrònim anglès) i l'estudi de les seves potencials aplicacions com a Agents de Contrast (AC) en Imatgeria per Ressonància Magnètica. En conseqüència, dos línies de treball es distingeixen al llarg de la lectura d'aquesta Tesis: (ii) el desenvolupament de una nova metodologia per a sintetitzar NMOFs, i (ii) la síntesis de nous NMOFs que puguin complir els requeriments específics per tal de ser utilitzats com a AC.

En el primer capítol, revisem la evolució que ha viscut el camp dels MOFs, des de els seus antecedents que van fer possible el seu descobriment fins a les seves aplicacions actuals i les seves noves perspectives. Prestem especial atenció a les actuals metodologies emprades per a sintetitzar NMOFs, i al adveniment de noves aplicacions aparegudes gràcies a la seva mida nanoscòpica.

El en Capítol 3 descrivim la validació de la tècnica coneguda com Spray-Drying (SD) com a nova metodologia per sintetitzar NMOFs i les superestructures buides que se'n deriven. S'estudia l'impacte dels principals paràmetres experimentals en la síntesi del NMOFs així com les diferents modalitats de usatge que ofereix la tècnica. Precisament, la versatilitat de la tècnica ens ha permès sintetitzar un ampli ventall de NMOFs pertanyent a les subfamílies més representatives.

El Capítol 4 explica les possibilitats de utilitzar la tècnica de SD per a combinar NMOFs amb altres especies funcionals per tal de sintetitzar compòsits basats en MOFs. Demostrem com les superestructures buides de NMOFs poden ser utilitzades per a encapsular diferents materials, tals com cristalls de NaCl, molècules fluorescents i nanopartícules magnètiques. A més, també demostrem com cristalls de NMOFs poden ser fàcilment encapsulats en matrius polimèriques mitjançant la tècnica de SD. La varietat de compòsits basats en MOFs que es pot obtenir utilitzant la tècnica de SD permet ampliar el ventall d'aplicacions dels NMOFs.

En el capítol 5 es descriu la segona línia de treball que conforma la present Tesis doctoral referent a la síntesis de una nova generació de NMOFs amb propietats de AC. La estratègia consisteix en utilitzar lligands heterocíclics emprats en la síntesis dels AC moleculars, els quals presenten una gran afinitat per als ions de Gd(III). El lligand heterocíclic DOTP s'utilitza per l'assemblatge de un MOF bimetàl·lic i porós. Aquest MOF és miniaturitzat a la nanoescala per a forma dispersions col·loïdals estables; és estable en medi fisiològic, en cultiu cel·lular i no presenta citotoxicitat. A més, presenta unes propietats de AC interessants, com ho demostra la relaxativitat mesurada a camp magnètic alt (r_1 = 5 $mM^{-1}·s^{-1}$ a 500 MHz) i una relaxativitat màxima a 40 MHz de 15 $mM^{-1}·s^{-1}$, la qual es manté constant al llarg de un ampli ventall de pH.

Acknowledgements

Voldria agrair en primer lloc al Institut Català de Nanociència i Nanotecnolgia per haver-me donat la possibilitat de desenvolupar aquesta tesi doctoral en la millor de les condicions, i en especial al Prof. Jordi Pascual. També vull agrair la Generalitat de Catalunya i al seu programa de beques predoctorals per a haver-me concebut la beca que m'ha permès realitzar la present Tesis Doctoral.

Sens dubte, aquest treball no hagués arribat a bon port sense el guiatge dels meus dos excel·lents directors de tesis, Daniel Maspoch i Inhar Imaz, amb qui he après tantíssim. He pogut aprendre moltíssim gracies a la seva increïble capacitat de treball, la seva intuïció científica i motivació. Cal dir també, que els agreixo especialment la paciència que han demostrat durant el meu aprenentatge. Estic segur que el que he après durant aquests anys fent la Tesi Doctoral sota la seva supervisió hem servirà per a la resta dels meus reptes amb que em pugui trobar. També vull expressar la meva gratitud al Prof. Félix Busqué qui m'ha ensenyat tot el que sé de química orgànica.

Durant la Tesi he tingut la oportunitat de visitar altres laboratoris per tal de enriquir encara més la meva experiència. Així doncs, m'agradaria agraïr tots els membres del grup de "Complexes métalliques pour applications biomédicales" del Centre de Biophysique Moleculaire a Orleans i dirigit per la Prof. Eva Toth. En especial, m'agradaria donar les gràcies a la Dr. Célia Bonet qui m'ha ensenyat el poc o molt que pugui saber dels agents de contrast i amb qui tantes estones vaig passar analitzant i mesurant relaxativitats.

Gràcies al servei de Microscòpia de la UAB, per totes les hores que he passat allà i per tot el seu ajut que ha fet que aquesta tesi compti amb unes imatges tant bones.

Vull agrair també, de una forma molt especial, a tots els companys del grup NanoUp, perquè han estat els millors companys que podia tenir. Amb ells he passat per tots els estats d'ànim tant a dins com a fora del laboratori i han sigut sempre un enorme suport. De forma especial voldria agrair amb qui he compartit la major part d'aquests anys; la ja doctora Marta Rubio, amb qui tantíssim he rigut, en Xavi i l'Ivan, molt més que companys de tesi, per les incomptables hores de discussió sobre qualsevol cosa, l'Àngels per aportar una mica de distinció al grup, en Carles per les excursions que ha dissenyat, en Kyriakos per transmetre'm el seu entusiasme per la ciència i les seves "delicatessen" culinaries i també tot el grup de "encapsuladores" que amb tanta paciència ha aguantat el meu caos en el seu laboratori.

També vull agrair a tots els amics de Manresa, ja sabeu qui sou, per...per això per ser els meus amics ara i des de fa tant. També a l'Ester que ha escoltat tots els meus nervis i inquietuds i sempre m'ha

sabut ajudar. I com no agrair a la Sílvia amb qui he compartit el final d'aquesta tesi, ajudant-me en tot moment i fent que el tram més difícil hagi sigut també el més feliç.

Per últim voldria expressar tota la meva gratitud a la meva família, en especial als meus pares. Si això és el final de una etapa, ells han estat amb mi des de el principi, donant-me sempre un suport incondicional. No és exagerat dir que tots els atributs que es necessiten per a completar una Tesi Doctoral me'ls han inculcat ells. La paciència quan les coses no surten, l'esforç i la perseverança són coses que he vist a casa des de sempre i que els meus pares sempre m'han transmès.

Chapter 1

Introduction to Nanoscale Metal-Organic Frameworks (NMOFs)

In this Chapter, the current state of MOF applications is discussed. Then, a comprehensive review of the methodologies proposed to synthesise MOFs at the nanoscale (NMOFs) and their potential impact in classical applications are presented. Finally, the possibilities of these NMOFs in new fields of applications are considered.

1. Porous materials

Since the ancient Greeks, the idea of a defined space without matter has always attracted philosophers and scientists. Vacuum was a matter of philosophic discussion and even its existence was questioned as exemplified by the famous sentence: "Nature abhors vacuum (*Horror Vacui*)". It was not until the 17th century when Torricelli clearly demonstrated its existence. In 1644, Torricelli filled a glass tube of about 1 m in length with mercury. The open end of this glass tube was sealed and with a fingertip. The tube was then brought to an upright position with the end sealed with the fingertip pointing downward. This end was immersed in a mercury reservoir and the fingertip removed, so that the mercury inside the tube was in free contact with the reservoir. The mercury column in the tube sank to a height of 76 cm, measured from the liquid surface of the reservoir. The experiment demonstrated that the space left above the mercury after turning the tube upside down was in fact vacuum: the mercury level was independent of the volume above, and it could be filled completely with water admitted from below.[1] After this pioneer experiment, advances in the physical study of the vacuum and its distinct properties gave rise to improved theories of gas pressure and energy propagation, all of them later exploited in a myriad of technological advances.

When the vacuum is defined and confined inside a given material it becomes a porous material. Porous materials aim to generate voids inside matter through their pores. Voids confined in the pores can be employed to store, to sort by molecular size acting as molecular sieving, to promote catalytically enhanced chemical transformations within their pores and to transport active species. The most distinguishing characteristic to differentiate porous materials is their pore size. In 1972, the International Union of Pure Applied Chemistry (IUPAC) made a classification, dividing the porous materials in three categories (**Table 1**): micro-, meso- and macroporous materials.[2]

Table 1. Classification of the porous materials as a function of their pore size.

Type of porous material	Pore size (Å)
Microporous materials	< 20
Mesoporous materials	20 – 500
Macroporous	> 500

To date, both Nature and man hands have given a wide range of different porous materials, from the naturally occurring porous inorganic materials, like activated carbon and zeolites, to the rationally designed Metal-Organic Frameworks (MOFs).

From a historical perspective, activated carbons solids are considered the first porous materials. The first recorded application of charcoal for medicinal purposes was cited in an Egyptian papyrus as early as 1550 B.C. It seems that its main use was to adsorb odorous vapours from putrefying wounds as well as within the intestinal tract. Later in 400 B.C., Hippocrates and Pliny recorded the use of charcoal to treat a wide range of complaints, including epilepsy, chlorosis and anthrax. Activated carbon is the result of the pyrolysis of organic matter, usually wood, peat or even coconut shells. This pyrolysis gives rise to inorganic carbon with pores in its structure. Since its first discovery, the process has lived a strong evolution and now, activated carbon materials with high surface areas (up to 3000 $m^2 \cdot g^{-1}$) can be fabricated. Their applications are diverse, mainly focused on air purification or as decolourants. In chemistry, they are largely used as catalysts in hydrogenation reactions where Pd is employed. However, the bigger limitation of activated carbons resides in the low organisation of their porosity; that is, their pore size distribution, arrangement and functionality are not controlled making difficult to upgrade their current applications.

Today, one of the most representative porous materials in the market are aluminosilicates or zeolites. They are based in silicate frameworks in which the substitution of some tetrahedrons of SiO_4 by $[AlO_4]^-$ leads to a negatively charged structure that is compensated by a counterion. This combination results in a family of materials with the general formula $M^{n+}_{x/n}[(AlO_2)_x(SiO_2)_y]^{x-}$, where M is a metal, generally an alkali or alkali earth metal. Zeolites show a crystalline nature that guarantees an ordered arrangement of the pores and narrow size distribution. The structure can be defined by the number of tetrahedrons surrounding the pores, being generally from 3 to 6 members per pore.

Zeolites can be either natural or synthesised. In Nature, they are produced in the form of minerals under alkaline conditions. Their discovery dates back to 1756 when a Swedish mineralogist called Axel Fredrick Crönstedt discovered that a mineral called Stilbite released water when it was heated. This observation revealed the capacity of this mineral to adsorb and release substances. He named the family of these minerals as zeolites, a word coming from the classical Greek that means “boiling stones”. The sorbent properties of zeolites indicated its porous nature, a property that was very attractive for the industry because it could be used in a variety of applications such as cation exchange, adsorbents and heterogeneous catalysis. All this interest made zeolites a valuable material for a myriad of engineering and chemical processes and motivated the research in the synthesis of new zeolites with optimised properties. In the

1940's,[3] several companies, especially in the oil sector, started a race to synthesise new zeolites with increased performance. Oil industry was particularly interested in zeolites due to their high thermal stability and their catalytic properties; particularly for their isomerization activity and cracking of hydrocarbons. Thus, it is not surprising that the synthesis of one of the most used zeolites so far, ZSM-5, was patented by the Mobile Oil Company in 1975.

As mentioned above, zeolites are inorganic frameworks that in Nature have a metal ion as a counterion. These metal ions are generally located in the pores of their structure. The industrial synthesis of zeolites replaced this inorganic counterion by bulky organic cations, such as quaternary amines. The organic cations served as structure directing agents, inducing the inorganic polymerization around them. After the synthesis, the organic cations could be simply removed through calcination because its thermal stability is lower than the aluminosilicate. Therefore, the role of the organic molecule is similar to a template. This approach was a major breakthrough in the synthesis of zeolites as the pore size obtained in the final material is related to the template used during its synthesis. Also, it was very important because it proved that a certain degree of pore size design could be achieved. This approach also allowed to obtain a better size distribution, defect free and ordered arrangement of the pores, which improved their applications in the fields of molecular sieves, cation exchange and catalysis.[4]

In order to further increase the control on pore functionality, different inorganic oxides were also incorporated in the zeolite synthesis. In 1982, Flanigen and co-workers replaced the SiO_2 by the isoelectric $AlPO_2$ to synthesise a new class of inorganic porous crystalline materials noted as aluminophosphonates (AlPOs).[5] These materials had a structure related to the zeolites. However, crystalline studies revealed an important difference between the two class of materials: in AlPOs, some Al(III) ions adopt an octahedral coordination, whereas in zeolites only the tetrahedral coordination is present. This difference has an enromous impact on the structure: it allows more membered rings. While zeolites commonly have from 10 to 12 membered rings, aluminophosphates could reach up to 20 membered rings. As a result, the pore size is increased. In fact, the AlPOs noted as VPI-5 was the first crystalline microporous material with a pore diameter exceeding 10 Å.[6] Interestingly, this potential use of non tetrahedral oxides for the synthesis of inorganic porous materials allowed the incorporation of other metal ions in the structure. For example, a series of mixed tetrahedral-octahedral frameworks were prepared using arsenates and metallosilicates.[7]

The possibility to use a variety of inorganic oxides and phosphates enabled wider composition diversity. Nevertheless, the structures were still based on corner sharing of inorganic polyhedrons which limited the modulation of inorganic crystalline materials. A strategy that was evaluated to solve this problem was to use the organic molecules not only as

templates but as a part of the structure. Pioneer works were carried out by Clearfield and co-workers in the 1970's. These authors used long diphosphonates to connect bidimensional phosphates layers, and found that by increasing the size of the diphosphonate, the interlayer distance could be tuned.[8] This means that it was possible to create new porous solids by an appropriate choice of the inorganic metal oxide and the organic spacer. The use of an organic moiety as a part of a building block of a porous structure (and not only as a template) provided a tremendous increase of the structural flexibility owing to the richness of Organic Chemistry.

2. MOFs: a new class of porous materials

Coordination bond is defined as a supramolecular interaction between an organic molecule (noted as ligand) with at least one lone pair of electrons and a metal ion that has a Lewis acid character. Based on these interactions and the pioneering work of Clearfield, the strategy to synthesise a new class of porous materials (later on, called Metal-Organic Frameworks (MOFs)) is simple: use organic compounds with more than one site capable to coordinate metal ions (*eg.* Polycarboxylate, N,N'-ligands, polyposhpates) as linkers to connect metal ions along the space, thus forming infinite 1D, 2D and 3D coordination porous structures. This approach has practically endless possibilities owing to the infinite combinations between metal ions and organic linkers. In fact, since the discovery of these materials in the early 1990's, the number of reported MOF structures has not stopped growing. As an example, more than 6000 structures have been reported in 2011.[9] Overall, there are two main factors that have contributed to the development of MOFs: the continuous synthetic efforts of many scientists around the world, and the development of structural studies that enabled their structural rationalization and subsequent design.

Robson and co-workers made a major contribution in rationalising the structure of MOFs. They described the structure of MOFs as a combination of nodes (0 D clusters) and linkers.[10] This simplification allowed anticipating some of the fascinating properties latter exhibited by these materials, such as gas sorption and cation exchange. Yaghi and co-workers further developed the theory by considering the inorganic nodes as Secondary Building Units (SBUs). In these hybrid materials, SBU are defined as the environment of the metallic ions with the chelating moiety of the linker.[11] By considering the points of extension of the SBU, it is possible to assign a geometric form to each SBU (**Figure 1a**). Organic linkers can also be rationalized according to the geometric orientation of the coordination nodes (**Figure 1b**). Thus, the MOF porous structure can be explained as the connection between the SBU with the organic linkers, as shown in **Figure 1c**.

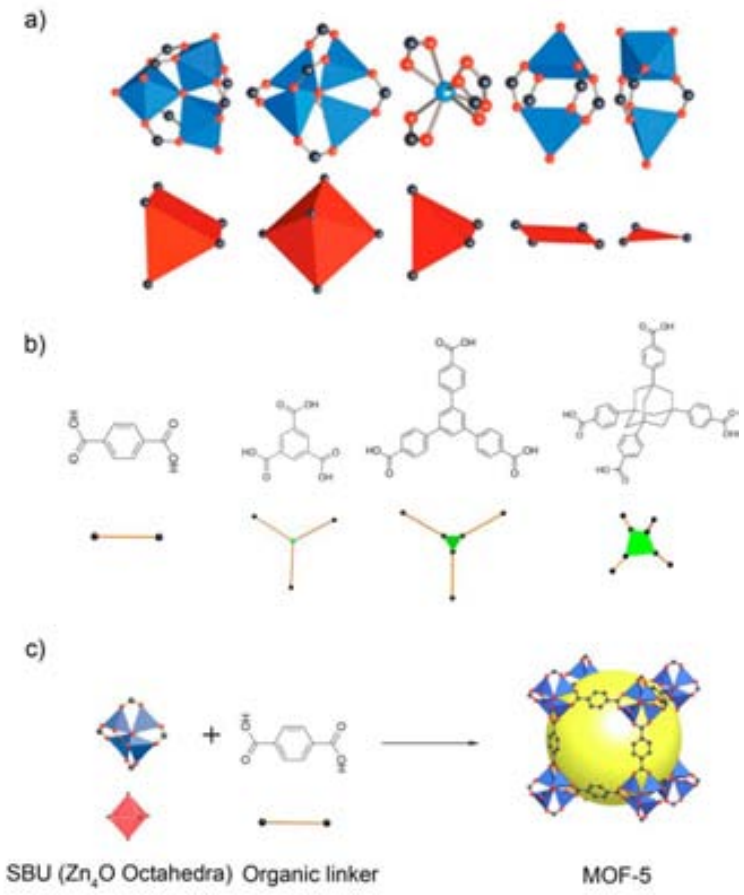

Figure 1. (a) Inorganic metal-oxygen polyhedra represented in blue, showing the coordination of the metal ion with the carboxylate oxygen atoms and their related polyhedron defined by carboxylate carbons in red (down). (b) Representative organic linkers represented as simple geometric figures. (c) MOF-5 structure rationalised using the SBU theory.

The SBU theory in MOFs can also be exploited as a synthetic tool. One can assign a specific coordination and geometry to a combination of an organic moiety with a metal ion becoming a SBU that can be considered a synthon. A synthon is a structural unit that can be used in a retrosyntetic analysis and that allows to introduce rational design to the final structure. Therefore, by keeping the SBU but expanding systematically the organic linker, the porosity can be tuned. This approach was successfully applied to the structure of MOF-5. As shown in **Figure 2**, The original ligand 1,4-benzenedicarboxylic acid (BDC) was replaced by longer aromatic dicarboxylates linkers. These replacement gave rise to a series of MOFs that share the same topology and SBU called Isoreticulated MOFs (IRMOFs). As expected, the porosity of these MOFs increased with the length of the linker used. This example clearly illustrates the potential of the coordination chemistry to tailor the pore size in porous materials and the diversity of the building blocks that can be employed. However, even though some examples of MOF structures done by design can be found in the literature, it is also important to mention that the rational design of MOFs is still very challenging. The different, multiple coordination modes of metal ions and the influence of other factors, such as the solvent and the counterions,

among others, make difficult to predict which SBU will be generated in the reaction. So, it is very difficult to predict, for example, the final network topology, the dimensionality of the network and the degree of catenation. All of these factors have a great impact in the final structure and ultimately, in its properties.

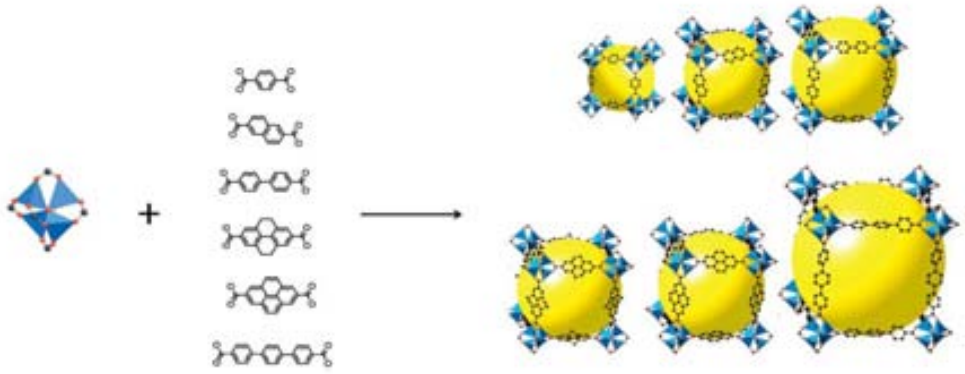

Figure 2. Stepwise increase of porosity in MOFs through reticular chemistry.[12]

2.1. Properties and Applications of MOFs.

The versatility of porous structures and compositions of MOFs make them excellent candidates in myriad applications. The most developed applications are the ones related to their porosity: gas sorption (storage and separation) and catalysis. In this Thesis, we termed these applications as "classical applications" since they appeared almost along with the discovery of the first MOFs. However, for example, with the advent of their miniaturisation at the nanoscale regime, new fields of applications are started to be proposed. Some of them include biological applications, such as drug delivery systems or contrast agents, and sensors. In this part of the Thesis, an overview of the classical properties will be given. In the next section, a review of synthetic methods to produce MOFs at the nanoscale (NMOFs) and their resulting new potential applications will be presented.

2.1.1. Gas storage and separation

The porous structure of MOFs enables them to be used as adsorbents of small molecules. However, this is only possible if guest species (such as solvents or unreacted reactants) located into the pores are removed after their synthesis. The first indication of reversible adsorption in MOFs was provided by Kitagawa *et al.* in 1997, who studied the porosity of a 1D coordination polymer with a general formula of $M_2(4,4'\text{-BPY})_3(NO_3)_4$ (where M is Co, Ni or Zn, and 4,4'-BPY is 4,4' bypiridine). They proved that this MOF could adsorb gas molecules (O_2, CH_4 and N_2) in its crevices at high pressure.[13] Permanent porosity of MOFs was further demonstrated in the layered zinc terephthalate $Zn_2(BDC)_4(H_2O)_2$ (nowadays known as MOF-2)[14] by conducting N_2 gas isotherms at low pressures and temperatures. A subsequent step forward in the development of MOFs as materials with gas storage properties was the synthesis of the first robust 3D MOF with formula $Zn_4O(BDC)_6$ (known as MOF-5).[15] MOF-5 exhibited a very high potential porosity of 63 % of the volume of the unit cell and a surface area of 2320 $m^2 \cdot g^{-1}$, which largely outperformed zeolites. First findings in gas sorption of MOFs and the increasing control in their synthesis motivated scientists to increase the porosity of these materials, reaching today unprecedented surface areas exceeding 7000 $m^2 \cdot g^{-1}$ (**Figure 3**).

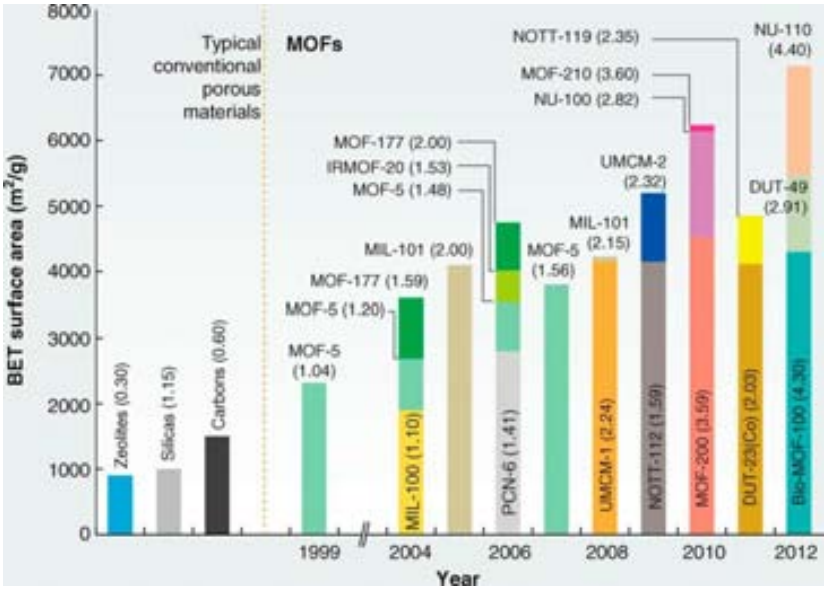

Figure 3. Evolution in porosity of MOFs assessed by the surface area estimated from gas sorption measurements. The value in parenthesis represents the pore volume ($cm^3 \cdot g^{-1}$).[9]

One of the strategies that allowed increasing the porosity of MOFs was based on their design using reticular chemistry. As state above, in order to increase the pore volume, a common strategy is to take as a reference an existing MOF structure and replace the original ligand by an expanded version of it (**Figure 2**). The topology and the SBU of the "parental" MOF are maintained, whereas the porosity can be increased even by a factor up to 17 (**Figure**

4). In fact, this strategy has allowed for the preparation of MOFs with pore size larger than 20 Å, thereby entering to the world of "mesoporous materials".[16]

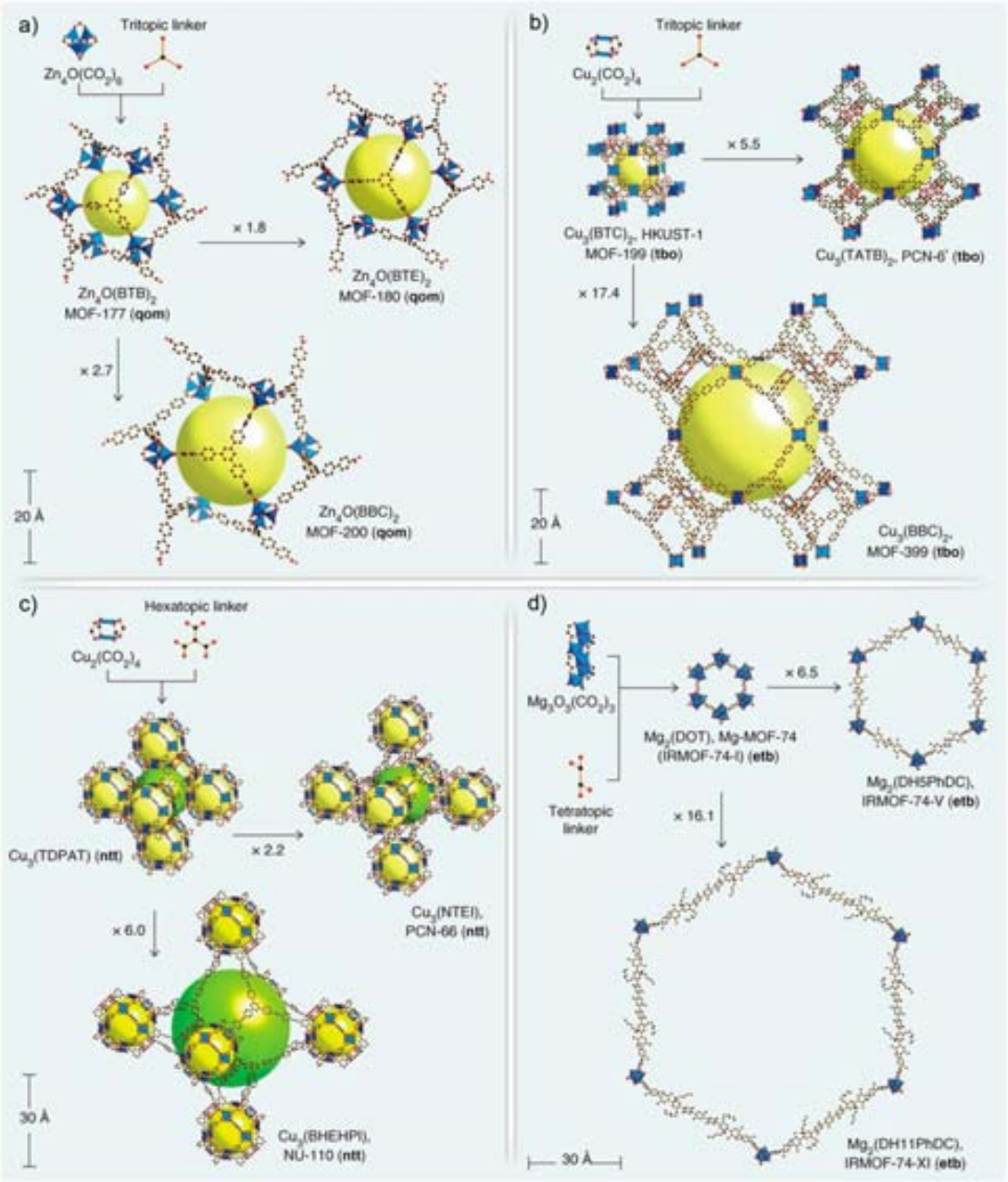

Figure 4. Isoreticular expansion of archetypical MOFs with different topologies (a to d).[9]

This storage capacity soon raised interest among the scientists, expanding their interest for storing other gases. These gases mainly include hydrogen, methane and CO_2, due to environmental reasons and economic factors related to energy costs. While hydrogen and methane can be used as alternative fuels, CO_2 sequestration is important to reduce the anthropogenic impact in the greenhouse effect. MOFs show high adsorption and storage capacities of these gases. In fact, their industrial potential for gas storage has been demonstrated due to their capacity to store gases exceeding the standard pressure-volume-temperature (PVT) curve of an empty tank; *i. e.* a tank filled with a MOF can store higher amounts of gas than an empty tank at the same pressure.[17] An overview of the adsorption of these three gases is presented in the following sections.

2.1.1.1. H_2 adsorption

H_2 is an ideal carrier and is considered the future fuel due to its abundance, high heat of adsorption (20 Mj/Kg of hydrogen compared to 44.5 Mj/Kg of gasoline) and its non-polluting post combustion products (mainly water). However, its storage and transport present both safety and economic challenges. To date, storage of H_2 is based in chemisorption, which gives high storage capacity but slow release kinetic and poor reversibility. For instance, metal hydrides such as $LaNi_5H_{6.5}$ bind strongly to H_2 with a heat of adsorption reaching 200 $KJ \cdot mol^{-1}$. However, this high heat of adsorption makes H_2 release kinetically unfavourable and only possible at high temperatures (400 K).[18] As an alternative, MOFs offer physisorption which would ensure a reversible loading and release of H_2, demanding less energy input in the desorption than the current chemisorbents. Since physisorption has good correlation with the surface area, one of the main strategies to increase hydrogen uptake is to increase the surface area of MOFs. For instance, low density MOFs made of carboxylate-based ligands such as $Cu_3L \cdot 3H_2O$ (known as NU-100; where L is (1,3,5-tris[(1,3-carboxylic acid-5-(4-(ethynyl)phenyl))ethynyl]-benzene))[19] and $Zn_4O(BTE)_{4/3}(BPDC)$ (known as MOF-210; where BTE is 4,4',4"-(benzene-1,3,5-triyltris(ethyne-2,1-diyl))tribenzoic acid and BPDC is biphenyl-4,4′-dicarboxylic acid)[20] have shown a high hydrogen adsorption of 9 % (wt%) at 56 bar and 77 K.

Structural features of the network can also have an impact on H_2 storage. Network catenation seems to have a positive effect in the H_2 storage, as demonstrated by the comparison of the H_2 adsorption of two otherwise isostructural MOFs with formula $(Cu_6(H_2O)_6(TATB)_4)$ (known as PCN-6; where TATB is 4,4′,4″-s-triazine-2,4,6-triyl-tribenzoate).[21] The catenated structure showed an uptake of 95 $mg \cdot g^{-1}$ at 77 K and 50 bar, while the non-catenated structure had an uptake of 58 $mg \cdot g^{-1}$ at the same conditions.

Also, exposition to open metal sites can increase enthalpy of adsorption for hydrogen. For example, the Ni(II) analogue of (M_2(DHTA)) (known as MOF-74 where DHTA is 2,5-dihydroxiterephtalic acid) presents an ordered arrangement of opened metal sites facing the 1D channels in its structure. This feature is responsible for its high enthalpy of H_2 adsorption, which results in high H_2 uptake particularly at low pressure.[22] However, the promising storage capacities demonstrated by MOFs have only been achieved at low temperatures (77 K) so far, becoming negligible when the room temperature is approached. For this reason, MOFs are still far from the targets (5.5 wt% at 233K) set for their practical application in H_2 storage.

2.1.1.2. CO_2 sequestration

CO_2 is one of the main gases responsible for the anthropogenic effect of the greenhouse. It is released during combustion of fossil fuels and therefore, it is both technical and economical challenging to significantly cut its emission. One of the strategies consists in sequestrating it at the point of emission, avoiding its release to the atmosphere. As CO_2 is produced after combustion processes, it is present in complicated mixtures. In fact, in a typical post combustion exhaust, it represents the 15% of the total mixture. Therefore, high selective adsorbents are required to sequestrate CO_2 from the gas mixture. However, if the affinity of the adsorbent is too high, the energy required to remove the adsorbed CO_2 and regenerate the adsorbent increases, thereby resulting in an energy penalty for the sequestration of CO_2. For example, approximately 70% of the overall cost of CO_2 sequestration is attributed to the adsorbent regeneration in the current technologies based on alkanolamine aqueous solutions.[23]

MOFs can contribute to address this over cost as their guest removal is less energy demanding while still achieving high selectivity for CO_2. Preferential adsorption for CO_2 can be achieved by two means: (i) size-based selectivity by which MOFs with small pores would allow only the diffusion of molecules up to a certain size into their pores (kinetic effect); and (ii) adsorptive selectivity arising from the difference in the affinity of the various components in the mixture to be adsorbed on the pore surface of the MOFs (thermodynamic parameter).[24] In regard to the kinetic-based selectivity, the small size of the molecules in the gas stream would require MOFs with very small pores. However, almost all MOFs with high surface areas and high storage capacities for CO_2 have pores with apertures larger than the CO_2 molecules, invalidating them for molecular sieving.

Therefore, the strategy based on differential heat of adsorption of the molecules composing the gas mixture seems more promising. Here, the higher quadrupolar moment of CO_2 compared with the other gases (specially N_2 and O_2) opens the door to design MOFs with pore surfaces having higher affinity for CO_2.[25,26] This affinity can be increased when unsaturated metal sites are decorating the pore wall. Unsaturated metal ions can act as a charge

dense binding sites that induce the polarisation of the adsorbed CO_2 and therefore, increase the selectivity for CO_2 over other gases less polarisable. Illustrative examples are the MOF-74 analogues, in which a strong interaction between the unsaturated Lewis metal sites decorating the pores and the CO_2 molecules is observed (**Figure 5**). This high interaction contributes to the high adsorption of 20 wt% CO_2 at 1 atm and 303 K of MOF-74 analogues.[27]

Introduction of basic Lewis moieties are also reported to be beneficial for CO_2 adsorption.[26] The amines with free electron pairs interact with the CO_2 quadruple increasing its heat of adsorption. For example, the diamine, N-dimethylethylenediamine (mmem), has been grafted in the Mn(II)-based MOF with formula $H_3[(Cu_4Cl)_3(BTTri)_8]$ (known as CuBTTri; where H_3BTTri is 1,3,5-tri(1H-1,2,3-triazol-4-yl)benzene) with exposed unsaturated metal sites, resulting in an increase of CO_2 heat of adsorption and in a higher selectivity.[28] The CO_2 adsorption reached 16 wt% at atmospheric pressure and 298 K. Here, tunnability of MOFs is a major advantage due to the ease incorporation of functional groups in the pore walls.

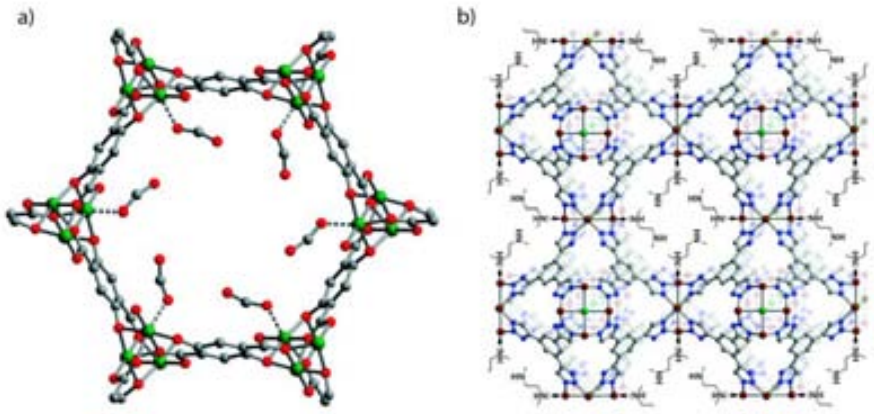

Figure 5. (a) Crystallographic structure of Ni-MOF-74 in which interaction of CO_2 with the unsaturated Ni(II) ions is shown by a doted line.[27] (b) Illustration of the Functionalization of Cu-BTTri through binding N,N-dimethylethylenediamine (mmen) to the open metal coordination sites to increase its CO_2 heat of adsorption.[28]

2.1.1.3. CH_4 adsorption

In the last years, economic and environmental considerations have increased the interest in natural gases, comprising mainly CH_4 as a fuel for transportation and especially, as a replacement for petrol (gasoline). From an environmental point of view, CH_4 delivers roughly twice the energy of coal with the same amount of carbon dioxide released. From an economical point of view, the price of natural gas has lived a spectacular recent drop in price due to deployment of inexpensive technologies for its recovery from shale.

The remaining challenge to use CH_4 as a source of energy is its mass- and volume-efficient, storage at ambient temperature and its delivery. Currently, CH_4 is stored at very high

pressures (250 bar) in most natural gas powered vehicles. While it is suitable for large vehicles such as buses, this solution is less than satisfactory for cars. The Department of Energy (DOE) of United States estimated that storage of 263 V/V is required for practical on board applications. Therefore, finding new alternative storing systems is today a priority.

In this sense, MOFs have shown excellent capabilities to store high amounts of CH_4 at low pressure compared to an empty tank. Hupp and co-workers recently reported a detailed comparison of CH_4 sorption capacities of a wide range of MOFs (**Figure 6**). Surprisingly, the archetypical $Cu_3(BTC)_2$ (known as HKUST-1; where BTC is 1,3,5-benzenetricarboxylic acid) exhibits the highest volumetric uptake, reaching 267 V/V storage at 65 bars and therefore, meeting the required target.[29] For comparison, an empty tank stores this amount of CH_4 at 255 bars. This high value is attributed to a combination of its high metal density which allows methane-metal interactions at low pressures, and of its small cages, which increase the methane-methane interactions at high pressure, favouring the cooperative adsorption. The combination of both effects explains why HKUST-1 outperforms MOFs with much larger surface areas.[30] This high methane storage capacity demonstrated by MOFs has attracted the attention of the chemical industry to use them as an on-board tank of CH_4 for vehicles. First prototypes of vehicles powered by CH_4 stored in a tank filled with a MOF have been yet developed by BASF.[31]

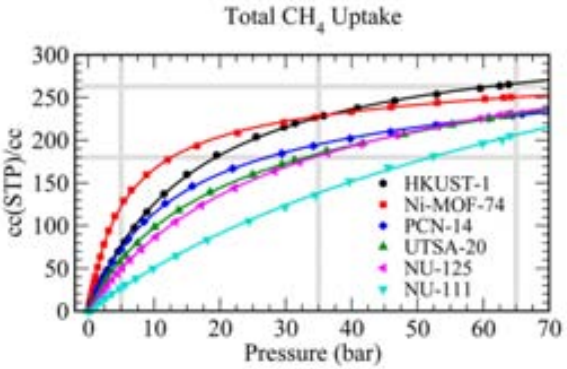

Figure 6. Comparison of the total volumetric and gravimetric uptakes for six iconic MOFs. The gray horizontal lines show the old and new Departmemt of Energy (DOE) targets for volumetric methane storage.[29]

2.1.1.4. Gas separation and purification

The preferential adsorptions of one gas over another can be exploited to purify or separate gas mixtures. One way of promoting gas selectivity is based on the relative size of the molecule compared to the pore (*i.e.* based on kinetics). Therefore, the ease of pore size tunning in MOFs can be used to prepare molecular sieving. For instance, $Zn(PhIm)_2$ (known as ZIF-7; where PhIm is benzimidazole) with an estimated pore size in between H_2 and CO_2 was used to separate mixtures of these gases.[32] The presence of metal open sites also promotes preferential interaction with gases depending on their chemical formulation (thermodynamic effect). De Long *et al.* demonstrated the potential of this approach by studing the different hydrocarbon affinity towards unsaturated Fe(II) ions in the Fe-MOF-74 structure (**Figure 7**).[33] It was observed that the adsorption capacity increased with the unsaturation, being the most adsorbed gas acetylene. This selectivity can therefore be exploited to separate pure gases from naphtha cracker. In conclusion, both topology and functionality in the pores of MOFs can be exploited to resolve gas mixtures.

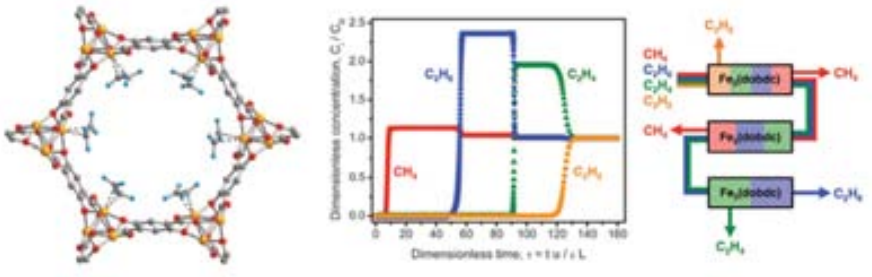

Figure 7. (Left) Structure of the complex Fe-MOF-74·acetylene determined by neutron powder diffraction, showing interactions between the triple bond and the Fe(II) ion. (Right) Breakthrough calculations for hydrocarbon mixtures.[33]

2.2. Catalysis

MOFs share with zeolites several characteristics that make them attractive for catalysis. Some of these characteristics are their ordered arrangement of active centres (metallic ions and organic moieties), homogenous and tunnable pore size and chirality. However, their use as catalysts suffers from drawbacks, including their low chemical stability in some solvents (especially water), low thermal stability and the fact that the metal centres are fully coordinated in many structures, provoking a decrease of their catalytic activity.

Lewis acid sites are long reported as catalytically active for a myriad class of reactions, such as oxidations, condensations and alkylations. In fact, they have been extensively exploited in zeolites. Thus, one way of conferring acidity to the MOF is through the generation of open-

metal sites. Open-metal centres in MOFs can be obtained by removing guest solvent molecules coordinated to these metal centres. For example, upon dehydration of HKUST-1, the water molecule coordinated to the Cu(II) ions is lost, changing the number of coordination of Cu(II) ions from 5 to 4. The formation of these metal open sites makes HKUST-1 an effective catalyst for acid catalysed reactions.[34] $Fe_3Cl(H_2O)_2O(NH_2\text{-}BDC)_3$ (known as MIL-101; where NH_2-BDC is 2-aminoterephthalic acid) has also shown good catalytic properties. As in the case of HKUST-1, it contains coordinated water molecules that can be removed upon dehydration giving rise to active metal sites. In addition, it can be synthesised with Cr(III) and Fe(III) ions, adding tunnability to its catalytic performance, it has very big pores, and it is thermally and chemically stable. All together make MIL-101 a good catalyst that showed its potential, for instance, in carbonyl cyanosilylation and oxidation reactions.[35-37]

The introduction of unsaturated metals in the structure is not the only approach to make catalytically active MOFs. Even if it is still rare, organic building blocks can also be used. For instance, Kitagawa *et al.* noted that the non-coordinated carbonyl oxygen found in the pillared Cu_2(PZDC)(PZ) (where PZDC is pyrazine-2,3 dicarboxylate and PZ is pyrazine) had a strong basic Lewis character. This feature was exploited to strongly adsorb acetylene and promote its polymerization on the microporous channel.[38] In another example reported by Hasegawa *et al.,* the Lewis basic character of non-coordinated amines or amides were used to catalyse Knovenagel condensation reactions. In this case, the organic ligand used to prepare the MOF had two distinct moieties: three pyridine groups to coordinate Cd(II) ions and three amide groups that were responsible for the catalytic activity. This structure was effective in catalysing the Knovenagel reaction with small substrates, reaching conversions up to 98%.[39]

This approach is somehow challenging because it is difficult to prepare MOF structures with free reactive organic ligands located on the pore surfaces since they always tend to coordinate with metal ions. As an alternative, post-synthetic procedures can be employed to introduce functional organic groups into the MOF structure. These functional groups can be introduced by two different ways: (i) covalent modification of the organic linker; and (ii) by grafting molecules at coordinative vacancies in the metal centre, as shown in **Figure 8.**[40] This last methodology was used to coordinate proline chiral molecules bearing a pyridine moiety to the open-metal site of Cr-MIL-101. This simple modification increased its performance in aldol reactions between aromatic aldehydes and ketones.[41]

MOFs can also incorporate catalytic activity by incorporating guest active species. These species can be metal complexes, such as metalloporphyrins, polyoxometalates or inorganic nanoparticles. One of the advantages of confining molecular complex catalysts in MOF cavities is that the catalytic system becomes heterogenous and therefore, the recovery of

the catalyst becomes simpler. An example of that was provided by Eddaoudi *et al*., who achieved the encapsulation of porphyrin inside the cages of $In(HImDC)_2$ (where HImDC is 4,5-imidazoledicarboxylic).[42] Here, the porphyrin was incorporated during the synthesis of the MOF because its post-synthetic incorporation was not possible due to the small size of the channels compared to the porphyrin. Finally, the metalloporphyrin was synthesised by impregnating the porphyrin@MOF in a solution containing the metal ion. The MOF supported catalyst proved its activity and recyclability in oxidation of alkanes.

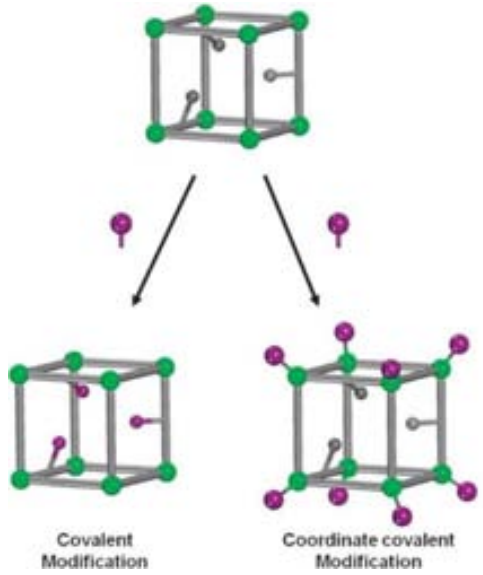

Figure 8. Schematic illustration showing the two exsisting strategies for the post synthetic modification of MOFs.[40]

Another type of species that can be incorporated in MOFs are catalytic inorganic nanoparticles (INPs). MOFs can be excellent support materials for INPs because they have high surface areas and an excellent regularity of the cavities, which enables narrow size distributions of the embedded INPs. INPs are generally incorporated into MOFs by first immersing the MOF into a solution containing the metal nanoparticle precursors (generally in their ionic form) or by gas phase loading when these precursors are volatile.[43] Then, a typical reduction reaction of the precursors adsorbed in the MOF is undertaken to form the INP inside its cavities. Thus, the MOF cavities become a template for the synthesis of the INPs.[44] To date, a great variety of INPs have been incorporated into MOFs, thereby allowing their use as heterogeneous catalysts for a wide range of reactions. For example, MOF-5 loaded with Pd NPs have shown good performance in the hydrogenation reaction of aromatic and aliphatic alkenes.[45] The use of MOFs loaded with INPs also enables size selective catalysis due to the tunnability of their pore size and shape. Thus, Fe-MIL-101 loaded with Pd nanoparticles showed good performance in the hydrogenation of ketones to alcohols. While conversions up to 100% were achieved for small ketones, no reaction was observed in the case of bulky ketones.[46]

Finally, chiral MOFs have also shown promising catalytic capacity for solid asymmetric catalysts. In fact, while zeolites outperform MOFs in Lewis acid catalysed reactions due to their superior thermal and hydrolytic stability, chiral catalysis in MOFs is unmatchable for zeolites due to their larger opened channels and richness in chiral structures. For example, the chiral MOF with formula $Cd_3Cl_6L_3$ (where L is (R)-6,6′-dichloro-2,2′-dihydroxy-1,1′-binaphthyl-4,4′-bipyridine) and post synthetically functionalized with Ti(IV) complex showed excellent activity in the addition of alkylzinc on aromatic aldehydes converted to chiral secondary alcohols (**Figure 9**).[47] Interestingly, the enantiomeric excess of the reaction was dependent on the pore size, reaching up to 84% for the larger pores.[48] The use of enantiomers of salen-based complexes have also been reported to make chiral MOFs. Enantiopure Mn(II)-based salen complexes functionalized with carboxylates were used as building block for the synthesis of a chiral MOF, which was catalytically active for the epoxidation of olefins, reporting an impressive enantiomeric excesses of 92 %.[49,50]

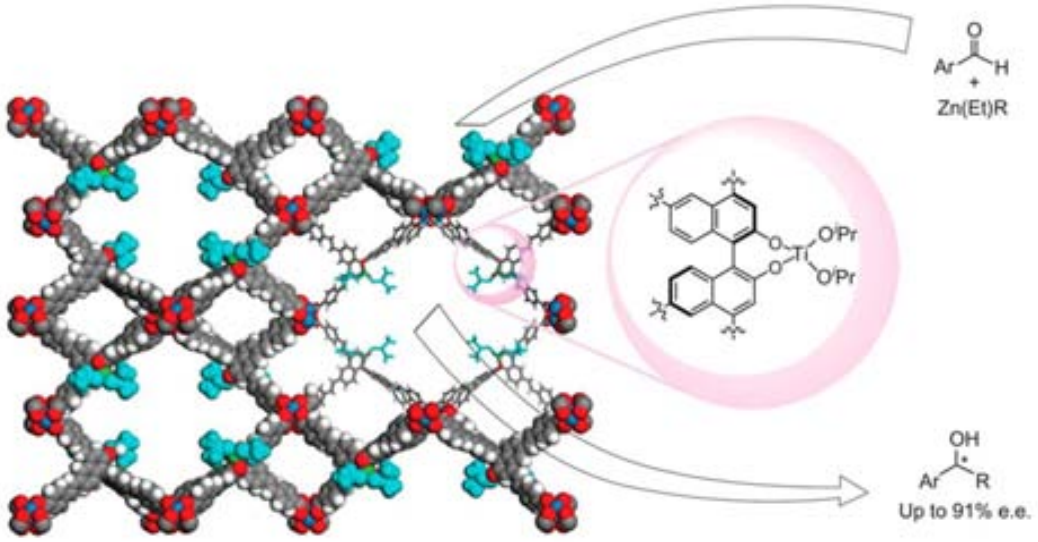

Figure 9. Schematic illustration of the homochiral [(BINOL-TC)Cu_2)] built up from the enantiopure binol tetracarboxylate and its asymmetric alkyl addition activity.[48]

3. Nanoscale Metal-Organic Frameworks (NMOFs)

Although MOFs show high promise for many of the aforementioned research areas, they do not always fulfill the relevant requirements for specific applications. For some applications, MOFs must be miniaturised. Miniaturisation of MOFs down to the sub-micrometer regime (100–1000 nm), and further down, to the nanoscale (1-100 nm), is very important, as it bridges the gap between current MOF science and device-material fabrication in nanotechnology. NanoMOFs may exhibit different and/or enhanced properties and reactivity compared to the traditional bulk materials.

For example, nanoscopic dimensions are typically required to provide materials of sufficiently small sizes for their internalisation into cells, and this limits the applications of macroscopic MOFs as delivery vehicles, diagnostics, etc. But NMOFs can combine these small dimensions with the possibility to design architectures with well-defined and uniform sizes and morphologies, to disperse them in aqueous media or other solvents, and to efficiently coat them for improving their biocompatibility or recognition capabilities. Of particular interest is also the fact that nanomaterials have higher surface areas than do their macroscopic counterparts. This property can strongly influence or even improve the catalytic, ion exchange, separation, sensing and sorption properties of NMOFs, which, in turn, can be dependent of their sizes and shapes. A similar situation occurs with some physical properties. It is well known that unique physical properties emerge when at least one dimension of a material is reduced to the nanometer scale. Thus, NMOFs are also expected to hold highly desirable size-dependent optical, electrical and magnetic properties.

Overall, NMOFs can show size-dependent properties which, if properly exploited, may expand the scope of these materials in numerous practical applications, including drug-delivery, contrast agents, sensor technology, functional membranes and thin-films, while opening up novel avenues to more traditional storage, separation, and catalysisapplications. Because of their potential advantages, huge efforts have been recently dedicated to develop synthetic methodologies and use them to prepare NMOFs. In the following section, the recent advances in the synthesis of NMOFs are discussed as well as the new prospects for these materials.

3.1. Synthesis of NMOFs

Two main approaches can be taken when it comes to miniaturise MOFs: (i) Confinement of the supramolecular assembly that leads to MOF formation at nanoscopic locations; for example by using emulsions or templates; and (ii) favouring the nucleation versus crystal growth, for example, by using fast precipitation methods or by using microwave and ultrasound synthesis. The two approaches are schematised in **Figure 10**.

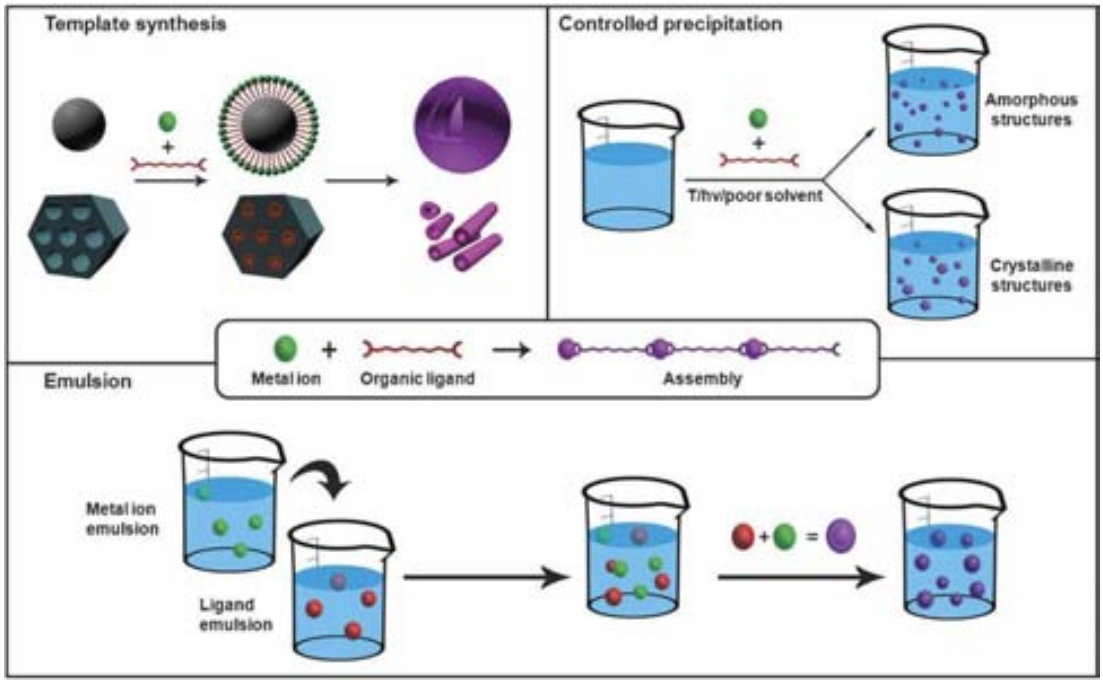

Figure 10. Schematic representation of the principal synthetic approaches for synthesising NMOFs, including the layer by layer growth on templates, the controlled precipitation and the microemulsion techniques.[51]

3.1.1. Emulsion based methods

Nanoemulsions are suspensions of small droplets, usually stabilised by surfactants, with diameters ranging from 50 to 1000 nm of one liquid in a second liquid, being the mixture not miscible. These droplets can be used as "nanoreactors" to confine the self-assembly, nucleation and growth of NMOFs. Briefly, this approach usually consists of first dissolving each precursor in the solvent that will be dispersed. A water-in-oil, or reverse phase emulsion, is then prepared with the aid of a surfactant, and the collisions between droplets containing those precursors or the application of external stimulus, such as temperature, light or microwave radiation, induce their polymerisation, thus delimiting their growth inside the nanodroplet. For example, by dissolving Prussian blue precursors in water, using this solution to create a water–in-oil emulsion and further exposing this emulsion to daylight, Mann *et al.* synthesised the first example NMOF: Prussian blue nanocrystals.[52] Since then, emulsions have been successfully used to produce nanocrystals of heterometallic cyanometalates, Prussian blue analogues using triazole instead of cyano groups and Gd(III)-based NMOFs. For example, Lin *et al*. successfully applied the solvothermal assisted reverse phase emulsion method to prepare a series of lanthanide-based NMOFs. Interestingly, the size of synthesised NMOFS was tuned with the *w* ratio (water to surfactant molar ratio), ranging from 50 nm in length at low *w* to 2 μm in leght at high *w*.[53]

Besides the use of the internal volume of the nanodroplet as "nanoreactors", these emulsions have also the potential to be used as templates to prepare metal-organic nanoshells. In this case, the polymerisation must be induced on the surface of the emulsion droplet by using, for instance, a chemical affinity surfactant. Thus far, this strategy has been used by Wang *et al*., who synthesised the first examples of Prussian blue nanoshells.[54] These shells were synthesised by preparing an oil-in-water emulsion with an organometallic surfactant terminated with pentacyano(4-dimethylamino)-pyridine)ferrate. Then, the addition of Fe(III) ions to the aqueous solution induced the coordinative polymerisation between them and the surfactant, thereby creating a metal-organic shell on the interface of each droplet.

An alternative method to confine the MOF synthesis in micrometic reactors uses microfluidic techniques. Coronas *et al.* used a microfluidic devise to disperse polar solvent droplets containing the MOF precursor into a continuous oil flow. The droplets were generated by breaking the polar solution off into the co-flowing oil flow. The confined reaction environment enabled a faster synthesis of the $Fe_3O(BDC)_3$ (known as MIL-88B). In addition, the size of the crystal could be controlled by varying the residence time of the microdroplets in the reactor. Thus, at short residence time (30 s), the mean crystal size was 180 nm, whereas when the residence time was increased to 900 s, the crystal size increased to 900 nm.[55]

3.1.2. Hard templates

Nanomaterials are also excellent candidates to be used as templates for fabricating NMOFs. In this methodology, a film of supramolecular metal-organic polymer is deposited on the template by using a deposition technique, such as layer-by-layer (LBL) growth. This deposition followed by the removal of the template using thermal or chemical techniques, can leave behind a metal-organic nanostructure that mimics the shape and size of this template. Martin *et al.* reported an example that illustrates how powerful this technique can be. The LBL growth of a film composed of Zr(IV) metal ions and diorganophosphonate ligand on the pores of an alumina membrane followed by the removal of this membrane using phosphoric acid allowed the formation of highly uniformed metal-organic nanotubes[56]. In this case, the interaction between the alumina and Zr(IV) ions was exploited to attach the metal-organic structure on the template during the growing process.

The intrinsic supramolecular character of NMOFs makes them very responsive systems towards weak interactions present in the reaction media. For example, metal nanoparticles functionalized with different active groups can be used to induce seeded nucleation by selective interaction with the building blocks, altering the formation rate and size of the final product. Oh *et al*. employed this template strategy to induce the nucleation of NZIF-8 ($Zn(MIM)_2$; where MIM is 2-methylimidazole) on the surface of a carboxylated polystyrene (PS) microsphere.[57]

Carboxylate-terminated polystyrene (PS) microspheres were added to the solution containing the precursors of ZIF-8, and the mixture was heated. By preferential interaction of the Zn(II) ions with PS surface, crystallisation was induced on the surface of the particle leading to a shell of NZIF-8. Interestingly, repeating the reaction in several cycles, the thickness of the shell increased and also its integrity. This process made possible the dissolution of the template without altering the shell of ZIF-8, leading to a hollow sphere of NZIF-8.

3.1.3. Controlled precipitation

A second family of methodologies to prepare NMOFs is based on mixing the precursors under certain reaction conditions that favour the fast nucleation (to increase the seed number and reduce the crystal growth rate). In most of the cases, these conditions involve the use of microwave radiation, ultrasounds, temperature or the addition of a base. For example, it is well known that at high temperatures, solubility of the precursor increases avoiding fast precipitation and allows crystallisation to occur. It is therefore a strategy generally used to produce bulk MOFs, crystals suitable for single crystal resolution. However, if one controls certain reaction conditions, including solvent, temperature, pH, and time, solvothermal synthesis can be a very productive strategy for synthesising a wide variety of NMOFs. Some of them were recently reported by Horcajada, Gref *et al,*. who synthesised a series of NMOFs (in particular, ($Fe_3O(H_2O)_2Cl(BTC)_2$), known as MIL-100, MIL-101 and $Fe_3O(fumarate)_3$, known as MIL-88) by simply mixing Fe(III) metal ions with a series of multitopic carboxylated ligands, BDC, BTC, fumaric acid, *etc*., in a variety of solvents above 100 ºC.[58] Here, it was found that the temperature and reaction time usually play a major role in the crystal size under solvothermal conditions. The effect of both parameters was studied in detail in the synthesis of NMIL-88A, showing that low temperatures and reaction times promote the formation of sub-200 nm crystals. However, under these conditions, it was also observed that good crystallinity and yields are difficult to obtain.[59]

The use of microwave radiation and ultrasounds can also be exploited to produce NMOFs. Ni and Masel reported for the first time the use of microwave radiation to induce the precipitation of the Zn(II)-based MOFs, IRMOF-1, 2 and 3 (based on the BDC ligand), at the nanometre scale.[60] This reaction consists in exposing a diethylformamide (DEF) solution of the building blocks at 150 W for only 25 seconds. Similarly, sonochemical synthesis can lead to homogeneous nucleation and a substantial reduction in crystallisation time. The well-known MOF-5 was miniaturised at the micrometric scale using this approach.[61]

Careful choice of reactants and solvents can assist in the fast nucleation and precipitation of NMOFs. The use of a poor solvent to induce fast precipitation is a technique generally used to synthesise amorphous coordination polymers.[62] However, in some cases, it can also lead to the precipitation of crystalline NMOFs. For example, the addition of ethanol to a solution of $Cu(Ac)_2$ and BTC in butanol led to the fast precipitation of HKUST-1 with an average size of 138 nm.[63] Interestingly, the amount of ethanol added had an influence on the crystal size; *i.e.* bigger amounts of ethanol induced a faster precipitation and therefore, the formation of smaller crystals.

Inorganic precursors can be delivered in a variety of forms depending on the counterion used. For instance, it is well known that acetates have different reactivity than sulphates or nitrates. The choice of these precursors can therefore alter the MOF crystallisation, which might have an impact on the final crystal size. With this concept, Férey *et al.* presented the so called controlled SBU approach, which consisted in using metal sources with the same coordination as the SBU of the desired MOF.[64] MOF reaction proceeded through a ligand exchange between the initial ligand in the metal source and the organic ligand of the MOF. Metal acetates are excellent inorganic precursor for this approach because, in many cases, the metal ion is found in the same coordination as in the SBU. For example, $Cu(Ac)_2$ is found in the form of a paddle-wheel with the formula of $Cu_2(Ac)_4(H_2O)_2$ in solution, which is the same coordination geometry found in many Cu(II)-based MOFs. Also, $Zn(Ac)_2$ in its basic form of $Zn_4O(Ac)_6$ presents the same Zn(II) coordination as in the IRMOF family. And the $Fe(Ac)_3$ with formula $Fe_3O(Ac)_3$ presents the same trimeric metallic cluster with octahedral coordination and connected through shared μ_3-O than MILs. Using this approach, due to the similarity in the coordination environment between the metal precursor and the MOF, the reaction proceeds faster resulting in smaller crystals. In addition, the basic character of the acetate anion promotes the ligand deprotonation, which also fastens the reaction. Furthermore, the precursor ligand (generally a monocarboxylic acid, and more commonly acetate) can also act as a capping agent, further preventing the crystal growth (see also below). To date, the potential of this approach has been demonstrated by synthesising a wide variety of NMOFs: $Fe_3O(CH_3OH)_3Cl(BDC)_3$ (known as MIL-89)[65], MOF-5[66], MOF-74[67] and HKUST-1[68] are just some examples of MOFs nanostructured by this methodology.

The use of an excess of the ligand can also induce fast nucleation and reaction times. ZIF-8 nanocrystals of 70 nm were prepared in aqueous media and room temperature just by mixing $Zn(NO_3)_2$ and a big excess of the ligand MIM. In this case, the excess of ligand may have two roles: (i) induce a fast reaction with the metallic precursor; and (ii) inhibit the growth of the formed seeds.[69] An alternative method to induce a fast nucleation is the use of a base that

deprotonates the ligand and accelerates the reaction. MOF-5 was miniaturised to a range of 100-350 nm by simply adding triethylamine to a solution of $Zn(NO_3)_2$ and BDC in DMF.[70]

Kitagawa *et al.* developed an alternative method to synthesize NMOFs. Conceptually, it consisted in preventing the crystal growth of the metal-organic seeds at an early stage with the aid of a capping agent or modulator. The capping agent has the same functionality as the organic building block and therefore, it can alter the coordination equilibrium between the metal ion and the organic linker. This competition between the capping agent and the linker offers the possibility to modulate the rate of the framework extension and the crystal growth.[71] The approach is illustrated in **Figure 11**. In a first example, acetic acid was used to compete with the coordination between the dicarboxylic acid, 1,4-naphtalenedicarboxylic acid (ndc), and Cu(II) ions in the formation of $Cu_2(NDC)_2(DABCO)$ (where dabco is 1,4-diazabicyclo[2.2.2]octane). The capping agent stopped the crystal growth to cubic nanocrystals of 77 ± 13 nm-in-size at short reaction times. In addition, the capping agent also induced an epitaxial growth of the crystals due to its preferential coordination to one of the crystals facets. Therefore, nanorods of 392 ± 210 nm-in-length of the same MOF were also achieved at longer reaction times. Recently, the use of surfactants and diblock polymers have also been employed to prevent the growth of the metal-organic seeds.[72]

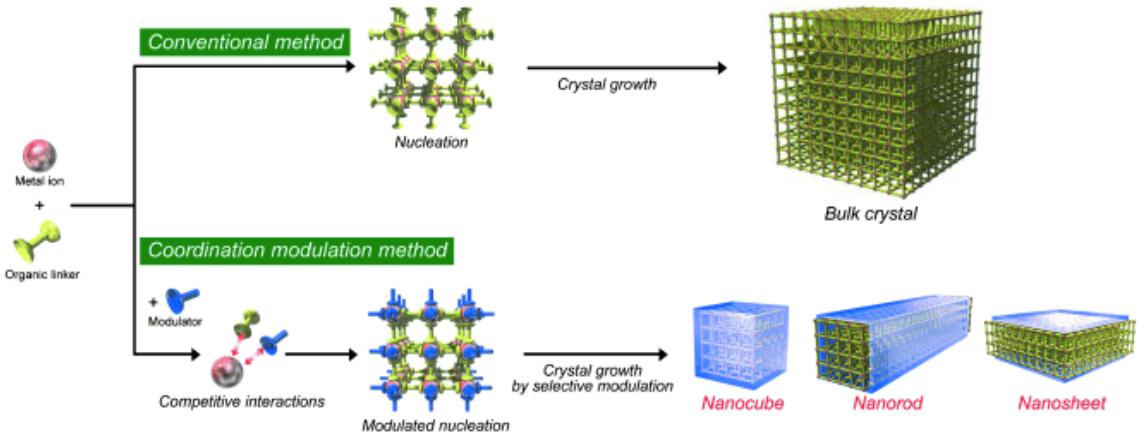

Figure 11. Effect of the capping agent on the crystal growth of a MOF.[71]

3.1.4. Top down approach

Even if it is still very rare, some advances in the use of top-down methods to synthesise NMOFs have been made. $Zn_2(BDC)_4(H_2O)_2$ (known as MOF-2) is based on the paddle-wheel SBU defined by the coordination of two Zn(II) ions with four BDC ligands, creating a 2D network. In the crystal structure, the 2D sheets pack through Zn···O interaction, which give rise to a 3D porous framework.[14] Xu *et al.* used ultrasounds to defoliate the structure to obtain nanosheets of MOF-2.[73] This approach relies on the delamination or exfoliation of MOF nanosheets from bulk MOF crystals using ultrasonication irradiation or other methods. The delamination step was performed by dispersing dried MOF-2 crystals in acetone, and then subjecting them to ultrasonic radiation at room temperature (confirmed from the observation of the Tyndall effect). Sedimentation of the ultrasonicated suspension afforded a colloidal suspension of MOF-2 nanosheets. The nanosheets had lateral dimensions of 100 to 1000 nm and a thicknesses of 0.7 to 6.0 nm (in agreement with the theoretical thickness of a single MOF-2 nanosheet: 0.7 nm). Similarly, Saines *et al.* obtained several Mn(II), Co(II) and Zn(II)-DMS MOF nanosheets by exfoliating the corresponding bulk MOF crystals.[74] In this case, the exfoliation was done *via* ultrasonication of an ethanolic colloidal suspension of the corresponding bulk MOF crystals. Importantly, some of the resulting nanosheets showed lateral dimensions close to 500 nm and unilamellar thicknesses around 1 nm. This approach has been also used by Xu *et al.*, who exfoliated the 2D layered structure of Cu-TCPP by a modular assembly strategy.[75] With this process, a "modularisation" step was used for the synthesis of highly crystalline "modules" with a nanostructure that can be conveniently assembled into a thin film in the following "assembly" step. This method affords MOF thin films, and it can be easily set up for different substrates at very high speed and with controllable thickness.

3.2. Applications of NMOFs

Miniaturization of MOFs at the nanometre length scale can be advantageous for optimizing their current applications as well as finding new ones because their properties at the nanoscale can be altered with respect to the bulk material, as observed in other nanomaterials. In the following sections, the advantages of NMOFs in the classical applications as well as in new areas such as nanomedicine will be discussed.

3.2.1. Gas sorption in NMOFs

Kitagawa *et al.* first studied the impact of the crystal size on gas sorption. They observed that while the total gas uptake does not seem to change greatly as a function of the crystal size, the adsorption kinetics show to be dependent. In fact, kinetics of gas adsorption seems to be faster in NMOFs.[76] In order to measure the sorption kinetics of HKUST-1, crystals of this MOF were integrated into a Quartz Crystal Microbalance that converts a change of mass to a change of oscillatory frequency. The high gravimetric sensitivity of the device allows quantitative analysis of molecular adsorption and real-monitoring of sorption process. The impact of the crystal size in methanol and hexane adsorption in HKUST-1 was measured by monitoring their adsorption in NHKUST-1 crystals of average size of 138 nm and in bulk HKUST-1 crystals of average size of 614 nm. It was observed that smaller crystals had a faster uptake than the larger ones for the two solvents tested at low partial pressure.[63] The sorption uptake became saturated in few seconds for the NHKUST-1, whereas it took more than 10 s for the larger crystals. However, the total uptake was similar in both crystals.

More surprising is the effect of downsizing the flexible entangled MOF with formula $Cu_2(BDC)_2(BPY)$ in guest sorption. When a bulk flexible MOF adsorb a guest molecule, their configuration change to a so called opened configuration. The crystal structure returns to the initial state (closed configuration) when the guest molecule is desorbed. Interestingly, when the same crystal structure is miniaturised to the nanoscale regime, its opened configuration can be retained upon guest removal. This non-reversibility can be considered a shape memory effect, which could be unique of NMOFs (**Figure 12**).[77] These findings can open new avenues in the field of environmental responsive materials.

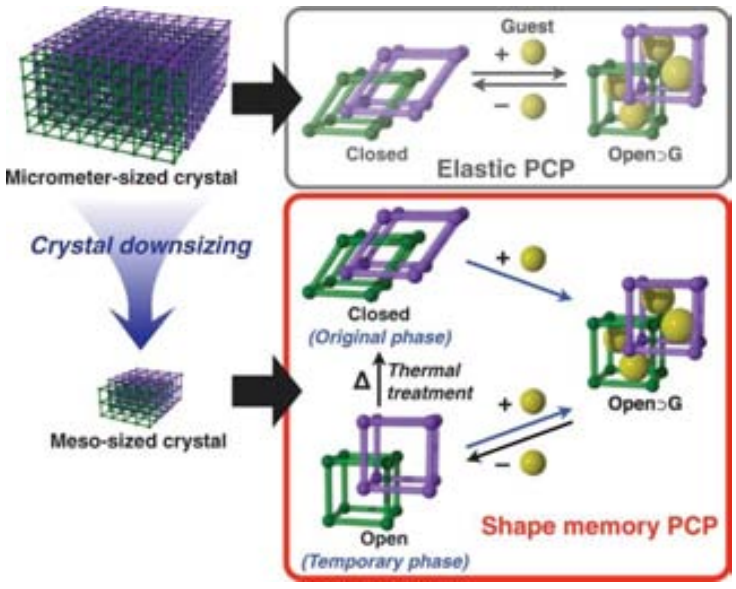

Figure 12. Shape memory effect of NMOFs.[77]

3.2.2. Catalysis in NMOFs

In catalytic systems based on INPs, the size reduction entails an increase of catalytic sites due to the increase of the surface to volume ratio. In this kind of catalytic systems, all the activity is concentrated on the surface of the nanoparticle. However, in a crystalline porous MOF the size dependence it is not so clear since, ideally, all the catalytic sites are available if there are no diffusion limitation problems. Garcia *et al.* studied the effect of downsizing a catalytic MOF by systematically studying bigger substrates and therefore, inducing diffusion limiting conditions. The results showed that by tuning the size of Fe-MIL-100, the catalytic oxidation of aromatic alkanes can be improved when bulky substrates are used.[78] Nevertheless, the effect of crystal size was not noticeable when small substrates were employed demonstrating that the advantage of nanostructuration only becomes evident in a diffusion limited scenario.

3.2.3. Biomedical applications

To date, two main biomedical applications have been explored for NMOFs: drug delivery and biomedical imaging. A crucial aspect to design a MOF for a targeted biomedical application is how the biomedically active agent is incorporated. Three major approaches have been explored: (i) the use of bioactive molecules as building blocks; (ii) adsorb the bioactive molecule in the NMOF's pores; and (iii) incorporate the bioactive molecule through post-synthetic modifactions. All three approaches are schematized in **Figure 13**.

The first approach takes advantage of the versatility in composition of NMOFs to incorporate molecules with biomedical activity in their structure (**Figure 13a**). The main advantage of this approach is the high loadings achieved, typically above 60% in weight. Metal ions with luminescent or magnetic properties, which can be used as probes for bio-imaging, are excellent candidates to be incorporated in the NMOF structure. On the other hand, drug molecules, even though they generally possess coordinating groups, are not specifically designed for NMOF synthesis and their incorporation into the structure of the NMOF is more challenging.

The adsorption of bioactive molecules in the structure of the NMOF, which is commonly carried out by immersing the activated MOF in a concentrated solution containing the desired molecule, is a second general approach.[58,79,80] The main advantage of this strategy relies on its versatility because the same NMOF can be used to adsorb a wide range of molecules, being the only limitation the relative size between the molecule and the pore aperture. The drawback is that, since only weak supramolecular interactions are present between the NMOF matrix and the guest molecule, the encapsulation becomes a reversible process

leading to molecular release. For this reason, the sustained release of the encapsulated bioactive molecules (drugs) can be exploited to prepare new drug delivery platforms. However, it is not a methodology generally employed for bio-imaging applications where, in most of the cases, the release of the encapsulated contrast agent has to be avoided due to its toxicity.

The third strategy is perhaps less common. It consists on the covalent attachment of the biomedically relevant molecule to the NMOF through post-synthetic modification. In this methodology, orthogonal non-coordinating groups of the NMOF structure are used to covalently attach the bio-active molecule (**Figure 13c**).[81] The covalent attachment of the bio-active molecule ensures a slower release, as it only takes place when the NMOF decomposes. In principle, it is also possible to exploit the chemistry of the covalent bond to cleave it under certain physiological conditions, inducing a triggered release. Even though the potential of the approach is high, it also presents some drawbacks, such as the multiple steps required to do the post-synthetic functionalisation and the low loadings typically achieved.

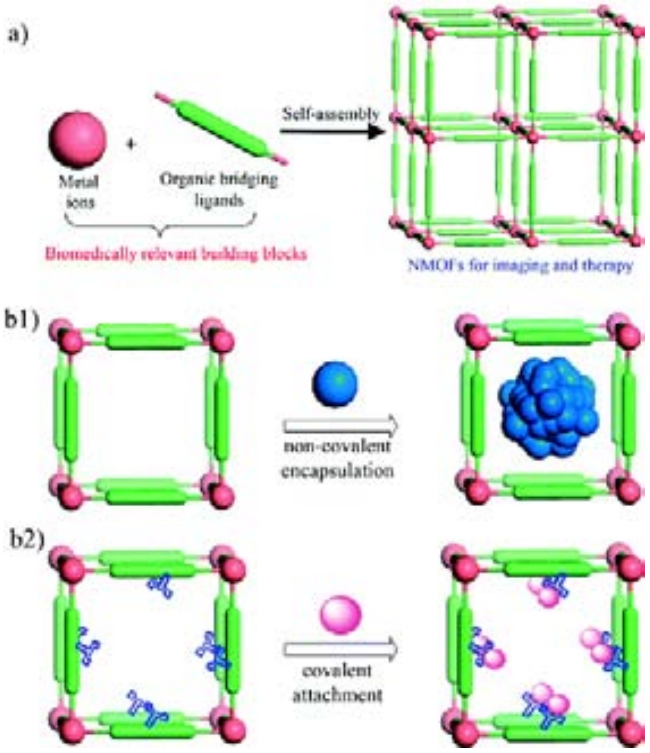

Figure 13. Proposed strategies incrorporate biomedical properties to MOFs: use biomedically relevant building blocks (a), incorporate bioactive molecules in a synthesised MOF by impregnation (b1) and post synthetic covalent attachment (b2).[82]

3.2.3.1. NMOFs for drug delivery

Nanostructured drug delivery agents can improve biodistribution of medicines and their pharmacokinetics, leading to less and more effective dose. In fact, the first drug delivery nanosystems based on liposomes have already been approved and commercialised (Doxil, Abraxane and Ambisome). Purely organic (like liposomes) and inorganic (like zeolites or mesoporous silica) nanomaterials have been proposed as nanocarriers. However, organic containers lack from low drug loadings (less than 5% w/w), whereas zeolites have some toxicity concerns. In this context, NMOFs seem to have great potential due to their superior drug loading and their low toxicity when non-toxic building blocks are used.[83,84]

First insights in the adsorption of drugs in MOFs were provided by Férey *et al.* The model ibuprofen drug was encapsulated in Cr-MIL-101 and Cr-MIL-100 by impregnation with exceptional loadings of 1.38 g and 0.35 g of ibuprofen per gram of Cr-MIL-101 and MIL-100 respectively. The large mesoporous cages present in MIL-101 were responsible of this high drug loading. Interestingly, the high drug loading was accompanied with a slow release in the order of days in a simulated body fluid.[79] The observed slow release was attributed to the stability of the NMOFs in the tested media. Since these first examples, the catalogue of encapsulated drugs as well as NMOFs used has grown substantially. Horcajada *et al.* recently published the successful encapsulation of a wide range of drugs of distinct size and hydrophobicity, including antitumoral drugs such as doxorubicin, busulfan, cidofovir) in NMOFs composed of Fe(III) and carboxylates ligands; namely, MIL-100, MIL-101, MIL-53 and MIL-88. Interestingly, in some of the cases, the successful design of the NMOF-based drug delivery system was confirmed by proving the controlled and progressive release of the encapsulated drug as well as their *in vitro* anticancer efficacies. All these examples open the way to start considering the use of NMOFs as novel drug delivery systems.[58]

Beyond the ability of NMOFs to adsorb drug molecules, their potential as effective drug carriers depends on the kinetics of the drug release. In this respect, a key parameter is the stability of NMOF in the delivery media. When the NMOF suffers from low stability in the delivery media, the drug release is strongly dictated by NMOF degradation. In these cases, the drug delivery is fast (within hours) and it is characterised by an initial burst release. However, in the cases where the NMOF is stable in the delivery media, the release is dictated by diffusion and intrinsic host-guest interactions play a crucial role. Under these circumstances, the release is slow and sustained, which are attributes desired for drug-delivery applications.[85] For example, the water stable M(OH)BDC (known as MIL-53; where M can be either Fe(III) and Cr(III)) showed a very slow release of the model drug ibuprofen (**Figure 14**). This slow release was not

only attributed to the stability of the MOF but also to its structural flexibility, which allowed for maximized supramolecular interactions between the NMOF matrix and the drug.

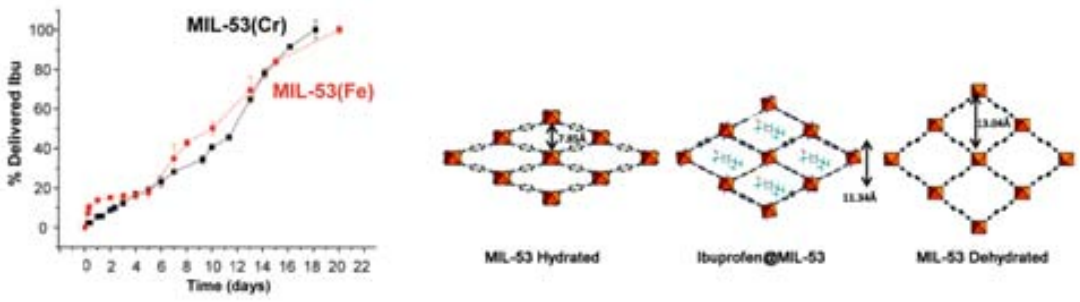

Figure 14. Kinetics release of Ibuprofen encapsulated in MIL-53 in Simulated Body fluid (SBF) (left) and the structure flexibility exhibited by MIL-53 (right).[80]

Lin et al. explored the possibilities of using drugs as building blocks. More than 80% of the drugs have one or more coordination sides such as carboxylates, amines, sulphates and phosphates. For instance, the chemotherapeutic drug Methotrexate (MTX) has two carboxylate groups and two amino groups. The surfactant assisted solvothermal reaction of MTX with transition metals (*eg*. Zn(II) and Zr(IV)) and Gd(III)) lead to nanostructured coordination polymers. In these cases, the average drug loading was higher than 70% in all cases.[86] In this approach, the drug release is related to the structure stability. The particles thus formed with MTX showed low stability and rapid release (half-life of 2 hours). In order to improve the release kinetics, these nanoparticles were coated with a lipid bilayer that significantly increased their stability, being the half-life 23 hours and makeing possible its application as drug delivery agents.

Finally, Serre *et al*. reported the first and, at the moment the only one, porous crystalline MOF based on a bioactive molecule. The isonicotinic acid (also known as vitamin B23) was used to coordinate Fe(II)/Fe(III) ions to give rise to a 3D structure. However, degradation studies showed little stability in physiological media, reporting a total release in 3 hours.[87]

3.2.3.2. NMOFs in biomedical imaging

Among all biomedical imaging techniques, Magnetic Resonance Imaging (MRI) is the most studied for NMOFs to date. MRI is based on the nuclear spin reorientation (also called relaxation) of water protons under a magnetic field. The reorientation process is highly dependent on the chemical environment of the water molecule, which allows mapping the tissue differentiating the diseased areas. However, sometimes, the sensitivity based on spatial resolution it is not sufficient. In these cases, highly paramagnetic ions acting as a Contrast

Agents (CA) are generally required to increase the sensitivity of MRI (detailed fundamental aspects of this technique is provided in Chapter 4). CAs interact with the protons in the water molecules on the tissue altering its relaxation times under the magnetic field. The performance of a CA is evaluated according to their capacity to increase water relaxation per concentration of CA; typically expressed as relaxivity ($mM^{-1} \cdot s^{-1}$). NMOFs are excellent candidates to act as CAs because they can be composed of highly paramagnetic metals ions, such as Gd(III) and Mn(II), and their small sizes allow different biodistribution and opportunities beyond the conventional imaging of chemical agents.

First reports evaluating the potential of NMOFs as CAs were provided by Lin *et al.* They used the reverse microemulsion method to synthesise NMOFs based on Gd(III) ions and carboxylic ligands (BDC, 1,2,4-tricarboxylic acid, and mellitic acid). The resulting NMOFs showed relaxativity values one order of magnitude higher than the commercially available molecular CA.[53,88] The increased performance was attributed to the high loading of Gd(III) ions per particle and their reduced mobility. However, the study on their degradation and stability was not reported. This is a key issue since the delivery of free Gd(III) ions is highly toxic. Here, due to the concerns raised by the Gd(III) toxicity, NMOFs based on the paramagnetic but less toxic Mn(II) ion have also been prepared. However, these NMOFs showed poor stability in water and therefore, could not be used as CAs by themselves. However, they were envisaged as carriers of Mn(II), ions which were delivered shortly after incubation acting as CAs in the delivered areas.[89]

Fe(III) is also active in MRI by shortening the transversal relaxation of water protons producing a negative contrast on the image. Férey *et al.* reported the synthesis of a wide range of NMOFs composed of Fe(III) and carboxylate ligands.[58] Among them, the CA properties of the NMIL-88A were evaluated. A transversal relaxivity of 56 $s^{-1} \cdot mM^{-1}$ was reported, which is considered sufficient for *in vivo* applications. In fact, and due to the NMOF's nontoxic behaviour, the first *in vivo* MRI image using a NMOF as a CA could be taken. **Figure 15** shows the negative contrast produced by the injection of a suspension of NMIL-88A on a rat.

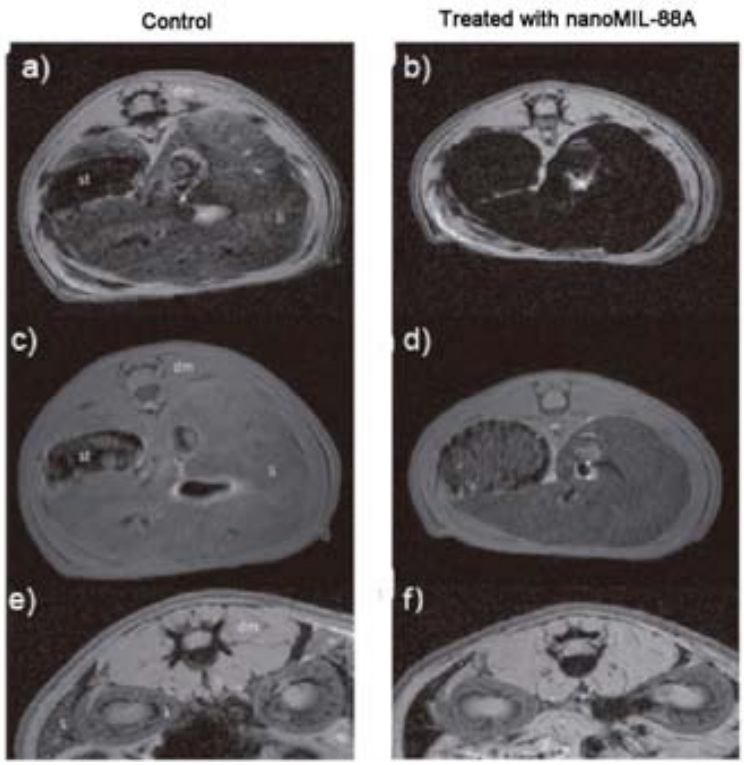

Figure 15. MRI images of control rates (left) and rats injected with 220 mg kg^{-1} of MIL-88A nanoparticles.[58]

Optical luminescence based on the excitation of dyes by visible light can also be a field of application for NMOFs. Especially owing to their capacity to carry high loadings of dyes, and if targeted, carry them to the point of interest. Even though many MOFs report luminescent properties,[90] it is still rare their evaluation in biomedical imaging. Lin *et al*. used the luminiscent Ru(IV) phosphorescent complex with formula Ru(5,5'-$(CO_2)_2$-BPY)$(BPY)_2$ as a building block to construct a NMOF by connecting it through Zr(IV) ions. The resulting NMOF particles showed *in vivo* optical imaging contrast and high cell uptake.[91]

The computed tomography (CT) imaging uses the X-ray attenuation caused by atoms with high atomic number (Z) as a diagnostic technique capable of providing *in vivo* three dimensional images with good spatial resolution. The potential of NMOFs as a CA for CT lies in their chemical versatility, which enables creating structures with high Z ions, such as Zr(IV) and Hf(IV)[92] as metal nodes. In a recent example, Zr(IV) or Hf(IV) were combined with BDC to synthesise two analogues of the UiO-66 structure, which has a high metal density. Remarkably, both UiO-66 analogues showed good dispersability and stability in physiologically simulated media. In addition, the Hf(IV) analogue showed higher X-ray attenuation efficiency than the iodinated molecular CA currently used in CT.

4. References

(1) Jousten, K. *Handbook of Vacuum Technology*; Wiley-VCH ed., 2008.
(2) Everett, D. H. *Pure. Appl. Chem.* **1972**, *31*, 578.
(3) Ma, Y.; Tong, W.; Zhou, H.; Suib, S. L. *Microporous Mesoporous Mater.* **2000**, *37*, 243.
(4) Davis, M. E. *Nature* **2002**, *417*, 813.
(5) Wilson, S. T.; Lok, B. M.; Messina, C. A.; Cannan, T. R.; Flanigen, E. M. *J. Am. Chem. Soc.* **1982**, *104*, 1146.
(6) Davis, M. E.; Saldarriaga, C.; Montes, C.; Garces, J.; Crowder, C. *Zeolites* **1988**, *8*, 362.
(7) Rocha, J.; Anderson, Michael W. *Eur. J. Inorg. Chem.* **2000**, *2000*, 801.
(8) Clearfield, A. *Current Opinion in Solid State and Materials Science* **1996**, *1*, 268.
(9) Furukawa, H.; Cordova, K. E.; O'Keeffe, M.; Yaghi, O. M. *Science* **2013**, *341*.
(10) Hoskins, B. F.; Robson, R. *J. Am. Chem. Soc.* **1989**, *111*, 5962.
(11) Tranchemontagne, D. J.; Mendoza-Cortes, J. L.; O'Keeffe, M.; Yaghi, O. M. *Chem. Soc. Rev.* **2009**, *38*, 1257.
(12) Eddaoudi, M.; Kim, J.; Rosi, N.; Vodak, D.; Wachter, J.; O'Keeffe, M.; Yaghi, O. M. *Science* **2002**, *295*, 469.
(13) Kondo, M.; Yoshitomi, T.; Matsuzaka, H.; Kitagawa, S.; Seki, K. *Angew. Chem. Int. Ed.* **1997**, *36*, 1725.
(14) Li, H.; Eddaoudi, M.; Groy, T. L.; Yaghi, O. M. *J. Am. Chem. Soc.* **1998**, *120*, 8571.
(15) Li, H.; Eddaoudi, M.; O'Keeffe, M.; Yaghi, O. M. *Nature* **1999**, *402*, 276.
(16) Farha, O. K.; Eryazici, I.; Jeong, N. C.; Hauser, B. G.; Wilmer, C. E.; Sarjeant, A. A.; Snurr, R. Q.; Nguyen, S. T.; Yazaydın, A. Ö.; Hupp, J. T. *J. Am. Chem. Soc.* **2012**, *134*, 15016.
(17) Czaja, A. U.; Trukhan, N.; Muller, U. *Chem. Soc. Rev.* **2009**, *38*, 1284.
(18) Schlapbach, L.; Zuttel, A. *Nature* **2001**, *414*, 353.
(19) Farha, O. K.; Özgür Yazaydın, A.; Eryazici, I.; Malliakas, C. D.; Hauser, B. G.; Kanatzidis, M. G.; Nguyen, S. T.; Snurr, R. Q.; Hupp, J. T. *Nat. Chem.* **2010**, *2*, 944.
(20) Furukawa, H.; Ko, N.; Go, Y. B.; Aratani, N.; Choi, S. B.; Choi, E.; Yazaydin, A. Ö.; Snurr, R. Q.; O'Keeffe, M.; Kim, J.; Yaghi, O. M. *Science* **2010**, *329*, 424.
(21) Ma, S.; Eckert, J.; Forster, P. M.; Yoon, J. W.; Hwang, Y. K.; Chang, J.-S.; Collier, C. D.; Parise, J. B.; Zhou, H.-C. *J. Am. Chem. Soc.* **2008**, *130*, 15896.
(22) Rowsell, J. L. C.; Yaghi, O. M. *J. Am. Chem. Soc.* **2006**, *128*, 1304.
(23) Haszeldine, R. S. *Science* **2009**, *325*, 1644.
(24) Sumida, K.; Rogow, D. L.; Mason, J. A.; McDonald, T. M.; Bloch, E. D.; Herm, Z. R.; Bae, T.-H.; Long, J. R. *Chem. Rev.* **2011**, *112*, 724.
(25) Cho, H.-Y.; Yang, D.-A.; Kim, J.; Jeong, S.-Y.; Ahn, W.-S. *Catal. Today* **2012**, *185*, 35.
(26) Zhang, Z.; Zhao, Y.; Gong, Q.; Li, Z.; Li, J. *Chem. Commun.* **2013**, *49*, 653.
(27) Dietzel, P. D. C.; Johnsen, R. E.; Fjellvag, H.; Bordiga, S.; Groppo, E.; Chavan, S.; Blom, R. *Chem. Commun.* **2008**, 5125.
(28) McDonald, T. M.; D'Alessandro, D. M.; Krishna, R.; Long, J. R. *Chem. Sci.* **2011**, *2*, 2022.
(29) Peng, Y.; Krungleviciute, V.; Eryazici, I.; Hupp, J. T.; Farha, O. K.; Yildirim, T. *J. Am. Chem. Soc.* **2013**.
(30) Makal, T. A.; Li, J.-R.; Lu, W.; Zhou, H.-C. *Chem. Soc. Rev.* **2012**, *41*, 7761.
(31) Mueller, U.; Schubert, M.; Teich, F.; Puetter, H.; Schierle-Arndt, K.; Pastre, J. *J. Mater. Chem.* **2006**, *16*, 626.
(32) Li, Y.-S.; Liang, F.-Y.; Bux, H.; Feldhoff, A.; Yang, W.-S.; Caro, J. *Angew. Chem. Int. Ed.* **2010**, *122*, 558.
(33) Bloch, E. D.; Queen, W. L.; Krishna, R.; Zadrozny, J. M.; Brown, C. M.; Long, J. R. *Science* **2012**, *335*, 1606.
(34) Alaerts, L.; Séguin, E.; Poelman, H.; Thibault-Starzyk, F.; Jacobs, P. A.; De Vos, D. E. *Chem. Eur. J.* **2006**, *12*, 7353.
(35) Kim, J.; Bhattacharjee, S.; Jeong, K.-E.; Jeong, S.-Y.; Ahn, W.-S. *Chem. Commun.* **2009**, 3904.

(36) Hwang, Y. K.; Hong, D.-Y.; Chang, J.-S.; Seo, H.; Yoon, M.; Kim, J.; Jhung, S. H.; Serre, C.; Férey, G. *Appl. Catal., A* **2009**, *358*, 249.
(37) Henschel, A.; Gedrich, K.; Kraehnert, R.; Kaskel, S. *Chem. Commun.* **2008**, 4192.
(38) Matsuda, R.; Kitaura, R.; Kitagawa, S.; Kubota, Y.; Belosludov, R. V.; Kobayashi, T. C.; Sakamoto, H.; Chiba, T.; Takata, M.; Kawazoe, Y.; Mita, Y. *Nature* **2005**, *436*, 238.
(39) Hasegawa, S.; Horike, S.; Matsuda, R.; Furukawa, S.; Mochizuki, K.; Kinoshita, Y.; Kitagawa, S. *J. Am. Chem. Soc.* **2007**, *129*, 2607.
(40) Tanabe, K. K.; Cohen, S. M. *Chem. Soc. Rev.* **2011**, *40*, 498.
(41) Banerjee, M.; Das, S.; Yoon, M.; Choi, H. J.; Hyun, M. H.; Park, S. M.; Seo, G.; Kim, K. *J. Am. Chem. Soc.* **2009**, *131*, 7524.
(42) Alkordi, M. H.; Liu, Y.; Larsen, R. W.; Eubank, J. F.; Eddaoudi, M. *J. Am. Chem. Soc.* **2008**, *130*, 12639.
(43) Hermes, S.; Schröter, M.-K.; Schmid, R.; Khodeir, L.; Muhler, M.; Tissler, A.; Fischer, R. W.; Fischer, R. A. *Angew. Chem. Int. Ed.* **2005**, *44*, 6237.
(44) Meilikhov, M.; Yusenko, K.; Esken, D.; Turner, S.; Van Tendeloo, G.; Fischer, R. A. *Eur. J. Inorg. Chem.* **2010**, *2010*, 3701.
(45) Sabo, M.; Henschel, A.; Frode, H.; Klemm, E.; Kaskel, S. *J. Mater. Chem.* **2007**, *17*, 3827.
(46) Hermannsdörfer, J.; Kempe, R. *Chem. Eur. J.* **2011**, *17*, 8071.
(47) Wu, C.-D.; Hu, A.; Zhang, L.; Lin, W. *J. Am. Chem. Soc.* **2005**, *127*, 8940.
(48) Ma, L.; Falkowski, J. M.; Abney, C.; Lin, W. *Nat. Chem.* **2010**, *2*, 838.
(49) Cho, S.-H.; Ma, B.; Nguyen, S. T.; Hupp, J. T.; Albrecht-Schmitt, T. E. *Chem. Commun.* **2006**, 2563.
(50) Song, F.; Wang, C.; Falkowski, J. M.; Ma, L.; Lin, W. *J. Am. Chem. Soc.* **2010**, *132*, 15390.
(51) Carne, A.; Carbonell, C.; Imaz, I.; Maspoch, D. *Chem. Soc. Rev.* **2011**, *40*, 291.
(52) Vaucher, S.; Li, M.; Mann, S. *Angew. Chem. Int. Ed.* **2000**, *39*, 1793.
(53) Rieter, W. J.; Taylor, K. M. L.; An, H.; Lin, W.; Lin, W. *J. Am. Chem. Soc.* **2006**, *128*, 9024.
(54) Liang, G.; Xu, J.; Wang, X. *J. Am. Chem. Soc.* **2009**, *131*, 5378.
(55) Paseta, L.; Seoane, B.; Julve, D.; Sebastián, V.; Téllez, C.; Coronas, J. *ACS App. Mater. Inter.* **2013**, *5*, 9405.
(56) Hou, S.; Harrell, C. C.; Trofin, L.; Kohli, P.; Martin, C. R. *J. Am. Chem. Soc.* **2004**, *126*, 5674.
(57) Lee, H. J.; Cho, W.; Oh, M. *Chem. Commun.* **2012**, *48*, 221.
(58) Horcajada, P.; Chalati, T.; Serre, C.; Gillet, B.; Sebrie, C.; Baati, T.; Eubank, J. F.; Heurtaux, D.; Clayette, P.; Kreuz, C.; Chang, J.-S.; Hwang, Y. K.; Marsaud, V.; Bories, P.-N.; Cynober, L.; Gil, S.; Ferey, G.; Couvreur, P.; Gref, R. *Nat. Mater.* **2010**, *9*, 172.
(59) Chalati, T.; Horcajada, P.; Gref, R.; Couvreur, P.; Serre, C. *J. Mater. Chem.* **2011**, *21*, 2220.
(60) Ni, Z.; Masel, R. I. *J. Am. Chem. Soc.* **2006**, *128*, 12394.
(61) Son, W.-J.; Kim, J.; Kim, J.; Ahn, W.-S. *Chem. Commun.* **2008**, 6336.
(62) Oh, M.; Mirkin, C. A. *Nature* **2005**, *438*, 651.
(63) Uehara, H.; Diring, S.; Furukawa, S.; Kalay, Z.; Tsotsalas, M.; Nakahama, M.; Hirai, K.; Kondo, M.; Sakata, O.; Kitagawa, S. *J. Am. Chem. Soc.* **2011**, *133*, 11932.
(64) Serre, C.; Millange, F.; Surblé, S.; Férey, G. *Angew. Chem. Int. Ed.* **2004**, *43*, 6285.
(65) Horcajada, P.; Serre, C.; Grosso, D.; Boissière, C.; Perruchas, S.; Sanchez, C.; Férey, G. *Adv. Mater.* **2009**, *21*, 1931.
(66) Wiktor, C.; Turner, S.; Zacher, D.; Fischer, R. A.; Tendeloo, G. V. *Microporous Mesoporous Mater.* **2012**, *162*, 131.
(67) Yue, Y.; Qiao, Z.-A.; Fulvio, P. F.; Binder, A. J.; Tian, C.; Chen, J.; Nelson, K. M.; Zhu, X.; Dai, S. *J. Am. Chem. Soc.* **2013**, *135*, 9572.
(68) Du, H.; Bai, J.; Zuo, C.; Xin, Z.; Hu, J. *CrystEngComm* **2011**, *13*, 3314.
(69) Pan, Y.; Liu, Y.; Zeng, G.; Zhao, L.; Lai, Z. *Chem. Commun.* **2011**, *47*, 2071.
(70) Panella, B.; Hirscher, M. *Adv. Mater.* **2005**, *17*, 538.

(71) Tsuruoka, T.; Furukawa, S.; Takashima, Y.; Yoshida, K.; Isoda, S.; Kitagawa, S. *Angew. Chem. Int. Ed.* **2009**, *48*, 4739.
(72) Pan, Y.; Heryadi, D.; Zhou, F.; Zhao, L.; Lestari, G.; Su, H.; Lai, Z. *CrystEngComm* **2011**, *13*, 6937.
(73) Li, P.-Z.; Maeda, Y.; Xu, Q. *Chem. Commun.* **2011**, *47*, 8436.
(74) Tan, J.-C.; Saines, P. J.; Bithell, E. G.; Cheetham, A. K. *ACS Nano* **2011**, *6*, 615.
(75) Xu, G.; Yamada, T.; Otsubo, K.; Sakaida, S.; Kitagawa, H. *J. Am. Chem. Soc.* **2012**, *134*, 16524.
(76) Tanaka, D.; Henke, A.; Albrecht, K.; Moeller, M.; Nakagawa, K.; Kitagawa, S.; Groll, J. *Nat. Chem.* **2010**, *2*, 410.
(77) Sakata, Y.; Furukawa, S.; Kondo, M.; Hirai, K.; Horike, N.; Takashima, Y.; Uehara, H.; Louvain, N.; Meilikhov, M.; Tsuruoka, T.; Isoda, S.; Kosaka, W.; Sakata, O.; Kitagawa, S. *Science* **2013**, *339*, 193.
(78) Dhakshinamoorthy, A.; Alvaro, M.; Hwang, Y. K.; Seo, Y.-K.; Corma, A.; Garcia, H. *Dalton Trans.* **2011**, *40*, 10719.
(79) Horcajada, P.; Serre, C.; Vallet-Regí, M.; Sebban, M.; Taulelle, F.; Férey, G. *Angew. Chem. Int. Ed.* **2006**, *118*, 6120.
(80) Horcajada, P.; Serre, C.; Maurin, G.; Ramsahye, N. A.; Balas, F.; Vallet-Regí, M. a.; Sebban, M.; Taulelle, F.; Férey, G. r. *J. Am. Chem. Soc.* **2008**, *130*, 6774.
(81) Taylor-Pashow, K. M. L.; Rocca, J. D.; Xie, Z.; Tran, S.; Lin, W. *J. Am. Chem. Soc.* **2009**, *131*, 14261.
(82) Della Rocca, J.; Liu, D.; Lin, W. *Acc. Chem. Res.* **2011**, *44*, 957.
(83) Imaz, I.; Rubio-Martinez, M.; An, J.; Sole-Font, I.; Rosi, N. L.; Maspoch, D. *Chem. Commun.* **2011**, *47*, 7287.
(84) Horcajada, P.; Gref, R.; Baati, T.; Allan, P. K.; Maurin, G.; Couvreur, P.; Férey, G.; Morris, R. E.; Serre, C. *Chem. Rev.* **2011**, *112*, 1232.
(85) Cunha, D.; Ben Yahia, M.; Hall, S.; Miller, S. R.; Chevreau, H.; Elkaïm, E.; Maurin, G.; Horcajada, P.; Serre, C. *Chem. Mater.* **2013**, *25*, 2767.
(86) Huxford, R. C.; deKrafft, K. E.; Boyle, W. S.; Liu, D.; Lin, W. *Chem. Sci.* **2012**, *3*, 198.
(87) Miller, S. R.; Heurtaux, D.; Baati, T.; Horcajada, P.; Greneche, J.-M.; Serre, C. *Chem. Commun.* **2010**, *46*, 4526.
(88) Taylor, K. M. L.; Jin, A.; Lin, W. *Angew. Chem. Int. Ed.* **2008**, *120*, 7836.
(89) Taylor, K. M. L.; Rieter, W. J.; Lin, W. *J. Am. Chem. Soc.* **2008**, *130*, 14358.
(90) Allendorf, M. D.; Bauer, C. A.; Bhakta, R. K.; Houk, R. J. T. *Chem. Soc. Rev.* **2009**, *38*, 1330.
(91) Liu, D.; Huxford, R. C.; Lin, W. *Angew. Chem. Int. Ed.* **2011**, *50*, 3696.
(92) deKrafft, K. E.; Boyle, W. S.; Burk, L. M.; Zhou, O. Z.; Lin, W. *J. Mater. Chem.* **2012**, *22*, 18139.

Chapter 2

Objectives

As illustrated in **Chapter 1**, the last progresses done in the miniaturisation of Metal-Organic Frameworks (MOFs) at the nanoscale to form nanoscale MOFs (NMOFs) show promise to expand the scope of these materials in numerous practical applications. At the nanoscale, MOFs can have size dependent properties, which, if properly exploited, may expand their scope for numerous practical purposes, including drug delivery, contrast agents, sensor technology, functional membranes and thin films, while also opening up novel avenues to the more traditional storage, separation and catalysis applications. However, the miniaturisation of MOFs is still in its embryonic stage and therefore, there are many challenges that need to be overcome. Some of these challenges are: i) the lack of a general, reliable, fast, economic and scalable methodology to synthesise NMOFs; and ii) the discovery of new NMOFs that fulfil the required targets of the field of application. Thus, the main objective of this Thesis has been to face these challenges, introducing new synthetic methodologies to fabricate NMOFs and creating new NMOFs to exploit their high potentiality in biomedicine and medical imaging. Following these two main axes, the present Thesis has been organised around the following objectives:

1. Development of new synthetic methodologies for NMOFs

- Evaluate the potential of the Spray-Drying technique to synthesis NMOFs by studying the formation of HKUST-1. Here, we aim to identify the main parameters that influence the NMOF synthesis in terms of size and yield, and obtain insights regarding the reaction mechanism.

- Prove the generality of the Spray-Drying technique by synthesising a broad spectrum of NMOFs belonging to different subfamilies. Taking advantage of the versatility of the technique that enables different ways to process the precursor solutions, we aim to implement a variety of protocols to expand the family of NMOFs synthesised through Spray-Drying.

- Use the capabilities of the Spray-Drying to encapsulate and prepare multi component materials to synthesise MOF-based composite materials. Here, we aim to combine NMOFs with other functional materials to achieve composites with synergic and collective properties.

2. Design and synthesis of novel NMOFs with potential as Contrast Agents (CAs) for Magnetic Resonance Imaging (MRI)

- Design, synthesis and characterization of MOFs built up from Gd(III) ions and heterocyclic ligands generally used in the synthesis of molecular CAs. We aim to take advantage of the high affinity of these ligands towards Gd(III) ions to build up highly stable MOF structures. And more importantly, avoid an eventual leaching of the highly toxic free Gd(III) ion.

- Miniaturisation of the resulting MOFs at the nanoscale regime. We aim to achieve stable colloidal suspensions of the resulting NMOF in aqueous and physiologically simulated media.

- Evaluate the stability of the resulting NMOFs against different media and establish its cytotoxic character. Here, we aim to determine the amount and nature of Gd(III) ions leached under these conditions and establish its relation with the observed cytotoxicity.

- Fully characterise the CAs properties of the resulting NMOFs. Here we aim, to study the relaxivity under different conditions of magnetic field applied and pH.

Chapter 3

Spray-Drying: A new technique for scaling up the production of nanoscale Metal-Organic Frameworks and their related superstructures

Metal-organic frameworks (MOFs) are among the most attractive porous materials known today. Their miniaturisation to the nanoscale—into NMOFs—is expected to serve myriad applications from drug delivery to membranes, to open up novel avenues to more traditional storage and catalysis applications, and to enable the creation of sophisticated superstructures. Here, we report the use of spray-drying as a versatile methodology to assemble NMOFs, yielding spherical hollow superstructures with diameters smaller than 5 μm. This strategy conceptually mimics the emulsions used by chemists to confine the synthesis of materials, but does not require secondary immiscible solvents or surfactants. We demonstrate that the resulting spherical, hollow superstructures can be processed into stable colloids, whose disassembly by sonication affords discrete, homogeneous NMOFs. This spray-drying strategy enables the construction of multicomponent MOF superstructures, and the encapsulation of guest species within these superstructures. We anticipate that this will provide new routes to capsules, reactors and composite materials.

1. Spray-Drying: An introduction and its industrial applications

1.1. The principle

Spray-drying (SD) is a widely spread industrial process used to convert a liquid product in a dried powder in a single step. First patents describing its application in the chemical industry dates back to the 19th century.[1] However, it was not till SD was used to prepare milk powders and detergents when it was generally introduced in the industry. Since then, it has been applied to many industrial sectors, such as food, perfume and pharmaceutical.

The technique is based on the fast drying of an aerosol dispersion containing microdroplets of a solution with the active compound. The main principle of SD is based on the enhanced surface of the microdroplets, which promotes the fast evaporation and induces the precipitation in the aerosol droplet. From a mechanistic point of view, there is a first step in which the drying is controlled at the interface of the gas-droplet. At this stage, there is a heat transfer from the gas phase to the liquid phase and a mass transport from the liquid vapour of the droplet to the gas phase. The second step starts when the solid particle is already formed. Here, the evaporation rate is controlled by the diffusion of remaining vapours in the particle towards the particle surface. Therefore, the precipitation process is confined in the micronized droplet. At this stage, the temperature of the powder is increased as evaporation is not the main parameter (**Figure 1**).

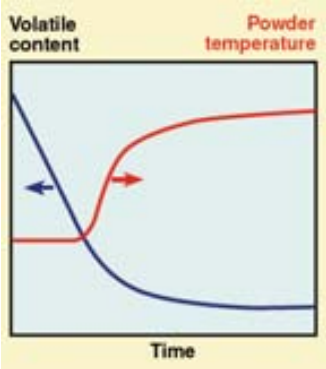

Figure 1. Evolution of the powder temperature and the volatile content during the SD.

From a technical point of view, the process starts with the atomisation of the solution. This step can be accomplished by different means, such as mixing the solution with compressed N_2 or air using a nozzle, forcing its pass through a membrane, cutting the solution with oscillatory discs or by ultrasonication. Then, the aerosol droplets are contacted and suspended in a hot gas stream causing the solvent to begin evaporating. The dried powder is accumulated in a collector and the process proceeds continuously. A schematic representation of the technique is shown in **Figure 2**. The main parameters to be controlled and that govern the drying process are: i) the temperature at which the solution is injected in the atomiser; ii) the feed rate of the liquid solution to the atomizer; and iii) the energy used for the atomisation. When a nozzle is used, it is described by the flow rate of the gas that is mixed with the liquid feed to break it into microdroplets.

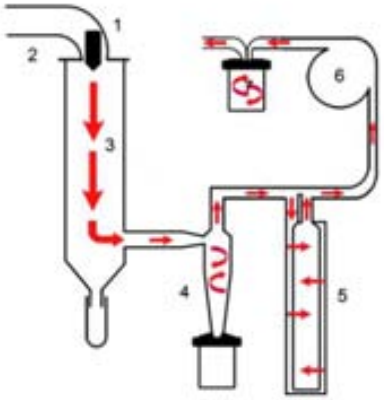

Figure 2. Schematic illustration of a Mini Spray Dryer: 1) Two-fluid nozzle operated by compressed air to disperse the solution as fine droplets; 2) Electric heating of the drying medium; 3) Spray cylinder for drying the droplets into solid material; 4) Separation of this solid product in the cyclone; 5) Outlet filter to remove fine particles; 6) Aspirator for generating the flow; and 7) Solvent condenser.

1.2. Applications of the Spray-Drying technique

Since the discovery of the SD, it has shown to be a very versatile technique for a wide range of purposes, from the mere drying of liquid solutions to the synthesis of complicated composite structures. The applications of the SD technique are summarized chronologically in this section.

1.2.1. Drying

In the early years, the focus of industrial applications of SD was put in its mere ability to remove solvent in a continuous, fast and single step fashion. Food industry readily introduced SD as an important process and exploited it to prepare dry food. The most relevant example is the preparation of milk powder,[2] which first SD productions dates back to the early 20th century. Importantly, other examples are the dairy industry, which also applied SD for the production of detergents powders,[3] and the pharmaceutical industry, which employed SD to obtain dry extracts of active raw materials from plants.[4]

1.2.2. Encapsulation

SD is a very versatile technique that enables to use a variety of precursor solutions that can be composed of mixtures of active compounds. Therefore, one can use the SD technique to combine different precipitation processes in a single droplet in order to produce capsules or composite materials. Food industry has taken advantage of that to encapsulate and protect flavours[5] and

fragrances.[6] As a matter of fact, SD is one of the oldest methods for encapsulating flavours. The first examples of flavour encapsulation using SD date back from the 1930's.

The process generally proceeds by combining in the feed solution the active compound, which should be encapsulated, and the wall material, which protects the active compound. Generally, the feed solution is in the form of an emulsion in which the dispersed phase is the core material and the wall material is the continuous phase. Oil-in-water emulsions are the most common formulations because the core material is usually hydrophobic, whereas the coating materials are hydrophilic. Then, the obtained emulsion is sprayed, and the evaporation of the water induces the precipitation of the wall material around the core, yielding the microcapsules that encapsulating the core material.[7-9]

1.2.3. Miniaturisation

The better comprehension of the technique and the advent of the microscopic techniques allowed expanding the applications of SD. The close observation of a product fabricated by SD revealed that it is usually composed of micronized powders, generally in the form of spherical microparticles. It is therefore a technique that can also be used to miniaturize active compounds, which might optimized their dispersability and density.

Powder miniaturisation is specially employed in pharmaceutical industry to increase the aqueous solubility of the Active Pharmaceutical Ingredient (API). The poor solubility of API due to their high hydrophobicity is responsible for its poor biodistribution and therefore, diminishes their beneficial effects. In this sense, miniaturisation increases the surface of the API exposed to the solvent, thereby increasing its solubility. For this reason, SD has been seen as an alternative method to miniaturize APIs.[10] In addition, the APIs miniaturized by SD are usually amorphous due to the fast drying. This amorphous character is also an advantage for the pharmaceutical industry because it is known that amorphous powders are easier to dissolve than crystalline materials.[11]

In this process, the APIs are solubilised in an apolar solvent that it is used as a feed solution to the spray dryer, which nebulizes it and induces the fast precipitation of the API in the aerosol droplet. It is the confined precipitation in the aerosol droplet which causes the miniaturisation of the APIs. In addition, the low boiling point of the solvent permits the use of low spraying temperatures, which guarantees that the APIs will not be chemically modified during the process. **Figure 3** shows an example of the miniaturisation of a precursor solution containing an antinflamatory drug using SD. Today, pharmaceutical industry is widely employing the SD as a tool to miniaturise and produce amorphous APIs with enhanced solubility,[12-15] with the intention to increase the API's pharmacokinetics.[16]

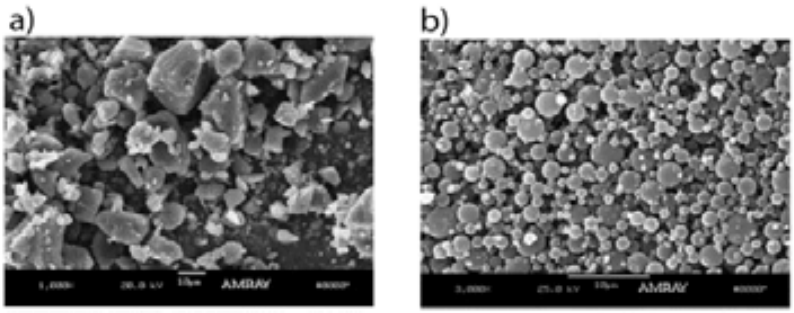

Figure 3. **a)** Commercial form of the antinflammatory drug piroxicam, and **b)** its micronized powder, comprising microspheres micronized by SD.[15]

1.2.4. Spray-Drying as a synthetic tool: Engineering new materials

As state above, SD is a tool to dry, miniaturise and coprecipitate desired compounds for creating composites. However, the intrinsic characteristics of the process make it also very attractive to tune chemical transformations that can be exploited in a synthetic process. In solid state reactions, good homogeneity of the reactants is important to increase both yield and purity. Here, SD can be used as a precursor step to spray reactants in order to prepare a miniaturised powder with good mixing of the components. For example, this technique can be used to synthesise hydroxyapatite from the calcination of a previously sprayed precursor solution.[17] The homogenous mixture of the reactants in the sprayed powder provides the good conditions to produce a nanostructured powder of pure hydroxyapatite after calcination.

Also, SD can be exploited in a chemical process to quench chemical transformations and isolate metastable phases difficult to obtain in batch reactors. This is due to the fast drying, which stops the chemical reaction at the desired stage. Muhler *et al*. exploited this characteristic to capture metastable phases of sodium zinc carbonate resulting from the precipitation of $Zn(NO_3)_2$ in the presence of $NaCO_3$.[18,19] In this process, the $Zn(NO_3)_2$ and the base were mixed and instantaneously sprayed, avoiding any aging and secondary reaction and producing the metastable phase of sodium zinc carbonate. This metastable phase could be further treated to yield ZnO nanoparticles with high surface areas (**Figure 4**). The use of SD as a part of the synthesis made this process easily scalable.

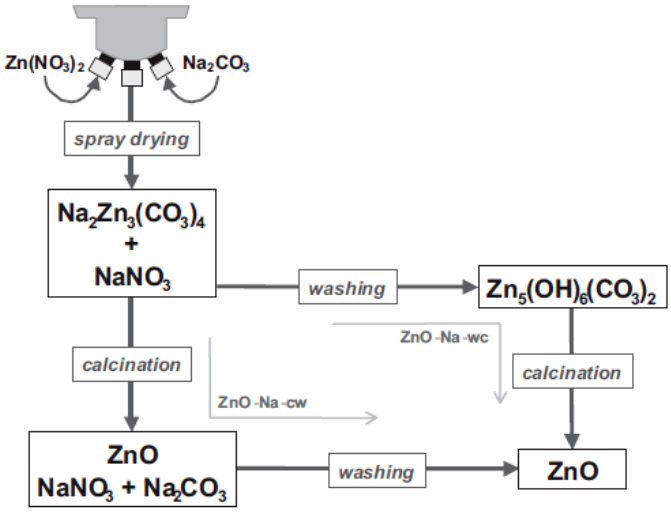

Figure 4. SD as a part of the chemical process for the synthesis of ZnO nanoparticles.

The unique conditions at which species are dried in the aerosol droplet can also be exploited to induce the self-assembly of the sprayed species inside the aerosol droplet to create higher order structures or superstructures. For example, hollow microspheres comprising carbon nanotubes on its walls can be prepared simply by spraying a precursor solution containing a dispersion of carbon nanotubes.[20] Interestingly, when the self-assembly of objects that are in the aerosol droplet is combined with the capture of metastable phases difficult to reproduce by other means, the SD process leads to the synthesis of new mesostructured materials with unique properties. This is the case of porous silica microparticles, which is one of the most relevant examples of the use of SD to synthesise new functional materials so far.[21]

Another excellent example of how SD can be used to synthesise new materials is the creation of hierarchical porous structures. This is possible because SD can combine the sol-gel chemistry with the one-step drying in a confined environment (**Figure 5**). First reported by Brinker *et al.,* this process is based on the induced self-assembly of the inorganic precursor in the evaporating droplet (Evaporation Induced Self-assembly, EISA). In this process, the precursors are generally delivered in the form of a solution, in which a certain degree of polymerization already occurred and the metal-oxo polymers are suspended in solution. Then, upon drying, the inorganic precursor self-assembles into ordered hierarchical structures. The particularity of the process allows "capturing" metastable states found during the fast drying, which are unreachable by most conventional template-directed sol-gel chemistry methods. The resulting organisation of the assembled inorganic precursors originates the porosity on the final product. The process can be coupled with the addition of structure directing agents, such as surfactants[22], sacrificial particles that once removed leave behind a pore,[23] and inorganic nanoparticles[24] to gain control on the resulting porosity. Interestingly, bimodal porosity can arise when different structure directing agents are combined. In addition, a variety of hierarchical

structures can be achieved simply by controlling the initial sol composition,[25,26] temperature[27] and post calcination.[28]

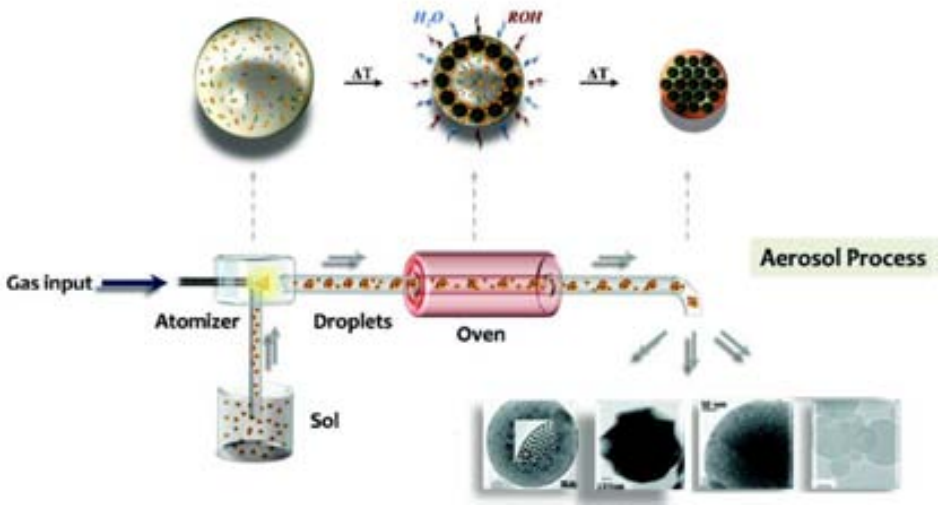

Figure 5. EISA process for preparing hierarchically structured mesoporous silica materials. First, the sol is sprayed. Then, the evaporation begins and the inorganic precursors self-assemble around the template (which can be a surfactant or an organic or inorganic nanoparticle). Finally, the particles fuse in a well packed sphere.[29]

The examples shown here illustrate the high versatility and peculiarity of SD. Nevertheless, SD has never been used to induce chemical reactions *in situ* in the aerosol droplets. This is an attractive strategy because it would entail an easy methodology to create microreactors (aerosol droplets) to confine chemical transformations. With this idea, in this Thesis, we have explored for the first time the use of SD to promote coordination reactions for the synthesis of Metal-Organic Frameworks (MOFs).

2. Synthesis of Metal-Organic Frameworks by Spray-Drying

In the current framework where there is an increasing need for new methodologies for scaling up the synthesis of MOFs, it was envisaged that SD could be exploited as an alternative, scalable synthetic technique. This technique has several characteristics that are very attractive for the synthesis of MOFs. It allows the use of a variety of solvents, combining solutions at different stages of the process, the use of a wide temperature window at which the precursor solution can be sprayed, and easy tuning of experimental parameters. In addition, SD is a continuous, single-step method that produces dried powders, allows solvent recovery and most importantly, it is an already common equipment in the chemical industry.

SD does not only offer the scalable synthesis of MOFs but also a method to confine their synthesis in micronized droplets. This is due to the requirements of the SD, in which all processes happen in the aerosol droplet during its drying. Therefore, a successful MOF synthesis using SD would entail its confinement in aerosol droplets. Nowadays, all methods for the confined synthesis of MOFs (in most of the cases to produce NMOFs) demand the generation and stabilization of droplets containing at least one of the corresponding precursors for the duration of the reaction.[30] Typically, this has been achieved by using emulsions created from at least two immiscible solvents and, in most cases, using surfactants. However, the use of these emulsions to synthesise NMOFs is extremely challenging and currently quite limited.[31] This is a result of several factors, including the complexity of preparing emulsions that mimic the required reaction conditions (for example, solvents, temperature, and bases), and solubility problems between the MOF precursors (metal ions and organic ligands) and the constituent polar/nonpolar solvents of the emulsions. The SD method avoids most of these problems, as it constitutes a general method for forming and homogeneously heating droplets of any desired solvent containing the precursors without the need for any additional immiscible solvents, surfactants, emulsifiers or agitation (for example, stirring or sonication).

2.1. Synthesis of HKUST-1

In order to evaluate the feasibility of using the SD technique to prepare MOFs, we first attempted the synthesis of $Cu_3(BTC)_2$ (known as HKUST-1 or MOF-199; where BTC is 1,3,5-benzenetricarboxylate). HKUST-1 is undoubtedly one of the most representative and studied MOFs. It was described for the first time by Williams *et al.* in 1999.[32] HKUST-1 is composed of dimeric Cu(II) units in a paddle-wheel coordination mode bridged by BTC ligands (**Figure 6a**). The framework is electrically neutral: the 12 carboxylate oxygens from the two BTC ligands bind to four coordination sites for each of the three Cu(II) ions of the formula unit. Each metal ion completes its coordination sphere with a solvent molecule. Interestingly, HKUST-1 shows 1-nm-size channels that intersect to provide a 3D connected network of pores. A view through the cell body diagonal [111] reveals a honeycomb arrangement of large hexagonal-shaped windows, each composed of a ring of six metal dimers and six BTC groups, which measure 18.6 Å between opposite vertices (**Figure 6b**). These windows are cross sections of the "cavities" formed at the intersection of the three orthogonal sets of channels. The high porosity indicated by the crystal structure and confirmed by absorptions measurements (Surface Area around 1200-1500 $m^2 \cdot g^{-1}$) and the presence of metal-opened sites have attracted the interest of many research groups towards HKUST-1. Particularly, it shows excellent gas sorption properties for H_2,[33] CO_2[34] and methane.[35]

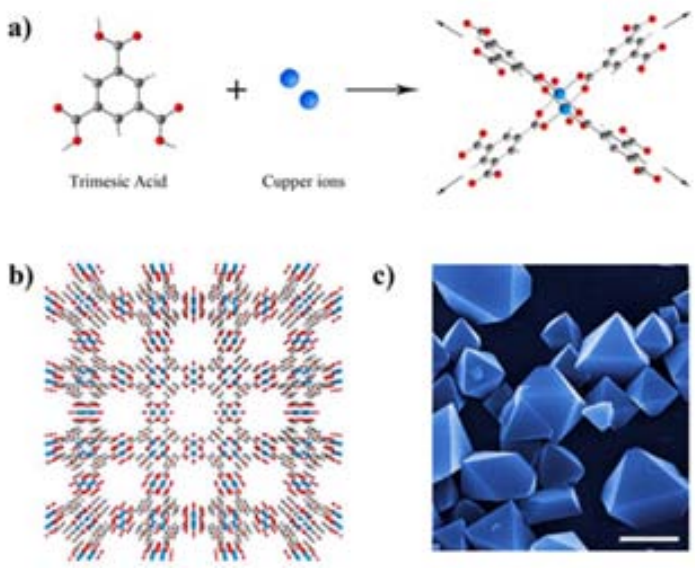

Figure 6. a). Cu(II) paddle wheel unit of HKUST-1. Key distances are Cu-Cu: 2.628 Å, Cu-OCO: 1.952(3) Å, and Cu-OH_2: 2.165(8) Å. **b)** Viewed down the [100] direction, showing nanochannels with four-fold symmetry. **c)** SEM colored image of HKUST-1 octahedral microcrystals synthesised by conventional heating methods. Scale bar represents 10 μm.

The synthesis of HKUST-1 by SD was achieved using a Mini Spray Dryer B-290 (BÜCHI Labortechnik) implemented with a 2-fluid nozzle (**Figure 7**). The process started by preparing the precursor solution in a mixture of DMF, ethanol and water (1:1:1). Accordingly, 50 ml of precursor solution containing $Cu(NO_3)_2 \cdot 2.5H_2O$ at a concentration of 0.0017 M and BTC at 0.0011 M was first prepared. The clear blue solution was brought to the two fluid nozzle through a peristaltic bomb at a feed rate of 4.5 $ml \cdot min^{-1}$ (**Figure 7a**). Once the solution was brought to the nozzle, it was mixed with N_2 gas at a certain flow rate (**Figure 7b**). At this moment, the N_2 flow broke the precursor solution and generated the aerosol droplets that enter into the drying chamber. The N_2 flow is therefore a crucial parameter to guarantee the formation of the final powder as an effective drying in this short period of time can only be accomplished when the solution enters into the drying chamber in the form of an aerosol. The flow rate of 336 $ml \cdot min^{-1}$ was enough to promote the aerosol formation of the HKUST-1 precursor solution. Once the solution entered into the drying chamber in the form of an aerosol dispersion, it was contacted with hot gas stream at a temperature (hereafter called inlet temperature) of 180 ºC, which immediately dried it.

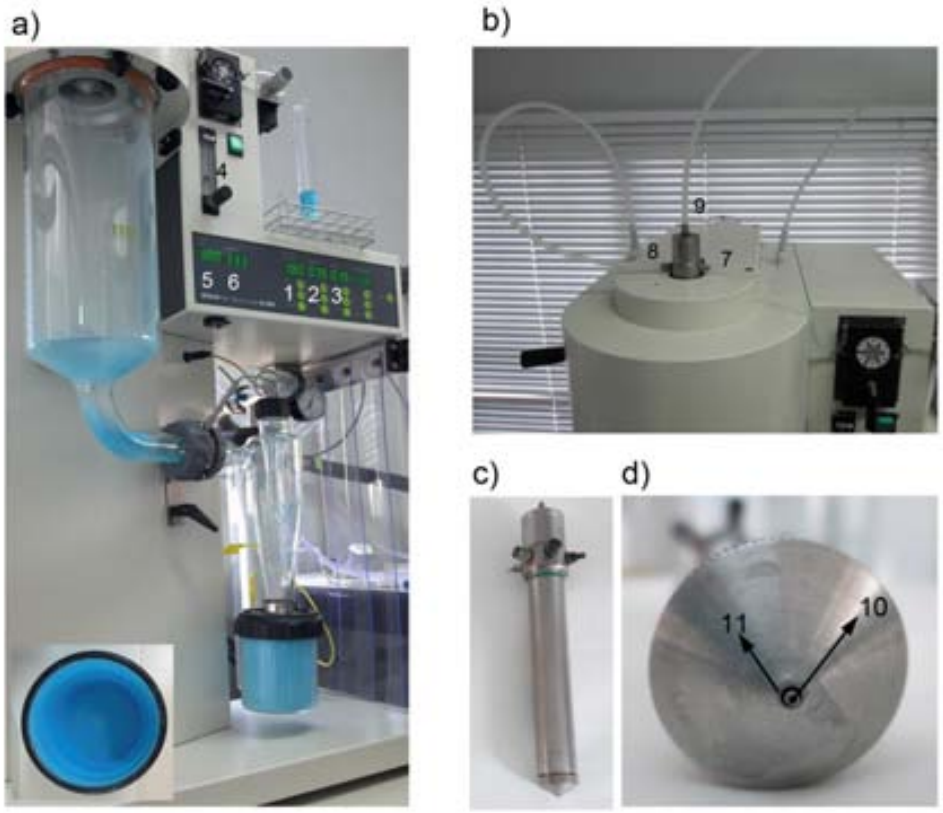

Figure 7. a) General image of the spray drier used for the synthesis of HKUST-1. The equipment allows the user to control the inlet temperature (1), the aspiration rate (2), the solution feed rate (3) and the gas flow rate (4). The display shows the actual inlet (5) and outlet (6) temperature. The inset shows the collector after spraying. **b)** Close image of the upper part of the equipment where the precursor feed solution is brought to the nozzle (7). Gas flow is also brough to the nozzle (8). There is an auxiliary air flow (9) that can be used in case of clocking of the nozzle. **c)** Image of a two-fluid nozzle. **d)** Close image of the end of the nozzle where the liquid solution and the gas are mixed. The liquid solution flows in the inner tube (10) while the gas flows through the outer tube (11). Both channels meet at the end where atomisation is produced.

This SD process of the precursor solution produced a blue powder that was accumulated in the collector (**Figure 7a**). After 12 min, the whole precursor solution was sprayed and 133 mg of powder was collected. No wetness in the drying chamber was detected, revealing good aerosol formation and drying. This powder was analysed by XRPD. As shown in **Figure 8**, the experimental XRPD pattern showed perfect match with the pattern simulated from the atomic positions extracted from the crystallographic file of the reported structure of HKUST-1.[32] This agreement confirmed that the chemical reaction of the building blocks to yield the desired MOF successfully occurred during the fast aerosol droplet drying.

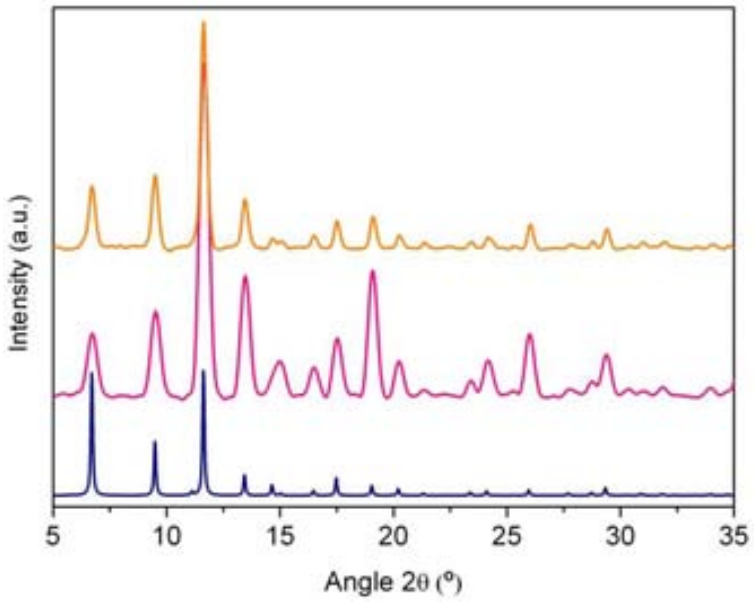

Figure 8. XRPD patterns of the as-sprayed (pink) and washed (orange) powder compared with the simulated XRPD pattern of HKUST-1 (blue).

The collected powder was washed with methanol and dichloromethane and finally dried. 120 mg of pure HKUST-1 was recovered, which represents a reaction yield of 70%. The purity of the as-sprayed powder was 90%. Purity was calculated according to equation 1:

$$Purity\ (\%) = \frac{Weight\ of\ purified\ product}{Weight\ of\ crude\ solid\ collected} \times 100 \qquad (Equation\ 1)$$

The sprayed HKUST-1 was analysed by FESEM. The images showed that the powder was comprised of micrometric spherical particles (average size of 2.5 ± 0.4 μm). A close observation revealed that the particles were hollow and made of the close packing of sub-100 nm octahedral HKUST-1 (NHKUST-1) crystals (**Figure 9**). Therefore, the SD induces not only the formation of NHKUST-1 but also their assembly in a higher order structure (also termed superstructure).

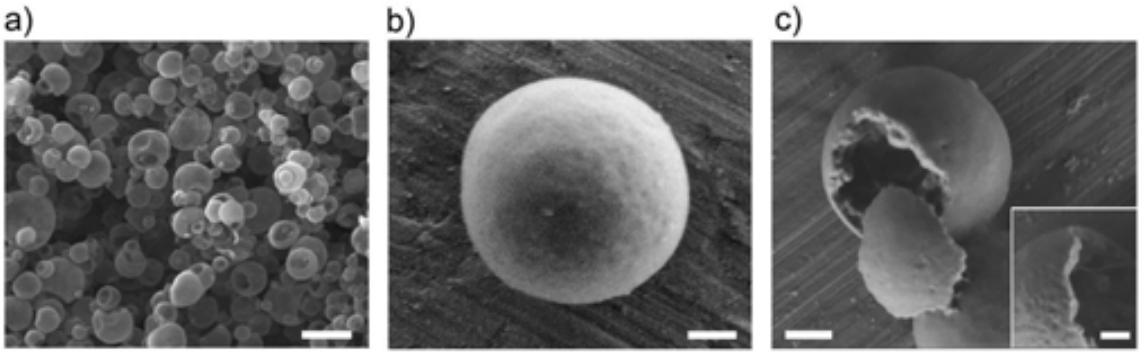

Figure 9. a) FESEM representative image of hollow HKUST-1 superstructures produced after spraying the precursor solution. **b)** Image of a single sphere showing the uniform wall. **c)** Mechanically broken HKUST- 1 superstructure showing the internal cavity and the close packing of NHKUST-1 crystals. Scale bars: 5μm (**a**), 500 nm (**b,c**) and 200 nm (**c, inset**).

The so formed superstructures showed good integrity when exposed to solvent or to moderate mechanical strength; they break upon a force greater than 80 μN. However, when a suspension of these superstructures in methanol was sonicated (130 W, 20 KHz), they readily disassembled into discrete NHKUST-1 crystals dispersed in a stable colloidal solution (**Figure 10a**). The average size determined by FESEM was 75 ± 28 nm (**Figure 10c**). The stability of the dispersion allowed for a precise Dynamic Light Scattering (DLS) analysis that showed good match with the crystal size determined through the FESEM images; average size by number was 84 nm with a polydispersity index (PDI) of 0.1. Therefore, the HKUST-1 superstructures can serve as an excellent source of colloidal suspensions of discrete crystals of NHKUST-1. However, the paramount property of HKUST-1 is its porosity. Accordingly, the porosity of NHKUST-1 synthesised by SD was evaluated by measuring its N_2 adsorption isotherm at 77 K. From this data, the Specific Surface Area was estimated using the Brunauer-Emmet-Teller (BET) method. The BET analysis revealed no significant differences between the superstructure and the disassembled nano crystals. The surface area of the superstructure was 1209 $m^2 \cdot g^{-1}$, whereas for the discrete NHKUST-1 was 1430 $m^2 \cdot g^{-1}$. Both values match well with the common reported values for HKUST-1,[36] confirming the good quality of the MOFs that can be synthesised by SD.

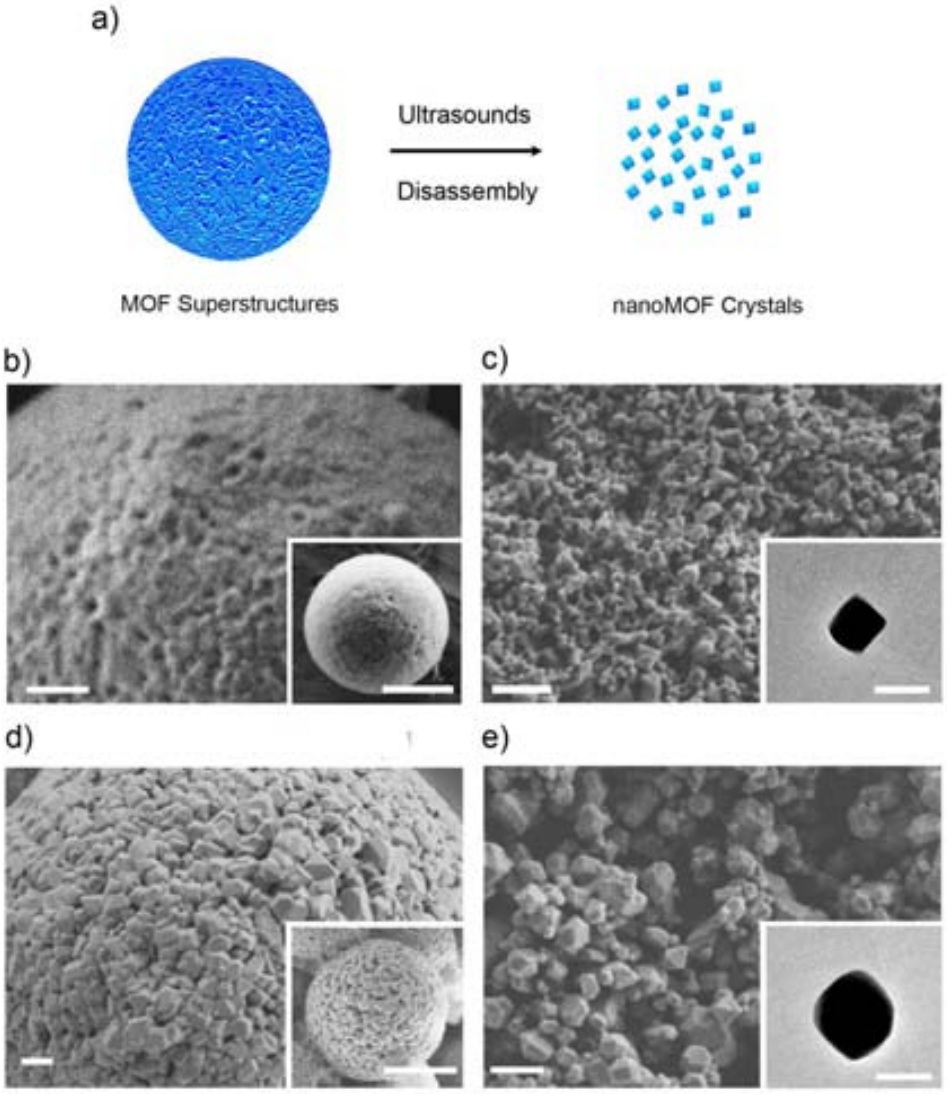

Figure 10. a) Schematic illustration showing the disassembly of the HKUST-1 superstructures upon sonication to form well-dispersed, discrete NHKUST-1 crystals. **b-e**) Representative FESEM and TEM images of the HKUST-1 superstructures and corresponding disassembled NHKUST-1 crystals synthesised using metal salt concentrations of 0.0017 M (**b**, **c**) or 0.17 M (**d**, **e**). Note the larger size at higher concentrations. The scale bars correspond to 500 nm (**b, d ,c, e**), 1 mm (**b, d**, **insets**) and 100 nm (**c, e**, **insets**).

2.1.1. Mechanistic considerations

The formation of HKUST-1 superstructures is most likely related to the *in situ* synthesis and assembly of nanocrystals of HKUST-1 at the liquid-air interface. This is further demonstrated by the fact that when colloidal suspensions of pre-formed NHKUST-1 were sprayed, we could not obtain the same higher-order structures. In this case, only drying of the initial crystals, without any signal of self-assembly, was observed. This rule out the possibility of a mechanism in which the crystals are first formed homogenously in the droplet, and then are diffused at the droplet interface, where they merge, due to the evaporation of the solvent. It is the localisation of the reaction at the liquid-air interface

what induces the crystallisation of NHKUST-1 and induces their self-assembly to create the MOF shell.

A plausible explanation of this mechanism is that, as the droplet begins to evaporate, its receding droplet surface leads to an increase of precursor concentration on the surface (**Figure 11, 1**). While the solvent is evaporates, there is a mass transfer from the droplet to the air, which might induce the diffusion of the reactants towards the droplet surface. Here, the reaction starts when a certain critical concentration of precursors is achieved (**Figure 11, 2**). The confinement of the reaction in the micrometric regime can also be another factor that explains the speed of the reaction, as previously demonstrated by Carbonell *et al*.[37] Finally, when the NHKUST-1 crystals are formed, their mobility is reduced and therefore, they accumulate on the surface where they merge into a well-packed shell (**Figure 11, 3**). Finally, the remaining solvent is evaporated leaving the spherical hollow superstructure (**Figure 11, 4**).

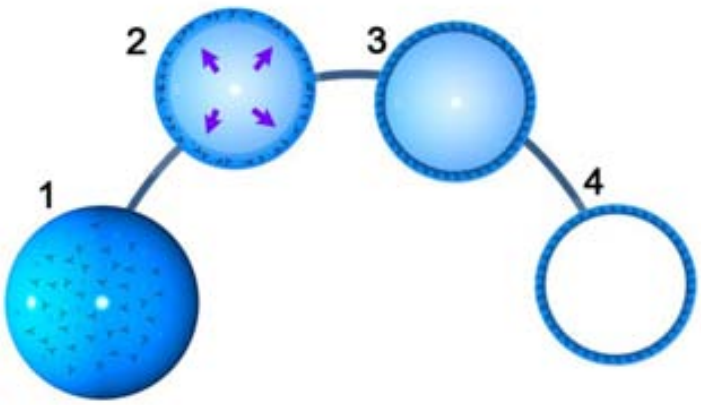

Figure 11. Schematic representation of the proposed mechanism of the SD synthesis of NHKUST-1. Initially, the building blocks are distributed in the aerosol droplet (1). The receding droplet promotes the diffusion of the building blocks towards the shell (2), where they react (3). Finally, the remaining solvent evaporates leading the hollow superstructure (4).

2.1.2. Study of the Spray-Drying parameters on the synthesis of NHKUST-1

To fully understand the formation of NHKUST-1 crystals and their assembly into hollow MOF superstructures, we studied the impact of the precursor concentration, inlet temperature and flow rate on the size of the crystals comprising the wall superstructure as well as on the yield and the purity of the MOF superstructures. All results are summarised in **Table 1.** First, the impact of the three parameters on the crystal size will be discussed followed by considerations on both purity and yield.

Table 1. Influence of the flow rate, precursor concentration and inlet temperature in the SD synthesis of NHKUST-1.

Ref	Cu^{2+} [M]	T (ºC)	Flow ($ml \cdot min^{-1}$)	Size (nm) determined by FESEM	Purity (%)	Yield (%)
SD1	0.0017	180	336	75 ± 28	90	70
SD2	0.017	180	336	85 ± 30	89	72
SD3	0.17	180	336	160 ± 40	67	78
SD4	0.17	180	474	107 ± 30	72	85
SD5	0.17	180	129	167 ± 50	73	68
SD6	0.17	100	129	-	-	-
SD7	0.17	100	474	80 ± 37	49	52
SD8	0.17	150	336	178 ± 50	56	67
SD9	0.17	100	336	172 ± 37	40	36
SD10	0.0017	150	336	82 ± 23	89	64
SD11	0.0017	100	336	75 ± 20	89	64

2.1.2.1. Impact of the Spray-Drying parameters on the crystal size

The effect of the precursor concentration was evaluated using three different Cu(II) concentrations: 0.0017 M, 0.017 M and 0.17 M (constant 3:2 molar ratio of Cu:BTC). The inlet temperature was fixed at 180ºC and the flow rate was maintained at 336 $ml \cdot min^{-1}$ for all the experiments. The FESEM studies and DLS measurements were performed on the colloidal suspensions from the disassembled superstructures. The output of these studies revealed that higher precursor concentration gave larger NHKUST-1 crystals. At a concentration of 0.17 M, NHKUST-1 crystals with average dimensions of 160 ± 40 nm (Reference SD3 in **Table 1**) determined by FESEM (**Figure 10e**) were obtained. On the other hand, when the concentration was reduced to 0.017 M and 0.0017 M, the crystal size was 85 ± 30 nm and 75 ± 28 nm, respectively (SD2-3). The size determined from FESEM images was consistent with the data given by the DLS measurements (**Figure 12**).

The relationship between the crystal size and the precursor concentration can be attributed to an increased accumulation of the building blocks at the liquid-air interface. Nonetheless, other factors can also have an effect on the crystal size. It is well known that there is a relationship between the aerosol droplet size and the solid content of the precursor solution: for lower solid content of the

precursor solution smaller droplets are normally produced.[38] This is also likely to have an effect on the final crystal size of NHKUST-1. Smaller droplets have higher surface area-to-volume ratios that promote a faster drying. In addition, because of these higher surfaces, the reaction proceeds with a solid content that is in comparison smaller, giving rise to the possibility of a major number of seeds. The combination of faster drying due to the reduced droplet and increased number of seeds would also explain the resulting smaller crystals at lower concentrations.

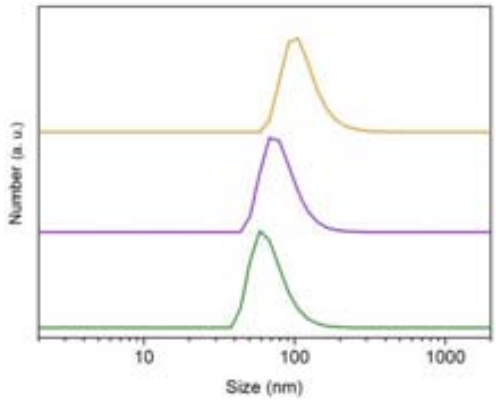

Figure 12. DLS measurements of the different colloids of NHKUST-1 crystals synthesised at different concentration of reactants: $[Cu^{2+}]$ = 0.0017 M, green; $[Cu^{2+}]$ = 0.017 M, purple; and $[Cu^{2+}]$ = 0.17 M, orange.

The impact of the flow rate on the crystal size was studied at high inlet temperature (180 ºC) and high metal concentration of 0.17 M. It was observed that an increase in the flow rate resulted in the formation of smaller crystals (**Table 1**; SD3 to SD5). Under otherwise identical conditions, the sample prepared at the highest flow rate (474 ml·min^{-1}) had a crystal size of 107 ± 30 nm, whereas the sample prepared at the lowest flow rate (129 ml·min^{-1}) had a size of 167 ± 50 nm. This tendency was also confirmed by the DLS analysis of the corresponding colloidal suspensions (**Figure 13**).

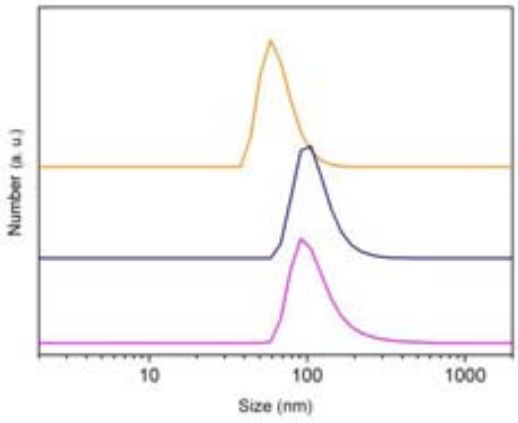

Figure 13. DLS measurements of the different colloids of NHKUST-1 crystals synthesised at constant 0.17 M $[Cu^{2+}]$ concentration and 180 ºC inlet temperature but different flow rates: low gas flow rate = 129 ml·min^{-1}, pink; medium flow rate = 336 ml·min^{-1}, blue; and high flow rate = 474 ml·min^{-1}, orange.

In contrast, when the SD reactions were performed at a constant precursor concentration and flow rate but varying the inlet temperature from 100 ºC to 180 ºC, it was not observed an effect on the crystal size even though at higher temperatures, one could expect a faster drying and consequently, the formation of smaller crystals. However, it is known that the inlet temperature does not affect the aerosol droplet size and that the aerosol droplet size has a very important role in the drying kinetics, which ultimately affect the crystal size.[30] Therefore, experiments performed under identical conditions but varying the inlet temperature would have similar drying kinetics and consequently, similar crystal sizes.

Importantly, the same behaviour was observed at different concentrations of precursors. Two sets of experiments were compared fixing the precursor concentration of Cu(II) to 0.0017 M and 0.17 M. In both cases, the inlet temperature ranged from 100ºC to 180ºC. In all six experiments, the flow rate was maintained constant 336 $ml \cdot min^{-1}$. In both set of experiments, the size remained constant throughout the temperature range, being the crystal size smaller for the samples sprayed at the lower concentrations (**Table 1**; SD1, SD10-11) than the samples sprayed at the higher concentrations (**Table 1**; SD 3, SD 8-9). **Figure 14** shows the DLS measurement of the colloidal suspensions of both set of experiments, which corroborates the tendencies observed through FESEM analysis. This clearly demonstrates the effect on the crystal size of the precursor concentration at all temperatures tested and confirms that the inlet temperature does not have an effect on this aspect, independently of the precursor concentration.

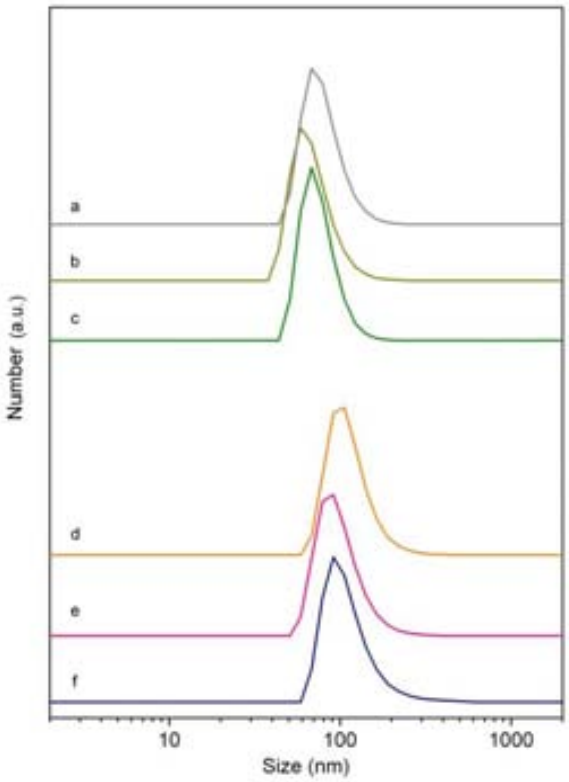

Figure 14. DLS measurements of the different colloids of NHKUST-1 crystals synthesised at: T_{inlet} = 180 ºC, (d) $[Cu^{2+}]$ = 0.17 M; (a) $[Cu^{2+}]$ = 0.0017 M; T_{inlet} = 150 ºC, (e) $[Cu^{2+}]$ = 0.17 M; (b) $[Cu^{2+}]$ = 0.0017 M; T_{inlet} = 100 ºC, (f) $[Cu^{2+}]$ = 0.17 M; (c) $[Cu^{2+}]$ = 0.0017 M.

2.1.2.2. Impact of the Spray-Drying parameters on the yield and purity

Both yield and purity of the SD synthesis of NHKUST-1 are also dictated by the precursor concentration, flow rate and inlet temperature. To summarize, higher precursor concentration gave higher yields but lower purities; higher inlet temperatures gave higher purities and yields; and higher flow rate gave higher yields.

It is important to distinguish here the information given by the parameters purity and yield. While the yield takes into account the overall process of SD considering both the chemical transformation and the powder recovery, the purity only accounts for the efficiency of the chemical transformation, not taking into account how much powder is eventually lost during the SD process. For example, if at a given condition the chemical transformation is highly efficient but the recovery of the powder is less efficient (*i.e.* a fraction of the formed NHKUST-1 powder is lost to the outlet filter), the resulting powder will have a good purity but, on the contrary, the yield will be low. For this reason, when low amounts of reactants are sprayed, their yields are systematically lower than would correspond to their high purities. This tendency is due to the high impact of the solid lost during the drying process. This effect of losing powder through the outlet filter becomes less important when

high concentrations are used. This explains why when high reactant concentrations are used, the yield increases even though the purity is reduced (in **Table 1** references SD 1-3).

The effect of flow rate does not significantly affect the purity of NHKUST-1, but it affects the yield. Higher flow rates produce dried powders which are easily recovered, thereby increasing the yield. Flow rate and inlet temperature are somehow related as both parameters are responsible for a good atomisation and drying. Thus, the effect of flow rate was tested at two extreme inlet temperatures, (100 ºC **Table 1**; SD 6, SD 7 and SD 9) and 180 ºC (**Table 1**; SD 3-5). The same effect was observed in both set of experiments: for high flow rates, the yield was higher but the purity remained constant.

It was observed that, at an inlet temperature of 180 ºC, a low flow rate of 129 $ml \cdot min^{-1}$ is enough to promote the atomisation and the chemical reaction. This was not the case when a lower inlet temperature of 100 ºC was used. This is a clear indication that heating the solution is not enough for the good formation of NHKUST-1. This heating must be coupled with the complete drying of the micrometric aerosol droplets.

The effect of the temperature was studied at two different concentrations: 0.0017 M (**Table 1**; SD1, SD10-11) and 0.17 M (**Table 1**; SD3, SD8-9). The trends observed at the two concentrations are coincident. Higher temperatures induce both better chemical reaction and recovery of the powder, which are translated in higher purities and yields. This can be rationalised by the improved atomisation and droplet drying at higher temperatures. As seen above, a successful drying is necessary to ensure the chemical reaction. Therefore, at higher temperatures, the aerosol drying is optimised and so it is the extent of the reaction. The obtained dried powders are easier to recover at high inlet temperatures which in turn contribute to increase the yield.

Thus, by controlling the parameters of the SD method, one can selectively prepare hollow MOF superstructures or discrete NMOF crystals at desired dimensions and with optimized purity and yield. For example, using the highest values for all the parameters (flow rate: 474 mL/min; inlet temperature: 180 ºC; and metal salt concentration: 0.17 M), which correspond to the reference SD4 in **Table 1**, it was possible to prepare hollow HKUST-1 superstructures and NHKUST-1 crystals (~100 nm in size) at a production rate of 140 $mg \cdot min^{-1}$ with yields up to 85%.

2.1.3. Scale up considerations

The wide range of applications that MOFs can offer has started to attract the attention of industry towards these materials. However, the implementation of MOFs in industry encounters several challenges being one of the most relevant their fabrication.[39] Specifically, the cost efficiency of the

reaction is a major factor to consider when assessing the feasibility of the industrial implementation. One way of evaluating the efficiency of the reaction in terms of scaled-up production is calculating the production rate (mass of MOF per unit of time) and its Space-Time-Yield (STY). The STY estimates the Kg of product (in this case, MOFs) per m^3 of solvent employed and day. Unlike the molecular yield, the STY takes into account the concentration of the product. High STY entails high concentration of product and therefore, more efficient use of solvents that reduces costs. Generally, the methodologies reported in the scientific literature (most of them at the lab scale regime) have very modest STY, with values typically between 0.1 and 1 $Kg \cdot m^{-3}$ per day. These low values are generally due to the low concentrations and low volumes of the solvothermal reactions used in fundamental research. However, when the batch solvothermal reactions are scaled up, high STY can be achieved, as reported by the chemical company BASF SE (**Table 2**).[40] In fact, the scaled up solvothermal production of MOFs has made possible the current commercial distribution of some representative MOFs.

Even though batch solvothermal synthesis is the most common methodology in basic research facilities, alternative methodologies are under study in industry to make a more efficient use of reactants and solvents and to implement safer and greener processes. For instance, electrochemical methods are presented as salt free methods that can achieve high STY. In this methodology, the metal is used as a sacrificial anode, which is oxidised in the presence of the organic linker in an electrochemical cell. This method has been successfully applied to MOFs generally containing Cu(II), Zn(II) or Al(III) ions with promising results in terms of STY (typically values above 150).[40,41] In addition, this method prevents from using metal's counter ions, such as nitrates, which might present safety issues in an industrial process. Another concern regarding the synthesis of MOFs is the extensive use of solvents. In this respect, mechanochemical methods for the synthesise MOFs is a very attractive method. Mechanochemical synthesis consists on mixing and grinding the precursors of MOFs in solid state. Therefore, the method is solvent-free. To date, however, only a few representative MOFs have been synthesised through mechanochemical methods, including HKUST-1,[42] so the current main drawback of this technique is its current limited catalogue of synthesised MOFs.

One of the major drawbacks of the batch methods such as solvothermal or electrochemical reactions is generally the reaction time, which it is in the range of several hours up to several days. For this reason, continuous flow methods that allow faster reactions have emerged as an alternative to batch reactors. This approach is based on an efficient mixture of the reactants under a continuous flow for a given residence time (that can entail heating or not) after which the MOF is synthesised. This method has proven to shorten reaction times, and it has the intrinsic advantage of continuous production; that is, one does not need to stop the fabrication from batch to batch.[43,44]

Table 2. Summary of the reaction conditions of industrially relevant synthetic methods of MOFs.

Commercial name	MOF	Metal ion	Ligand	Synthetic method	STY	References
Basolite A100	Al(III) terephtalate	Al(III)	BTC	Solvothermal	160	[40]
Basolite A520	Al(III) fumarate	Al(III)	Fumaric acid	Hydrothermal	>3600	[45]
Basolite M050	Mg(II) formate	Mg(II)	Formic acid	Solvent free synthesis	>3000	[46]
	MIL-100(Fe)	Fe(III)	BTC	Hydrothermal	>1700	[47]
	HKUST-1	Cu(II)	BTC	Room temperature synthesis	57	[48]
Basolite C300	HKUST-1	Cu(II)	BTC	Electrochemical	225	[40]
Basolite Z1200	ZIF-8	Zn(II)	2-Methylimidazole	Electrochemical	60-160	[40]
	Zn-MOF-74	Zn(II)	DHTA	Electrochemical	258	[49]
	Al-MIL-53	Al(III)	BDC	Electrochemical	186	[41]
	HKUST-1	Cu(II)	BTC	Continous flow	17	[44]
	HKUST-1	Cu(II)	BTC	Continuous Flow	5.2	[43]

As a continuous flow method, SD has also the potential to become an industrial method for the production of MOFs. There are many characteristics that make SD very attractive: i) It allows continuous production; ii) The product is directly (one-step) recovered in the dry form, avoiding a filtration step; iii) Solvents can be easily recovered –SD is a closed system, where the evaporated solvents are condensed; and iv) SD is already a common industrial equipment.

The performance of SD as a mass production method was evaluated in our lab scale equipment. It was found that at a precursor concentration of 0.17 M, inlet temperature of 180 ºC, feed rate of 4.5 $ml \cdot min^{-1}$ and flow rate of 336 $ml \cdot min^{-1}$, a production rate of 7.2 $g \cdot h^{-1}$ was achieved. Considering these parameters, the estimated STY was 31 $Kg \cdot m^{-3} \cdot day^{-1}$ (**Table 3**). The critical parameter to increase the STY is the concentration of the reactants, as it ensures a more efficient use of the solvent if the yield is maintained. Due to solubility reasons, the maximum concentration that was tested was 0.85 M for Cu(II) and 0.57 M for BTC. Consequently, 20 ml of solution were sprayed in 4 min, from which 4.2 g of crude solid was recovered. The purity and yield of the powder was 67 % and 75 %, respectively. Therefore, the production rate under these new conditions (and using a laboratory equipment) was 38.4 $g \cdot h^{-1}$, which represents a STY up to 141, in the range of the other reported industrial values for MOFs.

Whereas the STY does not change with the feed rate (production rate increases proportionally to the amount of solvent used per unit of time), the production rate is largely affected by the feed rate. For example, we were able to increase the production rate of NHKUST-1 up to 117 $g \cdot h^{-1}$ by

increasing the feed rate from 270 $ml \cdot h^{-1}$ to 900 $ml \cdot h^{-1}$ and using highly concentrated precursor solution ([Cu(II)] = 0.85 M). With this production rate, it was possible to synthesise NHKUST-1 in the order of kilograms in a laboratory scale equipment (**Figure 15**) in 8 h. The industrial production rate can be estimated considering the drying capacity and assuming that the yield will not be largely affected in the industrial equipment. An average industrial SD could process 500 l of concentrated precursor solution ([Cu(II)] = 0.85 M), which would mean that the production rate would be of 70 $Kg \cdot h^{-1}$.

Furthermore, SD instruments are commonly equipped with an inert loop that allows very high solvent recovery. This recovery reduces the wasted solvent without affecting the reaction performance. Therefore, the extent of solvent recovery has a clear impact on the estimated STY. This effect has not been studied and optimised so far and therefore, there is room for a further increase of the STY of the SD synthesis of NHKUST-1. For example, with a solvent recovery of 80%, the STY values would be increased by a factor of five.

Table 3. Scale up paramaters for the SD synthesis of NHKUST-1. In all cases, the STY was calculated not taking into account the solvent recovery.

Precursor Concentration (M)	Feed rate ($ml \cdot h^{-1}$)	Production rate ($g \cdot h^{-1}$)	Calculation formula	STY
0.17	270	7.2	$\frac{7.2\,{}^{g}/_{h} \times 24\,{}^{h}/_{day} \times 10^{-3}\,{}^{kg}/_{g}}{270\,{}^{ml}/_{h} \times 24h \times 10^{-6}\,{}^{m^3}/_{ml}}$	31
0.85	270	38.4	$\frac{38.4\,{}^{g}/_{h} \times 24\,{}^{h}/_{day} \times 10^{-3}\,{}^{kg}/_{g}}{270\,{}^{ml}/_{h} \times 24h \times 10^{-6}\,{}^{m^3}/_{ml}}$	141
0.85	900	117	$\frac{117\,{}^{g}/_{h} \times 24\,{}^{h}/_{day} \times 10^{-3}\,{}^{kg}/_{g}}{900\,{}^{ml}/_{h} \times 24h \times 10^{-6}\,{}^{m^3}/_{ml}}$	130

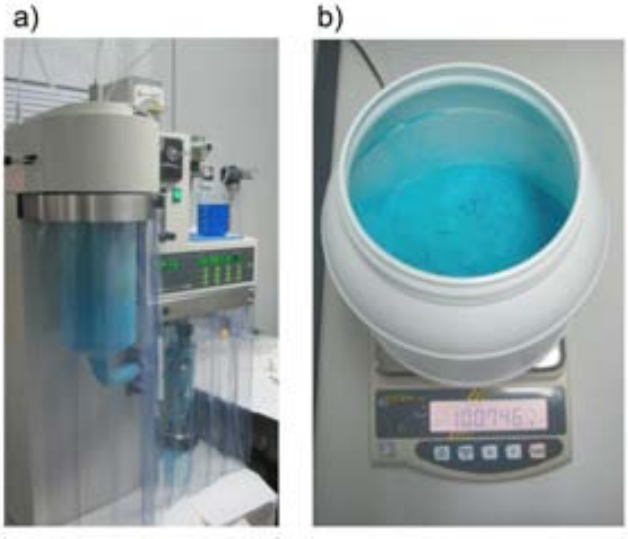

Figure 15. **a)** SD synthesis NHKUST-1 at a concentration of Cu(II) of 0.85 M and feed rate of 900 ml·h^{-1} **b)** Photograph of one kilogram of NHKUST-1 obtained after 8h of continuous SD.

2.2. Synthesis of broad spectrum of Metal-Organic Frameworks.

To demonstrate the scope of the SD technique beyond the archetypical compound HKUST-1, we also used it to prepare hollow superstructures and nanocrystals of a series of iconic MOFs that represent the major subfamilies of porous MOFs. The synthesised NMOFs comprised the two-dimensional Cu(BDC) (where BDC is 1,4-benzenedicarboxylate)[23]; the three-dimensional Cu_2(BPTC) (known as NOTT-100 or MOF-505; where BPTC is 3,3',5,5'-biphenyltetracarboxylic acid)[50]; Fe_3O(fumarate)$_3$ (known as MIL-88A)[51]; $Fe_3O(NH_2\text{-BDC})_3$ (known as MIL-88B; where NH_2-BDC is 2-aminoterephtalic acid)[51]; $Cu_3(BTB)_2$ (known as MOF-14; where BTB is 4,4′,4"-benzene-1,3,5-triyl-tribenzoic acid)[52]; M_2(DHBDC) (known as MOF-74 or CPO-27; where *M* is Zn(II), Mg(II), and Ni(II) and DHBDC is 2,5-dihydroxy-1,4-benzenedicarboxylic)[53] and $Zr_6O_4(OH)_4(BDC)_6$ (known as UiO-66)[54]. **Figure 16** shows typical FESEM and TEM images of the resulting sub-5µm hollow MOF superstructures and discrete NMOFs crystals, in which dimensions down to 150 nm were achieved for most of the cases. As for the HKUST-1 structures, their phase purity was assessed by XRPD. The experimental conditions used are summarized in **Table 4**. Interestingly, the range of the materials synthesised comprise MOFs with distinct SBU, including the Cu(II)-paddle wheel based MOFs, the μ_3-oxo-trimeric Fe(III) for the sub-family of MILs, the Zr(IV) oxocluster for the UiO-66, and the helical rod of Zn-O-C with composition $[Zn_2O_2](CO_2)_2$ of MOF-74 analogues. In addition, in this catalogue, it is also possible to find MOFs with metal open sites, such as HKUST-1, MILs and MOF-74. Therefore, the SD shows to be capable to expand the synthesis to different class of MOFs with different topologies and metal ions. In all cases, after exposing the MOF superstructures to ultrasounds, stable colloidal dispersions were obtained and the size determined by FESEM could be correlated with the values reported by the DLS measurements (**Figure 17**). These results make the SD

a most general and versatile approach for the continuous synthesis of MOFs when compared to the current methods based on continuous flow.[43,44,54]

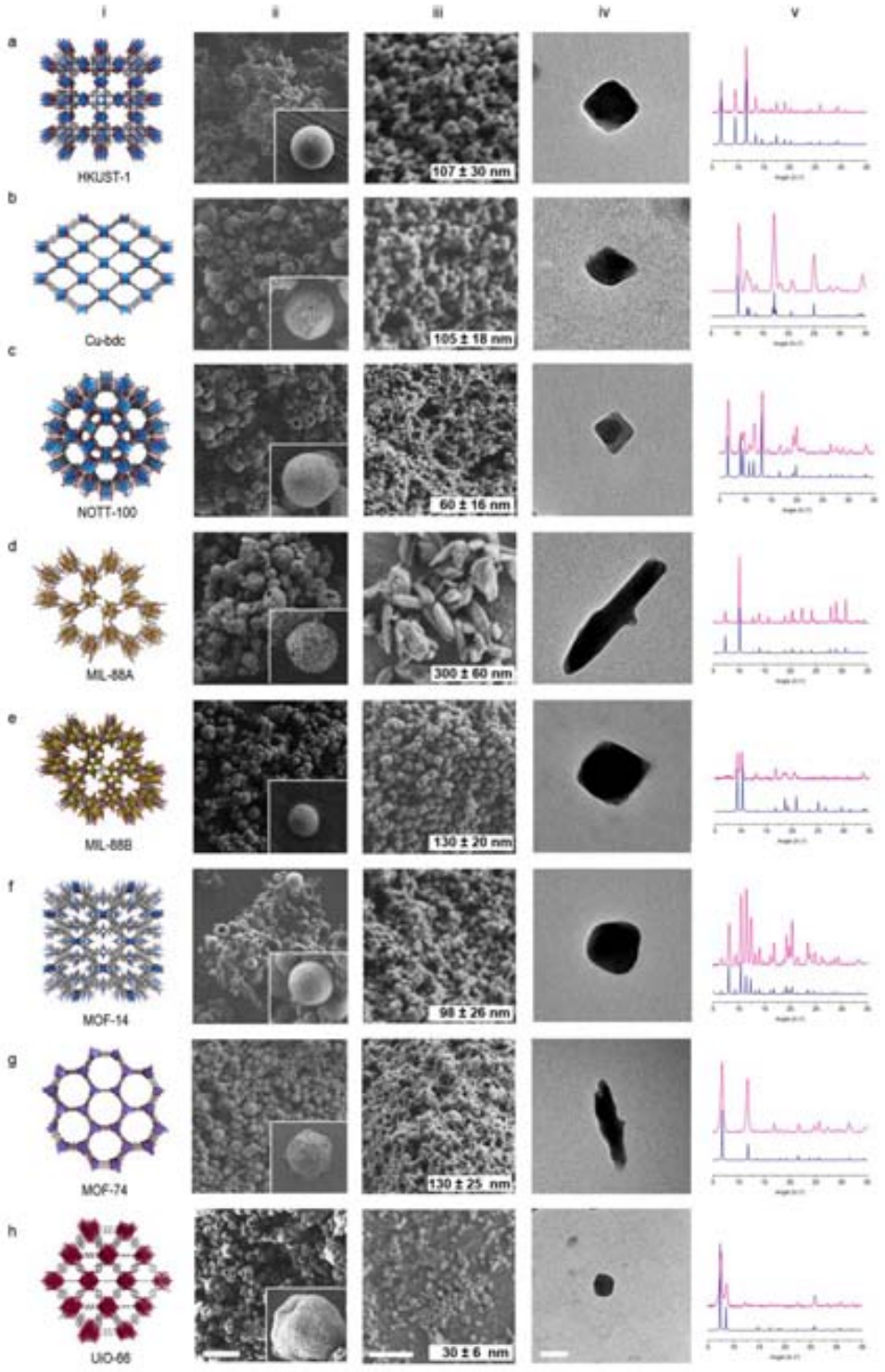

Figure 16. Series of MOF superstructures and discrete NMOF crystals synthesized by spray-drying. The list of synthesized MOFs comprises HKUST-1 (for comparison), Cu-BDC, NOTT-100, MIL-88A, MIL-88B, MOF-14 and Zn-MOF-74. The FESEM and TEM images of the synthesised MOF superstructures and discrete nanoMOF crystals, and the corresponding experimental (pink) and simulated (blue) XRPD patterns (for comparison), are shown for each MOF. The scale bars correspond to 10 μm, 2 μm, 500 nm and 50 nm (from left to right).

Table 4. Sumarize of the experimental conditions employed to synthesise MOFs through a two fluid nozzle. All experiments were performed using an inlet temperature of 180 ºC and a flow rate of 336 ml·min^{-1}.

NMOF	Metal precursor [M]	Ligand [M]		Solvent	Purity (%)	Yield (%)
Cu-BDC	$Cu(NO_3)_2 \cdot 2.5H_2O$ [0.17]	BDC	[0.17]	DMF	90	70
NOTT-100	$Cu(NO_3)_2 \cdot 2.5H_2O$ [0.028]	BPTC	[0.014]	DMF/Water (2:1)	75	54
MIL-88A	$FeCl_3 \cdot 6H_2O$ [0.2]	Fumaric acid	[0.2]	DMF	8	10
MIL-88B	$FeCl_3 \cdot 6H_2O$ [0.3]	NH_2-BDC	[0.15]	DMF	10	27
MOF-14	$Cu(NO_3)_2 \cdot 2.5H_2O$ [0.019]	BTB	[0.013]	DMF/EtOH/Water (3:3:2)	32	30
MOF-74	$Zn(NO_3)_2 \cdot 6H_2O$ [0.17]	DHTA	[0.06]	DMF/Water (17:1)	50	40
	$Mg(NO_3)_2 \cdot 6H_2O$ [0.05]		[0.013]	DMF/EtOH/Water (15:1:1)	45	35
	$Ni(NO_3)_2 \cdot 6H_2O$ [0.1]		[0.05]	DMF/EtOH/Water (1:1:1)	50	40
UiO-66	$ZrCl_4$ [0.024]	BDC	[0.024]	DMF	70	60

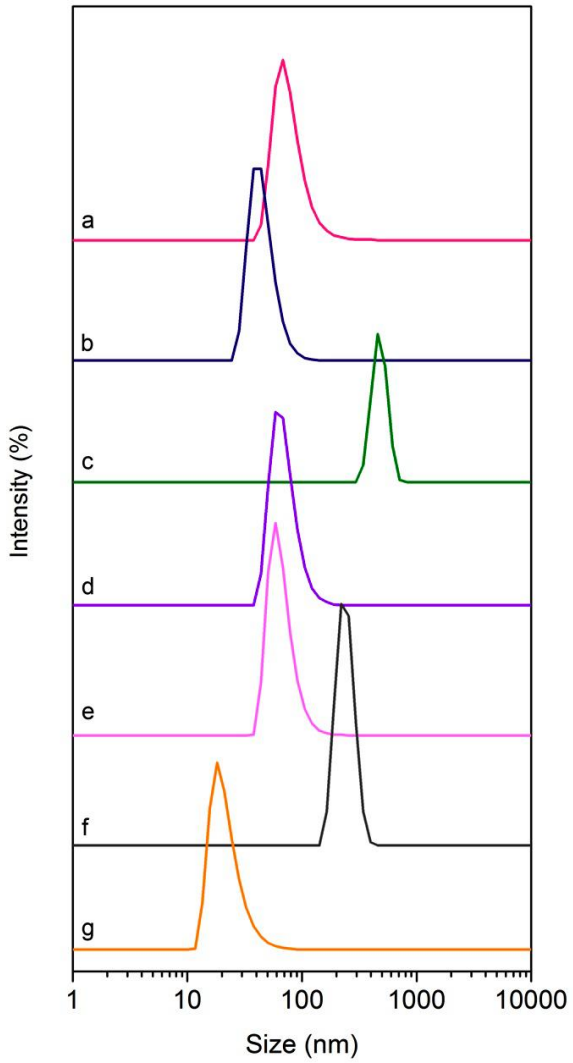

Figure 17. DLS measurements of the different colloids of NCu-BDC [a, Z-average diameter of 60 nm and the polydispersity index (PdI) of 0.241], NNOTT-100 [b, 45 nm (PdI = 0.152)], NMIL-88A (c, 688 nm (PdI = 0.432)], NMIL-88B [d, 76 nm (PdI = 0.330)], NMOF-14 [e, 76 nm (PdI = 0.300)], Zn-NMOF-74 [f, 240 nm (PdI = 0.383)], and NUiO-66 [g, 36 nm (PdI = 0.280)] crystals. Note that NMIL-88A and Zn-NMOF-74 show higher values due to some particle aggregation because values of 300 ± 60 nm and 98 ± 26 nm were observed by SEM, respectively.

2.3. Versatility of Spray-Drying

SD using a two fluid nozzle proved to be a successful strategy to synthesise MOFs from stable precursor solutions generally containing the two building blocks in organic solvents such as DMF. Nevertheless, the recipes to synthesise MOFs are very rich and varied. In some cases, additives are used to speed the crystallization of MOFs (*e.g.* bases, excess of one reactant and alternative solvents). In these cases, the precursor solution might not be stable throughout the spraying process, appearing undesired species or bulk crystals before the atomisation. In order to implement the SD methodology to unstable MOF precursor mixtures, we implemented two different methodologies named as I) "T-mode" and II) 3-fluid nozzle. Both strategies consist on mixing the precursor solutions shortly before the atomisation. **Figure 18** shows schemes of both strategies.

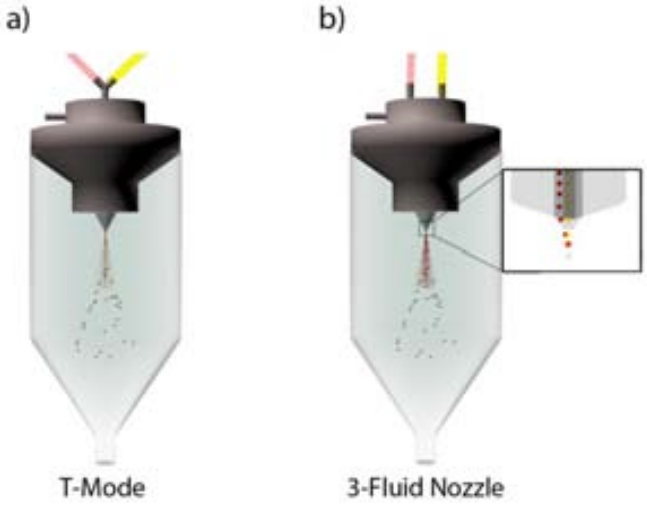

Figure 18. Schematic representation of the mode of operation using the T-mode approach **(a)** and the 3-fluid nozzle approach **(b)**.

2.3.1. T-Mode

In the T-mode, two precursor solutions are independently pumped to a T junction where they are mixed just before entering to the nozzle **(Figure 17a**). This methodology was first applied to the synthesis of HKUST-1. In previous experiments performed in bulk, it was found that HKUST-1 can be synthesised by simply mixing $Cu(Ac)_2 \cdot 2.5\ H_2O$ and BTC in a mixture of ethanol and water (1:1). However, a precipitate appears shortly upon mixing both precursors. This fast precipitation prevents to use this formulation for the SD synthesis of HKUST-1 using the conventional 2-fluid nozzle. To overcome this limitation, two precursor solutions one containing an ethanolic solution of BTC (0.03 M) and the other an aqueous solution of $Cu(Ac)_2$ (0.045 M), were prepared separately. Then, both solutions were independently pumped and mixed just before entering the two fluid nozzle (and consequently, sprayed) through a pipe tee (**Figure 19b**).

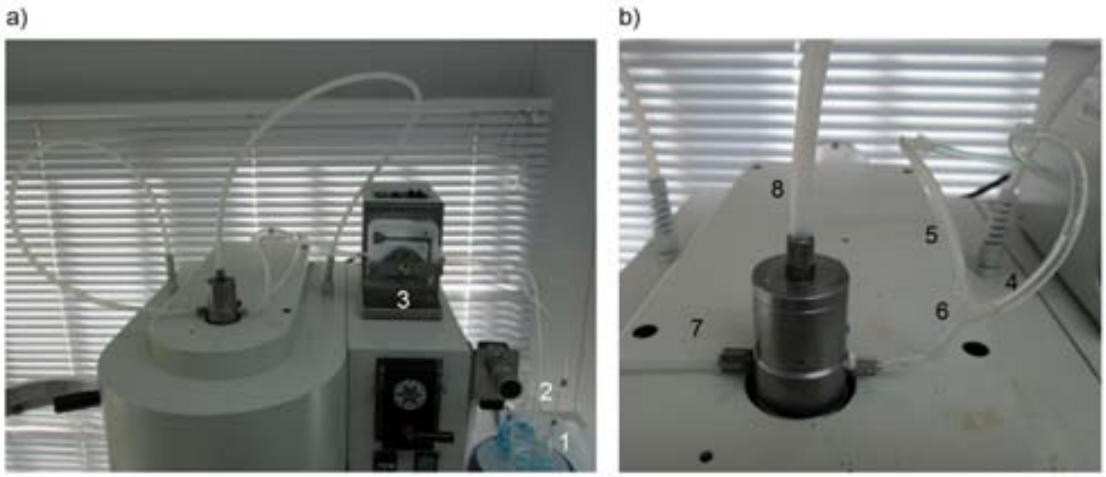

Figure 19. a) General view of the spray dryer, showing that aqueous $Cu(NO_3)_2$ solution (1) and an ethanolic BTC solution (2) are independently pumped with a peristaltic bomb (3). **b)** Close image of the upper part showing the two fluid nozzle. Note that the two independently pumped solutions (5, 6) are mixed just before the spraying at the "T" junction (6). The resulting mixed solution is then atomized with the gas flow (7). In case of eventual clocking, there is an extra gas flow that can clean the nozzle (8).

During the experiment, no clocking of the nozzle was observed indicating that no reaction happened in the nozzle. The obtained HKUST-1, also composed of spherical superstructures (**Figure 20b**), was phase pure as revealed by XRPD (**Figure 20a**). Interestingly, a high surface area of 1600 $m^2 \cdot g^{-1}$ was measured for this formulation. The calculated purity and yield was 60% and 40%, respectively. In addition, the use of more volatile solvents allowed for a lower inlet temperature of 80ºC to be used.

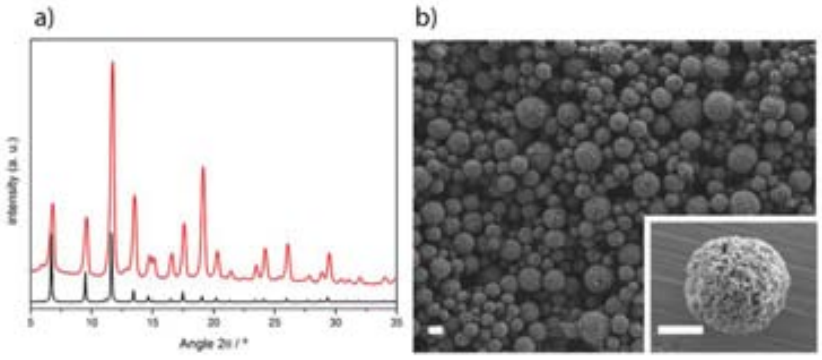

Figure 20. a) XRPD pattern of the as-sprayed HKUST-1 (red) and simulated pattern (black). **b)** FESEM images of the as-sprayed powder. The scale bars correspond to 2 μm and 1 μm (inset).

$Zn_4O(BDC)_6$ (known as MOF-5) belongs to the family of isoreticulated MOFs (IRMOFs), and it has been extensively studied due to its high N_2 and H_2 adsorption.[55] However, its synthesis is quite challenging as the reaction of its building blocks can give rise to a variety of products.[52] As a matter of fact, the first attempts to produce MOF-5, in which a DMF or DEF precursor solution with $Zn(NO_3)_2$ as the metallic precursor was spray-dried using a 2-fluid nozzle, resulted in the synthesis of $Zn_2(BDC)_4(H_2O)_2$ (known as MOF-2). Another strategy to synthesise MOF-5 uses $Zn(Ac)_2$ as the metallic precursor.[53] Following this approach, MOF-5 was synthesised by pumping two DMF solutions one containing $Zn(Ac)_2$ and the other BDC, and mixing them with the "T" connector. Again, no clocking of the nozzle was observed. The resulting powder was comprised of spherical MOF-5 superstructures of 5-10 μm-in-diameter. The resulting colloidal suspensions obtained after sonicating these superstructures were made of monodisperse crystals of 60 nm, as observed by FESEM and DLS (**Figure 21**). Here, the purity and the yield were 50% and 60%, respectively, and the BET analysis confirmed a porosity of 1215 $m^2 \cdot g^{-1}$. A very similar methodology was also applied for the synthesis of IRMOF-3; an analogue MOF-5 structure built up from Zn(II) and 2-aminoterephtalic acid. This

NMOF was obtained in the form of monodisperse 60 nm-in-size crystals with a purity of 84% and a yield of 70%.

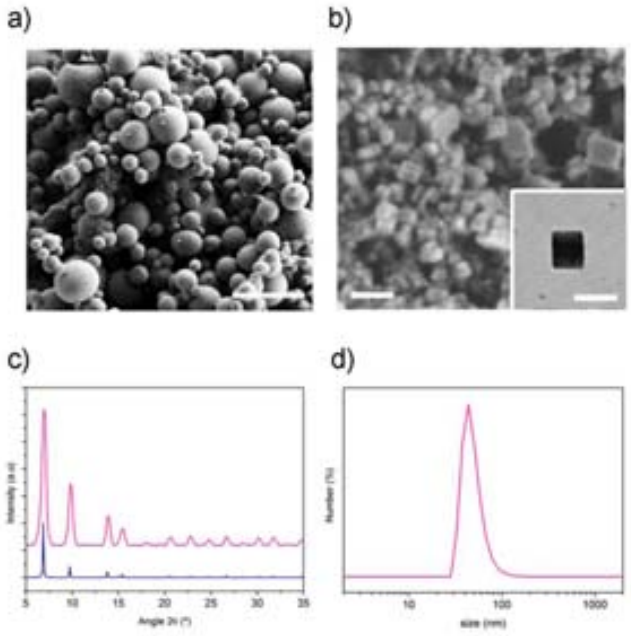

Figure 21. **a)** FESEM of the spherical MOF-5 superstructures. **b)** Representative FESEM image of discrete NMOF-5 crystals and TEM image of a single NMOF-5 crystal (inset). **c)** Experimental (pink) and the simulated XRPD patterns of MOF-5 (blue). **d)** DLS of the discrete NMOF-5 crystals (60 nm, PDI = 0.24). The scale bars correspond to 10 μm (**a**), 100 nm (**b**) and 50 nm (**inset**).

2.3.2. 3-Fluid nozzle

The T-mode approach is appropriate when unstable precursor MOF solution wants to be sprayed. However, in some cases, the precursor mixture is so reactive that even very short contact times can cause precipitation before spraying. In this case, the use of a three fluid nozzle is advantageous as the precursor solution only come in contact at the end of the nozzle (**Figure 22**). This reduces drastically the contact time of the two precursors before they are atomized, avoiding the bulk precipitation. In a typical experiment using this approach, the two solutions that contain the MOF prescursors are independently pumped in the same way that in the case of the T-mode (**Figure 22a**). However, as shown in **Figure 22b**, the two solutions enter separately to the three fluid nozzle. Here, Both solutions only mix at the end of the nozzle, where the three channels meet; one per each solution and an additional one for the gas flow (**Figure 22d**).

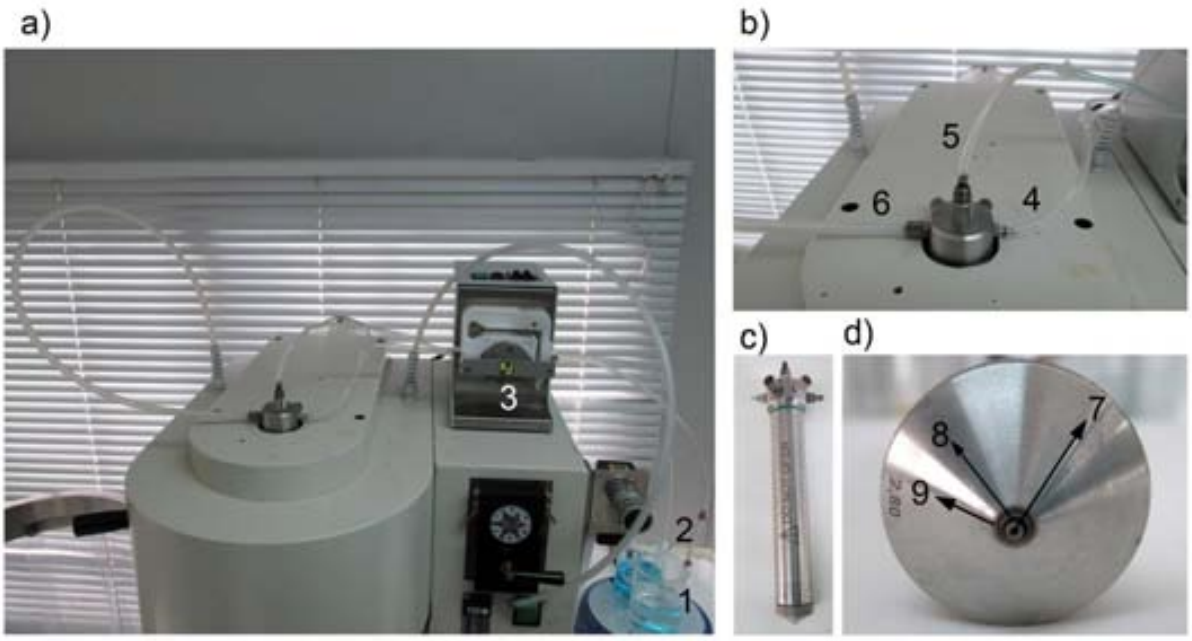

Figure 22. **a,b)** Photographs of the upper part of the spray dryer when a 3-fluid nozzle is implemented. Two solutions containing the MOF precursors or any reaction accelerator (1 and 2), such as bases, are independently pumped with a peristaltic pump (3). The two solutions enter into the 3-fluid nozzle through two different channels (4 and 5). Gas flow also enters to the nozzle through an alternative channel (6). **c)** Image of a 3-fluid nozzle. **d)** Close image of the end of the nozzle. Three concentrically orifices are observed. One of the precursor solution circulates in the inner channel (7). The other precursor solution flows in the middle channel (8). The gas flows through the external channel (9), which will produce the atomisation of the *in situ* mixed precursor solutions.

We tested this variation with the synthesis of NMIL-88A. In our previous synthesis using the 2-fluid nozzle, NMIL-88A was synthesised from a DMF precursor solution of $FeCl_3$ and fumaric acid with a poor yield and purity (10% and 8%, respectively). It is well known that MIL-88A can be prepared in higher yields when fumarate is used instead of fumaric acid and water is used as the solvent.[56] However, the instantaneous precipitation of an amorphous product prevented us to use this mixture with a 2-fluid nozzle. This was not the case with the 3-fluid nozzle. Here, two aqueous solutions, one containing Fe(III) and the other containing fumarate at basic pH due to the addition of NaOH, were independently sprayed using the 3-fluid nozzle. **Figure 23** shows the resulting powder composed of spherical NMIL-88A superstructures and the resulting NMIL-88A nanocrystals after sonicating these superstructures. The phase purity was again confirmed by XRPD (**Figure 23c**). Importantly, both yield (40%) and purity (79%) were significantly higher using this variation.

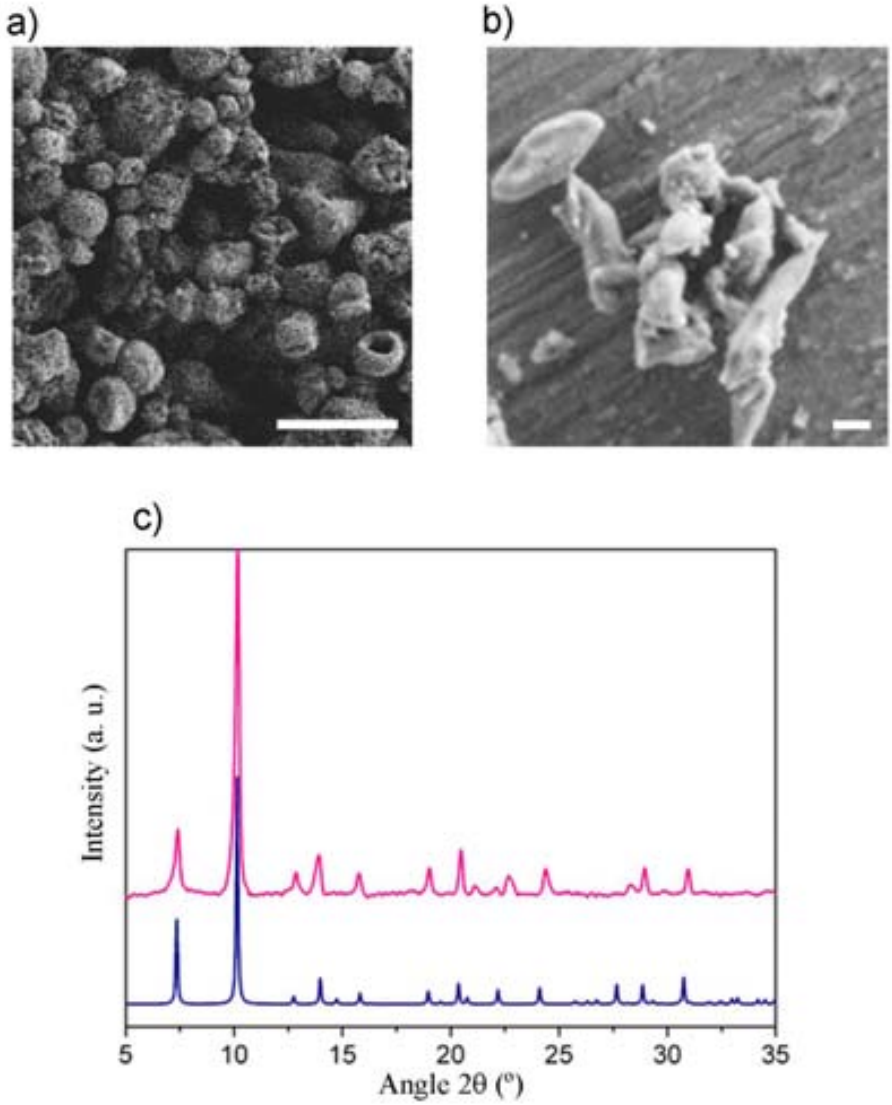

Figure 23. **a)** Representative FESEM images of spherical MIL-88A superstructures. **b)** Representative FESEM of NMIL-88A crystals synthesised using the 3-fluid nozzle. **c)** XRPD pattern of NMIL-88A crystals (pink) compared with its simulated XRPD pattern (blue). The scale bars correspond to 2 μm (**a**) and 200 nm (**b**).

ZIF-8 was also successfully synthesised using a 3-fluid nozzle. The previous attempts to produce it by spraying a precursor solution containing DMF, $Zn(NO_3)_2$ and 2-methylimidazole (MIM) using a 2-fluid nozzle were unsuccessful. In order to increase the reactivity of the precursor solution, other formulations were tried. For instance, aqueous solutions with high excess of MIM are reported to yield instantaneous precipitation of NZIF-8.[50] Nevertheless, the high excess of MIM ligand in this synthesis (molar ratio Zn:MIM (1:70)) was not suitable for SD in any of the methodologies. Alternatively, we found that spraying an aqueous solution of $Zn(Ac)_2$ and MIM (molar ratio Zn:MIM (1:10)) using the 3-fluid nozzle produced pure ZIF-8, as confirmed by XRPD (**Figure 24**). As for the other cases, spherical superstructures were formed and monodisperse crystals of 92 nm were obtained after their sonication. Both purity and yield were 60% and 10%, respectively. The low yield achieved

is partially due to the difficult recovery of the powder, which was sticky on the glass walls of the spray dryer. Porosity studies confirmed a BET surface area of 941 $m^2 \cdot g^{-1}$.

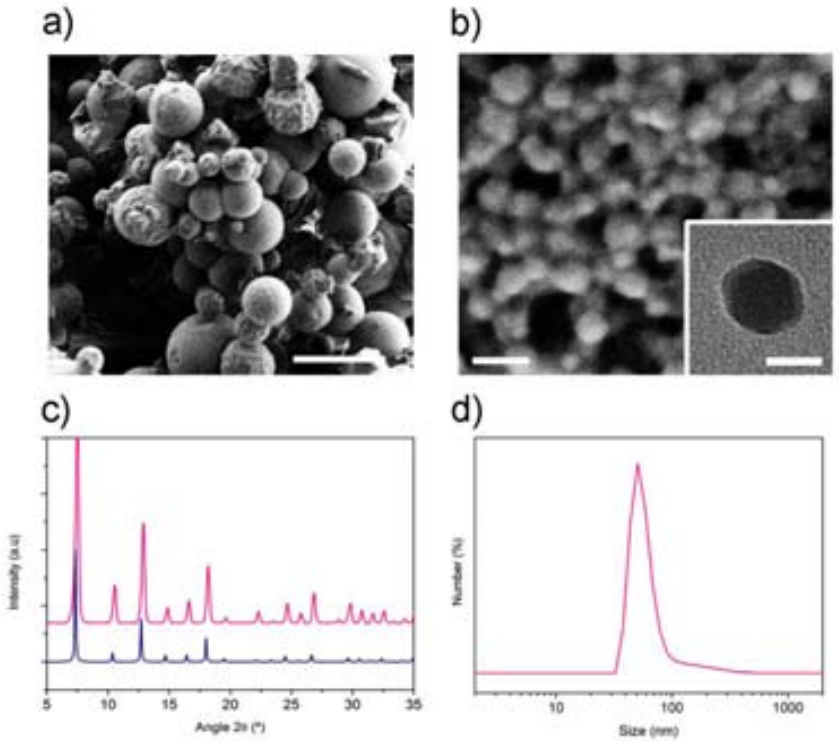

Figure 24. **a)** Representative FESEM image of spherical ZIF-8 superstructures. **b)** Representative FESEM image of the discrete NZIF-8 crystals and TEM images of one of these crystals. **c)** Experimental (pink) and simulated (blue) XRPD pattern . **d)** DLS of the discrete NZIF-8 crystals (92 nm, PDI = 0.22). The scale bars correspond to 10 μm (**a**), 100 nm (**b**) and 50 nm (**inset**).

Table 5. Experimental conditions employed to synthesise of the different MOFs through SD using the T-mode and the 3-fluid nozzle. All experiments were performed at an inlet temperature of 180ºC and a flow rate of 474 $ml \cdot min^{-1}$.

MOF	Metal precursor [M]	Ligand [M]		Solvent	Purity (%)	Yield (%)
Operation Mode: T-type junction						
HKUST-1	$Cu(Ac)_2 \cdot XH_2O$	BTC		Water/EtOH	40	60
MOF-5	$Zn(Ac)_2 \cdot 2H_2O$ [0.1]	BDC	[0.04]	DMF	60	50
IRMOF-3	$Zn(Ac)_2 \cdot 2H_2O$ [0.1]	NH_2-BDC	[0.004]	DMF	70	84
Operation Mode: 3-fluid nozzle						
PB	$K_3Co(CN)_6$ [0.16] $Cu(NO3)_2$ [0.3]	CN	[0.46]	Water	52	20
MIL-88A	$FeCl_3 \cdot 6H_2O$ [0.2]	Fumaric Acid	[0.2]	Water	72	40
ZIF-8	$Zn(Ac)_2 \cdot 2H_2O$ [0.16]	2-Methylimidazole	[0.016]	Water	60	10

CN = cyanhydric acid

3. Conclusions

In conclusion, it was proven that each aerosol droplets generated during the SD process can act as a very efficient micrometre reactor where the coordination and crystallization of MOFs occurs in a confined environment. The reaction in the aerosol droplets was demonstrated for a variety of MOFs. Importantly, the MOF synthesis occurs mainly on the shell of the aerosol droplet. This localization induces the self-assembly of the *in situ* created MOF nanocrystals, rendering hollow MOF spherical superstructures that can be disassembled upon sonication to yield stable colloidal suspensions. In addition, the SD technique allows a continuous production of MOFs with reduced time and easy recovery of solvents, making it very attractive as an industrial method.

The new methodology described in this Chapter enables for the first time the continuous and fast synthesis of MOF hollow superstructures. The higher order structures should promote new properties arising from the collective and synergistic properties of the assembled MOF crystals. One can envisage MOF superstructures as advanced encapsulating systems with selective release, heterogeneous catalysts or coupled to other materials to become new composites. The possibilities offered by the combination MOF superstructures with other functional materials will be discussed in the next **Chapter 4**.

4. References

(1) Masters, K. *Spray drying handbook*; George Godwin Ltd.: London, 1979.
(2) Birchal, V. S.; Passos, M. L.; Wildhagen, G. R. S.; Mujumdar, A. S. *Dry. Technol.* **2005**, *23*, 611.
(3) Huntington, D. H. *Dry. Technol.* **2004**, *22*, 1261.
(4) Sollohub, K.; Cal, K. *J. Pharm. Sci.* **2010**, *99*, 587.
(5) Bhandari, B. R.; Dumoulin, E. D.; Richard, H. M. J.; Noleau, I.; Lebert, A. M. *Journal of Food Science* **1992**, *57*, 217.
(6) Gharsallaoui, A.; Roudaut, G.; Chambin, O.; Voilley, A.; Saurel, R. *Food Res. Int.* **2007**, *40*, 1107.
(7) Fäldt, P.; Bergenståhl, B. *J. Am. Oil Chem. Soci.* **1995**, *72*, 171.
(8) Jafari, S. M.; Assadpoor, E.; Bhandari, B.; He, Y. *Food Res. Int.* **2008**, *41*, 172.
(9) Turchiuli, C.; Fuchs, M.; Bohin, M.; Cuvelier, M. E.; Ordonnaud, C.; Peyrat-Maillard, M. N.; Dumoulin, E. *Innov. Food Sci. Emerg. Tech.* **2005**, *6*, 29.
(10) Vehring, R. *Pharm. Res.* **2008**, *25*, 999.
(11) Hancock, B.; Parks, M. *Pharm. Res.* **2000**, *17*, 397.
(12) Férey, G. *Chem. Mater.* **2001**, *13*, 3084.
(13) Wikarsa, S.; Durand, D.; Delarbre, J.L.; Baylac, G.; Bataille, B.; *Drug Develop. Ind. Pharm.* **2008**, *34*, 485.
(14) Chandrakant, V.; Pardeshi, P. V. R.; Veena S. B.; Avinash, R. T. *J. Microencap.* **2012**, *29*, 103.
(15) Wu, K.; Li, J.; Wang, W.; Winstead, D. A. *J. Pharm. Sci.* **2009**, *98*, 2422.
(16) Ambike, A.; Mahadik, K. R.; Paradkar, A. *Pharm. Res.* **2005**, *22*, 990.
(17) Luo, P.; Nieh, T. G. *Mater. Sci. Eng. C* **1995**, *3*, 75.
(18) Kaluza, S.; Schröter, M. K.; Naumann d'Alnoncourt, R.; Reinecke, T.; Muhler, M. *Adv. Func. Mater.* **2008**, *18*, 3670.
(19) Kaluza, S.; Muhler, M. *J. Mater. Chem.* **2009**, *19*, 3914.
(20) Xu, H.; Tan, Z.; Abe, H.; Naito, M. *J. Ceram. Soc. Jpn.* **2011**, *119*, 180.
(21) Nicole, L.; Rozes, L.; Sanchez, C. *Adv. Mater.* **2010**, *22*, 3208.
(22) Lu, Y.; Fan, H.; Stump, A.; Ward, T. L.; Rieker, T.; Brinker, C. J. *Nature* **1999**, *398*, 223.
(23) Iskandar, F.; Mikrajuddin; Okuyama, K. *Nano Letters* **2002**, *2*, 389.
(24) Comotti, A.; Bracco, S.; Sozzani, P.; Horike, S.; Matsuda, R.; Chen, J.; Takata, M.; Kubota, Y.; Kitagawa, S. *J. Am. Chem. Soc.* **2008**, *130*, 13664.
(25) Andersson, N.; Alberius, P. C. A.; Skov Pedersen, J.; Bergström, L. *Microporous Mesoporous Mater.* **2004**, *72*, 175.
(26) Colilla, M.; Manzano, M.; Izquierdo-Barba, I.; Vallet-Regí, M.; Boissiére, C.; Sanchez, C. *Chem. Mater.* **2009**, *22*, 1821.
(27) Alonso, B.; Douy, A.; Veron, E.; Perez, J.; Rager, M.-N.; Massiot, D. *J. Mater. Chem.* **2004**, *14*, 2006.
(28) Lind, A.; du Fresne von Hohenesche, C.; Smått, J.-H.; Lindén, M.; Unger, K. K. *Microporous Mesoporous Mater.* **2003**, *66*, 219.
(29) Boissiere, C.; Grosso, D.; Chaumonnot, A.; Nicole, L.; Sanchez, C. *Adv. Mater.* **2011**, *23*, 599.
(30) Vaucher, S.; Li, M.; Mann, S. *Angew. Chem. Int. Ed.* **2000**, *39*, 1793.
(31) Taylor, K. M. L.; Jin, A.; Lin, W. *Angew. Chem. Int. Ed.* **2008**, *120*, 7836.
(32) Chui, S. S.-Y.; Lo, S. M.-F.; Charmant, J. P. H.; Orpen, A. G.; Williams, I. D. *Science* **1999**, *283*, 1148.
(33) Krawiec, P.; Kramer, M.; Sabo, M.; Kunschke, R.; Fröde, H.; Kaskel, S. *Adv. Eng. Mater.* **2006**, *8*, 293.
(34) amon, olima tre, Pi rngruber, D *Ind. Eng. Chemi. Res.* **2010**, *49*, 7497.
(35) Peng, Y.; Krungleviciute, V.; Eryazici, I.; Hupp, J. T.; Farha, O. K.; Yildirim, T. *J. Am. Chem. Soc.* **2013**, *135*, 11887.
(36) Lin, X.; Jia, J.; Hubberstey, P.; Schroder, M.; Champness, N. R. *CrystEngComm* **2007**, *9*, 438.
(37) Carbonell, C.; Imaz, I.; Maspoch, D. *J. Am. Chem. Soc.* **2011**, *133*, 2144.
(38) Elversson, J.; Millqvist-Fureby, A.; Alderborn, G.; Elofsson, U. *J. Pharm. Sci.* **2003**, *92*, 900.
(39) Czaja, A. U.; Trukhan, N.; Muller, U. *Chem. Soc. Rev.* **2009**, *38*, 1284.
(40) Čejka, *Angew. Chem. Int. Ed.* **2012**, *51*, 4782.

(41) Martinez Joaristi, A.; Juan-Alcañiz, J.; Serra-Crespo, P.; Kapteijn, F.; Gascon, J. *Cryst. Growth Des.* **2012**, *12*, 3489.
(42) Klimakow, M.; Klobes, P.; Thünemann, A. F.; Rademann, K.; Emmerling, F. *Chem. Mater.* **2010**, *22*, 5216.
(43) Faustini, M.; Kim, J.; Jeong, G.-Y.; Kim, J. Y.; Moon, H. R.; Ahn, W.-S.; Kim, D.-P. *J. Am. Chem. Soc.* **2013**, *135*, 14619.
(44) Kim, K.-J.; Li, Y. J.; Kreider, P. B.; Chang, C.-h.; Wannenmacher, N.; Thallapally, P.; Ahn, H.-G. *Chem. Commun.* **2013**.
(45) Gaab, M.; Trukhan, N.; Maurer, S.; Gummaraju, R.; Müller, U. *Microporous Mesoporous Mater.* **2012**, *157*, 131.
(46) Emi Leung, U. M., Gerhard Cox; SE, B., *Solvent-free preparation of magnesium format-based metal-organic framework.* Ed. 2009.
(47) Seo, Y.-K.; Yoon, J. W.; Lee, J. S.; Lee, U. H.; Hwang, Y. K.; Jun, C.-H.; Horcajada, P.; Serre, C.; Chang, J.-S. *Microporous Mesoporous Mater.* **2012**, *157*, 137.
(48) Majano, G.; Pérez-Ramírez, J. *Adv. Mat.* **2013**, *25*, 1052.
(49) Ulrich Mueller, H. P., Michael Hesse, Markus Schubert, Helge Wessel, Juergen Huff, Marcus Guzmann, Menos SE, B., Ed. 2011.
(50) Pan, Y.; Liu, Y.; Zeng, G.; Zhao, L.; Lai, Z. *Chem. Commun.* **2011**, *47*, 2071.
(51) Kaye, S. S.; Dailly, A.; Yaghi, O. M.; Long, J. R. *J. Am. Chem. Soc.* **2007**, *129*, 14176.
(52) Chen, B.; Wang, X.; Zhang, Q.; Xi, X.; Cai, J.; Qi, H.; Shi, S.; Wang, J.; Yuan, D.; Fang, M. *J. Mater. Chem.* **2010**, *20*, 3758.
(53) Tranchemontagne, D. J.; Hunt, J. R.; Yaghi, O. M. *Tetrahedron* **2008**, *64*, 8553.
(54) Gimeno-Fabra, M.; Munn, A. S.; Stevens, L. A.; Drage, T. C.; Grant, D. M.; Kashtiban, R. J.; Sloan, J.; Lester, E.; Walton, R. I. *Chem. Commun.* **2012**, *48*, 10642.
(55) Rosi, N. L.; Eckert, J.; Eddaoudi, M.; Vodak, D. T.; Kim, J.; O'Keeffe, M.; Yaghi, O. M. *Science* **2003**, *300*, 1127.
(56) Chalati, T.; Horcajada, P.; Gref, R.; Couvreur, P.; Serre, C. *J. Mater. Chem.* **2011**, *21*, 2220.

Chapter 4

Synthesis of Metal-Organic Framework based composites through Spray-Drying.

The combination of Metal-Organic Frameworks (MOFs) with exogenous functional materials to synthesise MOF-based composites enables to synergically or collectively combine the merits of both materials reaching properties unattainable for the individual components. Here, we report the synthesis of MOF-based composites through the Spray-Drying (SD) technique. The process relies on the confined mixture of the components of the composite in micronized aerosol droplets. The versatility of the SD technique enables to combine MOFs with a variety of materials, thus forming a wide variety of structurally different composites in the form of capsules in which the MOF constitutes the shell or in which the MOF is the encapsulated material.

1. MOF composites: Current compositions and synthetic methodologies

The careful choice of the building blocks in the synthesis of Metal-Organic Frameworks (MOFs) has strongly contributed to their rapid development in the past 20 years. Over this period, a vast catalogue of MOFs with a great variety of structures and properties has been reported, which have been proposed for myriad applications such as gas sorption and catalysis. However, beyond the improvements that an adequate design can induce in the MOF properties, the optimisation and the presence of MOFs in future real applications must come also from their combination with other type of materials, thereby creating composites.

The combination of MOFs with other functional materials has been recently proposed as a strategy to combine the merits of both components and mitigate their shortcomings. These materials, named as MOF composites, are composed of MOFs and one or more constituent materials. To date, MOFs have been combined with inorganic nanoparticles (INPs),[1] metal oxides,[2] quantum dots,[3] organic polymers[4], polyoxometalates[5] and silica.[6] A list of these MOF-based composites together with their potential properties is given in **Table 1**. To date, two main strategies can be distinguished in the synthesis of these MOF-based composites, depending on whether the MOF is synthesised prior the synthesis of the composite or it is synthesised *in situ* along with the composite (**Figure 1**).

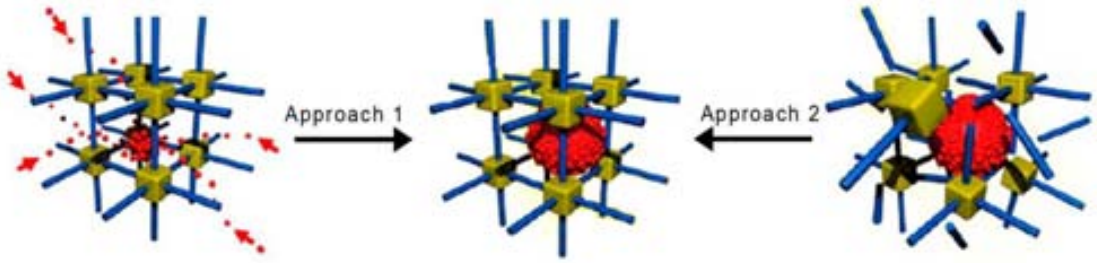

Figure 1. Strategies to incorporate nano-and microparticles to MOFs: infiltration of nanoparticle precursors (left) and induced nucleation and synthesis on preformed particles (right).[7]

1.1. MOFs as scaffolds for the synthesis of composites.

MOFs can be used as scaffolds to create composites by taking advantage of their high porosity to induce the direct formation of other materials in its pores. To date, this strategy proved to be very successful for the synthesis of composites combining MOFs with inorganic nanoparticles (INPs).[1] Here, the evacuated MOF is contacted with the molecular precursors of the INPs (by inmersion, solid grinding or vapour diffusion) to allow the diffusion of the reactants through the MOF channels. After this step, the precursors are reduced to produce the desired INPs, such as Ag,[8] Au,[9] Pd[10] and Pt,[11] inside the pores of the MOF structure. The combination of the catalytic activity of the INPs coupled with the narrow pore distribution of the MOF can be exploited to design size selective composite catalysts. For example, Kempe *et al.* synthesised Pd@$Fe_3O(H_2O)_2Cl(BTC)_2$ (also known as MIL-100; where BTC is 1,3,5-benzenetrycarboxylic acid), which showed a highly size selective catalysis of the hydrogenation of ketones to alcohols.[12]

This strategy was also employed by Kitagawa and co-workers for the synthesis of polymer@MOF composites. In this case, the monomers are adsorbed by the evacuated MOF followed by their polymerization to produce the polymer@MOF composite.[13] Following this strategy, divinyl crosslinkers, 2,5-divinyl-terephtalate (DVTP), were used to prepare a MOF with formula $Cu(DVTP)_x(BDC)_{1-x}(triethylamine)_{0.5}$. Therefore, the crosslinking monomer is incorporated in the channels of the structure. Then, the subsequent polymerization of adsorbed vinyl monomers in the channels gave rise to a highly ordered polystyrene@MOF composite. Interestingly, polystyrene retained its crystalline arrangement even after selective removal of the MOF (**Figure 2**).[14] The same strategy was used to confine the hydrolysis of tetramethoxysilane (TEOS) within the channels of Cu_3BTC_2 (also known as HKUST-1; where BTC is 1,3,5-benzenetricarboxylic acid). In this case, the inclusion of silica within the pores of the MOF allowed the selective adsorption of hydrophilic molecules.[15]

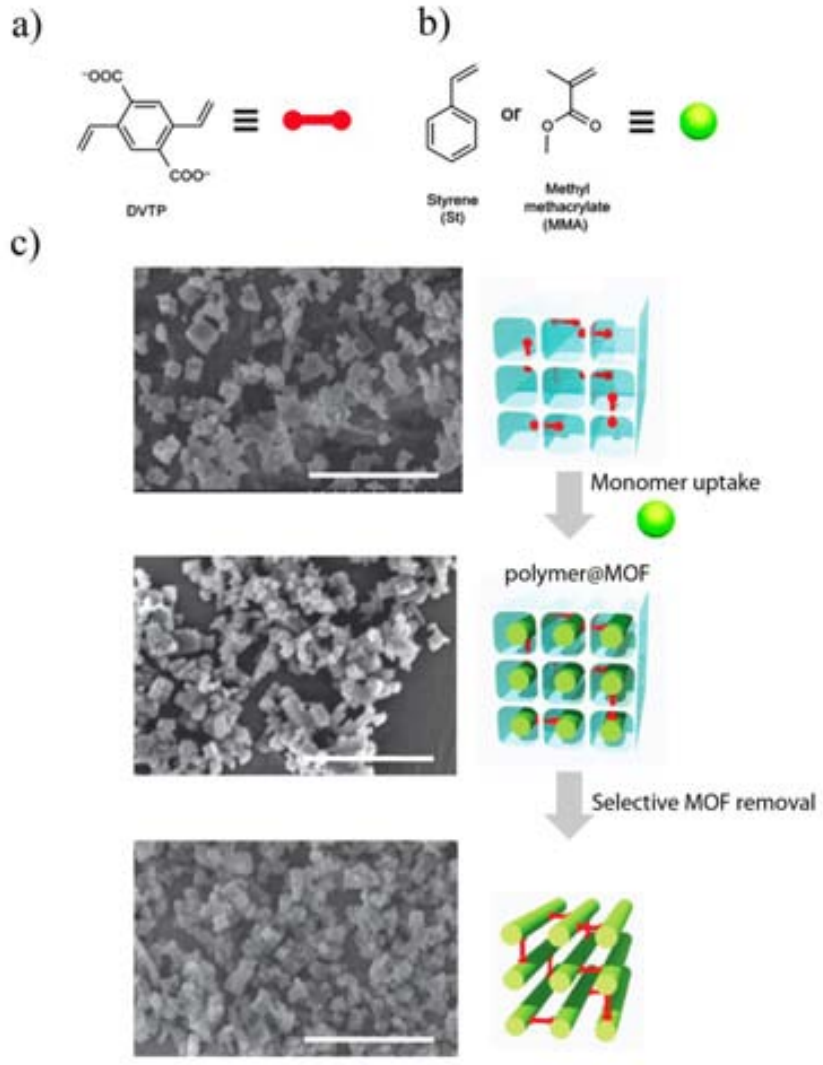

Figure 2. a) Representation of the linker used for the synthesis of the $Cu(DVTP)_x(BDC)_{1-x}(triethylamine)_{0.5}$. **b)** Representation of the monomers used in the confined polymerisation. **c)** Scheme of the confined polymerisation and selective removal of the MOF template and the corresponding actual FESEM images at every stage of the process. Scale bar corresponds to 5 μm.[14]

Using a different approach, MOFs can also serve as scaffolds to synthesise composites where they are coated or encapsulated by a functional material such as an organic polymer or silica. This alternative approach is of interest when the relation of the MOF with the environment wants to be changed; for example, to protect the MOF from water degradation. For example, Boyes *et al*. coated nanoscale $Gd(BDC)_{1.5}(H_2O)_2$ (where BDC is 1,4-benzenedicarboxylic acid) with biopolymers containing thiol groups. The selective coating relied on the interaction of the free thiol groups present on the polymers with the Gd(III) ions (with vacancies in their coordination) located on the MOF surface.[16] The so-coated nanoscaled MOF (NMOF) presented an increase hydrolytic stability, showing slower degradation in water than the non-coated analogue. Silica is another interesting coating material for MOFs not only due to the enhanced water stability that they can provide but also because they are a versatile platform to further functionalise the structure. Li and co-workers reported

the silica coating of $Mn_3(BTC)_2$ block-like nanocrystals of 50-300 nm by first coating them with polyvinylpirrolidine and exposing them to a tetraethylorthosilicate solution under sol-gel conditions. The coated NMOFs showed higher stability in aqueous media and could be further functionalized with a luminescent prove and a cell targeting peptide (**Figure 3**).[17]

Figure 3. Scheme showing the coating and functionalization of $Mn_3(BTC)_2$ nanocrystals.

1.2. Localised MOF synthesis on functional materials.

The second strategy consists on localising the synthesis of the MOF on the surface of the desired secondary component of the composite. The main challenge of this strategy consists on avoiding the self-nucleation and growth of the MOF in solution rather than on the surface of the functional material. Therefore, the surface of the functional material plays a very important role to induce both nucleation and growth of the MOF. In some cases, some bare surfaces of the material can serve to localise the MOF formation. This is the case of some metal oxides that can serve as a source of metal ions and structure directing agents. For example, Kitagawa *et al.* coated an aluminium oxide template with the MOF with formula Al(OH)(NDC) (where NDC is 1,4-naphtalenedicarboxylic acid). The aluminium oxide template was immersed in a solution containing the linker, and then heated through microwave radiation. The localised source of metal ions induced the selective precipitation of the MOF on the template (**Figure 4a**). This simple strategy afforded the synthesis of 2D alumina oxide@MOF composites with bimodal porosity; macroporosity arising from the alumina oxide template and microporosity arising from the MOF (**Figure 4b**).[18] The same approach was utilised by Kuang, Kong and co-workers to coat semiconductor ZnO nanorods with ZIF-8. The freestanding ZnO@ZIF-8 composites were used to selectively detect small oxidisers, such as H_2O_2.[2]

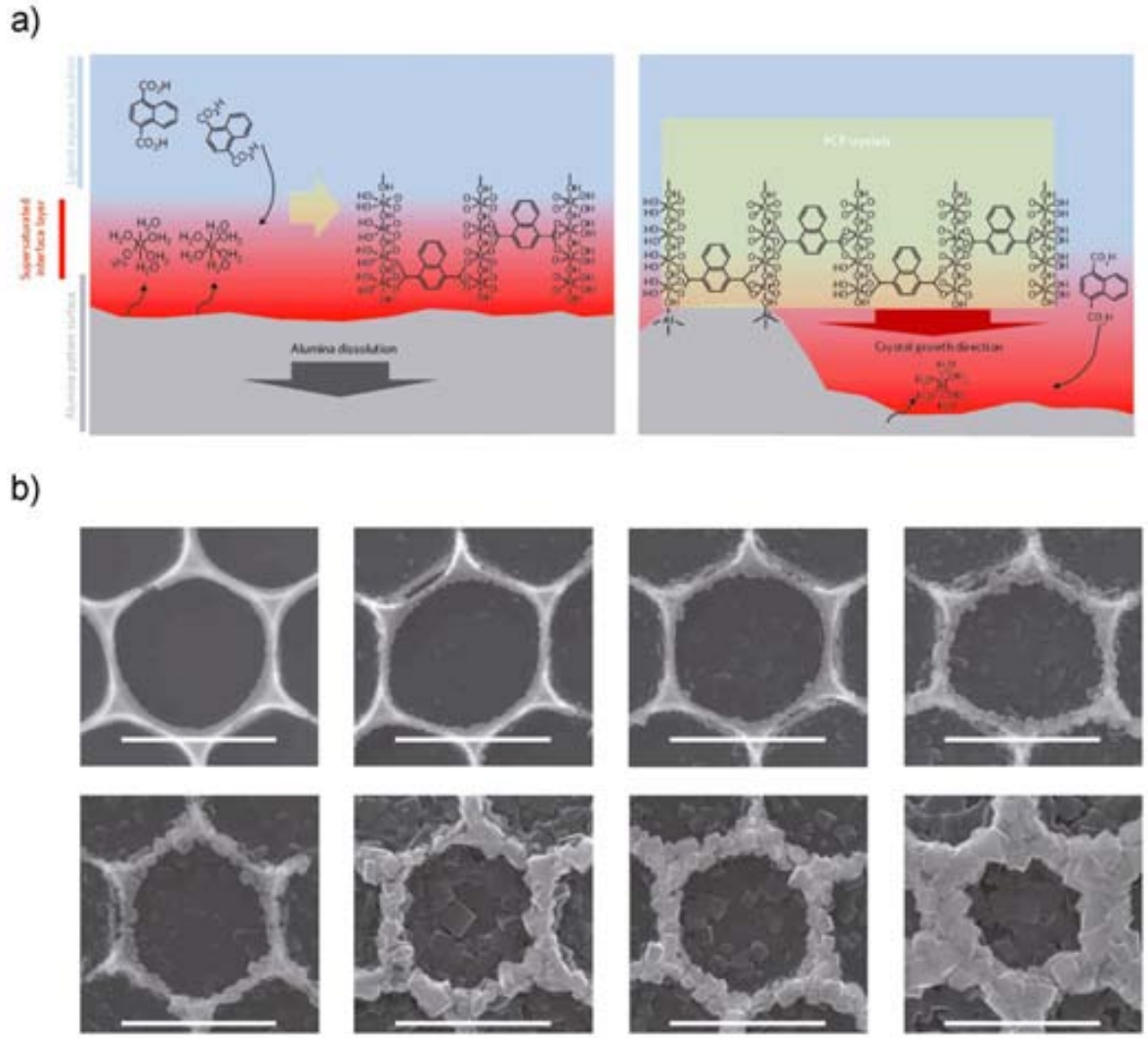

Figure 4. a) Proposed mechanism of the formation of Al(OH)(NDC) on the alumina oxide template. **b)** FESEM images of the time course evolution of the synthesis of Al(OH)(NDC) on the template. Scale bar corresponds to 1 μm.[18]

In some other cases, the bare surface of the functional material alone is not enough to direct and localise the synthesis of the MOF. In these cases, surface functionalization with reactive groups is an elegant approach to increase the affinity of the MOF precursors towards the surface of the material. Interesting functional groups include carboxylic, hydroxyl, sulphonate, phosphonate and nitrogenated groups; basically, those that are currently used to make MOFs. Hupp, Huo and co-workers used this strategy to encapsulate polyvinylpirrolidine (PVP) coated INPs of different functionalities, shapes and sizes in the structure of ZIF-8. The encapsulation process relied on the successive adsorption of the coated INPs by the growing ZIF-8 crystal. Thus, it is important to highlight that the spatial distribution of these INPs could be controlled through the addition sequence of the INPs to the reaction mixture (**Figure 5**). Here, the encapsulation of Pd nanoparticles afforded MOF-based composites with size selective hydrogenation of alkenes.[19]

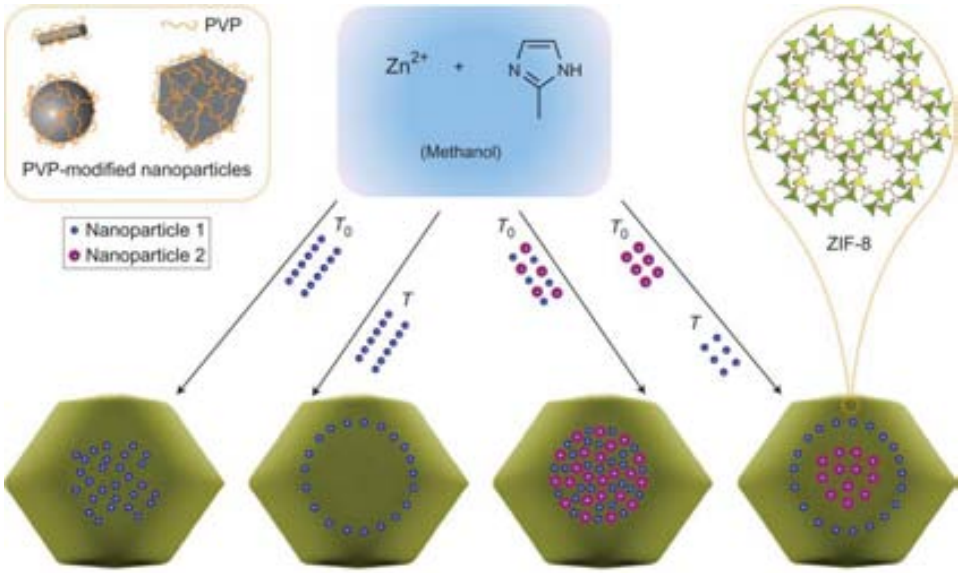

Figure 5. Scheme of the controlled encapsulation of INPs in ZIF-8. The spatial distribution of INPs in the crystals of ZIF-8 could be controlled depending on when the INPs are added to the reaction mixture. INPs were located in the core of the crystals when they were added at the beginning of the reaction (T_0), whereas they were located in the periphery when added later (T).[19]

Ke *et al*. also used this strategy to integrate Fe_3O_4 nanoparticles within HKUST–1 and MIL-100 (**Figure 6a,b**).[20] They synthesized core–shell Fe_3O_4@HKUST–1/MIL–100 nanocomposites using a step–by–step methodology, in which mercaptoacetic acid–functionalized Fe_3O_4 nanoparticles were dispersed alternatively in ethanol solutions of the corresponding metal salt and organic ligand precursors. The resulting composites showed the ability to be magnetized, and therefore, their location could be controlled through the use of an external magnetic field.

From all these examples, one can see that it is possible to take advantage of the reactivity of metal oxides or of the functionalized surface of a material to localise the MOF synthesis on their surfaces. Recently, Furukawa and co-workers combined the two strategies to synthesise a three component composite based on gold nanorods (GNR), alumina oxide and Al(OH)(NDC). The strategy consisted on first functionalising GNR with alumina oxide to promote its interaction with the ligand NDC. In a second step, the GNR functionalized with alumina were immersed in a solution of NDC and then heated through microwave radiation. The alumina coated surface served as a localised source of Al(III) ions and directed the formation of Al(OH)(NDC) on the surface of the composite, yielding the GNR@Alumina@Al(OH)(NDC) composite (**Figure 6c**). Here, the combination of the MOF, which allows encapsulating guest molecules, with the photothermal behaviour of the GNR gave rise to a composite with light triggered release of adsorbed molecules such as the dye antracene.[21]

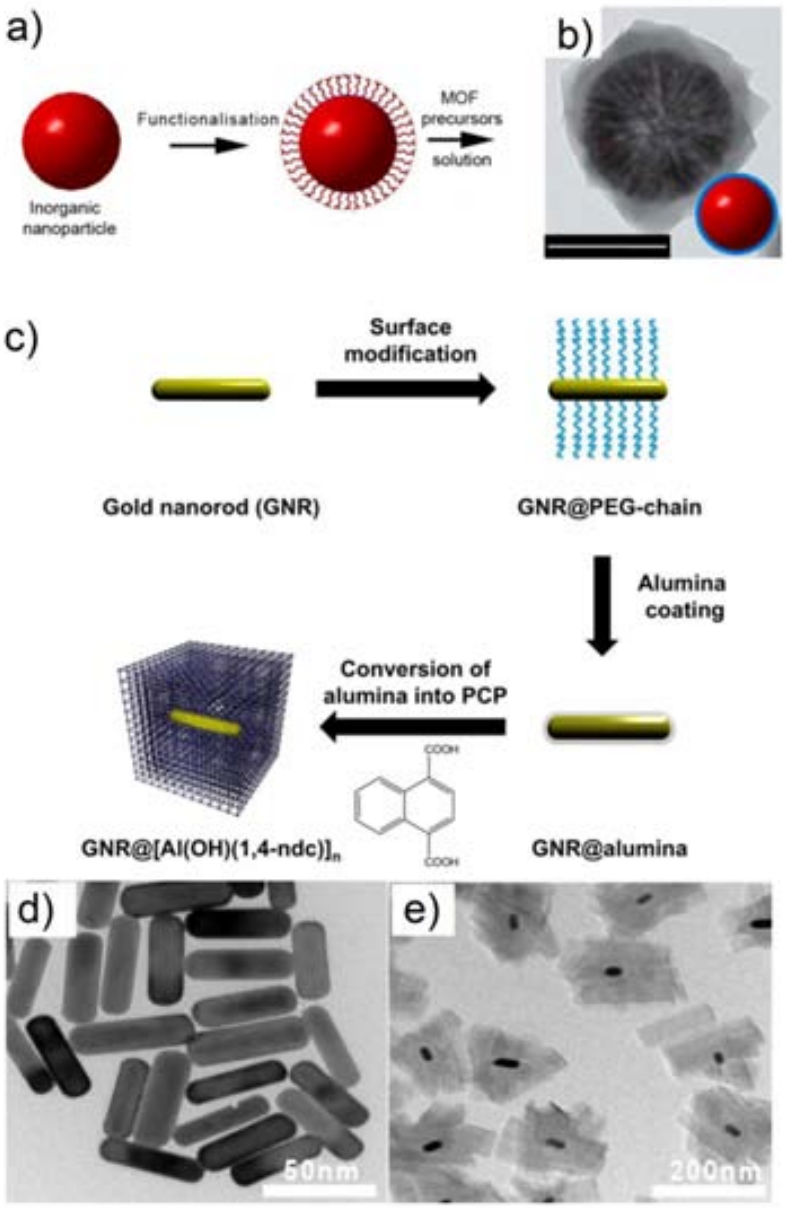

Figure 6. **a)** Schematic illustration of the surface functionalization of INPs with reactive groups such as carboxylates. **b)** Representative TEM image of Fe_3O_4@NHKUST-1. Scale bar corresponds to 500 nm.[20] **c)** Illustration of the protocol developed to synthesise Au nanorods@alumina@[Al(OH)(NDC)] (NDC = 1,4-naphtalene dicarboxylate). **d)** TEM images of the Au nanorods employed in the synthesis of the composite. **e)** TEM image of the resulting composites.[21]

Table 1. Representative summary of MOF-based composites and their applications.

Composite Composition	Property	Reference
Pd@MIL-100	Hydrogen storage	[22]
Pd@ZIF-8	Size selective hydrogenation	[23]
CdSe/ZnS@DA-MOF[1]	Light harvesting	[3]
FeO_X-MOF-5	Solid phase pollutant removal	[24]
PTA[2]@MIL-101	Catalysis of epoxidation reactions	[25]
$PW_{12}O_{40}$[3]@NHKUST-1	Increased water stability	[26]
SiO_2@ZIF-8	Selective adsorption based on hydrophobicity	[16]
$Ln(BDC)_{1.5}(H_2O)_2$@SiO_2	Increased MOF biocompatibility and stability	[17]
Polystyrene@ZIF-8	Templated synthesis of hollow MOF superstructures	[4]
$Gd(BDC)_{1.5}(H_2O)_2$@Methacrylamides	Increased MOF biocompatibility and stability	[16]

[1]DA-MOF ($Zn(DA)_2$, where DA is [5,15-Bis[4-(pyridyl)ethynyl]-10,20-diphenylporphinato) [2]Phosphotungstic acid [3]Keggin polyoxometalate

2. HKUST-1-based composites synthesised by Spray-Drying

The Spray-drying (SD) technique has long been used to combine different materials to create capsules and composites. In addition, as shown in **Chapter 3**, it can also be used to synthesise a wide range of NMOFs in the form of superstructures. Therefore, in this Chapter, it is shown that the synthesis of MOFs through SD can be coupled with exogenous functional materials to synthesise MOF-based composites.

The first approach to prepare MOF-based composites consisted on encapsulating exogenous species in the interior of the hollow HKUST-1 superstructures. The mechanism to explain the formation of hollow HKUST-1 superstructures relies on the diffusion of its precursors to the surface of the receding aerosol droplets. Therefore, the presence of a guest specie with faster precipitation process than HKUST-1 in the aerosol droplet enables the precursors to still diffuse to the droplet shell while the specie precipitate in the core of the droplet, yielding its encapsulation within the HKUST-1 shell. In order to achieve this, one can chose either a guest molecule that easily precipitates in the precursor solution or use stable colloidal nanoparticles, which will diffuse slower than the precursors.

The second kind of HKUST-1 based composites corresponds to the opposite situation, *i. e*. the encapsulation of HKUST-1 within a wall material such as a polymer. In this case, the precursor solution consists on a colloidal suspension of nanoscale HKUST-1 (NHKUST-1) in which a polymer has been solubilized. The precipitation of the polymer in the aerosol droplet containing NHKUST-1 generates a sphere in which the NHKUST-1 is entrapped.

2.1 Encapsulation of species inside the NHKUST-1 superstructures

2.1.1. The case of NaCl@NHKUST-1 composites

The potential of using MOF superstructures (see **Chapter 3**) to entrap guest species and thus, form MOF-based composites was first tested with sodium chloride (NaCl) as the guest specie and HKUST-1 as the MOF. NaCl was selected because it easily crystallises, it forms cubic crystals that can be easily identified using microscopic techniques and it shows a different crystallographic pattern than HKUST-1, making easier the identification of both species by XRPD. All together makes NaCl an excellent model to study the entrapment of functional species inside the MOF superstructures.

To synthesise the NaCl@HKUST-1 composites, NaCl (0.017 M) was dissolved in a solution of $Cu(NO_3)_2 \cdot 2.5H_2O$ (0.017 M) and BTC (0.0011 M) in 50 mL of a 1:1:1 mixture of DMF, ethanol and water, and the resulting clear solution was sprayed at a flow rate of 336 $ml \cdot min^{-1}$ and inlet temperature of 180 ºC. The correct formation of the composite was confirmed by XRPD, FESEM and dispersive X-ray (EDX) mapping. First, the XRPD showed peaks corresponding to both phases of HKUST-1 and NaCl (**Figure 7**). Second, FESEM analysis of the collected blue solid revealed the formation of superstructures with a golf ball-like shape and the absence of cubic NaCl crystals. And third, EDX mapping performed in isolated superstructures clearly showed the presence of both Na and Cl within the interior of the superstructure (**Figure 8a,b**). In addition, the encapsulation of cubic NaCl crystals into the superstructures was further confirmed by FESEM analysis of broken NaCl@NHKUST-1 superstructures, in which cubic crystals of NaCl were clearly identified within the internal void volume (**Figure 8d**). All these observations confirmed the successful entrapment of NaCl crystals in the HKUST-1 superstructures by SD. Here, the precipitation/crystallization of NaCl in the aerosol droplet is faster than NHKUST-1 crystallization. Therefore, when cubic crystals of NaCl are formed, the HKUST-1 precursors are still mobile diffusing towards the droplet surface where NHKUST-1 crystallises and assembles to form the hollow superstructures.

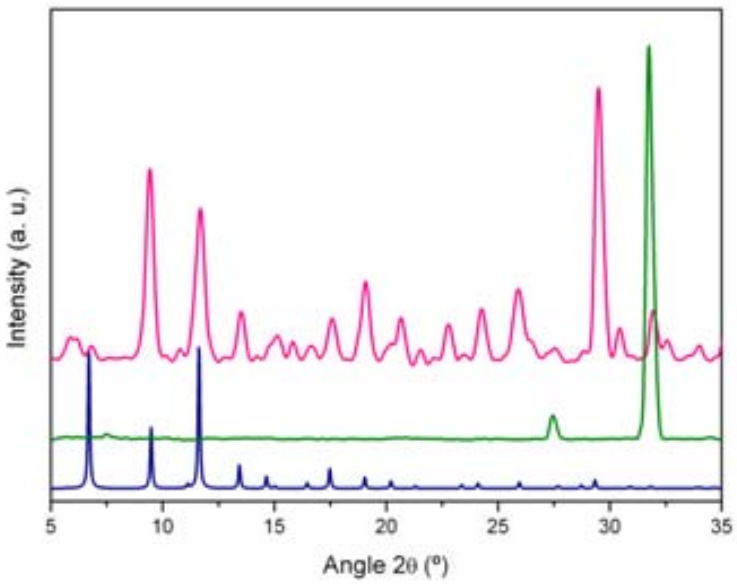

Figure 7. XRPD diffraction patterns of NaCl@NHKUST-1 composite (pink), NaCl (green) and NHKUST-1 (blue).

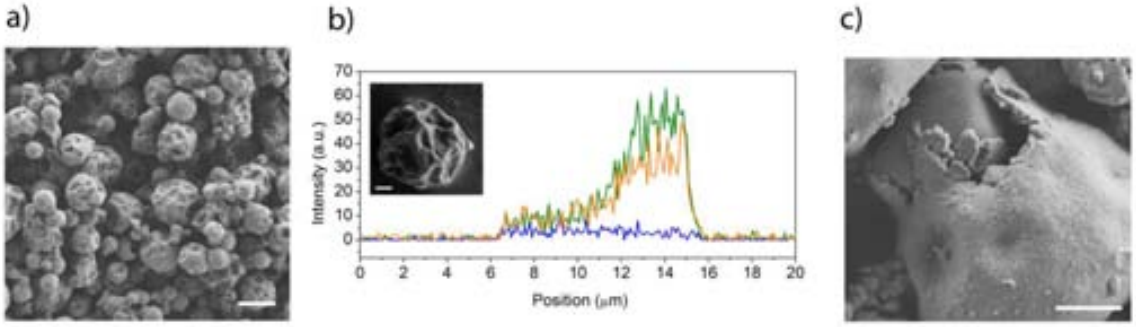

Figure 8. a) Representative FESEM image of golf ball-shaped NaCl@NHKUST-1 superstructures. Scale bar corresponds to 5 μm. **b)** EDX mapping of a single NaCl@NHKUST-1 superstructure (inset), showing the Na (yellow), Cl (green) and Cu (blue) distribution. Scale bar corresponds to 1 μm. **c)** FESEM image of a mechanically broken NaCl@NHKUST-1 superstructure illustrating the presence of a single NaCl cubic crystal inside the internal void volume. Scale bar corresponds to 1 μm.

2.1.2. The case of pyrene@NHKUST-1 composites

To further demonstrate the ability of NHKUST-1 superstructures to encapsulate guest species, the inclusion of a dye such as pyrene was attempted. Pyrene was chosen as the guest specie due not only to its luminescent properties but also to its highly apolar character. Many substances of interest, such as drugs, have a hydrophobic character. Therefore, pyrene was used here as a model apolar compound which inclusion within the MOF superstructure could be easily detected through fluorescent optical microscopy.

MOF precursor solutions are generally highly polar solutions, in which the solubilisation of apolar species is complicated. This lack of solubility could be a limitation for the encapsulation of these species within the NMOF superstructure. The most common strategy to mix polar and apolar species is their dispersion in the form of an emulsion. Emulsions are a suspension of one liquid in the form of microdroplets (dispersed phase) into a second liquid (continuous phase) in which the first will not mix. In most of the cases, a surfactant is needed to stabilize the emulsion. In oil-in-water emulsions, the dispersed phase is an organic solvent, whereas the continuous phase is water or a mixture of polar solvents. This is a good system to disperse highly apolar molecules into polar solvents. For this reason, we envisaged the SD of emulsions as an alternative approach to obtain HKUST-1 composites incorprating highly hydrophobic molecules. The MOF precursor solution can be used as the continuous phase in an oil-in-water emulsion, where the oily microdroplets contain the lipophilic substance. This is achieved by first dispersing or dissolving the target molecule in an oil, and then creating an emulsion between the resulting oil phase and the MOF precursor solution (which constitutes the continuous phase), using a surfactant. When this emulsion is SD, the reaction proceeds in the continuous phase. Therefore, MOF superstructures incorporating the lipophilic guest species in their cavity are formed (**Figure 9**).

Following this approach, the hydrophobic fluorescent dye pyrene was encapsulated in NHKUST-1 superstructures. The process started with the preparation of the oil-in-MOF precursor emulsion. Pyrene (0.1 g) was dissolved in the oil phase lemon oil (7.5 g) containing 0.37 g of the pluronic surfactant (P-123). The oil phase was then added to the NHKUST-1 precursor solution containing 30 ml of a mixture of DMF and water (3:1) and 0.0017 M $Cu(NO_3)_2 \cdot 2.5H_2O$ and 0.011 M of BTC. The two phases were homogenised with an ultra-Turrax (IKA T18 basic) for 10 minutes. The stable emulsion was then sprayed at 180 ºC of inlet temperature and 336 $ml \cdot min^{-1}$ of flow rate. Remarkably, the XRPD measurements performed in the recovered blue powder showed the diffraction pattern of NHKUST-1, confirming that the synthesis of NHKUST-1 was not affected by either the presence of surfactant, oil phase or the pyrene (**Figure 9b**). The integrity of the capsules comprising the powder was observed through FESEM (**Figure 9c**). Finally, the successful encapsulation of the lipophilic dye was confirmed by the confocal images, where both, the intensity profile of an isolated capsule and the confocal image, revealed that the dye was homogenously distributed in the void volume of the superstructures (**Figure 9d**).

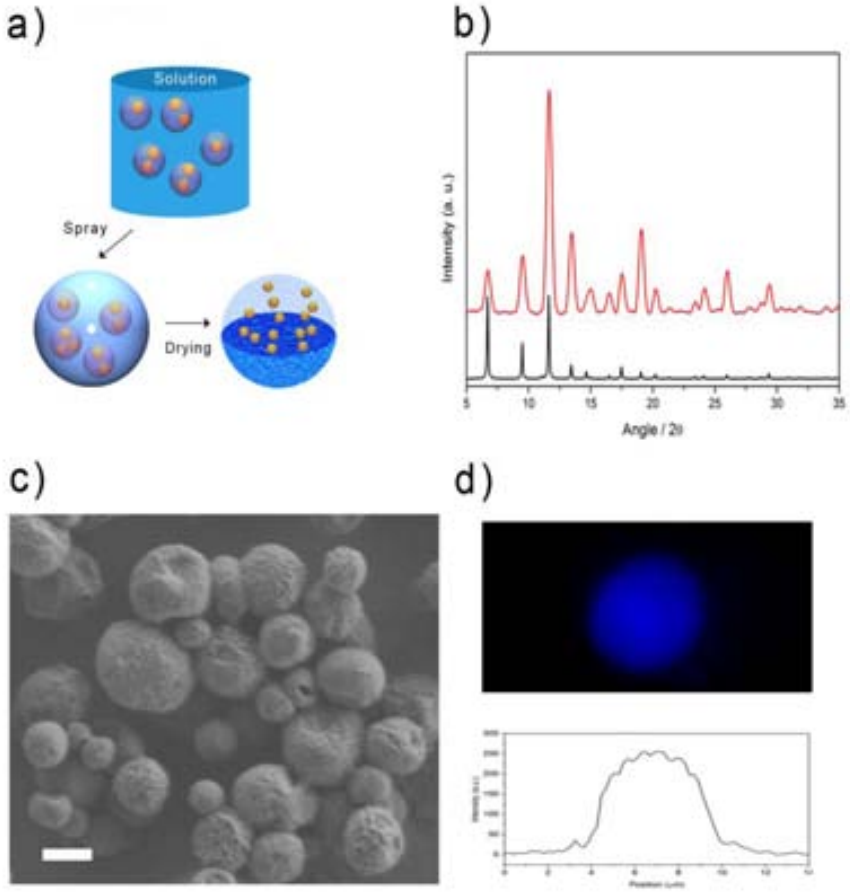

Figure 9. **a)** Schematic representation of the emulsion-based encapsulation of lipophilic substances. The scheme shows the entrapment of pyrene (orange) within the enclosed space of MOF superstructures (blue, only partially shown for clarity), by SD an oil (purple spheres, lemon oil containing dissolved pyrene)-in-MOF precursor solution. **b)** XRPD of simulated NHKUST-1 (black) and as-made pyrene@NHKUST-1 composite. **c)** Representative FESEM image of the pyrene@NHKUST-1 composite. **d)** Intensity profile of an isolated pyrene@NHKUST-1 capsule (down) and its 3D image (up)

2.1.3. The case of FeOxINPs@NHKUST-1 composites

One of the most interesting features of composites incorporating INPs is their potential response to external stimulus.[27] For example, the combination of magnetic INPs and MOFs is a promising strategy to localise, position and collect MOFs under an external magnetic field. These magnetically guided MOF composites can then be used as pollutant removals.[24,28] In these composites, the high porosity of MOFs facilitates the accumulation of pollutants in its pores, whereas the magnetic counterpart of the composite enables its easy separation from the liquid phase.

We incorporated magnetic INPs into NHKUST-1 superstructures by dispersing FeOx INPs to the NMOF precursor solution, and subsequently spraying the resulting dispersion. In a typical experiment, 500 µl of an aqueous dispersion of FeOx nanoparticles (concentration of 25 $mg \cdot ml^{-1}$, average size of 10 nm and surface functionalised with oleic acid) were added to 50 ml of a 1:1:1

mixture of DMF, ethanol and water containing $Cu(NO_3)_2 \cdot 2.5H_2O$ (0.017 M) and BTC (0.0011 M). The suspension was sprayed at standard conditions of inlet temperature (180 ºC) and flow rate (336 $ml \cdot min^{-1}$). Importantly, the presence of FeOx INPs did not affect the synthesis of NHKUST-1 superstructures, as confirmed by FESEM and XRPD. First indication of the successful entrapment of FeOx INPs into the superstructures was given by the simple observation that all superstructures move towards a magnet when a colloidal suspension was exposed to it. As shown in **Figure 10a, b**, all superstructures were attracted to the magnet leaving the solution completely transparent. The encapsulation of FeOx INPs was further confirmed by TEM analysis of a mechanically broken superstructure. The images revealed that FeO_x INPs are located in the inner part of the wall, probably dragged there during solvent evaporation (**Figure 10c**).

Once demonstrated the encapsulation of FeOx INPs, the solid phase pollutant removal properties of the FeOx@NHKUST-1 composites were tested. We used the organosulfur dibenzothiophene (DBT) as a model pollutant. Prior the experiment, the composites (50 mg) were activated under vacuum at 150 ºC for 12 h in order to evacuate the pores of NHKUST-1 and promote the pollutant adsorption. Then, the activated composites were added to a solution of 8700 ppm of DBT in isooctane at room temperature. Following an incubation period, the superstructures were collected by a magnet in the same way as explained earlier. The DBT in the clear solution of isooctane was then determined by UV-Visible spectroscopy. Redispersing the FeOx@NHKUST-1 composites and repeating this process for different incubation periods (up to 3h) demonstrated the efficient extraction of 200 g of DBT (or 35 g of sulphur) per Kg of composite, which is in agreement with other reported values for HKUST-1 (**Figure 10d**).[29]

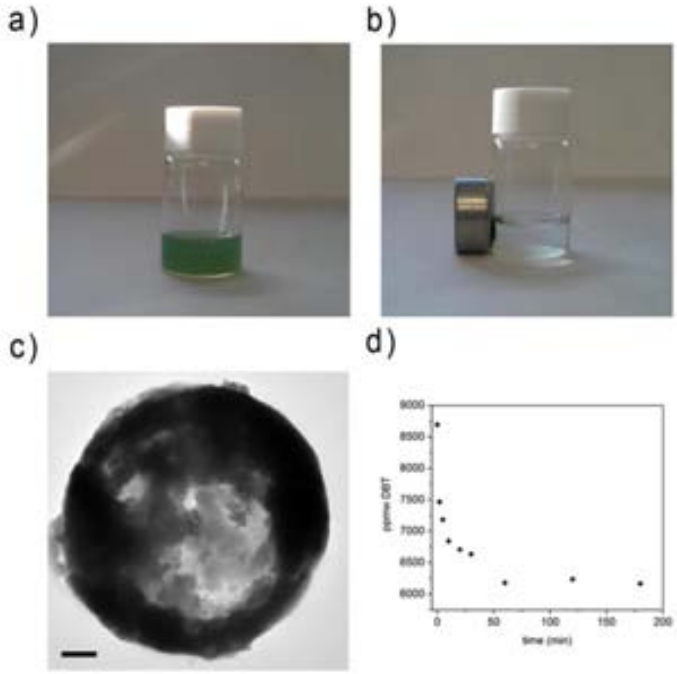

Figure 10. a) Photograph of FeOx@NHKUST-1 composites dispersed in a solution of DBT in isooctane. **b)** Photograph showing the magnetic attraction of FeOx@NHKUST-1 composites dispersed in a solution of DBT in isooctane when they are exposed to a magnet. **c)** TEM image of a single FeOx@NHKUST-1 composites. Scale bar corresponds to 200 nm. **d)** Time dependence of the removal of DBT. Ppmw, parts per million weight.

2.2. Encapsulation of NHKUST-1 into polystyrene spheres

In the previous MOF-based composites, the NMOF was forming the shell of the composite. However, the encapsulation of the NMOF in the interior of an organic polymer sphere also offers prospective applications. In this Chapter, we also explored the well-known micro and nanoencapsulation skills of SD to encapsulate pre-formed NMOFs crystals into polymer matrices to generate MOF@polymer composites in the form of microsized spheres. This is of interest because the polymeric coating can be used to prevent the interaction of NMOFs with agents that cause their degradation. Probably the most common degradation agent that NMOFs must face is water molecules, which interact with the metal clusters, displacing the organic linker and leading to structure collapse and subsequent loss of porosity. This is a challenge for the industrial and real world applications of MOFs. Thus, we rationalized that SD can be used to coat NMOFs with highly hydrophobic polymers to protect them from water degradation, and therefore increase their applicability. To prove this concept, we have chosen the polystyrene (PS) as the organic hydrophobic polymer and NHKUST-1 as the iconic water-sensitive MOF.

2.2.1. Synthesis of NHKUST-1@PS composites

The synthesis of NHKUST-1@PS started with the independent preparation of a stable colloidal suspension of NHKUST-1 crystals of average size of 150 nm, which were prepared as described in **Chapter 3** (10 $mg \cdot ml^{-1}$; Surface Area (S_{BET} = 1430 $m^2 \cdot g^{-1}$) in DMF and a solution of PS (Molecular weight = 250000, 10 $mg \cdot ml^{-1}$) in dichloromethane (DCM). Then, 30 ml of the NHKUST-1 colloid were mixed with 150 ml of the PS solution. This mixture was atomized using a two-fluid nozzle at a feed rate of 4.5 $ml \cdot min^{-1}$ and inlet temperature of 130 ºC. After 40 min of continuous spraying, 1.7 g of blue powder of NHKUST-1@PS composites was recovered with a yield of 95 %. This powder was analysed through FESEM revealing that it was composed of smooth microspheres of average size of 3.6 ± 1.7 μm (**Figure 14a**) but not of free NHKUST-1 crystals. The XRPD analysis of these spheres showed a perfect match with the pattern of NHKUST-1 (**Figure 14b**). The presence only of microspheres and the evident match in the XRPD patterns evidenced that NHKUST-1 crystals were indeed entrapped within the polymeric matrix of PS. This entrapment was further confirmed by embedding these HKUST-1@PS spheres in a polymeric resin, cutting this resin into nanometric slices (average thickness: 100 nm) using a microtome, mounting the slices onto a TEM grid and analyzing them by FESEM. The images showed numerous holes, mainly in the core of the microspheres, further proving the encapsulation of NHKUST-1 crystals. We reasoned that the holes had formed during the slicing process, when the crystals, which were in the same size range as the slices themselves, were pushed out by the mechanical force of cutting (**Figure 14c**).

The content of NHKUST-1 in the composite was estimated by dissolving the PS spheres in DCM and recovering the crystals by centrifugation. The crystals were dried and weighted, from which a NHKUST-1 content of 18 % w/w (hereafter defined as $w_{NHKUST-1}/w_{composite}$) in the composite (hereafter called NHKUST-1@PS_18) was determined. This percentage was similar to the initial 20 % w/w, confirming that SD is a very efficient method for encapsulating NMOF crystals. In addition, N_2 sorption measurements at 77 K and 1 bar performed on these NHKUST-1 crystals proved that they retain their sorption properties (S_{BET} = 1301 $m^2 \cdot g^{-1}$) after their encapsulation into the PS matrix, also confirming that the SD conditions does not affect the NMOF. It is worth mentioning that in the whole process there is not any washing or filtration step as the composites are prepared in a single step without the need of any further treatment.

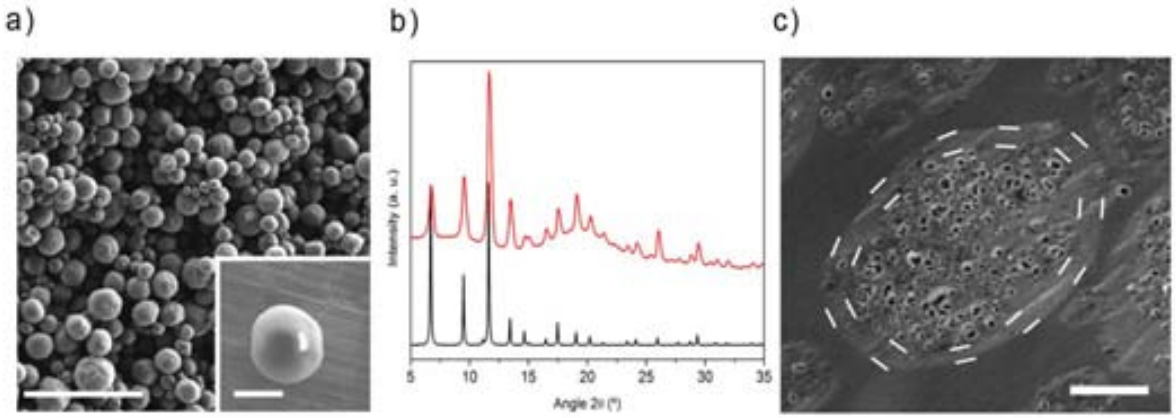

Figure 14. a) Representative FESEM images of NHKUST-1@PS_18 and a discrete composite sphere (inset). The scale bars corresponds to 10 μm and 2 μm (inset). **b)** XRPD of the simulated pattern of NHKUST-1 (black) and the as-made NHKUST-1@Ps_18 (red). **c)** FESEM image of the microtomic slice of the NHKUST-1@PS_18 showing its interior and highlighting the thick polymeric shell (dotted line).

2.2.2. Hydrolytic stability of NHKUST-1@PS_18

Once determined that NHKUST-1 crystals retain their porosity properties during the composite formation, the capacity of PS to protect them against water as well as their sorption capacity inside the matrix were evaluated. To study the protection, a sample of NHKUST-1@PS_18 was incubated in water and in more harsh conditions such as acidic media (pH < 1) under stirring overnight. In all cases, the incubated composites maintained the same spherical morphology, as confirmed by FESEM, and their XRPD patterns were coincident with the expected pattern of NHKUST-1 (**Figure 15a**). On the contrary, non-encapsulated NHKUST-1 incubated in water under identical conditions suffered from structure degradation and morphology change, leading to a new non-porous phase (S_{BET} = 0 $m^2 \cdot g^{-1}$) composed of BTC and copper oxo-species (**Figure 15b**).[30] A more pronounced effect was also observed when these crystals were incubated in acid media, in which their complete dissolution was observed after a few minutes. Thus, it is clear that PS effectively protects the NHKUST-1 crystals from their degradation when are in contact with water. However, we found that this protection implies the loss of the porosity properties of NHKUST-1 crystals. Since PS capsules are non-porous, we attributed the non-porous character of NHKUST-1@PS_18 (S_{BET} = 0 $m^2 \cdot g^{-1}$) to the thick layer of PS, which does not allow the N_2 molecules to diffuse until the NHKUST-1 crystals embedded mainly in the core of the composite.

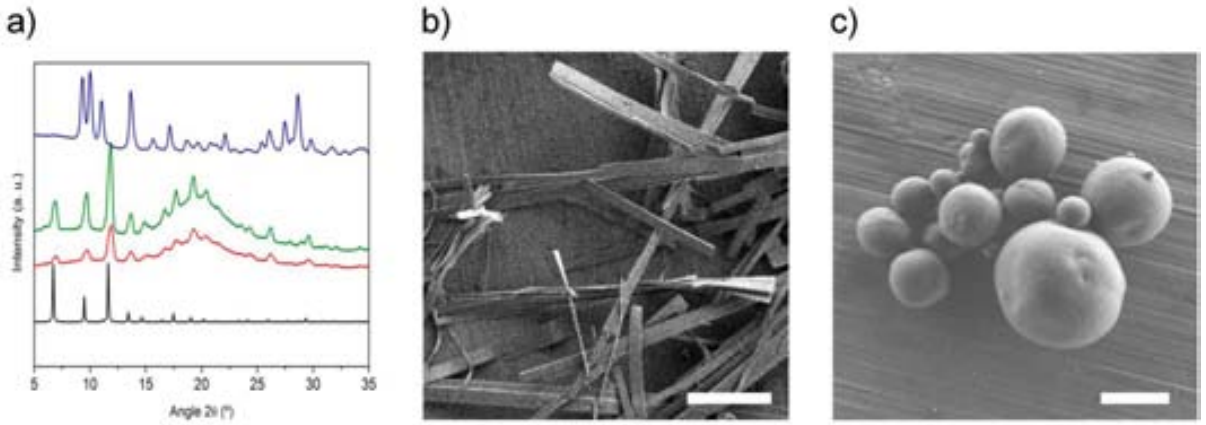

Figure 15. a) XRPD of the simulated pattern of NHKUST-1 (black), NHKUST-1@PS_18 incubated overnight in water (red) and in 10 % HCl (V/V) (green) and bare NHKUST-1 incubated in water (blue). **b)** FESEM images of the rod-like crystals obtained after incubating bare NHKUST-1 crystals in water. Scale bar corresponds to 2 μm. **c)** FESEM of NHKUST-1@PS_18 incubated in 10 % HCl (V/V). The scale bar corresponds to 2 μm.

2.2.3. Optimisation of NHKUST-1@PS composites

Given the excellent hydrolytic stability of NHKUST-1 embedded in the PS matrix but their lack of porosity in the initial NHKUST-1@PS_18, we optimised the synthesis in order to retain the protection properties maintaining the sorption capacities of NHKUST-1. A series of NHKUST-1@PS composites which vary in the ratio of NHKUST-1 crystals to PS (w/w: 33 %, 50 %, 63 %, and 80 %) were systematically synthesised to study the influence of the PS matrix in the diffusion of N_2 molecules, and thus, reach the MOF crystals without losing their protection against water molecules.

Initially, the composites were analysed through FESEM (**Figure 16**). It was observed that the roughness of the surface of the composites increased with the content of NHKUST-1 in the composite due to the increasing filling degree of the PS matrix. In fact, when the content of NHKUST-1 exceeded the 63%, its complete entrapment could not be achieved as there is not enough PS to cover all NHKUST-1 crystals located on the surface of the composite (**Figure 16d**). This has a direct implication on its water resistance since the product that results from its incubation in water under stirring overnight showed the absence of any XRPD peaks attributable to NHKUST-1, confirming the complete degradation of NHKUST-1 crystals. On the contrary, the other composites proved to be stable under the same incubation conditions (**Figure 17**).

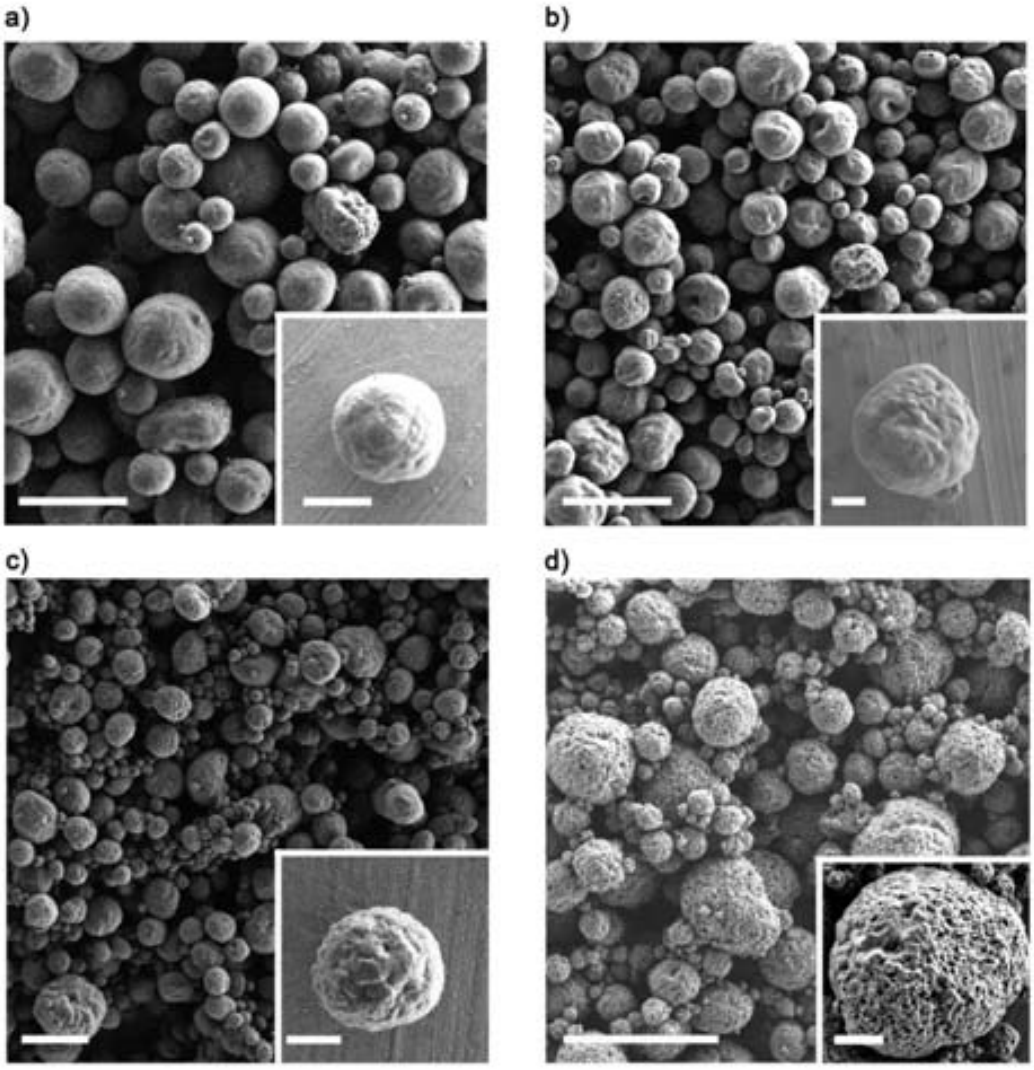

Figure 16. a) Representative FESEM images of the composites: NHKUST-1@PS_33, **b)** NHKUST-1@PS_50, **c)** NHKUST-1@PS_63 and **d)** NHKUST-1@PS_80. Scale bar corresponds to 10 μm and 2 μm (inset).

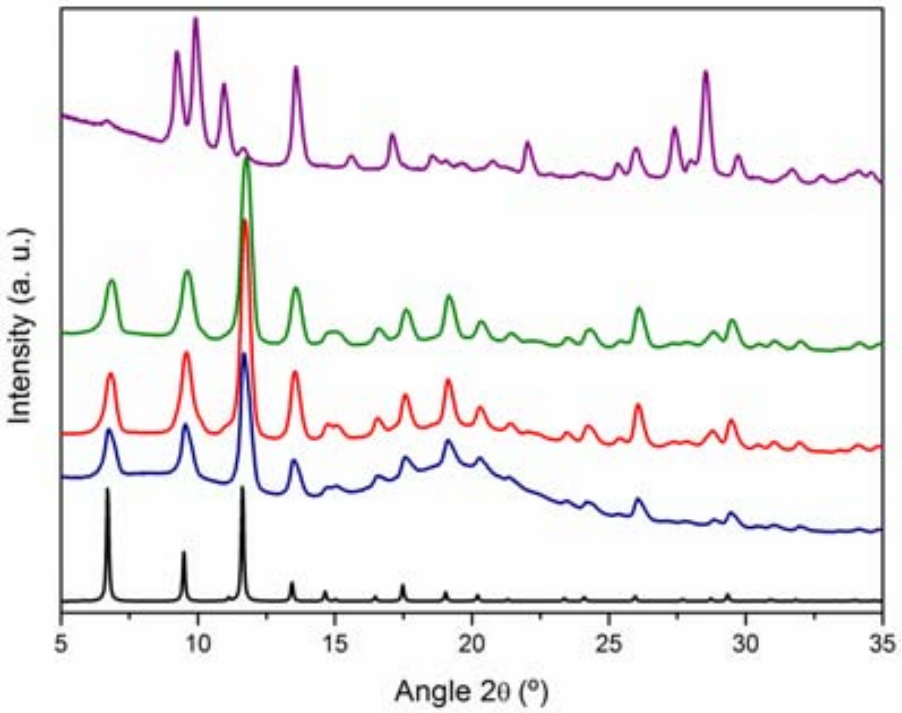

Figure 17. Simulated XRPD pattern of NHKUST-1 (black) and XRPD patterns of all synthesised composites after their incubation in water overnight (NHKUST-1@PS_33 (blue), NHKUST-1@PS_50 (red), NHKUST-1@PS_63 (green) and NHKUST-1@PS_80 (purple)).

2.2.4. Sorption properties of NHKUST-1@PS composites

The porosity properties of the water-stable NHKUST-1@PS_33, NHKUST-1@PS_50 and NHKUST-1@PS_63 were again studied through N_2 sorption measurements at 77 K and 1 bar. Remarkably, all these composites showed now to be porous to N_2 with increasing S_{BET} with the relative content of NHKUST-1: S_{BET}: 32 $m^2 \cdot g^{-1}$ for NHKUST-1@PS_33; S_{BET}: 277 $m^2 \cdot g^{-1}$ for NHKUST-1@Ps_50; and S_{BET}: 757 $m^2 \cdot g^{-1}$ for NHKUST-1@Ps_63 (**Figure 18**). According to the non-porous character of PS to N_2 (S_{BET} = 0 $m^2 \cdot g^{-1}$), the sorption properties of each composite can be attributed solely to the entrapped NHKUST-1 crystals and therefore, these S_{BET} values can also be expressed in grams of NHKUST-1: S_{BET}: 97 m^2/g for NHKUST-1@PS_33; S_{BET}: 554 $m^2 \cdot g^{-1}$ for NHKUST-1@Ps_50; and S_{BET}: 1202 $m^2 \cdot g^{-1}$ for NHKUST-1@Ps_63. From these values, we found that the sorption performance retention (SPR) percentage of each composite when compared to the initial NHKUST-1 crystals was 7 % for the NHKUST-1@PS_33, 39 % for NHKUST-1@PS_50 and 84 % for NHKUST-1@PS_63. The observed increase of porosity correlates well with the presence of thinner PS shell layers in the composite with higher ratios of NHKUST-1 crystals to PS (**Figure 19**). Thus, it appears that thin PS layers are accessible enough for the N_2 molecules to diffuse until the embedded NHKUST-1 crystals and that they are still capable to protect these crystals against water molecules.

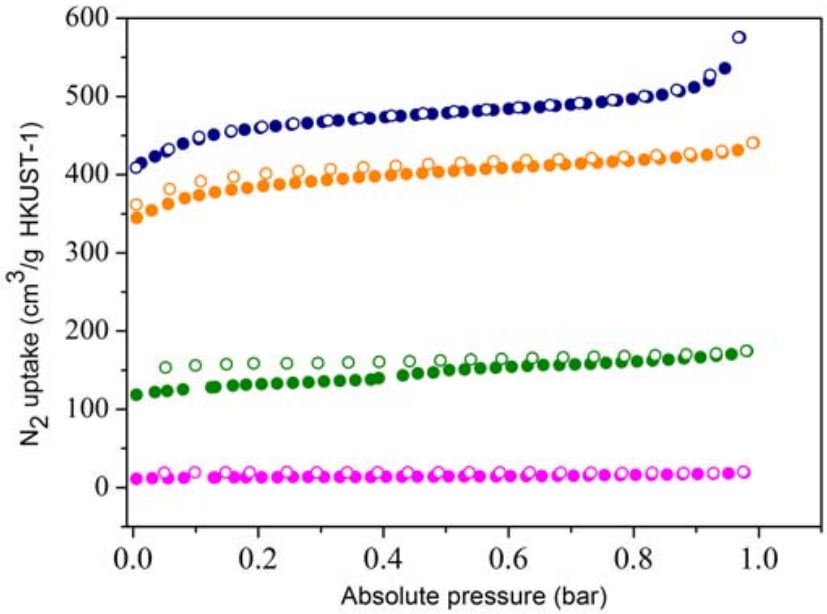

Figure 18. N_2 isotherms at 77 K (calculated per gram of NHKUST-1) of NHKUST-1@PS_33 (pink), NHKUST-1@PS_50 (green), NHKUST-1@PS_63 (orange) and NHKUST-1 (blue) used in the synthesis of the composites.

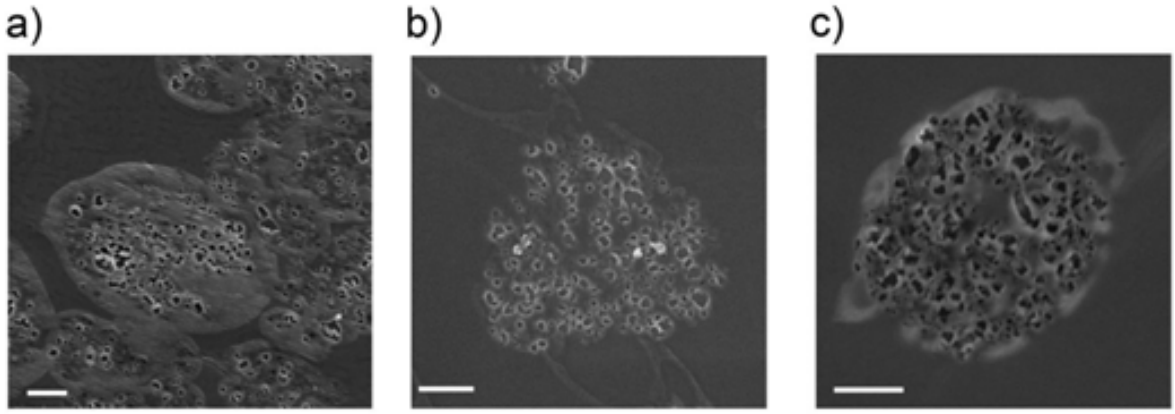

Figure 19. a) FESEM image of the microtomic slice of the NHKUST-1@PS_33, **b)** NHKUST-1@PS_50 and **c)** NHKUST-1@PS_63. The scale bars correspond to 1 µm.

Considering the excellent N_2 SPR of HKUST-@PS_63, we also studied its CO_2 and CH_4 sorption capacity. Type I CO_2 and CH_4 isotherms were collected at 295 K and 0.96 bar on both NHKUST-1 and NHKUST-1@Ps_63. It was found that NHKUST-1@Ps_63 adsorbs 61.6 and 13.0 cm^3/g of CO_2 and CH_4 (expressed in grams of NHKUST-1: 97.8 and 20.7 cm^3/g), respectively. These values are in the range of 93.9 $cm^3 \cdot g^{-1}$ (CO_2) and 16.5 $cm^3 \cdot g^{-1}$ (CH_4) measured for the non-encapsulated NHKUST-1 crystals. The small differences in the uptakes when expressed in grams of NHKUST-1 can be attributed to the slight CO_2 (4.38 cm^3/g) and CH_4 (2.62 cm^3/g) sorption capacity already exhibited by the bare PS spheres. These results revealed that the composite is porous not only

to non-polar molecules such as N_2 and CH_4, but also to polar as is confirmed by the CO_2 uptake, retaining most of the NHKUST-1 sorption capacities (**Figure 20**).

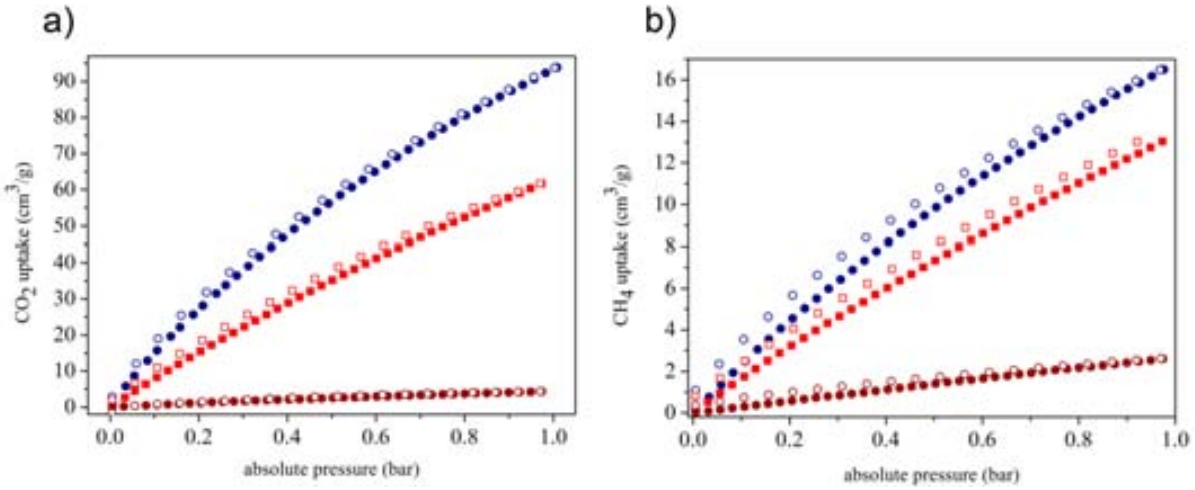

Figure 20. a) Adsorption (filled circles) and desorption (opened circles) isotherms of CO_2 at 295 K of NHKUST-1 (blue), NHKUST-1@Ps_63 (red) and PS (brown). **b)** Adsorption (filled circles) and desorption (opened circles) isotherms of CH_4 at 295 K of NHKUST-1 (blue), NHKUST-1@Ps_63 (red) and PS (brown).

2.2.5. Hydrolytic stability of NHKUST-1@PS composites

To study the hydrolytic stability of NHKUST-1 when encapsulated into PS microspheres in terms of its porosity performance, a sample of NHKUST-1@PS_63 was incubated in water under stirring overnight, as explained above. Again, NHKUST-1@PS_63 spheres did not experience any morphological change and its XRPD pattern was comparable with the expected pattern of NHKUST-1. Importantly, these results were correlated with its sorption properties. The N_2 isotherm at 77 K and 1 bar revealed that the efficacy of the composite was practically maintained, with a SPR value of 72 % after its incubation in water (**Figure 21**). On the contrary, under identical conditions, bare NHKUST-1 crystals completely lost its sorption capabilities (S_{BET} = 0 m^2/g), being transformed again to the non-porous phase composed of BTC and copper oxo-species.

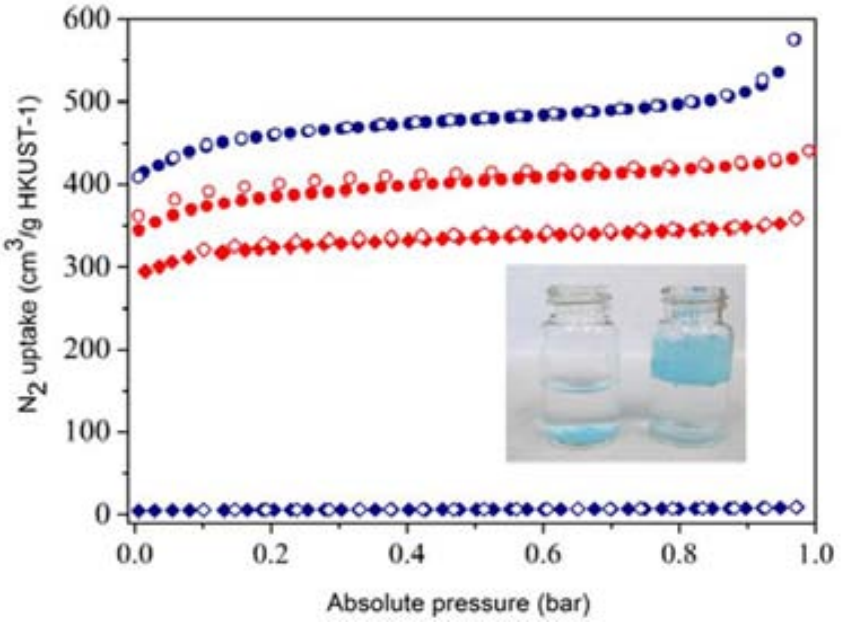

Figure 21. N_2 isotherms at 77 K of NHKUST-1 (blue) and NHKUST-1@PS_63 composite (red) before (spheres) and after (rhombus) water incubation. (Inset) Photograph of the incubated samples. NHKUST-1 (left) and the composite (right) when incubated.

This result prompted us to compare the long term hydrolytic stability of non-encapsulated NHKUST-1 crystals and NHKUST-1@PS_63 by exposing them to high relative humidity (RH) conditions. To test this, both materials were placed in a homemade incubation chamber at 80 % RH and 27 ºC (**Figure 22a**). Following an incubation period, samples of both materials were taken and their corresponding N_2 isotherms and XRPD were collected. Here, it was found that NHKUST-1 crystals showed a sharp decrease of 56 % and 78 % in its S_{BET} after 8 h and 24 h, respectively. After one week, its S_{BET} was 64.0 m^2/g (a decrease of 96 % of its original S_{BET}), confirming the practical loss of its adsorption capacities. In contrast, the composite showed enhanced resistance to the same humid conditions as its S_{BET} (expressed in grams of NHKUST-1) decreased from 1202 to 1111 m^2/g after 8 h (SPR = 77 %), whereas after one week its S_{BET} decreased to 782 m^2/g (SPR = 55 %). Interestingly, even after 1 month of incubation, the composite retained some of its initial sorption properties with a S_{BET} of 417 m^2/g (SPR = 29 %) (**Figure 22b**). The evolution of the stability was also followed by XRPD, from which we confirmed the same degradation of the bare NHKUST-1 (*vide supra*) and the fact that the crystallinity of NHKUST-1 encapsulated into the PS spheres were fully retained throughout the incubation period (**Figure 22c, d**). It is important to mention here the discrepancy between the XRPD and sorption measurements, confirming that XRPD is not sufficient if one wants to study MOF degradation processes in terms of its porosity performance.

Finally, the enhanced hydrolytic stability of NHKUST-1@PS_63 was also confirmed by measuring its CH_4 and CO_2 sorption performance after one month of incubation at 80 % RH. In both cases, type I isotherms collected at 295 K and 0.96 bar revealed that it still adsorbs 34.5 and 6.40 $cm^3 \cdot g^{-1}$ of CO_2 and CH_4 (expressed in grams of NHKUST-1: 54.76 and 10.16 $cm^3 \cdot g^{-1}$; SPR = 58 % and 63 % of its original sorption capacity), respectively.

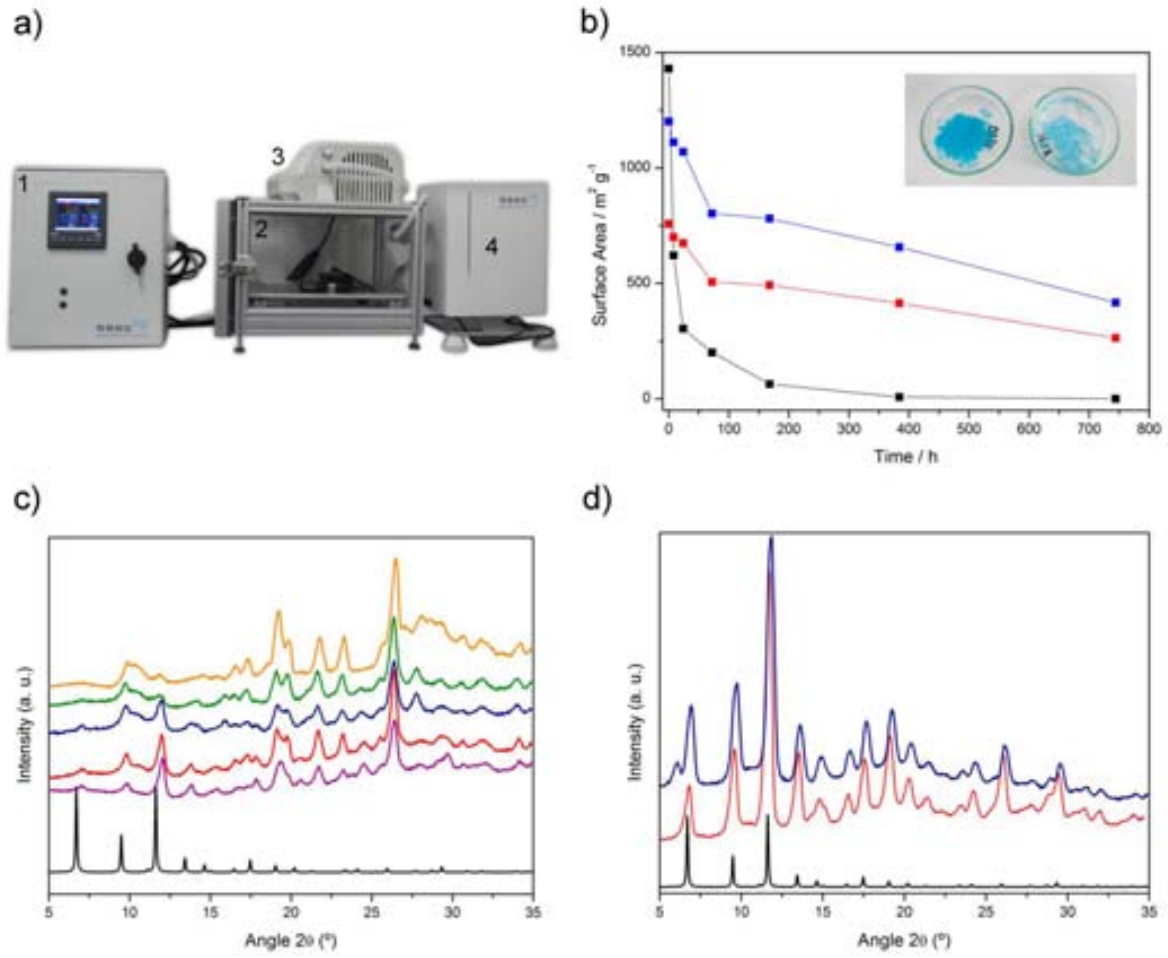

Figure 22. a) Homemade humidity chamber. 1. PID controller box; 2. Temperature and humidity controlled chamber 3.Vacuum dehumidification pump 4. Ultrasounds vapour generator. **b)** Evolution of S_{BET} of NHKUST-1 (black), NHKUST-1@PS_63 measured per gram of composite (red) and per gram of NHKUST-1 (blue). Photograph of the post incubated samples of NHKUST-1 (right) and the composite (left). **c)** XPPD of the simulated NHKUST-1 (black) and NHKUST-1 incubated at 80 % RH at 27 ºC at different incubation times: 8h (purple), 24 h (red), 72 h (blue), 7 days (green) and 16 days (orange). **d)** XRPD of the simulated NHKUST-1 (black), and NHKUST-1@PS_63% incubated at 80 % RH at 27 ºC at different incubation times: 16 days (red) and 1 month (blue).

3. Conclusions

The well-known capacities of the SD technique to synthesise composites have been exploited to synthesise a wide range of HKUST-1 based composite materials. The relative mobility of the components of the composites in the aerosol droplet has been exploited to control the position of the MOF in the composite. The family of MOF-based composites synthesised by SD in this Thesis includes those made of hollow HKUST-1 superstructures in which different species, such as NaCl crystals, dyes or INPs, have been incorporated in the internal void volume. On the other hand, a second family of composites made of PS spheres, in which NHKUST-1 crystals have been have been encapsulated has been developed. This variety in composition and structures can be exploited to achieve unattainable properties for the individual components of the composite. In terms of practical applications, the NHKUST-1@FeOx composite proved its potential as solid phase pollutant removal and NHKUST-1@PS composites showed to have high hydrolytic resistance maintaining excellent sorption properties.

4. References

(1) Meilikhov, M.; Yusenko, K.; Esken, D.; Turner, S.; Van Tendeloo, G.; Fischer, R. A. *Eur. J. Inorg. Chem.* **2010**, *2010*, 3701.
(2) Zhan, W.-w.; Kuang, Q.; Zhou, J.-z.; Kong, X.-j.; Xie, Z.-x.; Zheng, L.-s. *J. Am. Chem. Soc.* **2013**, *135*, 1926.
(3) Jin, S.; Son, H.-J.; Farha, O. K.; Wiederrecht, G. P.; Hupp, J. T. *J. Am. Chem. Soc.* **2013**, *135*, 955.
(4) Lee, H. J.; Cho, W.; Oh, M. *Chem. Commun.* **2012**, *48*, 221.
(5) Maksimchuk, N. V.; Kovalenko, K. A.; Arzumanov, S. S.; Chesalov, Y. A.; Melgunov, M. S.; Stepanov, A. G.; Fedin, V. P.; Kholdeeva, O. A. *Inorg. Chem.* **2010**, *49*, 2920.
(6) Sorribas, S.; Zornoza, B.; Tellez, C.; Coronas, J. *Chem. Commun.* **2012**, *48*, 9388.
(7) Doherty, C. M.; Buso, D.; Hill, A. J.; Furukawa, S.; Kitagawa, S.; Falcaro, P. *Acc. Chem. Res.* **2013**, *47*, 396.
(8) Houk, R. J. T.; Jacobs, B. W.; Gabaly, F. E.; Chang, N. N.; Talin, A. A.; Graham, D. D.; House, S. D.; Robertson, I. M.; Allendorf, M. D. *Nano Letters* **2009**, *9*, 3413.
(9) Suh, M. P.; Moon, H. R.; Lee, E. Y.; Jang, S. Y. *J. Am. Chem. Soc.* **2006**, *128*, 4710.
(10) El-Shall, M. S.; Abdelsayed, V.; Khder, A. E. R. S.; Hassan, H. M. A.; El-Kaderi, H. M.; Reich, T. E. *J. Mater. Chem.* **2009**, *19*, 7625.
(11) Proch, S.; Herrmannsdörfer, J.; Kempe, R.; Kern, C.; Jess, A.; Seyfarth, L.; Senker, J. *Chem. Eur. J.* **2008**, *14*, 8204.
(12) Hermannsdörfer, J.; Kempe, R. *Chem. Eur. J.* **2011**, *17*, 8071.
(13) Uemura, T.; Yanai, N.; Kitagawa, S. *Chem. Soc. Rev.* **2009**, *38*, 1228.
(14) Distefano, G.; Suzuki, H.; Tsujimoto, M.; Isoda, S.; Bracco, S.; Comotti, A.; Sozzani, P.; Uemura, T.; Kitagawa, S. *Nat. Chem.* **2013**, *5*, 335.
(15) Uemura, T.; Kadowaki, Y.; Kim, C. R.; Fukushima, T.; Hiramatsu, D.; Kitagawa, S. *Chem. Mater.* **2011**, *23*, 1736.
(16) Rowe, M. D.; Chang, C.-C.; Thamm, D. H.; Kraft, S. L.; Harmon, J. F.; Vogt, A. P.; Sumerlin, B. S.; Boyes, S. G. *Langmuir* **2009**, *25*, 9487.
(17) Rieter, W. J.; Taylor, K. M. L.; Lin, W. *J. Am. Chem. Soc.* **2007**, *129*, 9852.
(18) Reboul, J.; Furukawa, S.; Horike, N.; Tsotsalas, M.; Hirai, K.; Uehara, H.; Kondo, M.; Louvain, N.; Sakata, O.; Kitagawa, S. *Nat. Mater.* **2012**, *11*, 717.
(19) Lu, G.; Li, S.; Guo, Z.; Farha, O. K.; Hauser, B. G.; Qi, X.; Wang, Y.; Wang, X.; Han, S.; Liu, X.; DuChene, J. S.; Zhang, H.; Zhang, Q.; Chen, X.; Ma, J.; Loo, S. C. J.; Wei, W. D.; Yang, Y.; Hupp, J. T.; Huo, F. *Nat. Chem.* **2012**, *4*, 310.
(20) Ke, F.; Qiu, L.-G.; Yuan, Y.-P.; Jiang, X.; Zhu, J.-F. *J. Mater. Chem.* **2012**, *22*, 9497.
(21) Khaletskaya, K.; Reboul, J.; Meilikhov, M.; Nakahama, M.; Diring, S.; Tsujimoto, M.; Isoda, S.; Kim, F.; Kamei, K.-i.; Fischer, R. A.; Kitagawa, S.; Furukawa, S. *J. Am. Chem. Soc.* **2013**, *135*, 10998.
(22) Zlotea, C.; Campesi, R.; Cuevas, F.; Leroy, E.; Dibandjo, P.; Volkringer, C.; Loiseau, T.; Férey, G.; Latroche, M. *J. Am. Chem. Soc.* **2010**, *132*, 2991.
(23) Kuo, C.-H.; Tang, Y.; Chou, L.-Y.; Sneed, B. T.; Brodsky, C. N.; Zhao, Z.; Tsung, C.-K. *J. Am. Chem. Soc.* **2012**, *134*, 14345.
(24) Doherty, C. M.; Knystautas, E.; Buso, D.; Villanova, L.; Konstas, K.; Hill, A. J.; Takahashi, M.; Falcaro, P. *J. Mater. Chem.* **2012**, *22*, 11470.
(25) Bromberg, L.; Diao, Y.; Wu, H.; Speakman, S. A.; Hatton, T. A. *Chem. Mater.* **2012**, *24*, 1664.
(26) Mustafa, D.; Breynaert, E.; Bajpe, S. R.; Martens, J. A.; Kirschhock, C. E. A. *Chem. Commun.* **2011**, *47*, 8037.
(27) Ricco, R.; Malfatti, L.; Takahashi, M.; Hill, A. J.; Falcaro, P. *J. Mater. Chem. A* **2013**, *1*, 13033.
(28) Cychosz, K. A.; Wong-Foy, A. G.; Matzger, A. J. *J. Am. Chem. Soc.* **2009**, *131*, 14538.
(29) Cychosz, K. A.; Wong-Foy, A. G.; Matzger, A. J. *J. Am. Chem. Soc.* **2008**, *130*, 6938.
(30) Majano, G.; Martin, O.; Hammes, M.; Smeets, S.; Baerlocher, C.; Pérez-Ramírez, J. *Adv. Funct. Mater.* **2014**, n/a.

Chapter 5

Nanoscale Metal-Organic Frameworks as Contrast Agents for Magnetic Resonance Imaging

The macrocyclic ligand DOTP is used to assemble a porous, heterometallic MOF. This MOF is miniaturizable down to the nanoscale to form stable colloids; is stable in physiological saline solution and cell culture media; and is not cytotoxic. It shows interesting relaxometric properties with a r_1 at high field (500 MHz) of 5 $mM^{-1} \cdot s^{-1}$ and a maximum in r_1 of 15 $mM^{-1} \cdot s^{-1}$ at 40 MHz, which remains constant over a wide pH range and increases with temperature.

1. Magnetic Resonance Imaging and Contrast Agents: Fundaments

Magnetic Resonance Imaging (MRI) is one of the most powerful diagnosis tools in medical science thanks to its non-invasive character and sub-millimetric spatial resolution (**Figure 1**). It allows obtaining 3-D images of the soft tissue, which is of great interest in the diagnosis of cancer and brain diseases. In addition, MRI provides information regarding the physico-chemical state and flow diffusion. Unlike other imaging techniques, such as computed tomography and X-ray, MRI does not require ionized energy making it safer. Today, all these advantages makes MRI a commonly used diagnostic technique, with more than one million scans performed weekly.

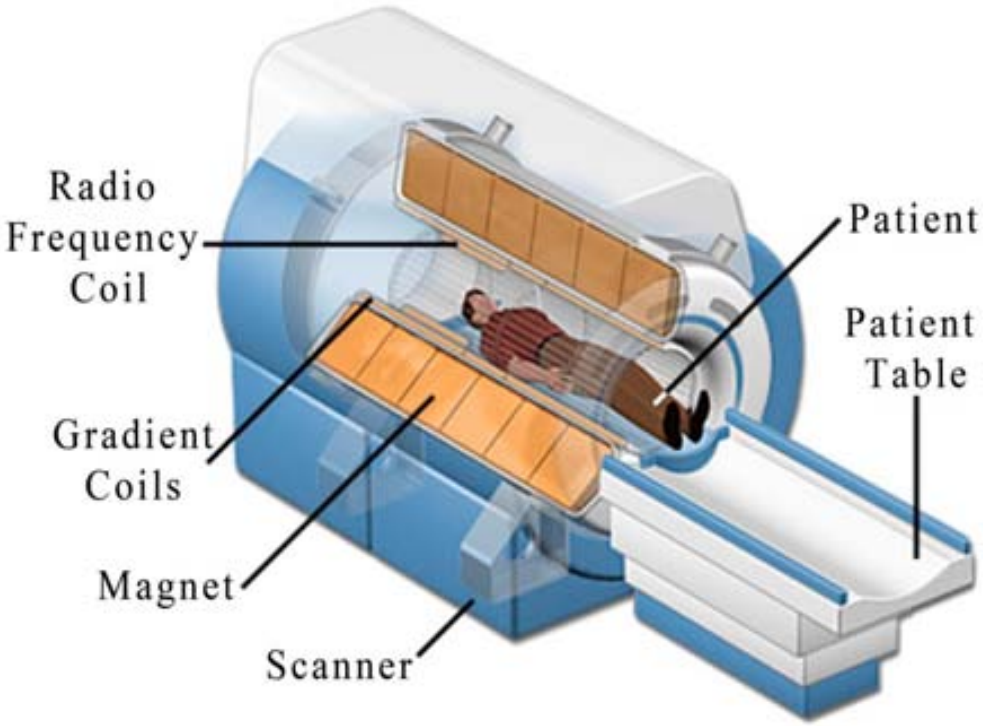

Figure 1. Schematic illustration of a MRI scanner.[1]

1.1. A brief history of Magnetic Resonance Imaging

Raymond Vahan Damadian was the first scientist to anticipate the use of NMR for the medical diagnosis of cancer in 1971.[2] Experimenting on rats, Damadian discovered dramatic differences in the quality and duration of the Nuclear Magnetic Resonance (NMR) signals emitted by cancerous versus healthy tissues. In this year, he reported these findings in the paper "Tumour Detection by Magnetic Resonance", which was met with scepticism from the scientific community. In 1972, however, he filled the first of his patents describing a MRI scanner. This scanner used liquid helium to supercool magnets in the walls of a cylindrical chamber: the nuclei of hydrogen atoms in the water,

which all cells contain, reacted to the resultant magnetic field, and a three-dimensional spatial localization method coordinated the signals into the scan. Later, Prof. Paul Lauterbur introduced the use of gradients in magnetic fields to generate 2D and 3D MRI images. The first MRI images corresponded to a test tube in which deutered water could be distinguished from non- deutered water. These images were published in Nature in 1973.[3] Meanwhile, Sir Peter Mansfield developed the mathematical treatment of the data to improve the MRI images. Finally, all these devolopments allowed performing the first human MRI image in 1977.[4] The development of MRI for medical diagnosis granted the Nobel Prize to Paul Lauterbur and Peter Mansfield in 2003.

1.2.Principles of Magnetic Resonance Imaging and Contrast Agents

1.2.1. Water relaxation

MRI technique is based on monitoring the protons of the water molecules found in the tissues applying the same principles than those used in NMR. Spins of water protons are aligned under an applied magnetic field. Upon a radiofrequency pulse (RF), their magnetisation is changed reducing its longitudinal component and appearing a new component in the transversal plane. The time that protons take to return to their initial magnetisation state after the RF pulse is called relaxation time; noted as T_1 and T_2 if it is the longitudinal and transversal magnetisation, respectively (**Figure 2**). Interestingly, the relaxation time depends on the chemical environment of the water molecules and therefore, it is dependent of the pH, water concentration, presence of salts or lipids, etc. The RF pulses can be designed to highlight these differences in order to distinguish between healthy and diseased tissues. The environment in both tissues is different and so, it is their relaxation times. The distribution of water protons with different relaxation times is used to generate the MRI image through Fourier transformations.

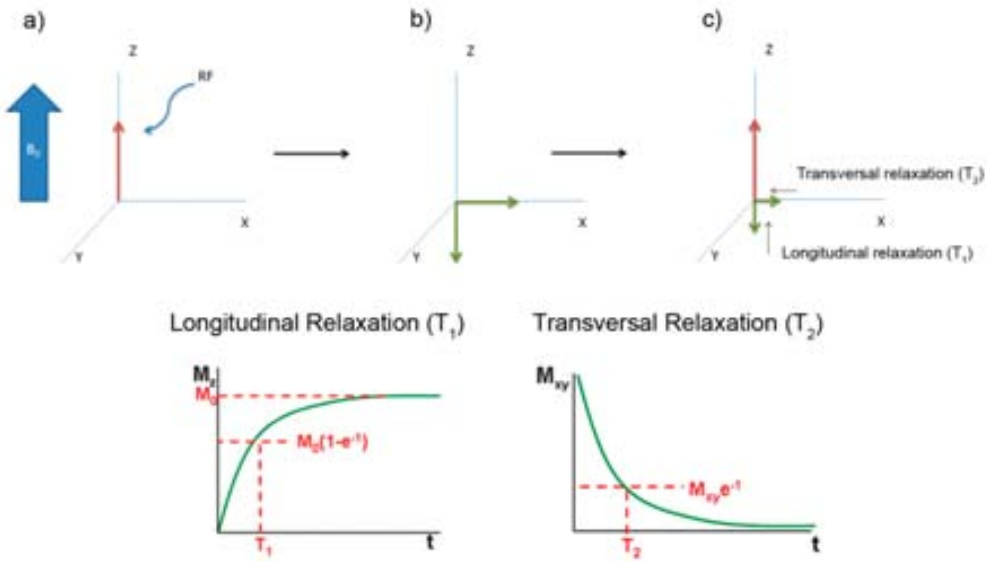

Figure 2. Scheme showing the relaxation process of water protons. **a)** Magnetisation of water protons under a magnetic field (B_0). **b)** The spin adsorbs the RF pulse reducing its longitudinal component and adding a new transversal component. **c)** When the RF stops, the spin returns back to the initial state in a process called relaxation. **d)** Graph showing the recovery of the longitudinal magnetisation. **e)** Graph showing the depletion of the transversal component observed during the proton relaxation.

1.2.2. Contrast Agents

Whereas *in vivo* spatial imaging of a soft tissue is the best advantage of MRI, its lack of sensitivity is still a remaining challenge. It is well known that higher sensitivity translates into higher spatial resolution, allowing for early diagnoses of diseased tissues. For this reason, Contrast Agents (CAs) that accelerate the water relaxation time and that increases the intrinsic contrast of the MRI images are used. There are two types of CAs, which can be classified depending on the relaxation process that they predominantly catalyse. T_1-CAs are more effective accelerating longitudinal relaxation, whereas T_2-CAs promote faster transversal relaxation. Regarding the chemical nature of both types of CAs, T_1-CAs are generally paramagnetic metal complexes. On the other hand, T_2-CAs are commonly inorganic superparamagnetic nanoparticles (for example, iron oxide nanoparticles). The outcome image in the MRI changes depends on the use of a T_1- or T_2-CA . When T_1-CA are used, the contrast is positive becoming the image brighter, whereas this contrast is negative when employing a T_2-CA. To date, the majority of clinically approved CAs are based on T_1-CAs.

Even though Fe(III) and Mn(II) complexes can be used as CAs, most of the CAs are today composed of Gd(III). The preferential use of Gd(III) ions is because they: i) are highly paramagnetic metal ions with seven unpaired electrons; ii) have slow electronic spin relaxation rate; and iii) show a high coordination versatility. The combination of its high magnetic moment and its slow relaxation makes them to be highly effective in the proton relaxation process, as it will be explained later. In fact, Gd(III) ions are currently employed in more than 35% of the scans. However, Gd(III) is also a

highly toxic metal ion (LD_{50} = 0.2 mmol·kg^{-1} in mice)[5] because it interferes with the Ca(II) ion channel dependent processes due to their similarity in size. Nevertheless, when Gd(III) is administrated in the form of stable chelates, its toxicity is largely reduced. Macrocyclic ligands with up to 8 coordinating moieties are usually employed in order to confer high stability to the Gd(III) complexes. **Figure 3** shows some of the commercially available Gd(III)-based CAs.

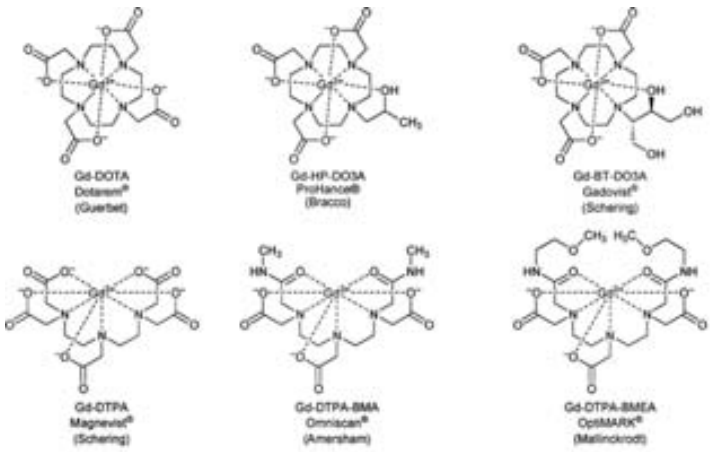

Figure 3. Clinically used Gd(III)-based CAs.[6]

1.2.3. Performance of Contrast Agents: Relaxivity

As an illustrative example, **Figure 4** shows the enhanced image contrast in MRI image of a human brain after injection a Gd(III)-based CA. Importantly, after their injection, CAs are usually homogeneously distributed in the extracellular space and accumulates in areas of increased vasculature, such as tumours and brain damages.[7] Typically, molecular CAs are administrated at a maximum concentration of 0.3 mM. In the tissue, water is at a concentration of approximately 90 M. Therefore, the performance of the CAs has to be catalytic in order to shorten the relaxation times of the bulk water protons.[8]

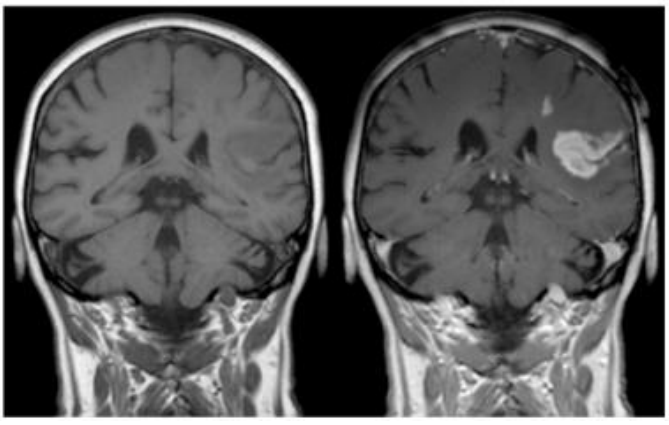

Figure 4. Effect of a brain stroke shown by MRI images. Left and right MRI images have been taken with the presence (right) and not (left) of CA.

The effect of relaxation enhancement is catalytically distributed to the overall bulk water through a mechanism of water exchange and second sphere relaxation contributions (**Figure 5**). Briefly, the fluctuating magnetic field generated on the Gd(III) ion interacts through dipol-dipol with the proton nuclear spin, thus enhancing its relaxivity. This is possible thanks to the high dipolar moment of Gd(III) (7.9 μB) and its slow electronic relaxation. The effect is dependent on the distance between the water molecule and the paramagnetic ion. Therefore, for the effect to be efficiently propagated through the water molecules, there has to be a water exchange between the water molecules in the vicinity of the CA and the bulk water.

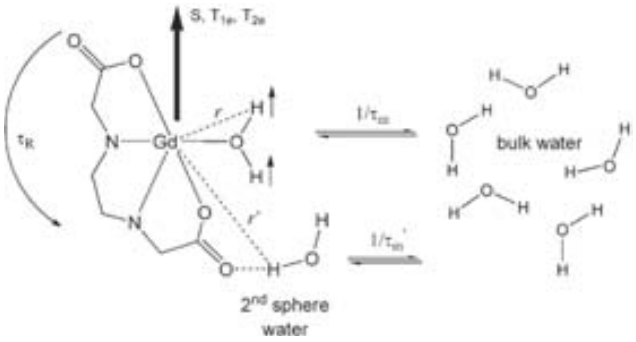

Figure 5. Molecular parameters that influence both inner- and 2nd-sphere relaxivity.[8] S is the magnetic moment of Gd(III), T_{1e} and T_{2e} are the longitudinal and transversal electron relaxation of Gd(III), $1/\tau_m$ is the water exchange ratio and τ_r is the rotational diffusion.

The change in the relaxation rate of water protons upon addition of a CA ($\Delta(1/T_1)$ normalised by the concentration of the CA is called relaxivity (r_1). It is calculated according to Equation 1, and it is used to assess the performance of any CA. Exactly the same procedure is used to assess the capacity of a CA to enhance the transversal relaxation rate ($1/T_2$) and to calculate the transversal relaxivity (r_2).

$$r_1 = \frac{\Delta(1/T_1)}{[CA]} \quad (Equation\ 1)$$

Relaxivity is an important parameter since compounds with higher r_1 provoke better or similar contrast at lower doses. It is therefore important to understand the parameters that rule this value in order to design more effective CAs that will provide better MRI images, and ultimately, better diagnosis. There are three major parameters that influence r_1 based on the mechanism described above: i) the number of coordinated waters to Gd(III), noted as q; ii) the water exchange ratio, noted as t_m; and iii) the rotational correlation time, noted as τ_r.[9,10]

The process of relaxation requires a close distance between the water molecule and the CA. In principle, the higher is the parameter q the higher will be r_1, as more water molecules will be close to the paramagnetic Gd(III) ion. However, when the coordination of the Gd(III) with the ligand is reduced to less than 8, the stability constant is also generally reduced, raising toxicity issues due to an eventual leaching of free Gd(III) ions. On the other hand, the water exchange ratio (t_m) should be fast to ensure a good propagation of the relaxation effect through the bulk water. Thus, for the relaxation to be efficient, water molecules must approach to the CA, undergo relaxation, and fast exchange with bulk water. Finally, the third parameter is related with the molecular rotation of the CA (τ_r). Slower motion of the CA in solution results in an easier interaction of the CA with the bulk water, giving rise to an increase of r_1.[11]

The relative importance of the three parameters varies with the applied magnetic field. At higher field (1.5 T or above; usually used for clinical images), the dominant parameter is the rotational diffusion.[12] While fast tumbling witnesses a decrease in r_1 at high fields, a CA with reduced tumbling due to supramolecular aggregation have higher r_1 values. **Figure 6** shows the overall effect of the water exchange ratio and molecular tumbling as a function of the applied magnetic field. There, the high impact that the molecular rotation rate has on r_1, especially in the clinical field, is evidenced. This is the reason why much efforts are currently focused on the development of new self-assembled CAs with reduced mobility.

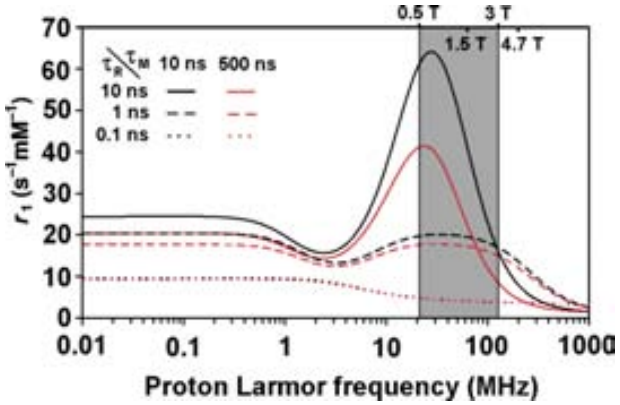

Figure 6. Simulations of r_1 as a function of the proton Larmor frequency. The grey area shows the range of imaging fields currently used in clinics.[6]

2. Nanostructured Contrast Agents

Beyond the use of soluble molecular CAs, structuring CAs at the nanoscale regime has become a promising strategy to develop a new generation of more efficient CAs. Nanostructured CAs carry a large number of Gd(III) ions per CA particle. The high loading of Gd(III) per CA particle can be exploited to localize and target areas of interest, where the image contrast will be maximized. In addition, the biodistribution of nanostructured CAs provide increased *in vivo* circulation time that prevents the fast clearance that molecular CAs lack from. Also, the relaxation mechanism is affected by the nanostructuration. Since the mobility of Gd(III) ions in the nanostructure is reduced, nanostructured CAs usually show increased r_1 values at clinical working fields.

There are two main strategies to develop Gd(III) based nanostructured CAs: i) grafting of Gd(III) complexes to nanoscopic scaffolds; and ii) use the Gd(III) ions as building blocks to synthesise the nanostructure. Both strategies are summarized in **Table 1**, where some representative examples are shown.

Regarding the first strategy, it exists a wide variety of nanotemplates in which Gd(III) ions can be incorporated. These nanoparticles include: inorganic nanoparticles,[13] viral capsids,[14] proteins,[15] mesoporous silica,[16] colloidal self-assembled nanoparticles,[17] zeolites,[18] nanotubes[19] and fullerenes.[20] In these cases, the strategy usually applied is a post-functionalization of the preformed nanoparticle. For instance, Gd(III) chelates with thiolated groups can be prepared to synthesise Gd(III)-coated gold nanoparticles (**Figure 7a**).[13,21] A similar approach can be taken to graft Gd(III) complexes on mesoporous silica using the chemistry of silanols. For instance, Lin *et al.* grafted Gd(III) chelates to nanoscopic spheres of mesoporous silica through siloxane linkage between the silanol groups of the silica and the triethyl siloxane moiety of the functionalized Gd(III) chelate (**Figure 7b, c**).[22] Generally, the r_1 of the molecular CAs anchored to the nanotemplates is higher than the one corresponding to the molecular CA because of the reduction of the tumbling.

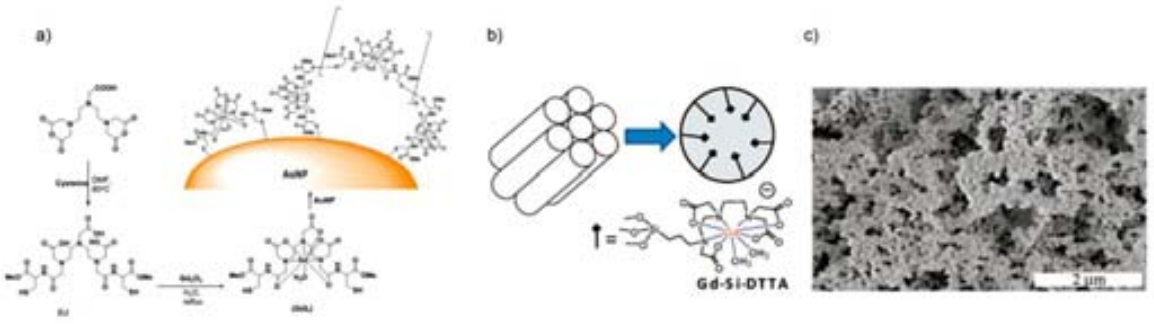

Figure 7. **a)** Schematic representation of the Gd(III) chelate that is coating gold nanoparticles.[23] **b)** Schematic representation of mesoporous silica coated with Gd(III) chelates. **c)** FESEM image of the Gd(III) functionalized silica nanoparticles.[22]

The second strategy consists on using the Gd(III) ions as the building blocks to construct the nanostructure. The different forms in which Gd(III) can be used allow for the generation of different

kinds of nanostructures; from purely inorganic to metal-organic structures. The inorganic structures are based on Gd(III) salts. For example, Gd(III) ions present in the inorganic crystal lattice of oxides[24], phosphates[25] and fluorides[26] have shown to have a good paramagnetic character for being T_1-CAs. In addition, these inorganic nanostructures have a densely packed structures that allow for a high density of Gd(III) ions per CA particle. However, there is still a big concern about the toxicity of these materials, as any eventual degradation would lead to the leaching of free Gd(III) ions.

When Gd(III) chelates are used as building blocks to synthesise nanostructured CAs, the most common strategy is based on supramolecular self-assembly. Between 1999 and 2002, Merbach and co-workers explored the self-assembly of amphiphilic Gd(III) complexes and its impact on r_1.[27,28] These amphiphilic complexes consisted in a chelating moiety covalently linked to a hydrophobic tail (**Figure 8a**). Under these conditions, this amphiphilic Gd(III) complex self-assembles into micelles at a certain concentration called Critical Micelle Concentration (CMC).[29] The micellisation of Gd(III) amphiphilic complexes provokes a decrease of the molecular tumbling, which results in an increase in r_1 when compared to the free monomeric complexes (**Figure 8b**).[28] The advantage of this methodology is that Gd(III) ions are in the form of a stable complex, limiting the eventual leaching of free Gd(III) ions. However, its drawback lies in its principle; the rise in r_1 is dependent on the concentration of the amphiphilic complex (*i. e.* CMC). Therefore, this increase can disappear upon dilution in the blood after the injection.[30]

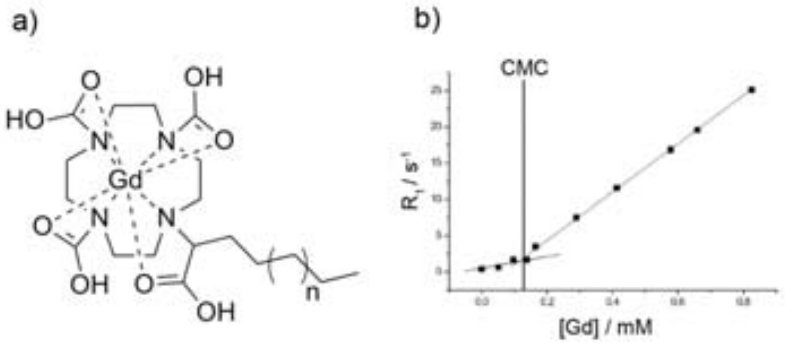

Figure 8. **a)** General structure of an amphiphilic Gd(III) complex. **b)** Characteristic [Gd(III)] dependence r_1 in these amphiphilic Gd(III) complexes. Here, r_1 sharply increases above the CMC value due to the reduced molecular tumbling.[31]

2.1. Metal Organic Frameworks as new class of Contrast Agents

Metal-Organic Frameworks (MOFs) are perfect systems to assemble metal ions and organic linkers into infinite, crystalline, 3D structures. Thus, these materials represent an attractive alternative to incorporate Gd(III) ions into crystalline nanostructures. In addition, the porosity (large surface areas) of MOFs is very advantageous for its performance as CAs, because not only the Gd(III) ions located on the external surface have the possibility to interact with bulk water (as is the case for other Gd(III)-based nanostructures including the inorganic Gd(III) salts and coated gold nanoparticles) but also the

ones located in the pore. Furthermore, the crystalline nature of these materials allows for a precise comprehension of the chemical environment of the Gd(III) ions, which enables obtaining more structure derived information of the observed r_1.

Lin *et al.* was pioneer on exploring the possibilities of nanoscaled MOFs (NMOFs) as potential CAs. Through the reverse microemulsion method, a carboxylated-based Gd(III) MOF with formula $Gd(BDC)_{1.5}(H_2O)_2$ (where BDC is 1,4-benzenedicarboxylic acid) was synthesised in the form of nanorods (**Figure 9a**).[32] Interestingly, the methodology allowed synthesising this NMOF at different sizes, from 100 nm to 1 μm in length. The r_1 data obtained for the two nanorods with different lenghts revealed that there is an inverse size dependence of the r_1 (35.8 $mM^{-1}\cdot s^{-1}$ for the 100 nm-nanorods and 20 $mM^{-1}\cdot s^{-1}$ for the 1 μm-rods at 127 MHz). This dependence was attributed to the decrease of the surface to volume ratio when the size of the nanorod was increased (**Figure 9b**). It is worth to mention that this observation implies that the water molecules were unable to diffuse through the NMOF particle, which correlates well with the dense structure of this NMOF. Furthermore, the authors reported that the structure was poorly stable in water media with an average half-life in the range of hours.

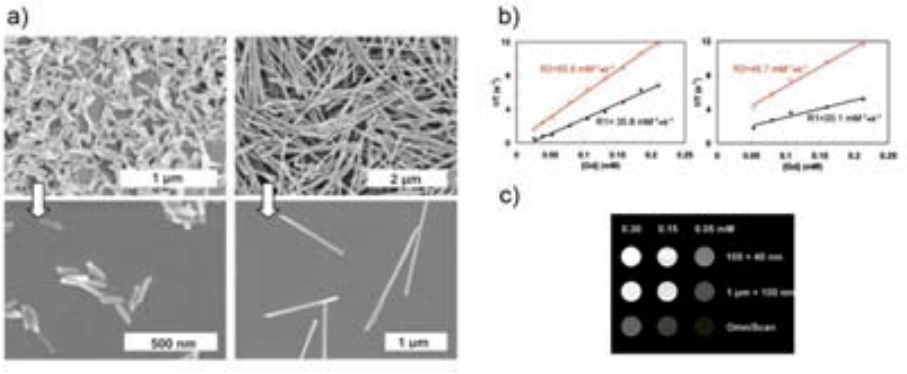

Figure 9. **a)** FESEM image of the NMOF $[Gd(BDC)_{1.5}(H_2O)_2]$. Left, nanorods of average size of 100 nm. Right, nanorods of average size of 1 μm. **b)** r_1 curves of the smaller (left) and bigger (right) nanorods. **c)** T_1-weighted images of suspensions of NMOFs in water containing 0.1 % xanthan gum.

Low stabilities in NMOF-based CAs is highly undesirable due to the potential release of free Gd(III) aqua ions. Gd(III) leaching is a major cause of toxicity but also a major drawback when performing relaxometry studies. Free Gd(III) ions have very high r_1 due to the high number of coordinated water molecules (up to 9), so it might be an overestimation of the r_1 attributed to the nanostructure if it is partially degraded. Polymer coatings of NMOFs can be used to increase their water stability. Boyes *et al.* used a biocompatible polymer containing a thiol group to functionalize the surface of $Gd(BDC)_{1.5}(H_2O)_2$.[33,34] The functionalization proceeded through thiol coordination to the free orbitals of the Gd(III) ions located on the surface of the NMOF. They observed that the degradation of the initially unstable NMOF could be partially avoided when the copolymer containing

N-isopropylacrylaminde, N-acryloxysuccinimide and fluorescein O-methacrylate was used. In addition, the succinimide group was also exploited to further functionalize the NMOF with the anticancer drug methotrexate (MTX) to construct a theragnostic platform. The polymer grafting on the surface also caused an important increase of r_1. The unmodified MOF showed a r_1 of 9.86 $mM^{-1}\cdot s^{-1}$ at 1.5 T, whereas the coated one had a r_1 of 33.4 $mM^{-1}\cdot s^{-1}$. This effect was attributed to the enhanced water retention of the hydrophilic polymer.

In order to increase the water stability of NMOF-based CAs, the use of other coordinating groups (apart from carboxylic groups) can be explored. For example, phosphonates are known to have stronger coordination capabilities than carboxylates, tending to form more water stable coordination structures.[35] Kimizuka *et al.* reported the self-assembly of nucleotides upon the addition of lanthanide ions. The self-assembly of 5'-adenosine monophosphate (5'-AMP) and 5'-guanosine monophosphate (5'-GMP) with Gd(III) ions gave rise to 40-nm-in-diameter nanospheres (**Figure 10**). Interestingly, the self-assembled nanospheres were stable in water and in 2-[4-(2-hydroxyethyl)piperazine-1-yl]ethanesulfonic acid (HEPES) buffered water at pH = 7.4. Even though the coordination structure was amorphous, and the precise coordination of Gd(III) ions could not be elucidated, the water stability was attributed to the strong coordination between the Gd(III) ions and the phosphonates groups.

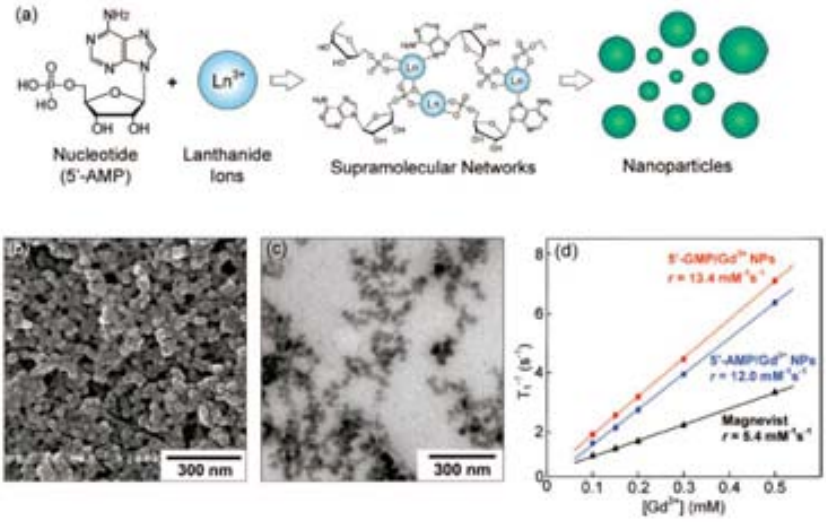

Figure 10. **a)** Schematic illustration of the self-assembly of 5'-AMP with lanthanides. FESEM (**b**) and TEM (**c**) image of the obtained nanospheres. **c)** r_1 curves of these nanospheres build up from the self-assembly of 5'-GMP (red) or 5'-AMP (blue) with Gd(III) ions at 12 MHz (0.3T).

Finally, Geraldes and co-workers prepared a range of lanthanide-based MOFs with the ligand (carboxymethyl)iminodi(methylphosphonic acid). The resulting NMOFs showed high water stability and very limited amounts of free Gd(III) leaching. This high stability afforded to perform a detailed relaxometric study which revealed that, while the longitudinal relaxivity was poor (r_1= 1 $mM^{-1}\cdot s^{-1}$),

the transversal relaxativity was high ($r_2 \approx 100$ $mM^{-1} \cdot s^{-1}$). This study also revealed that the relaxivity increased for smaller particles, indicating that water molecules are not able to diffuse inside the porous structure.[36]

Table 1. Summary of the most representative examples of nanostructured CAs.

	Observation*	r_1 ($mM^{-1} \cdot s^{-1}$)	B_0 MHz (T)	Ref.
Nanoscopic scaffolds				
Gold nanoparticles	2.3 nm AuNPs	60.0	30 (0.7)	21
	13 nm AuNPs	16.9	60 (1.4)	13
	20 nm AuNPs	20.0	60 (1.4)	13
Quantum dots	20 nm CdS:Mn@ZnS	20.5	200 (4.7)	37
Zeolites	30 nm Zeolite L	30	20 (0.47)	18
Biomolecules	MS2 Viral capside	41.6	30 (0.7)	14
	Heat Shock Protein (HSP)	25	30 (0.7)	15
Fullerenes	$C_{60}[C(COOH)_2]_{10}$	10.4 (pH dependent)	30 (0.7)	20
	$C_{60}(OH)_x$	38.5 (pH dependent)	30 (0.7)	20
Nanotubes	MWNT	50.3	20 (0.47)	20
	SWNT	500 (pH dependent)	60 (1.41)	19
Gd(III) based-building blocks				
Inorganic nanoparticles	Gd_2O_3	12	1 (0.02)	24
	GdPO4	13.9	20 (0.47)	25
	$KGdF_4$	5.86	400 (9.4)	26
Amphiphililc Gd(III) complexes	Gd-AAZTAC17 (17 aliphatic carbons linked to a coordination cage)	30	20 (0.47)	31
MOFs	$[Gd(BDC)_{1.5}(H_2O)_2]$	35.8	127 (3)	32
	$[Gd(1,2,4\text{-}BTC)(H_2O)_3]$	13.0	127 (3)	32
	$[Gd_2(BHC)(H_2O)_6]$	1.5	400 (9.4)	38
	$[Gd(H_2cmp)]$	1.08	500 (11.7)	36
	[Gd(5'-AMP)]	12.0	12 (0.3)	39
	[Gd(5'-GMP)]	13.4	12 (0.3)	29
	[Gd/(Fe(CN)$_6$]@PEG400	13.3	200 (4.7)	40
Comercial CA (Omniscan)		4.1	127 (3)	

*The observations refer to the characteristics of the Gd(III)-coated nanotemplates as well as to the composition of the Gd(III)-based nanoparticles. MWNT: multi walled carbon nanotubes; SWNT: single walled carbon nanotubes AAZTAC17: [6-bis(carboxymethyl)amino-4-carboxymethyl-6-heptadecyl-1,4diazepan-1-yl]; H_5CMP: (Carboxymethyl)iminodi (methylphosphonic acid); AMP: Adenosine monophosphate; BDC: 1-4 benzenedicarboxylic acid; 1,2,4-BTC: 1,2,4-benezenetricarboxylic acid; BHC: benzene hexacarboxylic acid

3. New MOFs with CA properties based on macrocyclic ligands as building blocks.

As seen above, the synthesis of Gd(III)-based NMOFs is a promising strategy to develop new nanostructured CAs with increased performance. However, it is still challenging to synthesise water stable NMOFs that can ensure high performances and low toxicity over the time. In this Thesis, we propose a new strategy to synthesise Gd(III)-based NMOFs that are stable in water by using ligands with high stability constants for Gd(III) ions. The idea is to prevent the leaching of free Gd(III) ions even in the case of eventual NMOF degradation. This is the reason why we focused on heterocyclic ligands that are generally used as Gd(III) chelators to form the clinically used molecular CAs. It is well-known that these heterocyclic-based ligands have shown great stability towards Gd(III), preventing the release of free Gd(III) under physiological conditions. In addition, these ligands have two different coordination functionalities: i) a core with tertiary amines; and ii) two, three or four pending arms with different functionalities, such as carboxylates, phosphonates and amines. These two coordination sites can be exploited to coordinate two distinct metal ions and therefore, form 3D NMOFs that incorporate Gd(III) ions (**Figure 11**). To prove the viability of this approach, the ligand 1,4,7,10-tetraazacyclododecane-1,4,7,10-tetra(methylene phosphonic acid) (DOTP) was selected as the heterocyclic building block.

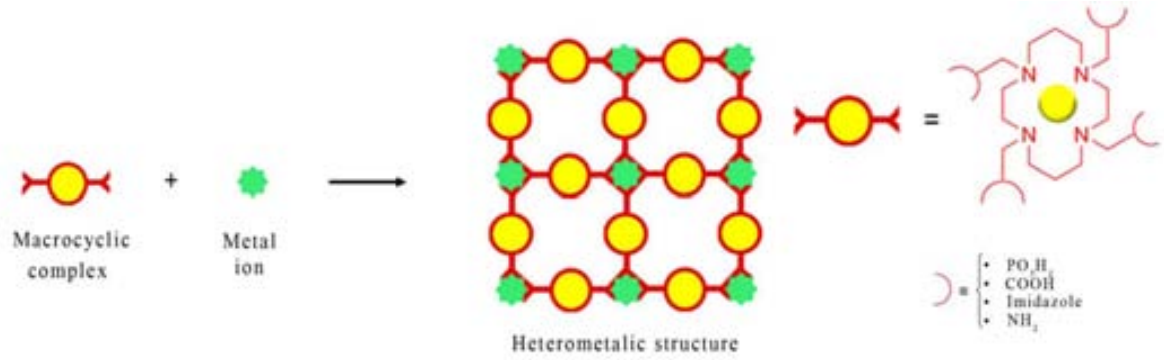

Figure 11. General strategy to create bimetalic extended structures from heterocyclic based ligands.

The choice of DOTP as the first candidate was governed by the following considerations: i) its structure offers two different coordination sites; the nitrogenated core and for phosphonate pendent arms; ii) it belongs to the family of strong chelating agents for Gd(III)[41]; and iii) phosphonates form stronger coordination bonds than carboxylates[35].

3.1. Reactivity of the DOTP ligand

As seen in **Figure 12**, the DOTP ligand forms stable chelates with Gd(III) ions, which are coordinated with the four amines in the core and the four phosphonates groups of the pendent arms.[42] In this configuration, complex $Gd(DOTP)^{5-}$ does not seem a suitable building block to form MOFs as it does not have free coordinating groups. This was demonstrated by reacting the $Gd(DOTP)^{5-}$ complex with different transition metal ions (Tm) (Tm(II) = Mn(II), Co(II), Zn(II), Mg(II), Ni(II), Fe(III) and Cu(II)) in water at basic pH. Under these conditions, it was not observed the precipitation of any solid that could indicate the formation of an extended structure. However, there was an exception: Cu(II) ions (**Figure 13**). Interestingly, when a Cu(II) solution at a concentration of Cu(II) = 0.018 M was added to a solution of $Gd(DOTP)^{5-}$ at a concentration of 0.018 M in a total volume of 4 ml, a blue precipitate appeared after few minutes. The reactivity of DOTP was also studied by doing the inverse experiment. First, the $Tm(DOTP)^{6+}$ was prepared and then, the Gd(III) was added. When $Tm(DOTP)^{6+}$ complexes were reacted with Gd(III) ions (at an equimolecular ratio and a concentration of 0.018 M), the same trend was observed. Again, no precipitation was observed except for the $Cu(DOTP)^{6-}$ complex. In this case, a blue precipitate appeared instantaneously. These observations indicated that the ligand DOTP was able to simultaneously coordinate Gd(III) and Cu(II) ions forming an extended structure insoluble in water.

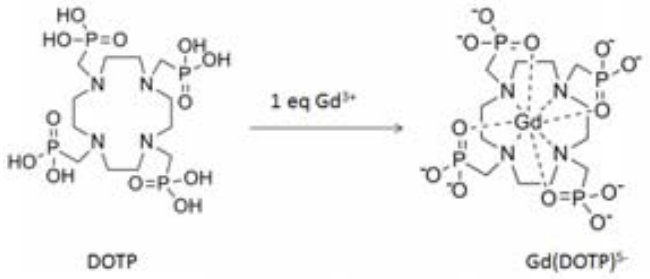

Figure 12. Reactivity of DOTP with Gd(III).

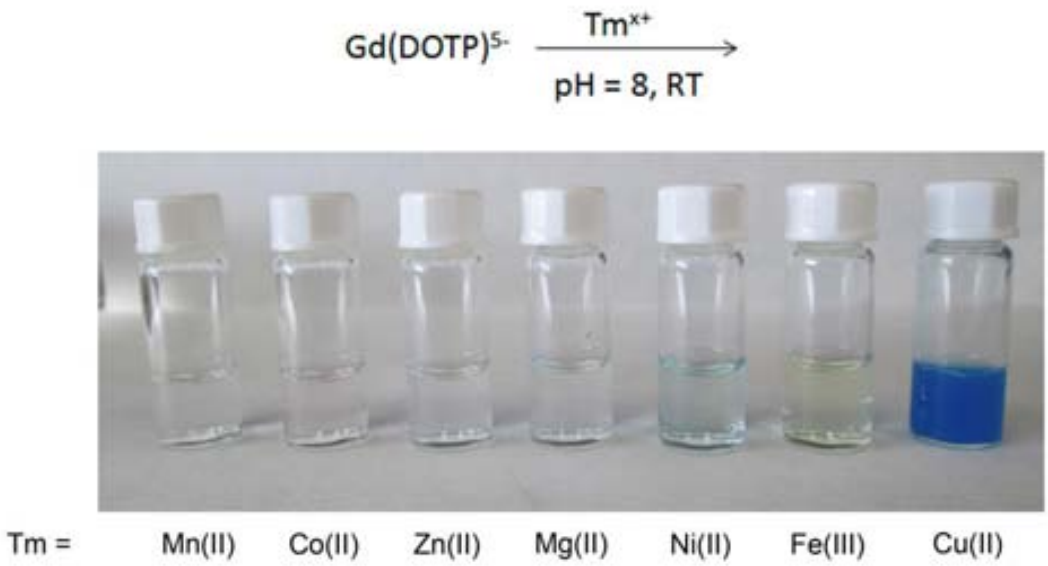

Figure 13. Screening of the reactivity of $Gd(DOTP)^{5-}$ reacting with different transition metal ions (Tm).

These results suggest that the $Cu(DOTP)^{6-}$ complex might be key in the formation of extended structures. In order to further understand the reactivity of DOTP, we also reacted the complex $Cu(DOTP)^{6-}$ with the other Tms. Accordingly, equimolecular mixtures of $Cu(DOTP)^{6-}$ were reacted with the same Tm^{x+} at pH = 8 (equimolar concentration of 0.018 M in a total volume of 4 ml). Here, it is important to point out that when Cu(II) was complexated inside the nitrogenated core, the colour shifted from green to cyan blue. Therefore, the colour evolution upon addition of other metal ions could be followed to get insights on the reactivity of $Cu(DOTP)^{6-}$ in a simple qualitative manner. We observed that the characteristic cyan blue colour of the Cu(II) complex was not disrupted upon addition of most of the metal ions, further evidencing the stability of $Cu(DOTP)^{6-}$ compared to the other $Tm(DOTP)^{6-}$ complexes (**Figure 14**). In addition, in the cases where a precipitate appeared (only for Gd(III) and Zn(II) ions), the precipitate had the characteristic cyan blue colour, indicating that Cu(II) ions were likely to be coordinated inside the core.

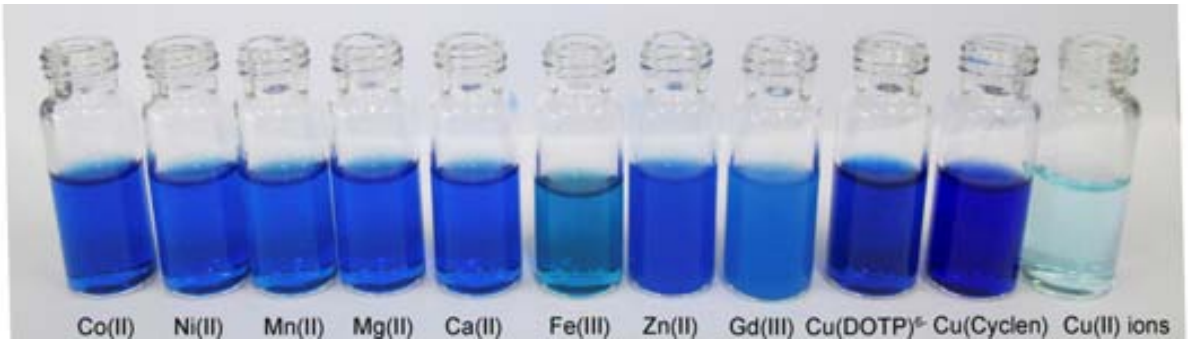

Figure 14. Photographs showing the vials containing the reaction mixture between the complex $(CuDOTP)^{6-}$ and the different Tms. The last three vials correspond to $Cu(DOTP)^{6-}$, Cu(Cyclen) and Cu(II) in water for comparison purposes.

3.2. Synthesis of a first example of Contrast Agent Metal-Organic Framework (CAMOF-1)

DOTP reactivity screening results suggested that the combination of DOTP with Cu(II) and Gd(III) ions is optimum to form an extended coordination structure. However, single crystals suitable for single-crystal X-ray diffraction could not be obtained when these three components were mixed in water at room temperature and at high pH. Thus, a high thermal reaction at low pH and high temperature was attempted in order to slow down the reaction and grow single crystals. It was found that the hydrothermal reaction of 5 mM DOTP, 5 mM $CuCl_2$ and 10 mM $Gd(NO_3)_3$ performed at low pH (pH < 4) and 80 ºC for 12 h afforded rod-like crystals suitable for single crystal analysis. The structure was determined from the data collected under synchrotron radiation at the ESRF facilities in Grenoble. The structure was solved by Dr. Inhar Imaz.

Crystal data confirms that DOTP coordinates to Cu(II) and Gd(III) ions forming a MOF structure with formula $[GdCu(DOTP)Cl]\cdot 4.5H_2O$; hereafter called **CAMOF-1**. Cu(II) ions are located in the centre of the cyclen core coordinated by the four amines and by a Cl^- in a square pyramidal geometry. Interestingly, Gd(III) ions are expanding the structure through phosphate coordination from different DOTP units. Each Gd(III) ion has an octahedral coordination with six phosphonate oxygens. The four deprotonated phosphonates groups of the DOTP ligands coordinate six Gd(III) ions, which are connected to six CuDOTP units resulting in a opened porous 3D structure with 1D channels (~ 5 X 5 Å; 23% of void space in unit cell) along the (113) direction (**Figure 15**).

With this structural information it is possible to rationalise the observations of the reactivity screening experiments. The stability constant of $Gd(DOTP)^{5-}$ is the highest among any other $Tm(DOTP)^{6-}$ complexes. However, Cu(II) ion has also a high stability constant with DOTP, which is comparable to $Gd(DOTP)^{5-}$ (28.8[42] for $Gd(DOTP)^{5-}$ and 25.4[43] for $Cu(DOTP)^{6-}$). We hypothesise that the close stability constants of the two metal ions make possible for Cu(II) ions to disrupt the formation of the highly stable $Gd(DOTP)^{5-}$ complex, allowing DOTP to simultaneously coordinate to the two metal ions and extend the metal-organic structure. In addition to the preference of Cu(II) ions

for nitrogen donors and the preference of lanthanides for oxygen donors, kinetics factors might also contribute to yield a structure in which the Cu(II) ions are in the polyamine cage and the Gd(III) ions are coordinated by the phosphonate groups.

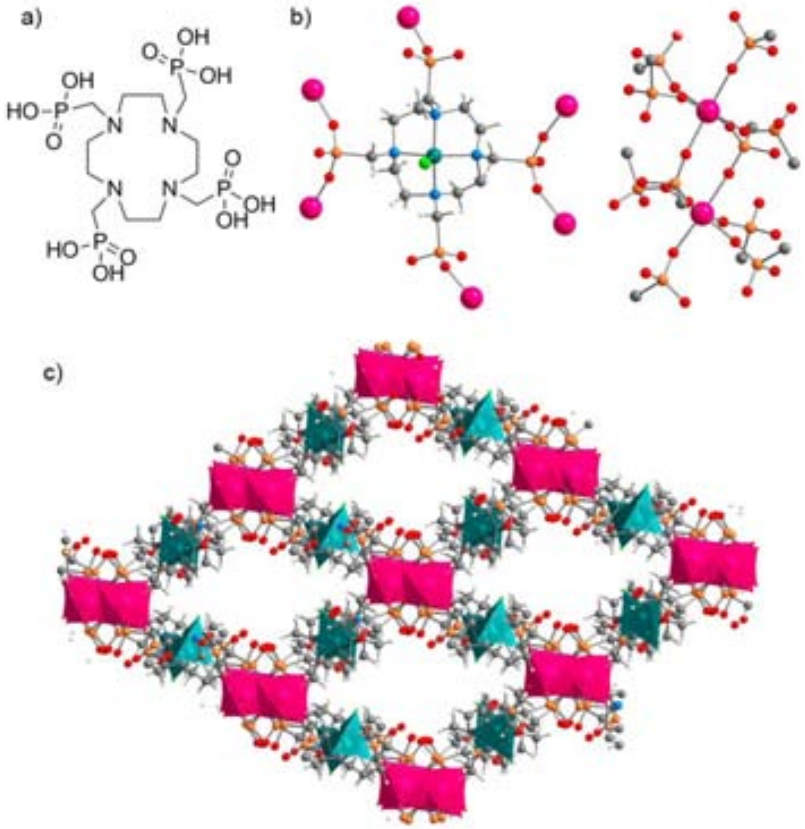

Figure 15. **a)** DOTP ligand. **b)** Crystal structure of **CAMOF-1**, showing the coordination of DOTP with one Cu(II) ion and six Gd(III) ions and the coordination geometry of Gd(III) ions. **c)** 3D extended structure of **CAMOF-1**, showing the presence of 1D channels. Color code: Gd, pink; C, gray; N, blue; Cu, dark green; Cl, light green; O, red.

The phase purity of the synthesised material was confirmed by XRPD. **Figure 16a** shows that the experimental XRPD pattern is in good agreement with the theoretical pattern simulated from the **CAMOF-1** structure. Thermal stability of the structure was also studied by thermogravimetric analysis (**Figure 16b**). It showed an initial mass loss of 10.57 % from 50 ºC to 150 ºC which is in good agreement with the loss of 4.5 water molecules per formula unit (expected value = 9.15 %). The structure decomposes at 375 ºC, where there is a sharp mass loss of 12.16 % at 375 ºC. However, the total mass lost at 500 ºC is less than 20 %, which is coherent with the formation of highly stable phosphate species as previously reported by Clearfield *et al*.[44]

Finally, in order to study the porosity **CAMOF-1**, it was first activated by the solvent exchange method. As-made **CAMOF-1** was first washed with methanol and then with chloroform. Finally, it was thermally treated at 120 ºC under vacuum overnight to ensure the removal of all solvent molecules located in the pores. The crystalline structure showed to be stable through the

desolvation process, as demonstrated by XRPD (**Figure 16a**). The porosity of **CAMOF-1** was studied through N_2 and CO_2 adsorption at 77 K and 195 K respectively. **CAMOF-1** showed not to be porous to N_2. However, it was porous to CO_2, presenting a hysteretic behaviour and a BET surface are of 110 $m^2 \cdot g^{-1}$ (**Figure 16c**).

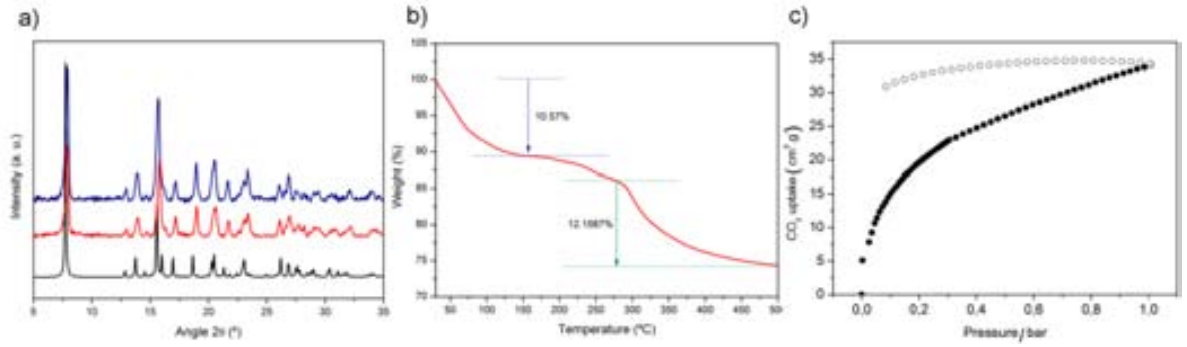

Figure 16. **a)** Comparision between the simulated XRPD of **CAMOF-1** (black), as-made **CAMOF-1** (red) and activated **CAMOF-1** (blue). **b)** TGA of **CAMOF-1**. **c)** CO_2 adsorption isotherm at 195 K.

3.3. Nanostructuration of CAMOF-1

A prerequisite to study the potential application of **CAMOF-1** as a T_1-CA is to control its size down to the nanoscale regime. The miniaturisation requirement is demanded mainly for two reasons: i) nanomaterials used in biomedical applications should not exceed 200 nm in size in order to take advantage of the Enhanced Permeability and Retention (EPR) effect and ensure good biodistribution and *in vivo* circulation; and ii) the relaxometry measurements require homogeneous distribution (that is, the formation of a good colloid) of the CA in the aqueous sample. This might be a challenge when structured supramolecular CAs are used due to their tendency to aggregate and fall, leading to a misunderstanding of the results. Highly homogenous nanoscopic objects have a better stability in water and therefore, lead to better quality results in relaxometry.

An important factor that strongly influences the reaction rate of our system is the pH because it alters the protonation state of the phosphonate groups of DOTP. At high pH, phosphonate groups are deprotonated and therefore, the coordinating capabilities of DOTP increase. For this reason, it was thought that the pH of the reaction could be used to tune the reaction rate and induce the miniaturization of **CAMOF-1**. Accordingly, an aqueous $CuCl_2$ solution (30 mM) was added to an aqueous DOTP solution (30 mM) at pH = 8. Then, a third aqueous $Gd(NO_3)_3$ solution at a concentration of 60 mM was added to the former solution under high stirring and final volume of 5 ml. Instantaneously, a blue colloidal precipitate appeared; hereafter noted as **NCAMOF-1** (**Figure 17a**). The resulting colloidal suspension was characterised by DLS and TEM (**Figure 17b**). TEM

images showed the formation of uniform nanowires of 10 nm in diameter and 200 nm in length. DLS measurements showed good correspondence with the TEM images.

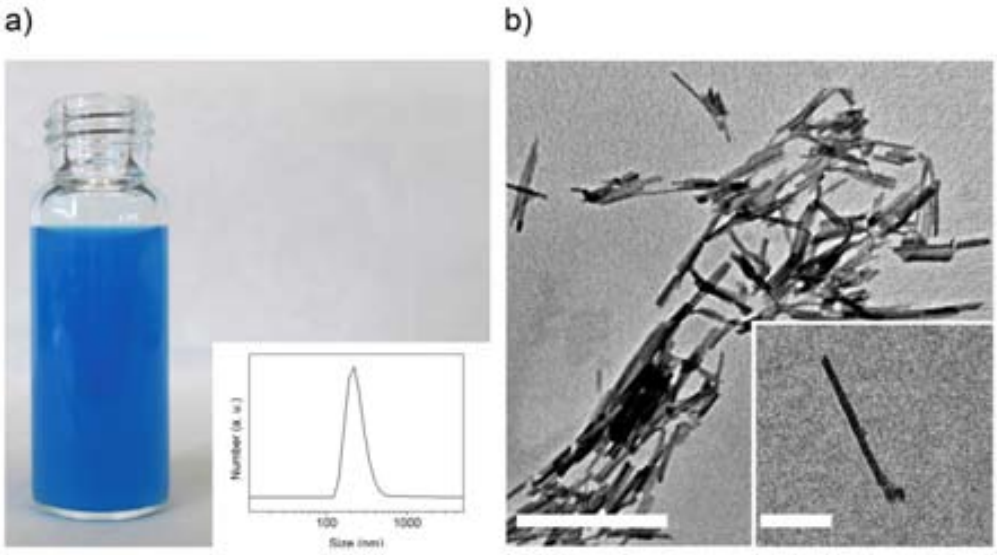

Figure 17. a) Photograph of **NCAMOF-1** colloidal suspension and its size distribution determined by DLS (inset). **b)** TEM images of **NCAMOF-1**. Scale bar corresponds to 500 and 100 nm (inset).

3.3.1. Characterisation of NCAMOF-1

The XRPD analysis of the **NCAMOF-1** wires showed no defined diffraction peaks, which is indicative of their poor crystallinity. In order to undoubtedly correlate the nanowires with the solved structure of **CAMOF-1,** further characterisation was carried out. Fourier Transformed Infrared (FTIR) analysis of both macroscopic **CAMOF-1** and **NCAMOF-1** showed good correspondence (**Figure 18**). FTIR spectra show the presence of an intense band centred at 1635 cm^{-1}, which can be assigned to the stretching of the N-H. In our case, the structure does not present protonated amines because they are coordinated to Cu(II) ions. Therefore, the stretching at 1635 cm^{-1} can be attributed to the coordination of the nitrogenated core to the Cu(II) ions. The typical splitting of the phosphate stretching band when it is coordinated to metal ions, centred at 1127 cm^{-1}, was also observed. These bands are in good agreement with the reported literature on MOFs based on phosphonate ligands.[44,45] Thus, the perfect match between both FTIR spectra is a first evidence that both structures have the same chemical connectivity.

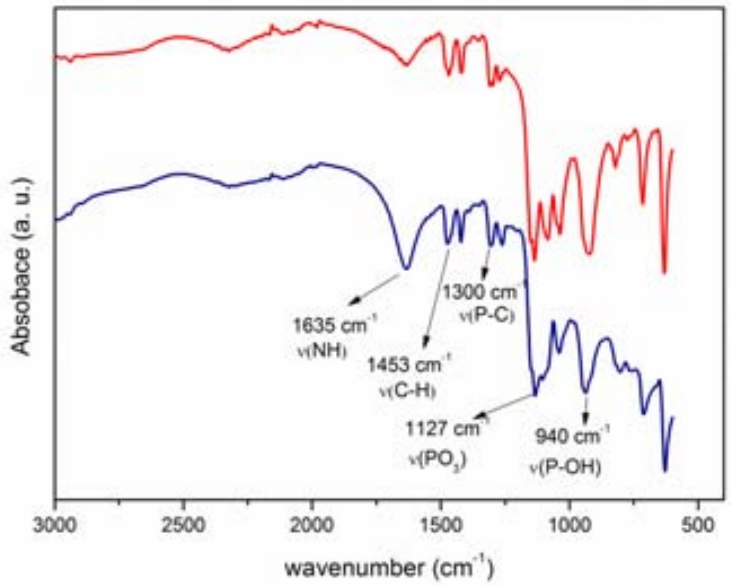

Figure 18. FTIR spectra of **CAMOF-1** (red) and **NCAMOF-1** (blue).

To further characterise **NCAMOF-1**, its elemental composition was elucidated. Elemental analysis showed the presence of carbon, hydrogen and nitrogen, whereas the metal content was determined by Induced Coupled Plasma – Optical Emission Spectrometry (ICP-OES) after digesting the samples in acidic water. The results are presented in **Figure 19**, showing perfect agreement with the expected molecular formula [GdCuDOTP·4.5H_2O] obtained from the crystal resolution of **CAMOF-1.** Magnetic properties were also measured through magnetic susceptibility measurements and calculated according to **Equation 2**. The observed $\chi_M T$ values of both nanoscopic and microcrystalline **CAMOF-1** has a good correspondence with 8.25 emu·K·mol^{-1}, a value expected for two non-magnetically interacting Gd(III) and Cu(II) ions.

$$\chi_m T = \frac{g^2}{8}\, s\,(s+1) \quad \text{where } g \sim 2 \text{ and } S = \text{Spin} \qquad \text{(Equation 2)}$$

a)

	Calc. [GdCuDOTP]·4.5H$_2$O	Exp.
C	16.26	15.56
N	6.32	6.11
H	4.12	4.40
Cu	7.18	7.04
Gd	17.76	17.75

b)

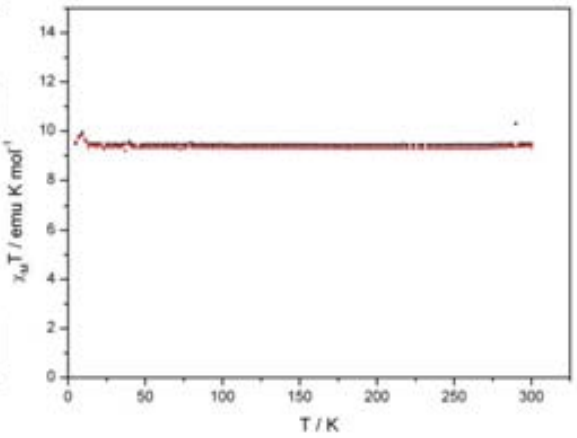

Figure 19. a) Elemental analysis of **NCAMOF-1** and expected values considering the formula [GdCuDOTP·4.5H_2O] determined by single-crystal X-ray diffraction**.** The content of Cu(II) and Gd(III) was determined through ICP-OES after digesting the sample. **b)** Temperature dependence of $\chi_M T$ of **NCAMOF-1** (red) and **CAMOF-1** (black).

3.3.2. Control of the length of NCAMOF-1

To evaluate if the length of the nanowires could be increased, we reproduced the same reaction but using the diffusion method. 2 ml of the solution containing the $Cu(DOTP)^{6-}$ at a concentration of 10 mM at pH = 8 was placed in the bottom of a test tube layered up with an aqueous interface (6 ml). On the top of the interface, 2 ml of an aqueous $Gd(NO_3)_3$ solution at a concentration of 20 mM was layered. The slow diffusion of the reactants through the interface slowed down the reaction and allowed the formation of longer fibres of up to 100 μm-in-length (**Figure 20a, b**). Interestingly, the XRPD experiments performed on this sample showed that the long fibres are more crystalline than the shorter nanowires. **Figure 20c** shows the good agreement between the XRPD of these fibres and the simulated pattern of **CAMOF-1**. In fact, this is a further prove that undoubtedly correlate the **NCAMOF-1** with the bulk **CAMOF-1**.

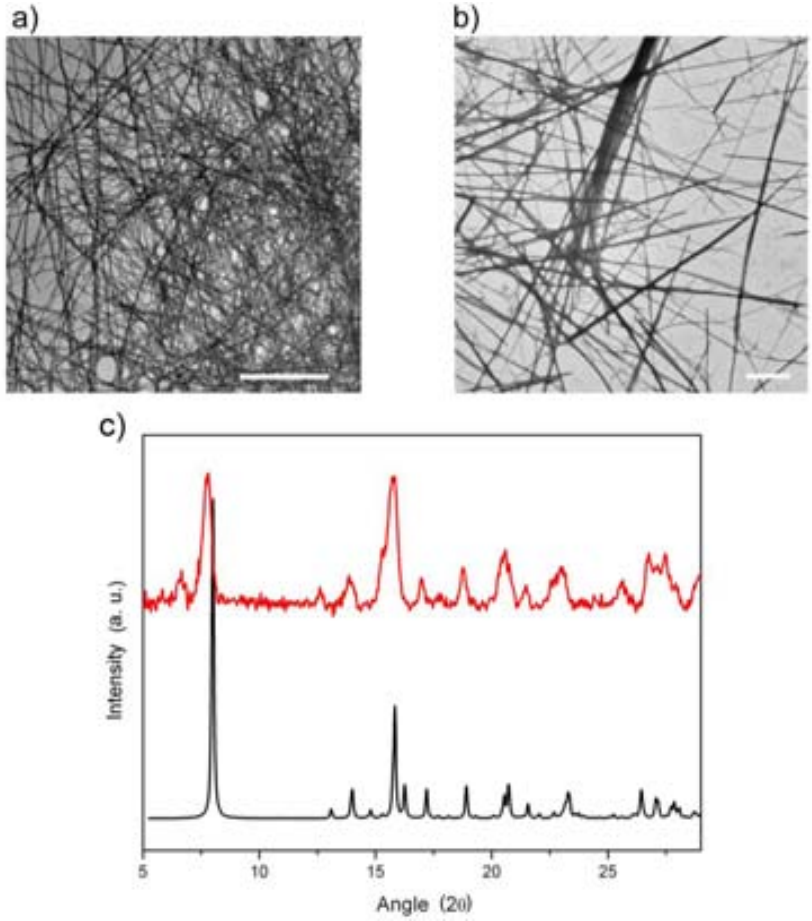

Figure 20. a, b) Representative TEM images of the nanofibres of **NCAMOF-1** synthesised through the diffusion method. **c)** XRPD diffraction pattern of the simulated **CAMOF-1** and **NCAMOF-1** synthesised through diffusion. Scale bars correspond to 5 μm (**a**) and 2 μm (**b**).

3.4. Stability of NCAMOF-1

Prior to any relaxivity measurements, the stability of **NCAMOF-1** in water was a very important factor to be studied in order to ensure that no free Gd(III) is leached. Besides their high toxicity, the release of free Gd(III) ions could lead to a misreading of the r_1 value (as mentioned earlier, free Gd(III) ions have large r_1). Two analytical methodologies were used in order to evaluate the amount of leached Gd(III) ions and in which form (free or complexated) they were released. The total content of Gd(III) ions in solution was determined by ICP-OES, whereas a colorimetric method was used to exclusively detect the free, non-coordinated Gd(III) ions in solution (**Figure 21**).

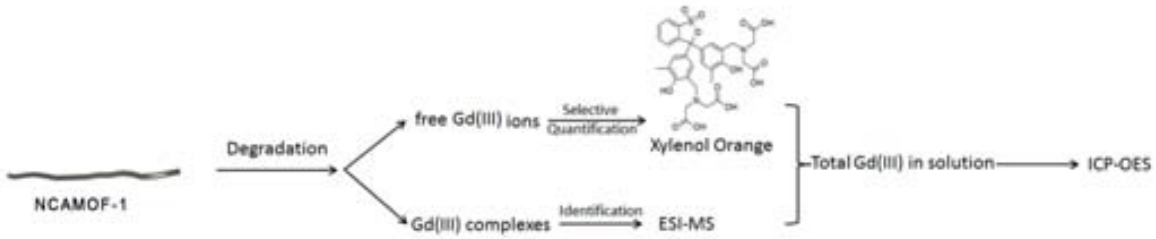

Figure 21. Analytical strategy to evaluate **NCAMOF-1** degradation in water and physiologically simulated conditions.

The colorimetric method was based on the Xyelenol Orange (XO) indicator. XO is a chelate with moderately high stability towards Gd(III) ions (log K = 5.8) that, once coordinated to Gd(III) ions, undergoes a colour shift from yellow to purple. However, XO cannot coordinate to Gd(III) ions forming more stable complexes (*e.g.* with DOTP), so it can be exclusively used to detect the non-coordinated free Gd(III) ions. The XO test was established according to reported protocols.[46] XO has an emission spectra with the adsorption maximum at 433 nm that shifts to 573 nm when the Gd(III) complex is formed. The ratio between the two wavelengths versus the free Gd(III) ions was used to draw the standard curve that was employed to determine the content of free Gd(III) ions in solution (**Figure 22**). However, it has to be taken into account that the eventual degradation of **NCAMOF-1** would also release Cu(II) ions. XO is also responsive to these ions. Therefore, the amount of free Gd(III) ions in solution might be overestimated due to the interference of Cu(II) ions. For this reason, in this study, the XO colorimetric method was used to estimate the maximum potential release of free Gd(III) ions.

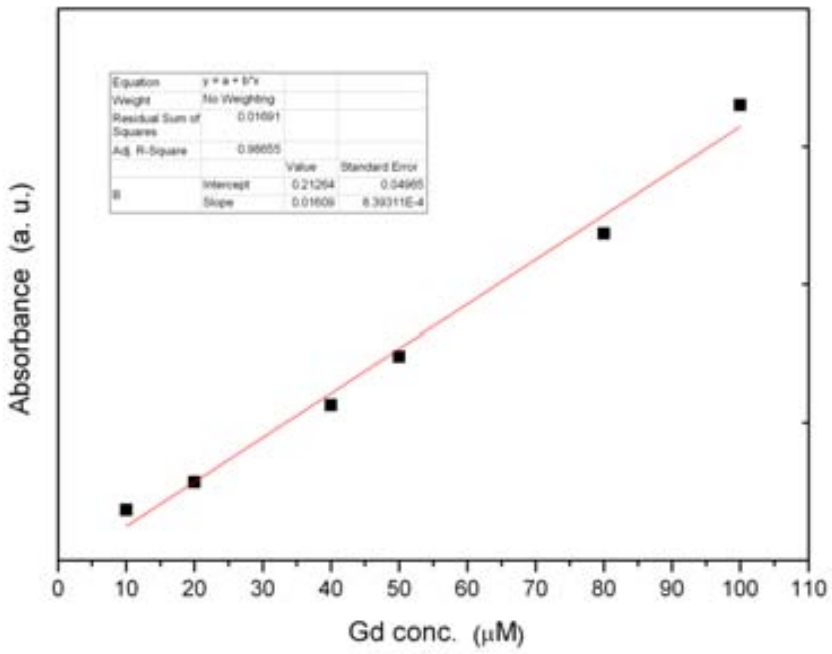

Figure 22. Standard curve used to determine the free Gd(III) ions.

In an initial experiment, the known stability constant for the XO-Gd(III) complex was used to range the stability of the **NCAMOF-1**. A previously washed **NCAMOF-1** was dispersed in water containing XO. The sample was incubated overnight and centrifuged. A simple naked eye observation revealed that the supernatant was yellow showing that no significant amounts of Gd(III) ions were leached from the nanowires. In addition, the suspension remained stable throughout the test. This simple observation indicated that the thermodynamic stability of Gd(III) ions forming **NCAMOF-1** structure is higher than for the Gd(III)-XO complex (log K = 5.8).

Once the methodology to determine Gd(III) ions in solution was established and the first insights on **NCAMOF-1** stability were obtained, we started evaluating its degradation profile in saline water solutions (NaCl at the physiological concentration of 0.9 % w/w) as a function of pH. For this, colloidal suspensions of **NCAMOF-1** at a concentration of 7mM were first prepared in water. Then, the colloidal suspensions were repeatedly centrifuged and dispersed in saline water to ensure the total removal of any eventual remaining reactant. Finally, the colloidal suspensions were adjusted to the desired pH values (*i.e.* pH = 4, pH = 7.4 and pH = 9). Samples were incubated at 37 ºC and after an incubation period, they were centrifuged and the supernatant analysed by ICP-OES and the XO colorimetric test.

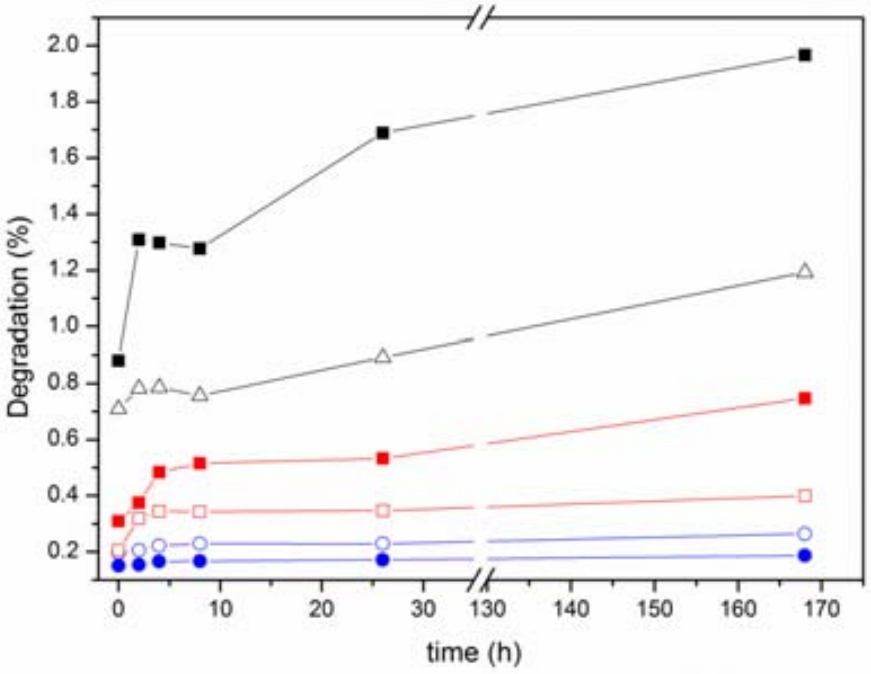

Figure 23. Time dependence of the percentage of the total Gd(III) [filled symbols] and the maximum potential free Gd(III) ions [empty symbols] relative to the total Gd(III) content in **NCAMOF-1** leached upon incubation in saline solution at pH = 4 (blue cercles), 7.4 (red squares) and 9 (black triangles).

Figure 23 shows the degradation profile of **NCAMOF-1** at different pHs calculated from the concentration of Gd(III) determined by the two different methods. Overall, the graph shows little degradation of **NCAMOF-1** at all pH tested after one week of incubation. Remarkably, at pH = 4, there is a good agreement between the two methods employed to determine the leached Gd(III). However, as the pH raises, the total content of Gd(III) is significantly higher than the maximum potential free Gd(III) ions determined by the colorimetric method. These discrepancies suggest the presence of coordinated Gd(III) species, which could be attributed to the strong coordination capabilities of the ligand DOTP. Two scenarios can be suggested. From one side, DOTP can complexate a fraction of the leached metal ions after partial degradation of **NCAMOF-1.** On the other side, the degradation of DOTP occurs via release of polymeric species, in which a fraction of the metal ions are more stable than with XO. Both hypothesis would explain why the content of maximum potential free Gd(III) is remarkably lower than the total water soluble Gd(III) ions determined by ICP-OES.

In order to support this hypothesis and to identify the "situation" of Gd(III) ions in solution, the supernatant solutions were further analysed by electrospray mass spectrometry (ESI-MS) (**Figure 24**). The analysis revealed species corresponding to CuDOTP ($[CuDOTP - 4H + 3Na]^+ = 675.96$, $[CuDOTP - 5H + 4Na]^+ = 697.94$) and CuDOTPGd complexes ($[CuGdDOTP - 5H - OH]^+ + 2MeOH = 810.96$, $[CuGdDOTP - 5H - OH]^+ + 2MeOH + H2O = 828.92$, $[CuGdDOTP - 6H - OH + Na]^+ + 2MeOH = 832.96$). The comparison between the experimental patterns and the simulated ones for the complexes corresponding to $[CuDOTP - 4H + 3Na]^+$ and to $[CuGdDOTP - 5H - OH]^+ + 2MeOH$ are shown in **Figure 25**. Note that the presence of methanol molecules is due to sample preparation (*i. e.* methanol is added prior injecting the sample). This results demonstrated that certain number of Cu(II) and Gd(III) ions are indeed attached to DOTP ligand in solution. In addition, the presence of supramolecular aggregates upon partial degradation of **NCAMOF-1** was further supported by relaxivity measurements, as it will be explained in the following section.

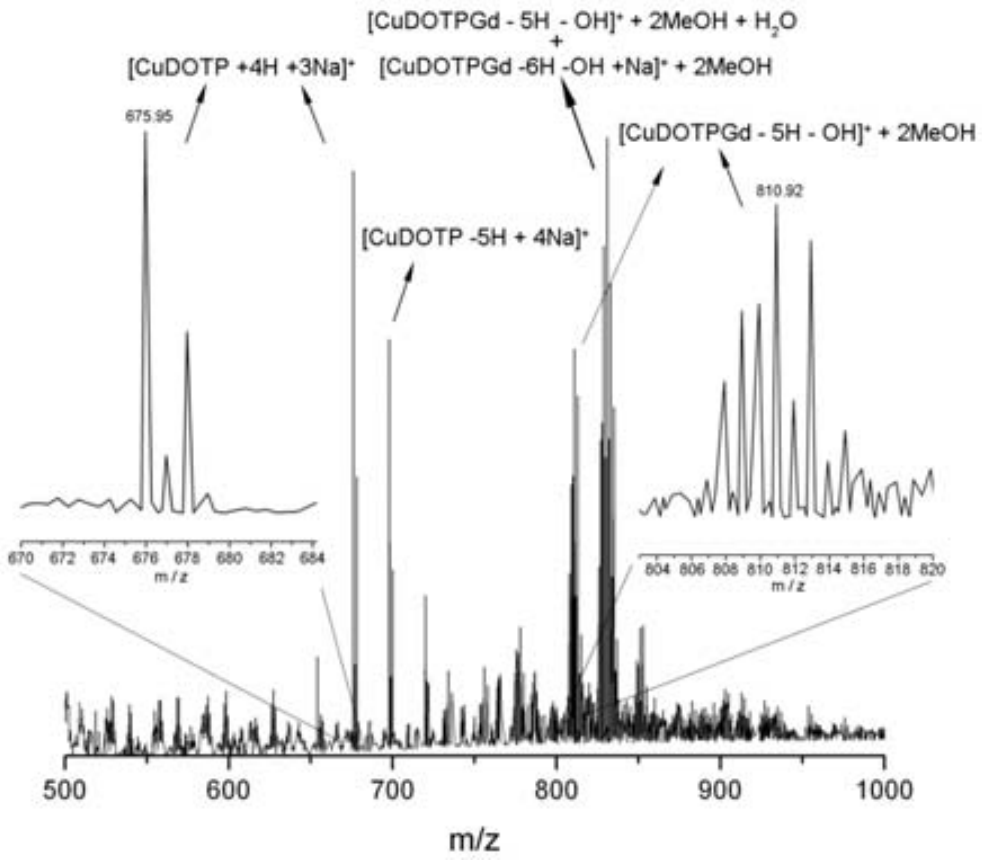

Figure 24. The ESI-MS spectrum obtained for the supernatant resulting from the incubation of **NCAMOF-1** in saline solution for 24 h at 37 ºC.

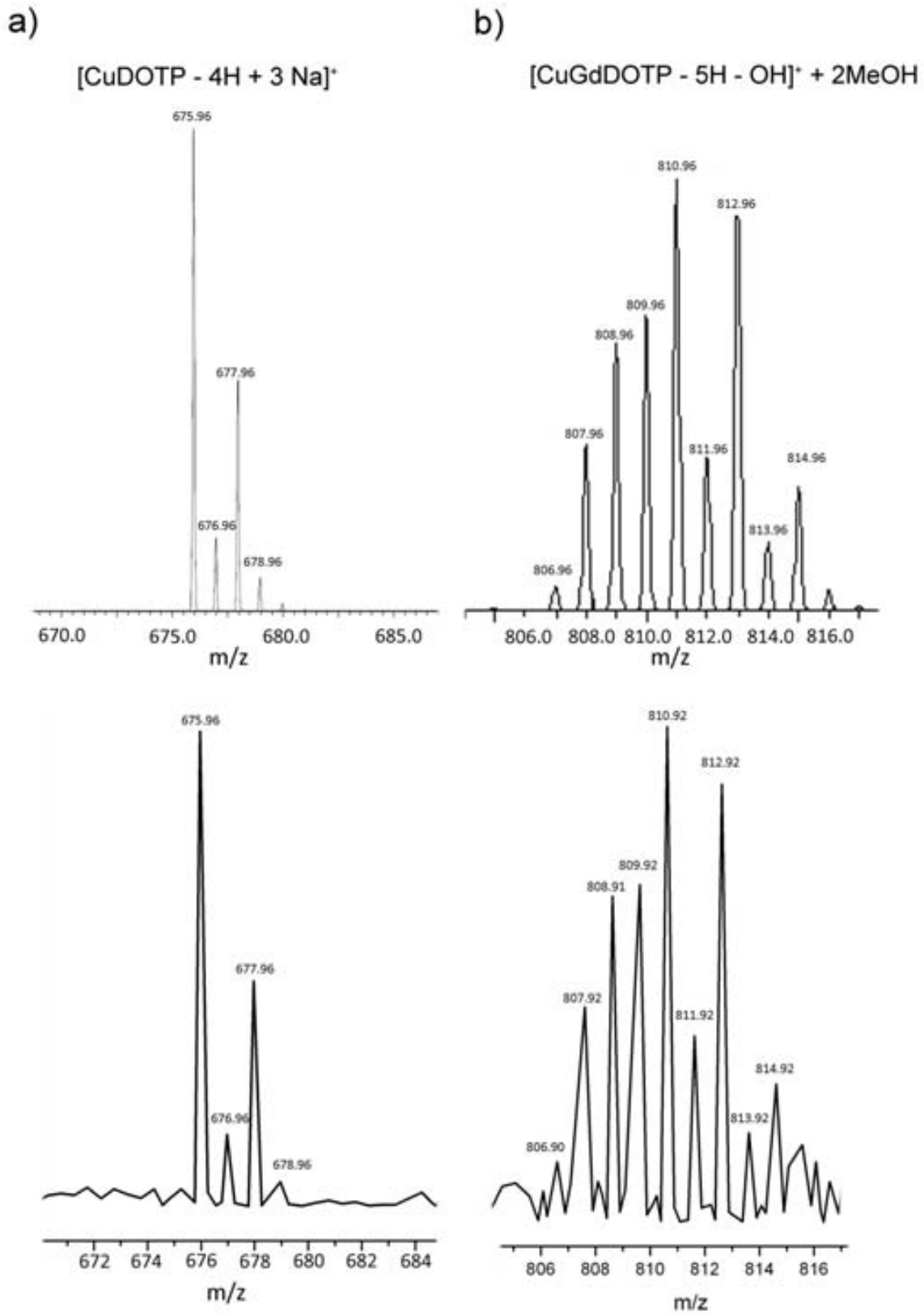

Figure 25. **a)** ESI-MS spectrum of peaks corresponding to [CuDOTP – 4H + 3Na]+ = 675.96 and **b)** [CuGdDOTP – 5H – $OH]^+$ + 2MeOH = 810.96 and their simulated isotopic pattern (top).

NCAMOF-1 was also exposed to HEPES buffered at pH = 7.4, also showing remarkable good stability with a degradation of 2.6 % after one week of exposure (**Figure 26**). In this case, Gd(III) concentration was determined only by ICP-OES due to the strong interference of the buffer with the XO test. Once the stability of **NCAMOF-1** at physiological pH was tested, its integrity in more closely simulated physiological conditions was evaluated. For this, colloidal suspensions of **NCAMOF-1** were dispersed and incubated in cell culture media Dulbecco's Modified Eagle's Medium (DMEM). Here, the degradation was significantly higher than in the earlier cases. Nevertheless, after 24 h, only 30% of the total Gd(III) content was leached from **NCAMOF-1** (**Figure 26).** Given the low stability of MOFs in this media, a degradation of only 30% can be considered highly remarkable.

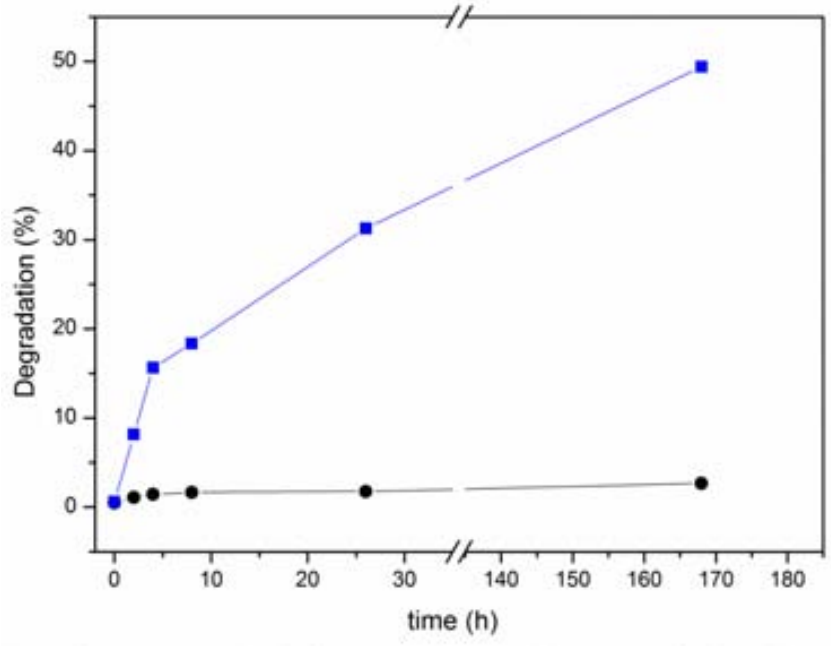

Figure 26. Time dependence of the percentage of the total Gd(III) ions relative to the total Gd(III) content in **NCAMOF-1** leached upon incubation in HEPES buffered media (black cercles) and DMEM cell culture media (blue squares).

The stability of **NCAMOF-1** in the different media tested was also evaluated in terms of structural integrity. Therefore, the samples incubated after one week were analysed by DLS and TEM. As shown in **Figure 27**, all stable suspensions were maintained with no significant change in the size of the nanowires, as determined by DLS. TEM images also corroborated that **NCAMOF-1** does not suffer from extensive morphological changes upon incubation at different pH or DMEM (**Figure 28**). Importantly, the fact that colloidal suspensions can be maintained throughout a wide range of pH ensures that r_1 measurements can be performed at different pHs with no concern of a possible misreading of the data due to eventual aggregation phenomena.

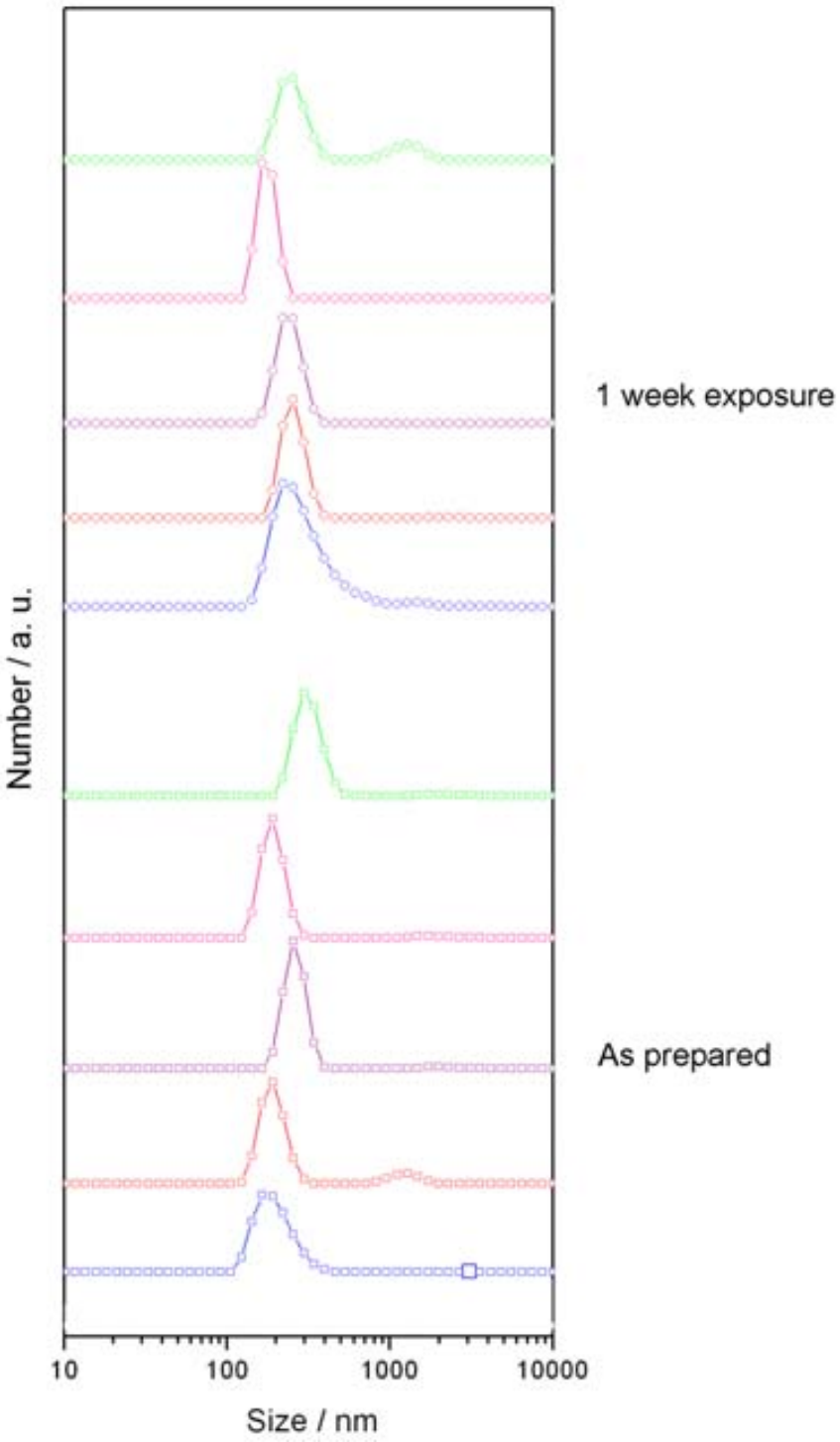

Figure 27. DLS measurements of the **NCAMOF-1** dispersed in different media: physiological saline solution (NaCl, 0.9% w/w) at pH = 4 (blue), pH = 7.4 (red), pH = 9 (purple), HEPES (25 mM) (pink) and DMEM (green). Samples freshly prepared are represented with squares (bottom), and circles represent the samples incubated for one week (top).

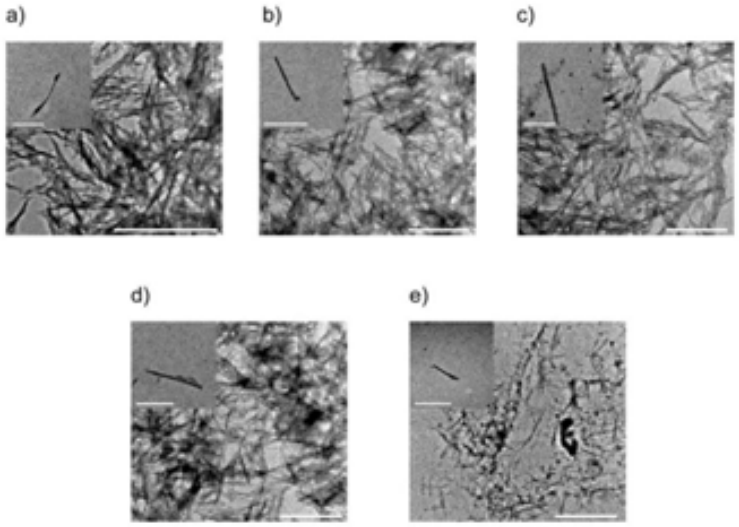

Figure 28. TEM images of **NCAMOF-1** after incubation in physiological saline (0.9% w/w) at pH = 4 (**a**), pH = 7.4 (**b**), pH = 9 (**c**), HEPES (**d**) and DMEM (**e**), showing the presence of wire-like nanocrystals. Inset shows isolated nanocrystals. Scale bars correspond to 2 μm and 200 nm (inset).

3.5. Cytotoxicity of NCAMOF-1

The non-cytotoxic character is a prerequisite for any material postulated for biomedical applications. In such a context, we performed cytotoxicity tests of **NCAMOF-1** in two different cell lines: MCF7, a human breast-cancer cell, and HepG2, a human Hepatocellular carcinoma cell. These cell lines were chosen due to their sensitivity to any change in the culture media. These experiments were carried out in collaboration with Dr. Julia Lorenzo. Cells were incubated in DMEM F12 or DMEM (Invitrogen) containing 10 % (v/v) heat-inactivated fetal bovine serum in the presence of **NCAMOF-1** at a concentration ranging from 20 to 200 μM for 24 h. **Figure 29** shows the results of the cytotoxic assay. Cells showed good viability (75 % for HepG2 and 74 % for MCF7) even at the higher concentration of 200 μM. This lack of toxicity can be attributed to the high stability of **NCAMOF-1** and to the capacity of DOTP to chelate a high percentage of the limited quantity of Gd(III) and Cu(II) ions that are leached upon degradation of **NCAMOF-1.**

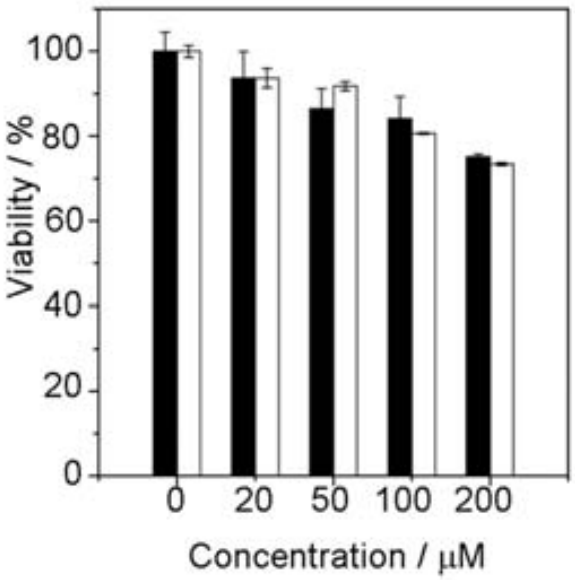

Figure 29. Effects of **NCAMOF-1** on the viability of HepG2 (filled bars) and MCF7 (empty bars) cells at 24 h. Error bars represent the standard error.

3.6. Relaxometry studies of NCAMOF-1

3.6.1. NMRD profile in water

In order to evaluate the performance of **NCAMOF-1** as a CA, the ^{1}H nuclear magnetic relaxation dispersion (NMRD relaxometry) profile was used to determine its r_1 at the frequency range of 10 KHz $\leq \nu \leq$ 500 MHz. The NMRD relaxometry was performed on a Stelar SMARtracer Fast Field Cycling NMR relaxometer (0.01-10 MHz) and a Bruker WP80 NMR electromagnet adapted to variable field measurements and controlled by a SMARtracer PC-NMR console (10-80 MHz). This equipment allows tuning the background magnetic field much faster than in conventional NMR relaxometry, which allows to precisely determine r_1 at each magnetic field. The r_1 at 500 MHz was determined using a Bruker Avance 500 spectrometer. All the relaxivity measurements were conducted in collaboration with the Prof. Eva Toth and Dr. Célia Bonet in the Centre de Biophysique Moleculaire.

NMRD profiles report more information than the determination of r_1 at a single magnetic field because it infers some mechanistic considerations. As seen above, the variance of r_1 with the magnetic field is closely related to the mechanism of relaxation process. It is important to highlight that a precise r_1 determination demands accurate knowledge of the Gd(III) concentration. This was ensured by the ICP-OES analysis of the digested samples after each measurement. Therefore, an initial experiment consisted on determining the r_1 of a colloidal suspension of **NCAMOF-1** at 25ºC. The resulting NMRD profile shows the r_1 dependency with the magnetic field for **NCAMOF-1** (**Figure 30**). At low magnetic fields, below 10 MHz, the r_1 remains constant at around 8 $mM^{-1} \cdot s^{-1}$. Then, at intermediate fields ranging from 10 MHz to 40 MHz, r_1 markedly increases reaching a value of 15

$mM^{-1}\cdot s^{-1}$ at 40 MHz, which is more than 3 times higher than the reported relaxivity for $[GdDOTP]^{5-}$ at pH = 7.4.[47] At high fields, r_1 decreases reaching a value of 5 $mM^{-1}\cdot s^{-1}$ at 500 MHz. This behaviour is characateristic of systems with slow rotational motion, typically observed in nanostructured systems.[18,48] In addition, **Figure 30** also shows how r_1 increases with temperature, which is indicative that the mean proton exchange between the nanowires and the bulk water is limiting the relaxivity, as previously observed in other nanostructured Gd(III)-based CAs.[49] This is a clear indication that an inner-sphere type of mechanism based on water exchange is the major contributor to the overall relaxivity. This is in contrast to other reported MOFs in which only outer-sphere mechanism contributed to relaxivity yielding low r_1 at high field (around 1 $mM^{-1}\cdot s^{-1}$ at 500 MHz at 298 K).[36] The observed temperature dependence allows drawing further conclusions on the relaxation mechanism. It is assumed that the Gd(III) ions located at the surface of the MOF have an increased hydration number and therefore, a fast water exchange ratio. Indeed, in general, Gd(III) complexes containing more than one inner sphere water molecules have relatively fast water exchange. This exchange is fast enough for not observing such temperature dependency of r_1. If the Gd(III) ions located at the surface cannot be responsible for this temperature dependency, it can be attributed only to the inner Gd(III) ions (located inside the structure). The Gd(III) centres inside the MOF channels might have slower water exchange, or the diffusion be limited. The temperature increase will result in an increase of the water exchange rate, yielding the observed increase in r_1. Consequently, the increase of r_1 observed upon increasing the temperature allows us to deduce that inner Gd(III) ions do contribute to r_1 in **NCAMOF-1**, and that this is only possible if water molecules can have access to the channels and there is sufficient water (or proton) exchange between the channels and the bulk. This is in contrast to previously reported MOFs were only Gd(III) ions located on the surface were responsible for r_1.[32,36] This is the first time that the effect of the porosity in r_1 is observed in a NMOF.

It should be mentioned that we can only obtain information on the average value of the proton (or water) exchange rate, as the different "sites" that can be found in the MOF structure (i.e., surface and inner centres) have different exchange rates and contribution to the overall r_1. The crystal structure shows that each Gd(III) ion inside the MOF is coordinated by six phosphonate oxygens, which yields a highly unsaturated coordination sphere for a lanthanide (typical CN = 8 or 9 in solution). However, it is impossible to assess the average number of water molecules per Gd(III) ions that can contribute to the r_1, their distance from paramagnetic centre, and their exchange rate with bulk water only with relaxometry. These parameters all influence the experimental r_1, but they cannot be assessed individually by relaxometry. Nevertheless, the relaxivity profile was used to get insights in the relaxation mechanism triggered by a MOF at the nanoscale for the first time.

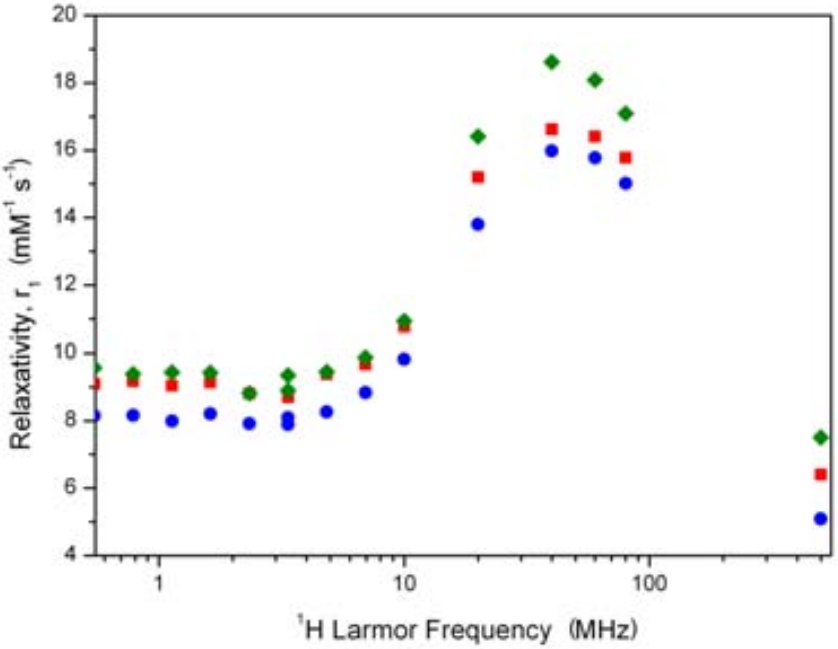

Figure 30. NMRD profile of a colloidal suspension of **NCAMOF-1** at pH = 4 at 25ºC (blue dot), 37ºC (red square) and 50 ºC (green rhombus).

3.6.2. Relaxivity dependence with pH

The stability at a wide pH range demonstrated by **NCAMOF-1** enabled us to study its CA properties as a function of pH. For this purpose, the pH of a colloidal suspension of **NCAMOF-1** was increased stepwise from pH = 4 to pH = 9 and r_1 was monitored at a fixed magnetic field of 40 MHz. The r_1 dependence as a function of pH is shown in **Figure 31**. A r_1 with a value of around 16 $mM^{-1}{\cdot}s^{-1}$ remained relatively constant over the pH studied, further supporting the integrity of the **NCAMOF-1** over this pH range. The small differences observed could be attributed to protonation of phosphonate groups.

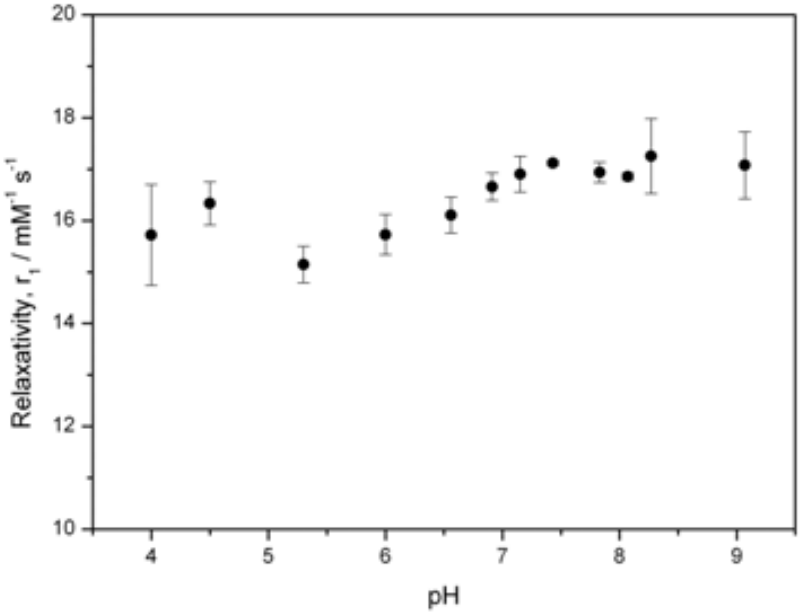

Figure 31. pH dependence of r_1 of **NCAMOF-1** measured at 40 MHz (25ºC). Error bars represent standard deviation of three replicates.

In order to further support that the r_1 observed is only attributed to the **NCAMOF-1**, we performed a full NMRD profile of the sample at pH = 7.4 (**Figure 32**). The same behaviour as in the case of the sample at pH = 4, with the characteristic hump in r_1 at intermediate magnetic fields, confirmed the supramolecular behaviour. This clearly indicates that the r_1 is not due to any leaching of Gd(III) ions as they would not present this r_1 dependence as a function of the magnetic field (no hump would be observed).

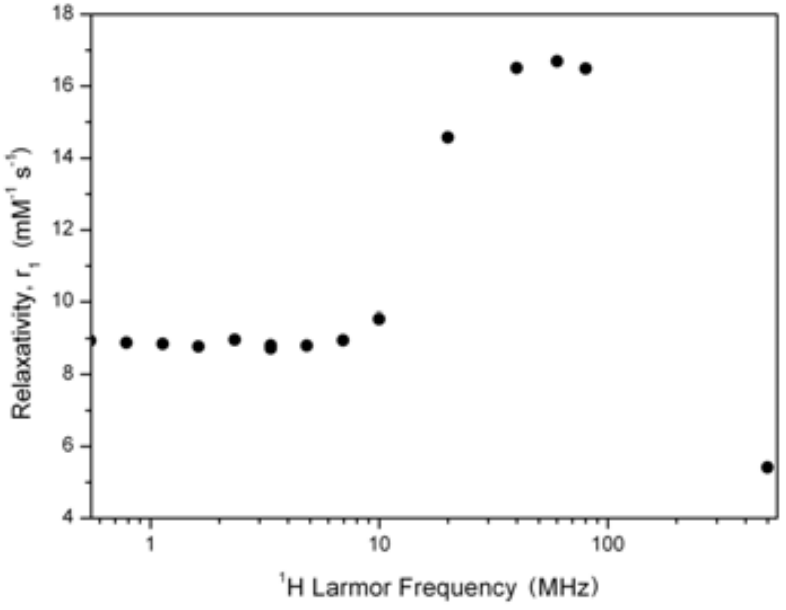

Figure 32. NMRD profile of a suspension of **NCAMOF-1** at pH = 7.4.

In light of the results above explained, we also measured r_1 of a supernatant solution of a sample incubated at pH = 9 at 37 ºC. The NMRD profile showed the typical behaviour of a supramolecular CA with slow molecular tumbling, as evidenced by the hump at intermediate fields (**Figure 33**). This behaviour further rules out the possibility of free Gd(III) ions on the supernatant. The observed higher r_1 compared to **NCAMOF-1** could be attributed to the smaller polymeric species with Gd(III) centers more accessible to water (**Figure 25**).

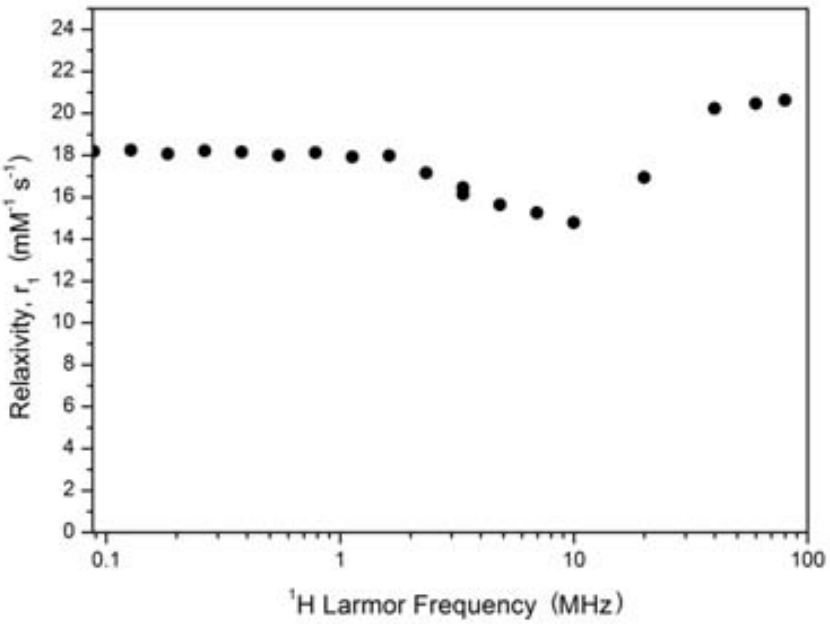

Figure 33. NMRD profile of the supernatant of **NCAMOF-1** incubated at pH = 9.

3.6.3. Relaxivity under physiological conditions

The high stability of **NCAMOF-1** at physiological pH and its lack of toxicity motivated us to evaluate its performance under physiologically more relevant conditions. To this end, r_1 of a colloidal suspension of **NCAMOF-1** in DMEM (prepared in a similar way as it was done for the degradation studies) was monitored over time at a fixed magnetic field of 40 MHz and 25ºC (**Figure 34**). Interestingly, r_1 of around 14 $mM^{-1} \cdot s^{-1}$ was constant up to 24 h of incubation, indicating that no sever structural changes happened. The fact that there was not an increase of r_1 during the incubation time also shows no significant Gd(III) leaching from the structure.

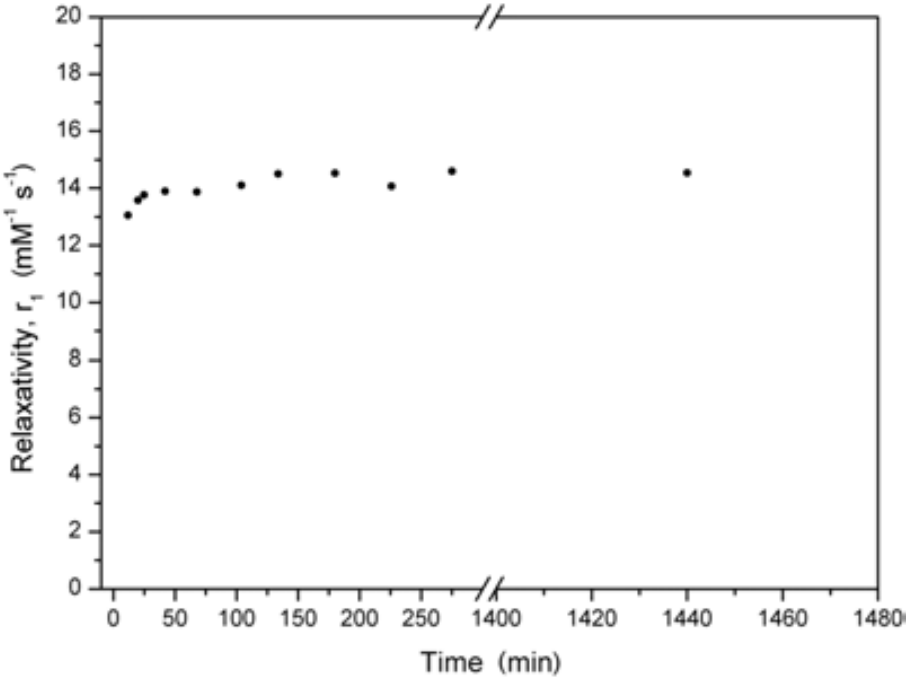

Figure 34. r_1 of a colloidal suspension of **NCAMOF-1** in DMEM over time at 40 MHz and 25ºC.

4. Conclusions

The use of macrocyclic ligands with high chelating capabilities has proven to be a valid strategy to synthesise bimetallic MOFs, which can incorporate metal ions with interest in biomedicine. The synthesis of **CAMOF-1** based on the macrocyclic ligand DOTP and the metal ions Cu(II) and Gd(III) represents the first example of this strategy. Its nanostructuration into 200 nm-in-length wires and its water stability has enabled to study its potential in biomedicine as a CA for MRI. The NMRD profile of **NCAMOF-1** showed the typical behaviour of a nanostructured CA with a maximum in r_1 of 15 $mM^{-1} \cdot s^{-1}$ at 40 MHz, which remains constant over a wide pH range (from pH = 4 to pH = 9) and increases with temperature. Importantly, the r_1 dependence as a function of the magnetic field, the pH and the temperature was studied for the first time in a NMOF structure. In addition, the in depth degradation study revealed that very little amounts of free metal ions are leached from the structure when incubated at different pHs. This has a positive impact on the cytotoxicity of **NCAMOF-1**, which shows a non-toxic behaviour in the two cell lines tested.

5. References

(1) Bromberg, L.; Diao, Y.; Wu, H.; Speakman, S. A.; Hatton, T. A. *Chem. Mater.* **2012**, *24*, 1664.
(2) Damadian, R. *Science* **1971**, *171*, 1151.
(3) Lauterbur, P. C. *Nature* **1973**, *242*, 190.
(4) Damadian, R.; Goldsmith, M.; Minkoff, L. *Physiol. Chem. Phys.* **1977**, *9*, 97.
(5) Ranganathan, R. S.; Raju, N.; Fan, H.; Zhang, X.; Tweedle, M. F.; Desreux, J. F.; Jacques, V. *Inorg. Chem.* **2002**, *41*, 6856.
(6) Hermann, P.; Kotek, J.; Kubicek, V.; Lukes, I. *Dalton Trans.* **2008**, 3027.
(7) Dorazio, S. J.; Morrow, J. R. *Eur. J. Inorg. Chem.* **2012**, *2012*, 2006.
(8) Caravan, P. *Chem. Soc. Rev.* **2006**, *35*, 512.
(9) Werner, E. J.; Datta, A.; Jocher, C. J.; Raymond, K. N. *Angew. Chem. Int. Ed.* **2008**, *47*, 8568.
(10) Caravan, P.; Ellison, J. J.; McMurry, T. J.; Lauffer, R. B. *Chem. Rev.* **1999**, *99*, 2293.
(11) Merbach, A.; Helm, L.; Tóth, É. *The Chemistry of Contrast Agents inMedical Magnetic Resonance Imaging*; second edition ed. Chichester, 2013.
(12) Caravan, P.; Farrar, C. T.; Frullano, L.; Uppal, R. *Contrast Media Mol. I.* **2009**, *4*, 89.
(13) Song, Y.; Xu, X.; MacRenaris, K. W.; Zhang, X.-Q.; Mirkin, C. A.; Meade, T. J. *Angew. Chem. Int. Ed* **2009**, *121*, 9307.
(14) Datta, A.; Hooker, J. M.; Botta, M.; Francis, M. B.; Aime, S.; Raymond, K. N. *J. Am. Chem. Soc.* **2008**, *130*, 2546.
(15) Liepold, L. O.; Abedin, M. J.; Buckhouse, E. D.; Frank, J. A.; Young, M. J.; Douglas, T. *Nano Letters* **2009**, *9*, 4520.
(16) Tse, N. M. K.; Kennedy, D. F.; Kirby, N.; Moffat, B. A.; Muir, B. W.; Caruso, R. A.; Drummond, C. J. *Adv. Healthcare Mater.* **2013**, *2*, 836.
(17) Moghaddam, M. J.; de Campo, L.; Waddington, L. J.; Weerawardena, A.; Kirby, N.; Drummond, C. J. *Soft Matter.* **2011**, *7*, 10994.
(18) Tsotsalas, M.; Busby, M.; Gianolio, E.; Aime, S.; De Cola, L. *Chemi. Mater.* **2008**, *20*, 5888.
(19) Richard, C.; Doan, B.-T.; Beloeil, J.-C.; Bessodes, M.; Toth, E.; Scherman, D. *Nano Letters* **2007**, *8*, 232.
(20) Tóth, É.; Bolskar, R. D.; Borel, A.; González, G.; Helm, L.; Merbach, A. E.; Sitharaman, B.; Wilson, L. J. *J. Am. Chem. Soc.* **2004**, *127*, 799.
(21) Moriggi, L. C.; Cannizzo, C.; Dumas, E.; Mayer, C. d. R.; Ulianov, A.; Helm, L. *J. Am. Chem. Soc.* **2009**, *131*, 10828.
(22) Taylor, K. M. L.; Jin, A.; Lin, W. *Angew. Chem. Int. Ed.* **2008**, *120*, 7836.
(23) Park, J.-A.; Kim, H.-K.; Kim, J.-H.; Jeong, S.-W.; Jung, J.-C.; Lee, G.-H.; Lee, J.; Chang, Y.; Kim, T.-J. *Bioorg. Med. Chem. Lett.* **2010**, *20*, 2287.
(24) Bridot, J.-L.; Faure, A.-C.; Laurent, S.; Rivière, C.; Billotey, C.; Hiba, B.; Janier, M.; Josserand, V.; Coll, J.-L.; Vander Elst, L.; Muller, R.; Roux, S.; Perriat, P.; Tillement, O. *J. Am. Chem. Soc.* **2007**, *129*, 5076.
(25) Hifumi, H.; Yamaoka, S.; Tanimoto, A.; Citterio, D.; Suzuki, K. *J. Am. Chem. Soc.* **2006**, *128*, 15090.
(26) Ju, Q.; Tu, D.; Liu, Y.; Li, R.; Zhu, H.; Chen, J.; Chen, Z.; Huang, M.; Chen, X. *J. Am. Chem. Soc.* **2011**, *134*, 1323.
(27) André, J. P.; Tóth, É.; Fischer, H.; Seelig, A.; Mäcke, H. R.; Merbach, A. E. *Chem. Eur. J.* **1999**, *5*, 2977.
(28) Nicolle, G.; Tóth, É.; Eisenwiener, K.-P.; Mäcke, H.; Merbach, A. *JBIC.* **2002**, *7*, 757.
(29) Accardo, A.; Tesauro, D.; Aloj, L.; Pedone, C.; Morelli, G. *Coord. Chem. Rev.* **2009**, *253*, 2193.
(30) Torres, S.; Martins, J. A.; André, J. P.; Geraldes, C. F. G. C.; Merbach, A. E.; Tóth, É. *Chem. Eur. J.* **2006**, *12*, 940.
(31) Gianolio, E.; Giovenzana, G. B.; Longo, D.; Longo, I.; Menegotto, I.; Aime, S. *Chem. Eur. J.* **2007**, *13*, 5785.
(32) Rieter, W. J.; Taylor, K. M. L.; An, H.; Lin, W.; Lin, W. *J. Am. Chem. Soc.* **2006**, *128*, 9024.
(33) Rowe, M. D.; Thamm, D. H.; Kraft, S. L.; Boyes, S. G. *Biomacromolecules* **2009**, *10*, 983.

(34) Rowe, M. D.; Chang, C.-C.; Thamm, D. H.; Kraft, S. L.; Harmon, J. F.; Vogt, A. P.; Sumerlin, B. S.; Boyes, S. G. *Langmuir* **2009**, *25*, 9487.
(35) Gagnon, K. J.; Perry, H. P.; Clearfield, A. *Chem. Rev.* **2011**, *112*, 1034.
(36) Pereira, G. A.; Peters, J. A.; Almeida Paz, F. A.; Rocha, J. O.; Geraldes, C. F. G. C. *Inorg. Chem.* **2010**, *49*, 2969.
(37) Yang, H.; Santra, S.; Walter, G. A.; Holloway, P. H. *Adv. Mater.* **2006**, *18*, 2890.
(38) Taylor, K. M. L.; Jin, A.; Lin, W. *Angew. Chem. Int. Ed.* **2008**, *47*, 7722.
(39) Nishiyabu, R.; Hashimoto, N.; Cho, T.; Watanabe, K.; Yasunaga, T.; Endo, A.; Kaneko, K.; Niidome, T.; Murata, M.; Adachi, C.; Katayama, Y.; Hashizume, M.; Kimizuka, N. *J. Am. Chem. Soc.* **2009**, *131*, 2151.
(40) Perrier, M.; Kenouche, S.; Long, J.; Thangavel, K.; Larionova, J.; Goze-Bac, C.; Lascialfari, A.; Mariani, M.; Baril, N.; Guérin, C.; Donnadieu, B.; Trifonov, A.; Guari, Y. *Inorg. Chem.* **2013**.
(41) Aime, S.; Botta, M.; Terreno, E.; Anelli, P. L.; Uggeri, F. *Magnet. Reson. Med.* **1993**, *30*, 583.
(42) Sherry, A. D.; Ren, J.; Huskens, J.; Brücher, E.; Tóth, É.; Geraldes, C. F. C. G.; Castro, M. M. C. A.; Cacheris, W. P. *Inorg. Chem.* **1996**, *35*, 4604.
(43) Geraldes, Carlos F. G. C.; Marques, M. Paula M.; Castro, Baltazar d.; Pereira, E. *Eur. J. Inorg. Chem.* **2000**, *2000*, 559.
(44) Kong; Medvedev, D. G.; Clearfield, A. *Inorg. Chem.* **2004**, *43*, 7308.
(45) Vilela, S. M. F.; Ananias, D.; Gomes, A. C.; Valente, A. A.; Carlos, L. D.; Cavaleiro, J. A. S.; Rocha, J.; Tome, J. P. C.; Almeida Paz, F. A. *J. Mater. Chem.* **2012**, *22*, 18354.
(46) Barge, A.; Cravotto, G.; Gianolio, E.; Fedeli, F. *Contrast Media Mol. I.* **2006**, *1*, 184.
(47) Laurent, S.; Elst, L. V.; Muller, R. N. C*ontrast Media Mol. I.* **2006**, *1*, 128.
(48) Guari, Y.; Larionova, J.; Corti, M.; Lascialfari, A.; Marinone, M.; Poletti, G.; Molvinger, K.; Guerin, C. *Dalton Trans.* **2008**, 3658.
(49) Platas-Iglesias, C.; Vander Elst, L.; Zhou, W.; Muller, R. N.; Geraldes, C. F. G. C.; Maschmeyer, T.; Peters, J. A. *Chem. Eur. J.* **2002**, *8*, 5121.

Conclusions

The efforts in this Thesis concentrated on addressing two of the challenges in the miniaturization of Metal-Organic Frameworks at the nanometre length scale (NMOFs): (i) the need of a general, reliable methodology to synthesise them at this length scale; and (ii) the synthesis of new NMOFs that meet the requirements for their use in new emerging fields such as biomedicine.

In the first part of this Thesis, we showed the potential of the Spray-Drying (SD) technique to synthesise NMOFs in the form of hollow superstructures that upon disassembly yield stable colloidal NMOF suspensions. HKUST-1 synthesis was used as the model reaction to identify the main experimental parameters affecting the SD synthesis of NMOFs in terms of yield and crystal size, and to postulate a plausible mechanism. The versatility of the technique enabled us to synthesise a broad spectrum of NMOFs belonging to the most representative MOF subfamilies.

Once the potential of SD in the synthesis of NMOFs and their related superstructures was confirmed, we exploited its capacities to synthesise MOF-based composites by combining NMOFs with other functional materials. We found that the mobility of the different species in the aerosol droplet plays an important role in the synthesis of these MOF-based composites. By controlling this mobility, we prepared two different classes of MOF-based composites. On one side, HKUST-1 hollow superstructures were used to prepare three composites by encapsulating three different species, NaCl crystals, dyes and FeOx inorganic nanoparticles (INPs), in them. On the other side, a second family of composites in which NHKUST-1 crystals were encapsulated inside a polymeric matrix was developed. This variety in compositions has been translated in a wide panel of applications, as demonstrated by the solid phase pollutant removal applications of the FeOx INPs@HKUST-1 composites and the increased water stability exhibited by the HKUST-1@polystyrene composites.

The second axis of this Thesis was focused on the synthesis of new NMOFs that meet the specific requirements for their use as contrast agents (CAs). Here, we developed a novel strategy based on the use of the macrocyclic ligands currently employed in the synthesis of molecular CAs, which possess high chelating capabilities towards Gd(III) ions. The combination of the ligand DOTP and two metal ions, Cu(II) and Gd(III), afforded a first NMOF named as Contrast Agent MOF (**CAMOF**). Importantly, this MOF was miniaturized down to the nanoscale regime (named as **NCAMOF-1**), allowing its study in terms of cytotoxicity, stability and CA properties. From these studies, **NCAMOF-1** showed to be very stable under physiologically simulated conditions and more importantly, it showed a very limited leaching of highly toxic free metal ions under these conditions.

The high stability of the NMOF combined with the reduced amount of free metal ions had a positive impact on its viability, revealing a non-cytotoxic character.

Once the prerequisites demanded by the biomedical field (i. e. lack of cytotoxicity, nanoscale size and stability) were studied, the CA properties of **NCAMOF-1** were evaluated. The impact of the magnetic field, pH and temperature on the relaxivity were studied for the first time in a NMOF. This study showed that **NCAMOF-1** behaves as a supramolecular CA, which enables it to outperform the commercial molecular CAs, exhibiting a relaxivity of 15 $mM^{-1} \cdot s^{-1}$ at 40 MHz. In addition, the relaxometry studies demonstrated that the inner Gd(III) ions in the structure also contribute to the water relaxation mechanism, highlighting the porous structure of **NCAMOF-1**.

Appendix

In the appendix of this PhD Thesis the four publications related to the main objectives of the Thesis are presented.

The first work presented is a comprehensive review of the current methodologies and applications of nanoscale metal-organic materials including both, crystalline Metal-Organic Frameworks (MOFs) and coordination polymers. These review has been reported in the manuscript entitled "Nanoscale metal-organic materials" Chem. Soc. Rev. (2011).

The second publication entails the results described in Chapter 3 and 4. Therefore, the Spray-Drying methodology to produce MOFs at the nanoscale (NMOFs) and their related superstructures is presented. In addition the combination of MOFs and exogenous functional species to create MOF-based composites is also described. This article was entitled "A spray-drying strategy for synthesis of nanoscale metal–organic frameworks and their assembly into hollow superstructures" Nat. Chem. (2013).

In the third work we present a review of the current trends related to MOF superstructutres, covering the synthetic methods and their prospects in terms of future applications. This concepts article was entitled "Metal–Organic Frameworks: From Molecules/Metal Ions to Crystals to Superstructures" Chem. Eur. J. (2014).

Finally, the fourth work is related to the results shown in Chapter 5. The synthesis and the Contrast Agent application of the first example of a new generation of bimetallic NMOFs based on heterocyclic ligands are presented. The article was entitled "Relaxometry Studies of a Highly Stable Nanoscale Metal–Organic Framework Made of Cu(II), Gd(III), and the Macrocyclic DOTP" J. Am. Chem. Soc. (2013).

Chem Soc Rev

Cite this: *Chem. Soc. Rev.*, 2011, **40**, 291–305

www.rsc.org/csr

TUTORIAL REVIEW

Nanoscale metal–organic materials

Arnau Carné, Carlos Carbonell, Inhar Imaz and Daniel Maspoch*

Received 15th July 2010
DOI: 10.1039/c0cs00042f

Metal–organic materials are found to be a fascinating novel class of functional nanomaterials. The limitless combinations between inorganic and organic building blocks enable researchers to synthesize 0- and 1-D metal–organic discrete nanostructures with varied compositions, morphologies and sizes, fabricate 2-D metal–organic thin films and membranes, and even structure them on surfaces at the nanometre length scale. In this *tutorial review*, the synthetic methodologies for preparing these miniaturized materials as well as their potential properties and future applications are discussed. This review wants to offer a panoramic view of this embryonic class of nanoscale materials that will be of interest to a cross-section of researchers working in chemistry, physics, medicine, nanotechnology, materials chemistry, *etc*., in the next years.

Introduction

Miniaturization to the nanometre scale regime is a very prolific strategy for the development of new materials with novel and often enhanced properties compared to traditional materials, opening up avenues for technological and biomedical applications in many areas, including drug-delivery, catalysis, diagnostics, solar cells, *etc*. To date, most nanoscale materials are either purely organic or inorganic in composition. However, architectures created from the supramolecular assembly of organic and inorganic components are rapidly growing as a very attractive alternative class of nanoscale materials.

Centre d'Investigació en Nanociencia i Nanotecnologia (CIN2, ICN-CSIC), Esfera UAB, 08193 Bellaterra, Spain. E-mail: daniel.maspoch.icn@uab.es; Fax: +34 93 581 4747

But, *why do we need another class of nanoscale materials?* Traditional metal–organic materials are a fascinating family of solids created from the supramolecular association of inorganic, such as metal ions and metal–organic or inorganic clusters, and organic building blocks, including organic molecules, biomolecules and organic polymers.[1] These bulk materials, in which both types of building blocks are assembled through metal coordination, hydrogen bonding, electrostatic interactions or π–π stacking, have the potential to be tailored to show adjustable structures, compositions and properties. As a consequence, they show promise for an impressive number of applications in gas storage, drug-delivery, diagnostics, sensing, catalysis, ion exchange or separation, magnetism, optics, *etc*. However, metal–organic materials in the form of traditional bulk crystalline materials do not always fulfill all specific needs for these applications. Depending upon

Arnau Carné

Arnau Carné Sánchez was born in Manresa (Catalonia, Spain) in 1985. He received his BSc degree in Chemistry at Universitat de Barcelona (UAB) in 2008. In 2009, he got his MSc in Environmental Diagnostics and Management from Cranfield University (UK). He is currently pursuing a PhD in Chemistry at the CIN2 (ICN-CSIC) under the supervision of Dr Daniel Maspoch and Dr Inhar Imaz in the field of metal–organic nanomaterials with special interest in developing new synthetic methodologies.

Carlos Carbonell

Carlos Carbonell (Barcelona, Spain, 1975) studied Technical Chemist Engineering (2002), Materials Engineering (2004) and obtained his MSc in Nanotechnology (2008) at the Universitat Autònoma de Barcelona. After working for 7 years at the industry, he started his PhD in 2009 at the CIN2 (ICN-CSIC) under the supervision of Dr Daniel Maspoch, leader of the Supramolecular Nanochemistry & Materials Group. His current field of interest includes the synthesis and patterning of metal–organic materials assisted by soft nanolithographic techniques, such as Dip-Pen Nanolithography.

the intended application, these materials require to be not only fabricated as bulk crystalline solids, but also miniaturized at the nanometre length scale and immobilized at specific locations on surfaces.

For example, nanoscopic dimensions are typically required to provide materials of sufficiently small sizes for their internalization into cells, and this limits the applications of metal–organic materials as delivery vehicles, diagnostics, *etc*. But nanoscale metal–organic materials combine these small dimensions with the possibility to design architectures with well-defined and uniform sizes and morphologies, to disperse them in aqueous media or other solvents, and to efficiently coat them for improving their biocompatibility or recognition capabilities. Of particular interest is also the fact that nanomaterials have higher surface areas than their macroscopic counterparts. This property can strongly influence or even improve the catalytic, ion exchange, separation, sensing and sorption properties of these metal–organic materials, which, in turn, can be dependent on their sizes and shapes. A similar situation occurs with some physical properties. It is well known that unique physical properties emerge when at least one dimension of a material is reduced to the nanometre scale. Thus, nanoscale metal–organic materials are also expected to hold highly desirable size-dependent optical, electrical and magnetic properties.

It is obvious, then, that by scaling them down to the nanometre length scale, the scope of metal–organic materials will be expanded. But, *how they can be prepared at the nanometre length scale*? Like their macroscopic counterparts, they can be basically prepared by using "bottom-up" synthetic methodologies based on self-assembly processes; however, assembly of both inorganic and organic building blocks needs now to be controlled at the nanometre scale. For this, there are two major strategies. One involves a set of synthetic methodologies that induce the controlled precipitation of self-assembled supramolecular metal–organic polymers once they are formed. To date, these methodologies include the use of poor solvents, microwaves, ultrasounds or thermal conditions. The second strategy consists of confining the supramolecular assembly at specific locations. For example, self-assembly processes can be confined into droplets by using micro- or nanoemulsion techniques. Or they can be precisely controlled on the surface of substrates, liquids, membranes or other nanostructures, which act as templates, by using deposition techniques, such as layer-by-layer (LbL) synthesis, Langmuir–Blodgett, *etc*. A specific case that fits in this second strategy is the use of techniques for their nanostructuration on surfaces. In fact, the growth and positioning control on surfaces of these materials is crucial to start to conceive their integration on supports for the fabrication of complex surface sensors, separation membranes, drug-delivery platforms and catalysts.

The miniaturization of metal–organic materials down to the nanometre length scale is therefore a unique opportunity to develop a new class of highly tailorable nanoscale materials that combine the rich diversity of compositions, structures and properties of classical metal–organic materials with the obvious advantages of nanomaterials. Note that we use the term metal–organic material here to include materials with extended metal–organic structures, crystalline or not, that are built up from the supramolecular assembly of inorganic (metal ions and metal–organic or inorganic clusters) and organic building blocks (organic ligands, polymers, and biomolecules). And the term nanoscale includes these materials with at least one dimension between 1 and 100 nm, although some representative examples with sizes comprised between 100 and 1000 nm have also been included due to their size-dependent characteristics and properties. Therefore, these nanoscale materials have been classified according to their dimensionality: 0-D (particles), 1-D (fibers, tubes, and rods), and 2-D (thin films and membranes). In this review, we describe the recent advances made on the synthesis, growth and nanostructuration of this class of materials, their potential properties and applications, and illustrate their future expectations.

Inhar Imaz

Inhar Imaz was born in Hendaia (Basque Country, France) in 1978. He received his PhD in Materials Science from the Université Bordeaux I in 2005, where he studied the formation of heterometallic metal–organic architectures from tetrahedral building blocks. He joined the CIN-2 (ICN-CSIC) centre in 2005 as a Postdoctoral fellow. At present, he is an associate professor under the "Ramón y Cajal" program at the Institut Català de Nanotecnologia. His research is focused on the design, the synthesis and the study of novel nanostructured metal–organic materials. He is exploring new synthetic methodologies, new properties and new applications of supramolecular nanomaterials.

Daniel Maspoch

Daniel Maspoch was born in L'Escala (Catalonia, Spain) in 1976. He received his BSc degree in Chemistry from Universitat de Girona, and he earned his PhD in Materials Science at the Universitat Autònoma de Barcelona and at the Institut de Ciencia de Materials de Barcelona. After postdoctoral work in Prof. Chad A. Mirkin's group at Northwestern University, he moved to the Centre d'Investigació en Nanociència i Nanotecnologia (ICN-CSIC), thanks to the Ramón y Cajal Program financial support. His group is working on controlling the supramolecular assembly of (bio)molecules, metal ions and nanoscale building blocks at the nanometre scale.

0- and 1-D metal–organic nanomaterials

Synthesis

There are two major strategies for synthesizing 0-D and 1-D nanoscale metal–organic materials (Fig. 1): (i) confinement of the supramolecular assembly at nanoscopic locations by using emulsions or templates; and (ii) the controlled precipitation of self-assembled metal–organic polymers once they are formed, thanks to the use of poor solvents, microwave radiation, ultrasounds or temperature.

Nanoemulsion is a suspension of small droplets, usually stabilized by a surfactant, with diameters ranging from 50 to 1000 nm, of one liquid in a second liquid in which the first will not mix. Because of these dimensions, these droplets can be used as "nanoreactors" to confine the self-assembly, nucleation and growth of metal–organic nanostructures. Briefly, this approach usually consists of first dissolving each precursor in the solvent that will be dispersed. A water-in-oil, or reverse, emulsion is then prepared from a surfactant, and the collisions between droplets containing those precursors or the application of an external stimulus, such as temperature, light or microwave radiation, spontaneously induce their polymerization, thus delimiting their growth inside the nanodroplet. For example, by dissolving Prussian blue precursors in water, using this solution to create a water-in-oil emulsion and further exposing this emulsion to daylight, Mann *et al.* synthesized the first examples of nanoscale metal–organic frameworks (NMOFs): Prussian blue cubic nanocrystals.[2] Since then, emulsions have been successfully used to produce nanocrystals of heterometallic cyanometalates, Prussian Blue analogues using triazole instead of cyano groups and Gd(III)-based MOFs.

Besides the utility of their internal volume as "nanoreactors", nanodroplets of these emulsions have also the potential to be used as templates to prepare metal–organic nanoshells. In this case, the polymerization must be concentrated on the interface of the droplets by using, for example, a chemical affinity surfactant. Thus far, this strategy has been used by Wang *et al.*, who synthesized the first examples of Prussian blue nanoshells.[3] These shells were synthesized by preparing an oil-in-water emulsion with an organometallic surfactant terminated with pentacyano(4-(dimethylamino)-pyridine)ferrate. Then, the addition of Fe(III) ions to the aqueous solution induced the coordinative polymerization between them and the surfactant, thereby creating a metal–organic shell on the interface of each droplet.

Nanomaterials are also excellent candidates to be used as templates for fabricating metal–organic nanostructures. In this methodology, a film of a supramolecular metal–organic polymer is deposited on the template by using a deposition technique, such as LbL deposition. This deposition, followed by the removal of this template using thermal or chemical techniques, can leave behind a metal–organic nanostructure that mimics the shape and size of this template. Martin *et al.* reported a brilliant example that illustrates how powerful can this approach be.[4] The LbL growth of a film composed of Zr(IV) metal ions and diorganophosphonate ligands on the pores of an alumina membrane, followed by the removal of this membrane using phosphoric acid, allowed the fabrication of highly uniform metal–organic nanotubes.

A second family of methodologies that enable the synthesis of 0-D and 1-D metal–organic nanostructures is based on mixing the precursors under certain reaction conditions that favor the fast nucleation (to increase the seed number)

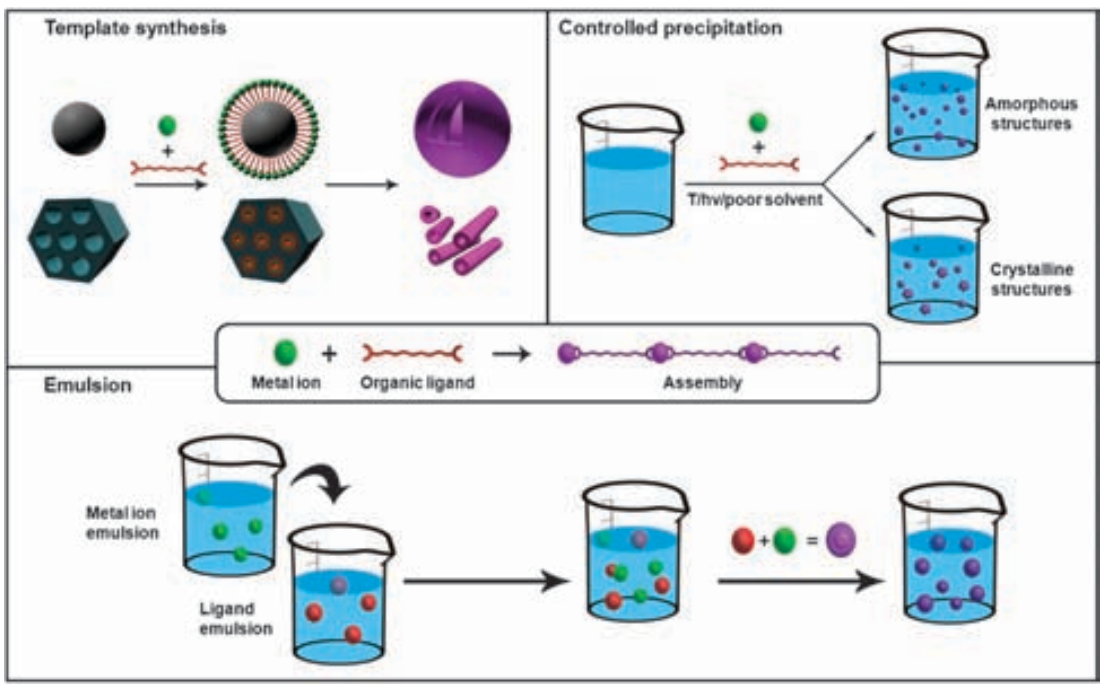

Fig. 1 Schematic representation of the principal synthetic strategies used for synthesizing 0- and 1-D metal–organic nanostructures using conventional coordination chemistry, including the LbL growth on templates, the controlled precipitation of metal–organic nanostructures and the microemulsion techniques.

of self-assembled metal–organic polymers. In most of the cases, these conditions involve the use of microwave radiation, ultrasounds or temperature. For example, it is well known that at high temperatures, solubility of precursors increases avoiding fast precipitation, and allows crystallization to occur. It is therefore a strategy generally used to produce bulk crystalline metal–organic materials. However, if one controls certain reaction conditions, including solvent, surfactant, temperature and time, solvothermal synthesis can be a very productive strategy for synthesizing a wide variety of NMOFs. Some of them were recently reported by Horcajada, Gref *et al.*, who synthesized a series of NMOFs by simply mixing Fe(III) metal ions with a series of multitopic ligands, such as 1,4-benzenedicarboxylate (BDC), benzene-1,3,5-tricarboxylate (BTC), fumaric acid, *etc.*, in a variety of solvents at temperatures usually above 100 °C.[5]

The use of microwave radiation and ultrasounds can also be exploited for miniaturizing MOFs. Ni and Masel reported for the first time the use of microwave radiation to induce the precipitation of an already known MOF (IRMOF-1, 2 and 3) based on Zn(II) metal ions and BDC ligands at the nanometre scale.[6] This reaction consists of exposing a diethylformamide (DEF) solution of both building blocks at 150 W for only 25 seconds. Similarly, sonochemical synthesis can lead to a homogenous nucleation and a substantial reduction in crystallization time. The well-known MOF-5 was miniaturized at the micrometre scale using this methodology.[7] And even more recently, nanoscale arrowheads NMOFs of Prussian blue analogues have been prepared by Wu *et al.* with the help of ultrasonic radiation.[8]

However, one of the most extensive approaches used so far for preparing metal–organic nanostructures is based on the use of poor solvents to induce the fast precipitation of metal–organic polymers. This strategy can be divided into two well-established synthetic methodologies: (i) self-assembly takes place in a solution in which the synthesized metal–organic polymers are not soluble, and therefore, the poor solvent is the initial solution used to mix the building blocks; and (ii) the use of an external poor solvent to precipitate the metal–organic polymers previously synthesized in the initial solution, and therefore, the poor solvent is an external one. Wang *et al.* and Oh and Mirkin simultaneously developed both synthetic methodologies.[9,10] The first authors exploited the insolubility of a coordination polymer built up from Pt(IV) metal ions and *p*-phenylenediamine in water to produce monodisperse spherical particles.[9] On the other hand, Oh and Mirkin first prepared a coordination polymer constructed from Zn(II), Cu(II) or Ni(II) metal ions and a carboxylate-functionalized binaphthyl bis-metallotridentate Schiff base (BMSB) in pyridine, and this polymer was then precipitated in the form of amorphous spherical infinite coordination particles (ICPs) by addition of a poor solvent, such as ether or pentane.[10] The versatility of this method has been proven by preparing a wide range of spherical amorphous ICPs, multi-shaped NMOFs and even nanoscale fibers.

Shapes and sizes

Even though we are in the early stages of their development,[11,12] the abovementioned synthetic methodologies have already facilitated the preparation of several metal–organic nanostructures, ranging from 0-D amorphous ICPs and crystalline NMOFs (with multiple shapes) to 1-D rod-like crystals, fibers and tubes (Fig. 2). In most of the cases, their preparation has allowed researchers to continuously improve these synthetic methodologies, thus starting to understand some of the reaction conditions that one needs to modify in order to control their

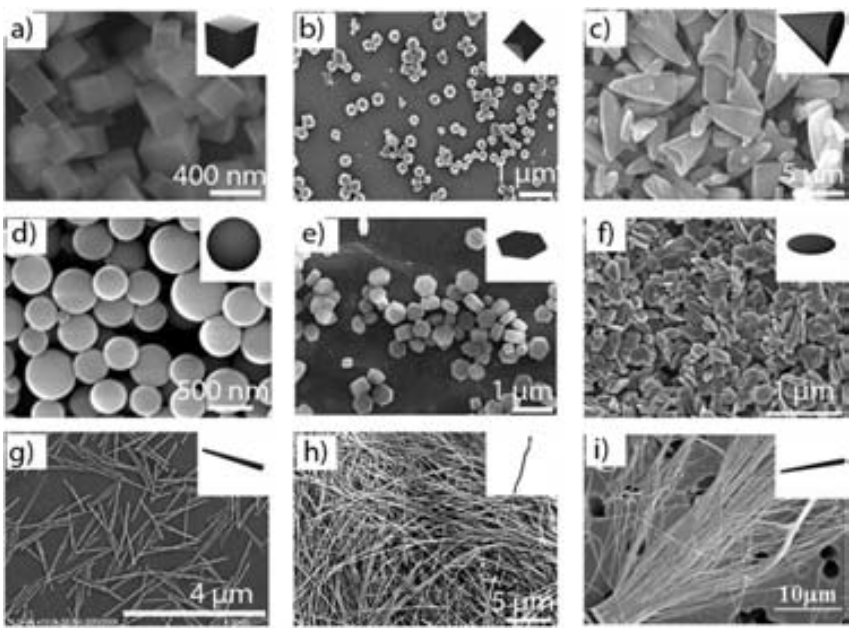

Fig. 2 Representative SEM images and their corresponding schematic figures of 0- and 1-D metal–organic nanostructures showing the wide diversity of morphologies obtained so far: (a) cubic particles, (b) octahedral particles, (c) arrow-like particles, (d) spheres, (e) hexagonal lumps, (f) plate-like particles, (g) rods, (h) fibers, and (i) tubes. (© The American Chemical Society, Springer and Wiley Interscience, reprinted with permission).

shapes and sizes. To date, the choice of the synthetic strategy as well as the corresponding reaction conditions seems crucial to prepare a certain type of nanostructure with precise control over its shape and size.

This is the case of amorphous spherical ICPs that have exclusively been prepared by using methods based on fast precipitation induced by poor solvents. This strategy provides further control on the size of the colloidal spheres through modifications in the reaction conditions. There are three known parameters that can be tuned in order to control their diameter. The first one is the characteristics of the poor solvent, such as the polarity. Oh and Mirkin reported that, under identical reaction conditions, the use of pentane as the poor solvent leads to Zn(II)–BMSB spherical ICPs with larger diameters (780 ± 230 nm) than the ones obtained using more polar diethyl ether (190 ± 60 nm).[10] The second parameter is the rate of addition of the poor solvent. Generally, larger spheres are obtained by decreasing the addition speed of the poor solvent in the reaction mixture. Finally, the third condition is the concentration of the reactants, which is inversely related to the diameter of the spheres. Maspoch *et al.* demonstrated that the diameter of ICPs built up from the connection of Zn(II) metal ions through bis(imidazole-1-ylmethyl)benzene (Bix) ligands was controlled from 130 ± 14 nm to 1050 ± 83 nm by decreasing the concentration of both Zn(II) metal ions and Bix components from 1×10^{-1} M to 5×10^{-3} M.[13]

Crystalline NMOFs are generally synthesized by using emulsions, solvothermal and sonochemical synthesis, poor solvents and microwave-assisted synthesis. In most of these strategies, the size and shape of the resulting NMOFs are closely dependent on the type of solvent, the nature, concentration and stoichiometry of the precursors, and the specific reaction conditions used in each one of these methodologies, such as the applied temperature in solvothermal synthesis, the microwave radiation intensity in microwave-assisted synthesis, *etc.*

There are several examples where the solvent has an effect on the shape and size of NMOFs. Jung and Oh found that cubic NMOFs built up from Zn(II) metal ions and metallosalen (MS) ligands were prepared with different sizes by performing identical solvothermal reactions under different DMSO/DMF mixtures.[14] Here, DMSO/DMF mixtures in proportions 1 : 1, 1 : 2, and 2 : 1 led to cubes with an average size of 308 ± 36 nm, 600 ± 94 nm, and 4860 ± 780 nm, respectively. The synthesis of NMOFs is also dependent on the nature, concentration and stoichiometry of the reactants. For example, Ni and Masel reported how the dimensions of cubic Zn(II)–BDC NMOFs prepared through microwave-assisted synthesis are reduced by decreasing the concentration of either Zn(II) metal ions or BDC ligands.[6]

Of special interest are the specific conditions, such as the temperature, the microwave radiation and the surfactant, used on these synthetic methodologies because they are excellent parameters to control for tailoring NMOFs. Among them, nanoemulsions are interesting because it is possible to tailor their droplet sizes, and therefore, the NMOFs sizes by controlling the composition of these emulsions, such as the relative composition of the surfactant, the oil phase and the aqueous phase. Lin *et al.* took advantage of this to prove that the dimensions (both diameter and length) of Gd(III)–BDC nanorods can be tailored by simply changing the water to surfactant molar ratio.[15] In solvothermal synthesis, the reaction temperature can also affect the dimensions of the produced NMOFs. This dependence was confirmed by Jung and Oh, who reported that smaller cubic Zn(II)–MS NMOFs are generated at lower reaction temperatures.[14] While cubes with dimensions of 166 ± 15 nm were obtained at 80 °C, an increase of the temperature up to 120 °C afforded bigger cubes with dimensions of 308 ± 36 nm.

The use of surfactants in methods based on fast precipitation is a further factor to be considered because they can play a critical role not only to control the morphology of NMOFs but also to increase their stability, avoiding agglomeration. For example, Thallapally *et al.* have recently highlighted the importance of using poly(diallyldimethylammonium chloride) as the surfactant to prepare hexagonally-shaped NMOFs built up from the connection of Zn(II) metal ions through imidazolate ligands.[16] The use of other surfactants did not result in the formation of these NMOFs. However, surfactants are not the only type of substances that can help researchers to control the NMOFs shape. Like in purely inorganic nanomaterials, organic ligands also show promise for acting as blocking agents, which can control the growth rate of NMOFs in certain directions. Oh *et al.* enormously contributed to prove this concept.[17] These authors reported that hexagonal rod-like In(III)–BDC NMOFs synthesized by solvothermal synthesis can be tuned to hexagonal lumps or disks by simply adding certain amounts of pyridine to the reaction solution.

Besides the formation of ICPs and NMOFs, there are other attractive nanoscale 1-D metal–organic materials: nanofibers and nanotubes.[18] To date, most of the metal–organic nanofibers have been prepared by using fast precipitation methods. Maspoch *et al.* reported the fabrication of chiral nanofibers by adding a solution of aspartate (Asp) ligands into a solution of Cu(II) metal ions.[19] Here, the length of these fibers was controlled by adjusting the addition rate of Asp solution, which is again inversely related to the length of the nanofibers produced. A mixture of both solutions by using a very slow diffusion led to very long (up to one centimetre) nanofibers, whereas a fast mixture decreased this length up to tens of micrometres. Nanotubes are also a very attractive type of nanoscale materials, but only one example made up from metal ions and organic ligands has been reported so far. As stated above, Martin *et al.* utilized alumina membranes as templates for synthesizing Zn(IV)–phosphonate nanotubes through a LbL synthesis.[4] This is a very versatile synthetic methodology, and it will certainly allow the preparation of more metal–organic nanotubes in the near future, opening the door to control their outside diameter and length by selecting the diameter of the pores and the thickness of the alumina membrane, respectively, whereas the pore size and the wall thickness can be controlled by the number of inorganic/organic layers deposited on the pore wall of the template.

Hierarchical metal–organic superstructures

Like pure inorganic nanomaterials, the research on metal–organic nanostructures has recently started to be extended to

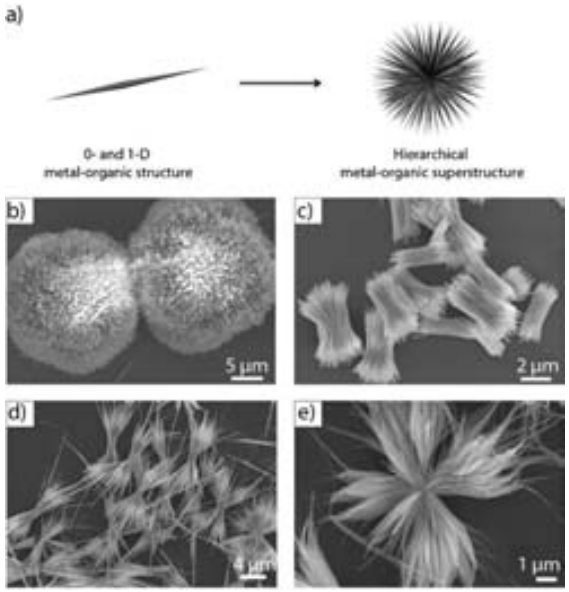

Fig. 3 (a) Scheme illustrating the formation of hierarchical metal–organic superstructures. (b–e) SEM images of representative hierarchical metal–organic structures: (b) urchin-like, (c) bundle-like, (d) sheaf-like, and (e) flower-like superstructures. (© The American Chemical Society and The Royal Society of Chemistry, reprinted with permission).

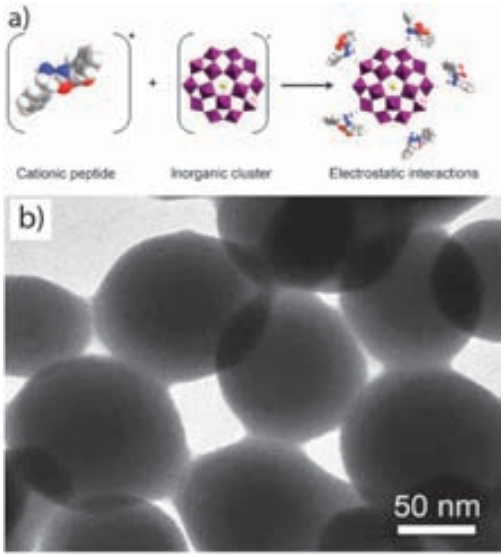

Fig. 4 (a) Scheme illustrating the formation of nanospheres through the supramolecular assembly (electrostatic interactions) between a cationic peptide and an anionic inorganic cluster. (b) SEM image of these spheres (© Wiley Interscience, reprinted with permission).

the assembly of ICPs or NMOFs into ordered hierarchical superstructures that are able to exhibit a rich range of complex architectures (Fig. 3a). For example, Zhang *et al.* demonstrated the formation of sheaf-, flower-, wheatear-, straw-, bundle-, urchin- and butterfly-like hierarchical architectures from connecting Eu(III), Tb(III) or Ce(III) metal ions through BTC ligands under simple fast precipitation methods (Fig. 3).[20] Among other functionalities, hierarchical superstructures can combine micro- and mesoporosity, thus having important prospects in industrial processes, such as catalysis, absorption, *etc.* Qiu *et al.* reported a versatile methodology based on the use of micelles as supramolecular templates for synthesizing hierarchically MOFs based on Cu(II) metal ions linked by BTC ligands.[21] One of the most important features of these materials is that they exhibit micro- and mesoporous structures with tunable adsorption capabilities.

Metal–organic nanostructures constructed from supramolecular non-coordination bonds

The diversity of 0-D and 1-D metal–organic nanostructures can be further expanded by using electrostatic interactions, hydrogen bonds, π–π stacking and van der Waals interactions as the main driving forces for the assembly of the organic and inorganic building blocks. The synthetic methodologies are not so different from those explained above. For example, hybrid spheres of about 150 nm in diameter were assembled from electrostatic interactions between cationic dipeptides and anionic polyoxometalate (POM) clusters by simply mixing both building blocks in the appropriate solvent (Fig. 4).[22] The fact that these interactions are weak makes these spheres to be easily disassembled by applying an external stimulus, such as pH (charge neutralization) and temperature. Thus, the sensitivity of electronic interactions to external stimuli could be of interest when thinking of controlled release of guest molecules or any other systems that require triggered disassembly. Based on the same approach, anionic POM clusters were electrostatically assembled with the cationic surfactant dimethyldioctadecylammonium bromide to yield nanostructures with different morphologies depending on the solvents used.[23]

It is known that polyion-neutral diblock copolymers self-assemble into nanoparticles when mixed with an oppositely charged polyelectrolyte in what can be termed complex coacervate core micelles. Particles thus synthesized are stabilized due to the electroneutral segments of the diblock polymer. Stuart *et al.* followed this approach to assemble a cationic organic polymer with a pre-synthesized coordination polymer with negative charge in its coordination center into nanospheres of about 50 nm in diameter.[24] Therefore, a reversible system such as a coordination polymer replaces a conventional polyelectrolyte conferring to the final system more versatility and sensitivity to external stimuli.

Another class of materials held entirely by non-coordination supramolecular interactions is those based on Pt–Pt interactions. It was found that square planar Pt^{II} self-assembles into 1-D structures through $Pt^{II}\cdots Pt^{II}$ interactions.[25]

Properties and applications

A wide range of promising properties can be obtained by taking advantage of the multiple inorganic and organic building blocks that can be combined to prepare nanoscale metal–organic materials. One can use the intrinsic properties of either the organic or inorganic components. The ability of metal ions to interact with phonons and electrons, to show luminescence and strong absorptions and to have interesting magneto-optical properties makes metal–organic materials suitable as functional materials in devices. The organic

components can also exhibit their own functionalities. For example, organic chromophores, radicals or biomolecules are excellent building units to prepare optical, magnetic and biocompatible nanoscale materials. New properties also arise from the polymerization of both building blocks. This is the case of the tailorable porous structures constructed from the linkage of inorganic building units through multitopic organic ligands. All these properties can take advantage of the benefits of working at the nanometre length scale, thus opening novel avenues for developing nanomaterials with astonishing properties and applications. Some of these can help to develop novel drug delivery systems, encapsulating matrices, contrast agents, porous catalytic materials, gas storage materials, magnetic and optical nanomaterials, gels, *etc*. Recent great advances have been made towards these directions.

Drug delivery systems. The development of nanoscale drug delivery metal–organic systems has been tackled by incorporating those drugs using different strategies: (i) drugs are one of the building blocks of the metal–organic structure; (ii) drugs are encapsulated inside a metal–organic matrix; and (iii) drugs are adsorbed in porous NMOFs. The three approaches have been recently tested. Lin *et al*. used the precipitation approach induced by a poor solvent to synthesize nanospheres built up from the coordination of a Pt(IV) based anticancer drug and Tb(III) metal ions (Fig. 5a–c).[26] The same authors also proved the postsynthetic covalent attachment of drugs in porous NMOFs built up from Fe(III) metal ions and 2-aminoterephthalic acid.[27] The free amino groups on the porous NMOFs were used to covalently interact with an ethoxysuccinato-cisplatin pro-drug activated with 1,1-carbonyldiimidazole. For the second strategy, Maspoch *et al*. proved that ICPs composed of Zn(II) metal ions linked by Bix ligands possess the ability to encapsulate a wide range of active species, including drugs such as doxorubicin (DOX), SN-38, camptothecin and daunomycin, within their amorphous matrix.[28] Horcajada, Gref *et al*. have recently developed the last strategy.[5] These authors used synthesized porous NMOFs composed of Fe(III) metal ions and different dicarboxylate ligands (*e.g*. BDC or BTC) to load a wide variety of antitumoral drugs, such as DOX, busulfan, cidofovir and azidothymidine triphosphate. The loading was achieved by soaking these porous NMOFs in saturated drug solutions. Interestingly, in all these cases, the successful design of the drug delivery system was confirmed by proving the controlled and progressive release of the encapsulated drug as well as their *in vitro* anticancer efficacies; thus opening the way to start considering the use of metal–organic nanostructures as novel drug delivery systems.

Encapsulating matrices. Amorphous metal–organic spheres can *in situ* encapsulate active species by previously incorporating them in the precursor solution (Fig. 5d–f). Since this discovery,[13] the classes of amorphous spheres that can be used as capsules have been extended. Kimizuka *et al*. fabricated ICPs able to encapsulate fluorescent dyes, metal nanoparticles and proteins.[29] In this case, the coordination polymer was created by connecting Gd(III) metal ions through adenosine 5′-monophosphate nucleotide. Encapsulation properties are not restricted to ICPs, and recently, electrostatic spheres composed of peptides and POMs have been used to encapsulate organic dyes.[22]

Contrast agents. Nanoscale metal–organic materials are excellent candidates to act as contrast agents because they

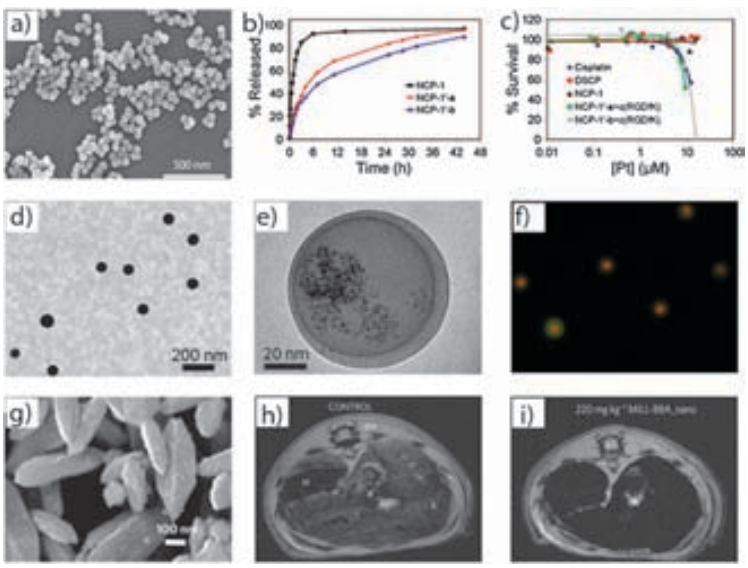

Fig. 5 Representative applications for the nanoscale supramolecular 0- and 1-D metal–organic structures. (a–c) Drug delivery systems. (a) Metal–organic nanospheres built up from the coordination of a Pt(IV) based anticancer drug and Tb(III) metal ions. (b) Drug release profile obtained by plotting %Pt released against time and (c) its *in vitro* cytotoxicity assay curves for HT-29 cells obtained by plotting the %cell viability against the Pt concentration of various samples. (d–f) Encapsulating systems. (d) TEM image of amorphous metal–organic ZnBix spheres. (e) TEM image of magnetic iron oxide nanoparticles encapsulated into ZnBix spheres. (f) Fluorescence optical image of fluorescein and quantum dots encapsulated into ZnBix spheres. (g–i) Contrast agents. (g) SEM image of metal–organic nanoparticles of $[FeO(H_2O)_2Cl(fumarate)_3]$ (MIL-88A). (h) Magnetic resonance images of control rats and (i) rats injected with 220 mg kg^{-1} of MIL-88A nanoparticles (© Wiley Interscience, The American Chemical Society and The Nature Publishing Group, reprinted with permission).

can be composed of highly paramagnetic metals ions, such as Gd(III) and Mn(II), and their small sizes allow different biodistribution and opportunities beyond the conventional imaging of chemical agents. Lin *et al.* have enormously contributed to demonstrate the efficiency of NMOFs to modify the relaxation times of the water protons in the surrounding medium when a magnetic field is applied. In such a context, Gd(III) based nanorods have shown exceptionally high longitudinal $R1$ and transverse $R2$ relaxivities of 35.8 s^{-1} and 55.6 s^{-1} per mM of Gd(III),[15] whereas nanoparticles built up from Gd(III) metal ions connected through benzene-hexacarboxylate ligands have an impressive $R2$ relaxivity of 122.6 s^{-1} per mM of Gd(III).[30] More recently, Horcajada, Gref *et al.* contributed to this field by synthesizing a NMOF built up from Fe(III) metal ions connected through fumarate ligands that shows a $R1$ relaxivity of 50 s^{-1} per mM of Fe(III), which can be considered as sufficient for *in vivo* use (Fig. 5g–i).[5]

Catalytic properties. Self-assembly of catalytic active metals into nanoparticles is a promising route towards a more efficient *heterogeneous catalysis* due to the possibility to increase the concentration of active sites. Sweigart *et al.* used the precipitation approach to assemble Rh based metal–organic catalysts and Al(III) metal ions into nanospheres.[31] Their nanostructuration increased the concentration of catalytic active sites, enhancing the stereoselective polymerization of phenylacetylene. In addition, the catalytic performance of these metal–organic nanocatalysts was dependent on their size. As expected, smaller spheres were more active than the bigger ones.

Gas sorption properties. Materials with a high capacity of gas sorption are gaining interest due to the need to store and handle new environmentally friendly fuels or remove green house gases. Because of the excellent properties exhibited by bulk porous MOFs, their nanoscopic counterparts are expected to exhibit interesting, novel and even improved gas sorption properties. This is the case of a NMOF built up from Zn(II) metal ions connected through isophthalate and 4,4′-bipyridyl ligands.[32] These porous nanocrystals reported by Groll *et al.* showed adsorption capacities almost identical to their bulk counterparts, but the shapes of the sorption isotherms differed significantly and the adsorption kinetics increased dramatically. The CO_2 and H_2 sorption properties of nanoscale metal–organic structures have also started to be investigated. Oh *et al.* successfully synthesized NMOFs based on In(III) metal ions and BDC ligands that showed a H_2 and CO_2 uptake of 140 $cm^3\ g^{-1}$ and 333 $cm^3\ g^{-1}$, respectively.[17] And Thallapally *et al.* have recently described a reversible uptake and release of CO_2 in an imidazolate NMOF with 35% of weight capacity at 30 bar.[16]

Optical properties. Luminescent coordination 5 nm-in-diameter nanoparticles were prepared by Mallah *et al.* by controlling the growth of the already known coordination polymer based on Tb(III) or Eu(III) metal ions and BDC ligands with poly(vinyl pyrrolidone).[33] Among them, the Eu(III)-based nanoparticles showed an intense red emission, remaining stable for at least 20 hours. The fact that the size of these particles did not exceed 10 nm together with their water dispersibility makes them interesting for biological applications. A different approach was followed by Loh *et al.* to prepare optically active nanofibers.[34] Two chromophores with good overlap between their respective emission and absorption bands were self-assembled into a 1-D nanostructured metal–organic polymer giving rise to a light harvesting antenna that transforms UV radiation into red radiation. Interestingly, the harvesting effect was only observed in the self-assembled system. This comes to prove that if the right building blocks are assembled into nanostructured metal–organic polymers, it is possible then to achieve interactions between functional molecules that otherwise would be impossible.

Magnetic properties. The family of Prussian blue nanoparticles has shown fascinating superparamagnetic properties.[35] In addition to these properties, spin crossover materials are perhaps the most attractive materials because thermal hysteresis takes place at room temperature in most of the cases. These materials undergo changes in their spin configuration from low spin to high spin due to external stimuli, such as temperature or light radiation. This usually implies a change in the magnetic properties, and therefore, it is of great interest for electronic devices, switches and memory devices. Coronado *et al.* made the first step to demonstrate that 10 nm-in-diameter coordination nanoparticles with the formula $[Fe(Htrz)_2(trz)(BF_4)]$ (where trz is a triazole derivative) retain their spin crossover properties.[36] Soon after, Ruiz-Molina *et al.* further proved that spherical ICPs can possess bistable spin crossover properties by polymerizing the electroactive complex with the general formula [Co (3,5-dbsq)(3,5-dbcat)(N–N)] (where 3,5-dbsq and 3,5-dbcat are, respectively, the semiquinonate radical and catecholate forms of 3,5-di-*tert*-butyl-1,2-benzoquinone) with the bitopic linker Bix.[37] More recently, interesting spin crossover properties have also been seen in NMOFs with the formula $[Fe(pz)Pt(CN)_4]$ (where pz is pyrazine) prepared by Gaspar, Real *et al.*[38]

Sensors. It is well known that the supramolecular interaction of external species in the structures of metal–organic materials can induce changes in their physical properties. This ability, together with the high surface areas that can be functionalized to recognize specific substances and the porous structures that can selectively adsorb species provide excellent characteristics to metal–organic structures for being used as novel sensors at the nanometre length scale. Thus far, however, not many sensors based on these structures have been reported. Oh and Mirkin demonstrated the ion-exchange capabilities of fluorescent Zn(II) based ICPs.[39] After exposing these spheres to Cu(II) metal ions, the cation-exchange reaction between Cu(II) and Zn(II) metal ions induced the disappearance of the fluorescence properties of these ICPs. Interestingly, the cation-exchange was faster for smaller ICPs, confirming the faster response that nanoscale sensors offer. Even though the detection response is not related to the NMOF, Lin *et al.* have recently reported an illustrative example of the potentiality of these structures to be functionalized for creating novel sensors.[40] Eu-doped NMOFs

composed of Gd(III) metal ions linked by BDC ligands were first coated with a silica shell, and then functionalized with a silylated Tb–EDTM monoamide derivative. The resulting nanoparticles were exposed to 2,2′-dipyridylamine (DPA), which constitutes up to 15% of the spores' dry mass. Upon excitation at 278 nm, the NMOFs only gave Eu luminescence because the complex Tb–EDTM is not luminescent. However, as DPA was added to the dispersion, the Tb luminescence became clearly visible owing to the formation of the complex Tb–EDTM–DPA. These modified NMOFs can therefore be used as sensors for anthrax and other bacterial spores.

Templates. As shown in Fig. 2, nanoscale metal–organic structures can exhibit a wide range of morphologies and functionalities. Thus, these materials show promise to be used as templates, transferring their complex morphologies to other materials, such as metal oxides, or acting as functional supports for synthesizing other nanoscale materials. With this concept, Oh *et al.* used a sub-1 μm, hexagonal, rod-shaped In(III) based NMOF to prepare hexagonally shaped hollow and non-hollow In_2O_3 rods by a simple calcination of the polymeric precursor.[41] The resulting In_2O_3 nanomaterials maintained the original morphology of the precursor MOFs. It is interesting to note that NMOFs also show promise for being used as templates to grow inorganic nanoparticles in their pores. Among others, Fischer *et al.* have enormously contributed to prove this application, showing the generation of Pd, Cu and Au nanoparticles in MOF-5 crystals by first loading the appropriate precursors in their porous structures and treating the resulting crystals with hydrogen gas.[42]

Other bioapplications. The use of bioorganic molecules expands the range of applications of metal–organic structures due to their assumed higher biocompatibility. Chmelewski *et al.* further expanded this range by using metal–organic fibers as scaffolds for cell culture.[43] Through smart peptide design, metal coordination nodes, such as nitrilotriacetic acid, histidine and bipyridyl, were incorporated into a peptide sequence. This allowed synthesizing collagen–metal frameworks that self-assembled into fibrous materials upon addition of transition metals (Zn(II), Cu(II), Ni(II) and Co(II)) able to adopt 3-D metal–organic scaffold for cell culture. Due to the nature of the interaction that holds these fibers, their assembly could be easily reverted by adding EDTA, which made more facile the cell recovering.

2-D metal–organic nanomaterials

Beyond the fabrication of discrete 0-D and 1-D nanostructures, another important challenge is to control the growth of these structures directly on surfaces, thus creating functional membranes, thin films, or devices based on these materials. The control of the supramolecular assembly of inorganic and organic building blocks on surfaces is especially of interest to fully exploit the exceptional adsorption properties of metal–organic materials, and create new functional surfaces for applications in electronic, sensing or photonics. An excellent review on this topic has also recently been published by Fischer *et al.*[44]

Synthesis

Chronologically, three principal strategies have been explored to fabricate metal–organic membranes and thin films (Fig. 6): (i) the LbL synthesis; (ii) the use of Langmuir–Blodgett (LB)

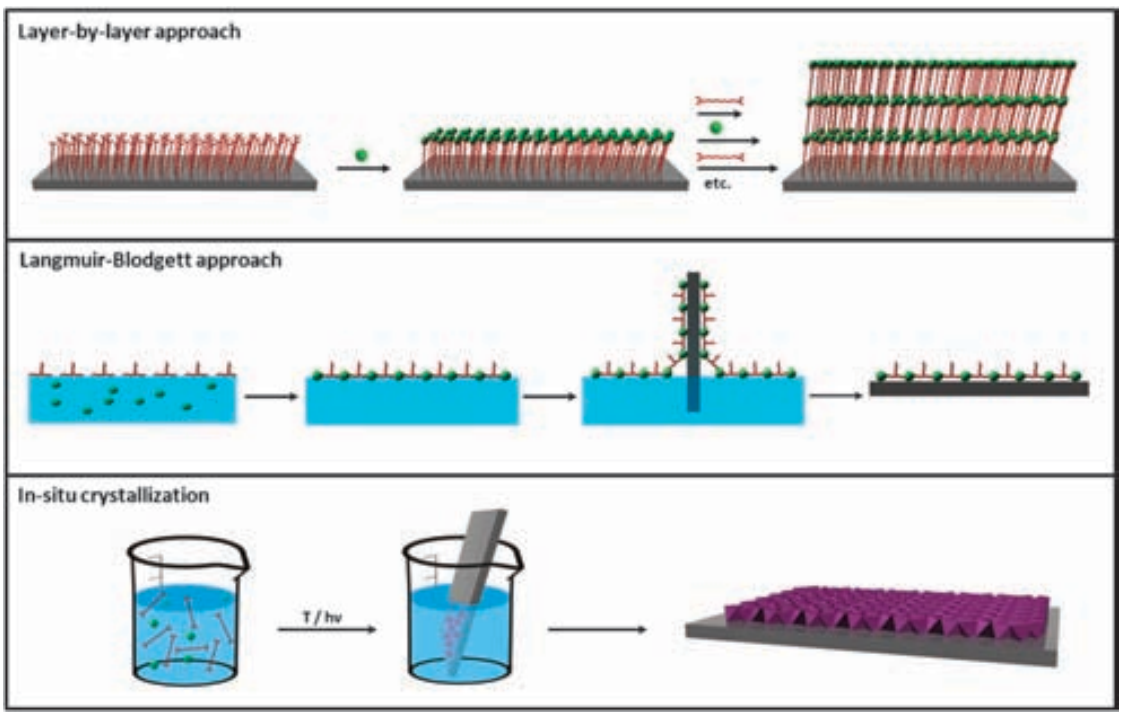

Fig. 6 Schematic illustration of the three principal synthetic strategies used for preparing 2-D metal–organic nanomaterials, including the layer-by-layer approach, the Langmuir–Blodgett approach and the *in situ* crystallization.

monolayer transfer technique; and (iii) the direct assembly and growth of metal–organic nanostructures on surfaces.

Initial efforts to fabricate nanoscale metal–organic surfaces began at the end of 80s decade with the use of the LbL synthesis (Fig. 6). The LbL synthesis is a well-known strategy that allows the step-by-step growth of hybrid organic–inorganic layers on surfaces by sequentially exposing them to solutions of both organic and inorganic building blocks. This approach was first used by Mallouk *et al.* in 1988 to fabricate an hybrid material composed of multilayers of Zr(IV) metal ions and 1,10-decanebisphosphonate (DBP) on a Si surface.[45] In this case, after an initial functionalization of the Si substrate with a phosphonate-terminated monolayer, the substrate was exposed alternatively to aqueous solutions of $ZrOCl_2$ and DBP. By repeating this process eight times, eight layers of Zr–DBP with a height of 13.6 nm (1.7 nm per layer) were fabricated. However, these adsorption steps can in principle be repeated as many times as desired in order to produce multilayer metal–organic films. The sequential dipping can be automated, and films containing more than 100 layers can be grown. Using the LbL synthesis, inorganic–organic multilayers composed of a wide variety of metal ions (*e.g.* Hf(IV), Ce(IV), Cu(II), *etc.*) and organic ligands (*e.g.* different types of diphosphonates, mercaptohexadecanoic acid, *etc.*) have nowadays been prepared on different surfaces (*e.g.* gold, silicon, *etc.*).

Beyond the stepwise coordination of metal ions and organic ligands, ultra thin metal–organic assemblies can also be grown with the electrostatic LbL self-assembly (ELSA) method. This methodology is based on the subsequent deposition of species with opposite charges on the surface. Generally, the inorganic species are anionic inorganic clusters or complexes (*e.g.* POMs), 2-D inorganic materials (*e.g.* clays and Zr(IV) phosphonates) and inorganic nanoparticles (*e.g.* gold nanoparticles). And the vast majority of organic species are oppositely charged organic polymers or large molecules. An illustrative example is the multilayer films of molybdenum oxide reported by Kunitake *et al.*[46] In this case, the inorganic species was the anionic POM $[Mo_8O_{26}]$, whereas poly-(allylamine hydrochloride) (PAH) was the cationic organic polymer. Alternate electrostatic adsorption cycles of both building blocks on a polymeric surface resulted in films with uniform thicknesses and extremely smooth surfaces.

A second general approach for fabricating nanoscale 2-D metal–organic materials is the LB technique (Fig. 6). LB is a well-known technique that allows the organization of organic molecules on air/liquid interfaces, creating ultra thin layers that can be further deposited on surfaces. To our knowledge, Nagel and Oertel first used this technique to fabricate coordination polymer monolayers on an air/water interface.[47] This process usually consists of four steps: (i) a multitopic organic ligand is first functionalized with alkyl chains to allow their organization on the air/water interface; (ii) small volume of a solution of the organic ligand is spread on the surface of an aqueous solution containing the metal ion; (iii) an interfacial coordination reaction occurs between the metal ions in the aqueous subphase and the organic ligands once they are spread or self-organized on the air/water interface; and (iv) the created ultrathin coordination polymer layers are transferred to a flat solid support by immersing the substrate through the compressed layer. Among others, Yuan and Liu followed these steps to fabricate chiral metal–organic monolayers. Initially, the naphtha[2,3]imidazole ligand was functionalized with a long alkyl chain. A chloroform solution of this ligand was then spread on pure water containing Ag(I) metal ions. Immediately, metal–organic monolayers were formed through an *in situ* coordination between both species, transferring them on mica.[48]

Both general strategies, the LB technique and the LbL synthesis, can also be coupled for producing metal–organic thin films on solid supports.[49] Makiura, Kitagawa *et al.* recently reported the LbL growth of pre-formed metal–organic sheets using the LB technique. First, these layers were formed by spreading a chloroform/methanol solution of a Co(II) metalloporphyrin complex and pyridine onto an aqueous solution containing Cu(II) metal ions, and instantly transferred on a Si substrate. Sequential sheet formation and deposition on the same substrate allows the LbL stacking, thereby resulting in the generation of MOF thin films of any desired thickness.

The last general strategy so far used for fabricating metal–organic thin films and membranes is the direct nucleation and growth of NMOFs on surfaces. Initial efforts for growing these crystals on bare surfaces (*e.g.* SiO_2, Al_2O_3, Au, graphite, *etc.*) were focused on a strategy based on immersing these substrates into a solution containing the precursors. Then, the NMOFs were grown on the surfaces by inducing their nucleation using methods analogous to those used for preparing 0-D and 1-D NMOFs, such as microwave radiation, temperature, *etc.* With these synthetic approaches, some metal–organic supports were successfully synthesized. However, most of the bare substrates inhibit the nucleation of NMOFs, and thus low crystal density is usually obtained.

A very promising solution to overcome this problem is the use of chemical affinity templates to promote the nucleation of NMOFs. Self-assembled monolayers (SAMs) are excellent candidates to act as such templates because they can be terminated with different functional groups that can direct the nucleation and growth of crystalline materials. The case of the HKUST-1 system is especially appropriate to describe this phenomenon. Bein *et al.* studied their nucleation and growth by immersing Au substrates previously functionalized with SAMs terminated with COOH–, OH– and CH_3– groups into a solution containing Cu(II) metal ions and BTC ligands.[50] Under the studied conditions, all terminated SAMs seemed to favor the nucleation, and therefore, increased the crystal density in comparison with bare Au surfaces. In addition, these authors also observed preferential crystal growth orientations depending on the terminal functional group of these SAMs. Indeed, the COOH-terminated SAM favored orientation along the [100] direction and the formation of pyramid-like crystals, whereas the OH-terminated SAM favored the [111] orientation and led to the formation of octahedral crystals. The third surface terminated with CH_3– groups did not favor any orientation. These results, even though are quite contradictory to latter exhaustive experiments performed by Fischer *et al.*,[51] confirm the

importance of SAMs for controlling not only the density of crystals (homogeneity) deposited on the surface but also their orientation.

More recently, the use of SAMs on surfaces has also shown to be important for selectively growing a certain MOF crystal phase in front of another. This is the case of MIL-88B, a MOF composed of Fe(III) metal ions connected through BDC ligands.[52] Scherb *et al.* demonstrated the preferential formation of crystals of this MOF by placing down a COOH-terminated SAM in a mother liquor solution containing both precursors. Surprisingly, even though the crystals formed in the solution corresponded to MIL-53, another MOF built up from Fe(III) metal ions connected through BDC ligands, the crystals that grew on the surface only corresponded to well-oriented MIL-88B crystals along the [001] direction. Also interesting is the work reported by Wöll *et al.*,[53] who controlled the formation of a non-interpenetrated phase of a MOF built up from the linkage of $[Zn_4O]$ clusters through 4,4′-biphenyldicarboxylate ligands. Besides bulk synthetic methods lead to the interpenetrated phase, these authors proved to control the formation of the non-interpenetrated one on surfaces by using SAMs as templates and the LbL synthesis, opening new possibilities to synthesize new types of MOFs on surfaces not accessible by conventional methods.

In addition to the use of SAMs, other ways have been proposed to promote the homogeneous nucleation and growth of NMOFs on surfaces. One of the most interesting approaches is the use of seeds to induce a better crystallization. Similar to the growth of zeolitic membranes, Caro *et al.* created a homogeneous and dense coating of imidazolate based MOFs (ZIF-7) on alumina supports by first dipping them into an aqueous polyethyleneimine dispersion of pre-synthesized ZIF-7 nanocrystals with dimensions of 30 nm.[54] These seeded supports were then immersed vertically into a solution containing the ZIF-7 precursors and heated up to 100 °C using microwave for three hours to obtain a large scale ordered polycrystalline ZIF-7 thin films.

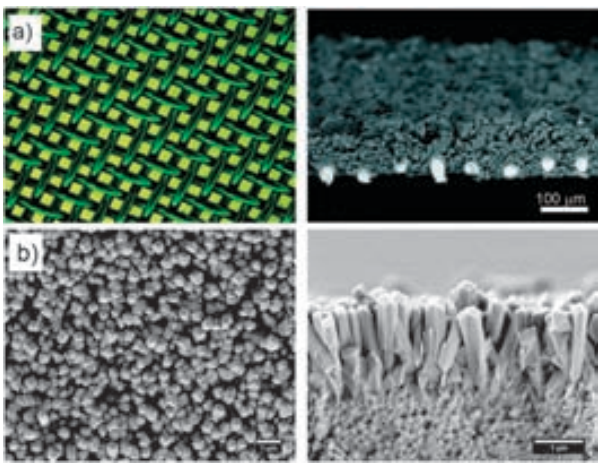

Fig. 7 (a) Optic micrographs of the copper net (left) and the net-supported HKUST-1 membrane (right). (b) SEM top (left) and cross-section (right) views of ZIF-7 membranes obtained after microwave assisted secondary growth (© Wiley Interscience and American Chemical Society, reprinted with permission).

A previous chemical modification of the surface is also an important factor to be considered in order to increase the crystal density on surfaces. One possibility is the "formate" route reported by Caro *et al.*,[55] which consists of pre-oxidation of the surfaces with sodium formate treatment. With this oxidation, the nucleation of $[Mn(HCOO)_2]$ was enhanced and rather dense coatings were obtained. Qiu *et al.* and De Vos *et al.* further proved this concept.[56,57] According to these authors, the oxidation of metallic copper surfaces generates Cu(II) metal ions process, creating more surface nucleation points during the HKUST-1 synthesis, and therefore, enhancing the crystal density on those surfaces (Fig. 7a).

Properties and applications

The exceptional advantages and properties already exhibited by nanoscale 0-D and 1-D metal–organic materials can be integrated on surfaces for fabricating metal–organic functional thin films and membranes with a wide range of properties and applications. Their use can allow the fabrication of electronic or optoelectronic thin films, membranes with gas separation capabilities, new surface sensors, magnetic platforms, *etc.*

Electronic and optoelectronic properties. The use of POMs to fabricate thin films is specially promising due to their ability to act as an electron reservoir, thereby giving rise to colored mixed-valence state species while retaining their structural integrity. Kurth, Volkmer *et al.* reported the formation of electrochromic thin films composed of multilayers of $[Eu(H_2O)P_5W_{30}O_{110}]^{12-}$, which exhibit reversible electrochemical behavior accompanied by a large electrochromic response, PAH and poly(styrenesulfonate) (Fig. 8a).[58] Because the properties of POM clusters are fully maintained in the multilayers, their LbL structuration on surfaces allows the fabrication of highly stable and reversible electrochromic films with high optical contrast (transparent to blue). In addition to electrochromic films, other electronic devices based on metal–organic thin films have also been reported. Nishihara *et al.* reported the formation of redox multilayer films of Fe(II) metal ions and terpyridine (tpy) derivative ligands on gold electrodes.[59] Using similar organic ligands, Rampi *et al.* fabricated highly conductive 40 nm long molecular wires based on Fe(II) or Co(II) metal ions.[60] More recently, a very important step has also been done for the fabrication of nanoscale devices based on optoelectronic multilayer systems. Dong *et al.* described the metal–organic thin film formation on the surface of multiwall carbon nanotubes.[61] This thin film was created from the assembly of transition metal ions and tpy ligands. The authors demonstrated that an effective photoinduced charge transfer was induced under irradiation, which increased by addition of bilayers.

Gas separation properties. The exceptional porous characteristics already exhibited by bulk MOFs make them excellent components for creating metal–organic membranes or thin films with potential properties in gas separation, gas storage, fabrication of novel sensors, *etc.* However, even though the preparation of these 2-D metal–organic systems has attracted much research interest in the last years, only a few efficient membranes for gas separation have been reported.

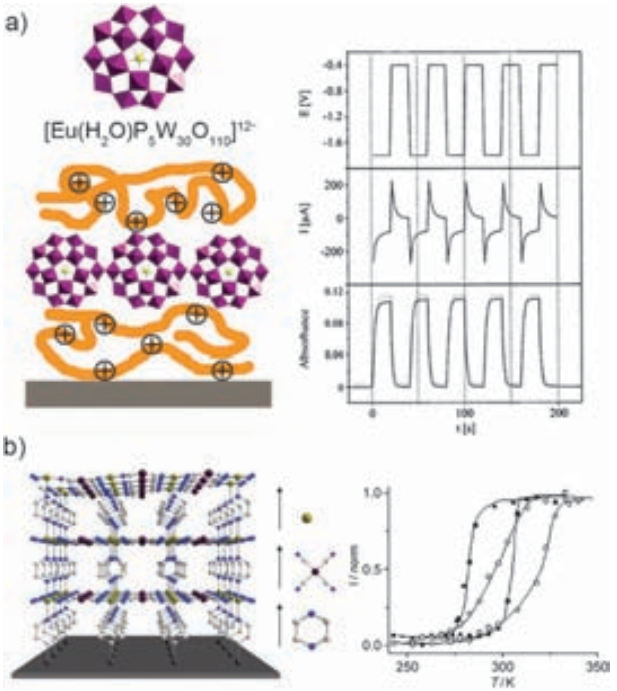

Fig. 8 (a) Schematic representation of the LbL film formation from the association of Eu–POM and a cationic polymer, and potential (Pt electrode), current, and absorbance at 700 nm of the LbL-coated ITO electrode during subsequent double-potential steps between ±0.4 and ±1.8 V. (b) Schematic drawing of the sequential assembly of [Fe(pyrazine){$M(CN)_4$}] (M = Ni, Pd, or Pt) films and the temperature dependence of the normalized Raman intensity ratio (I(norm) = I(1025 cm^{-1})/I(1230 cm^{-1})) for [Fe(pyrazine){$Pt(CN)_4$}] powder (■) and film samples (○) upon cooling and heating confirming the spin transition in LbL films (© Wiley Interscience, reprinted with permission).

The first metal–organic membrane showing separation performance was reported by Qiu *et al.*[56] This membrane, which was created with nanoscale HKUST-1 crystals on an oxidized copper grid, showed a higher permeation flux and excellent permeation selectivity for H_2 in comparison with CO_2, N_2 and CH_4. This phenomenon can be explained by the size selectivity occurred on the HKUST-1 channels. Thus, the small H_2 molecule goes through the membrane more easily than CO_2, N_2, and CH_4. However, the best gas selectivity exhibited for metal–organic membranes was recently reported by Caro *et al.*[54,62] Non-oriented and oriented membranes constructed with NMOFs of zeolitic imidazolate frameworks showed a high H_2 selectivity favored by a pore dimension of these NMOFs very similar to the size of H_2 (Fig. 7b).

Sensors. The combination of high porosity and physical properties certainly provides excellent conditions to use metal–organic thin films for sensing applications. Bein *et al.* reported the selective growth of HKUST-1 thin films on functionalized quartz-crystal microbalance (QCM) gold electrodes. This device was used to evaluate accurately the mass variations, making possible the detection of water adsorption when this thin film was exposed to atmospheres with different relative humidities.[63] More recently, Lu and Hupp constructed ZIF-8-based Fabry–Pérot devices that function as selective sensors for chemical vapors and gases. This sensor is based on the displacement of Fabry–Pérot interference peaks as a function of the exposure of the device to an analyte. The authors show the capabilities of such ZIF-8 based thin films to detect the presence of ethanol in the atmosphere.[64]

Magnetic properties. The interesting magnetic properties of metal–organic materials studied by the molecular magnetism field during the last decades can be certainly used to fabricate magnetic metal–organic thin films. The examples, however, are still scarce. An illustrative example is the work led by Bousseksou *et al.*, who fabricated metal–organic thin films displaying a room temperature spin-crossover behavior with hysteresis (Fig. 8b).[65] These authors demonstrated the formation of such thin films by stepwise synthesis of [Fe(pyrazine){$M(CN)_4$}] (where M is Ni, Pd or Pt) on surfaces.

Nanostructuration of metal–organic structures on surfaces

Control over the growth, orientation and positioning of metal–organic materials on surfaces is crucial to start to conceive the integration of these materials on supports for the fabrication of complex surface sensors, separation membranes, drug-delivery platforms and catalysts. There are three potential strategies to achieve this control at the nanometre scale length (Fig. 9): (i) the use of SAM features as chemical affinity templates to selectively control the nucleation and growth of metal–organic materials on them; (ii) the use of lithographic techniques to directly deliver or confine small volumes of the reaction solution containing the precursors, seeds or NMOFs at specific locations of a surface; and (iii) the growth of nanoscale metal–organic materials at specific locations of a surface by locally applying an external factor, such as temperature, addition of an external solvent, *etc.*, that induces their nucleation.

As stated above, it is well known that SAMs terminated with the appropriate functional group are able to coordinate with metal ions. One can then imagine to use patterned SAM features to control the positioning of the nucleation and growth of NMOFs. This approach starts with the fabrication of SAM features on surfaces by using conventional lithographic techniques, such as μ-contact printing (μCP) or photolithography. The NMOFs are then selectively grown on these features by exposing the surfaces to the precursor solution under optimum conditions or using the LbL synthesis. Fischer *et al.* first proved this concept by controlling the growth of MOF-5 crystals on square-like COOH-terminated SAM features of 40 × 40 μm fabricated by μCP (Fig. 10a–c).[66] After patterning these features, the remaining Au surface was passivated with a CF_3-terminated SAM in order to prevent the nucleation of MOF-5 in non-specific regions. The substrate was immersed into the mother solution, and this system was heated at 75 °C for 72 h. Interestingly, excellent adsorption properties of the resulting MOF-5 microarrays were successfully confirmed by exposing them to vapors of [(η^5-C_5H_5)Pd(η^3-C_3H_5)]. Using this method, Fischer's group also fabricated MOF-5 and HKUST-1 microarrays on

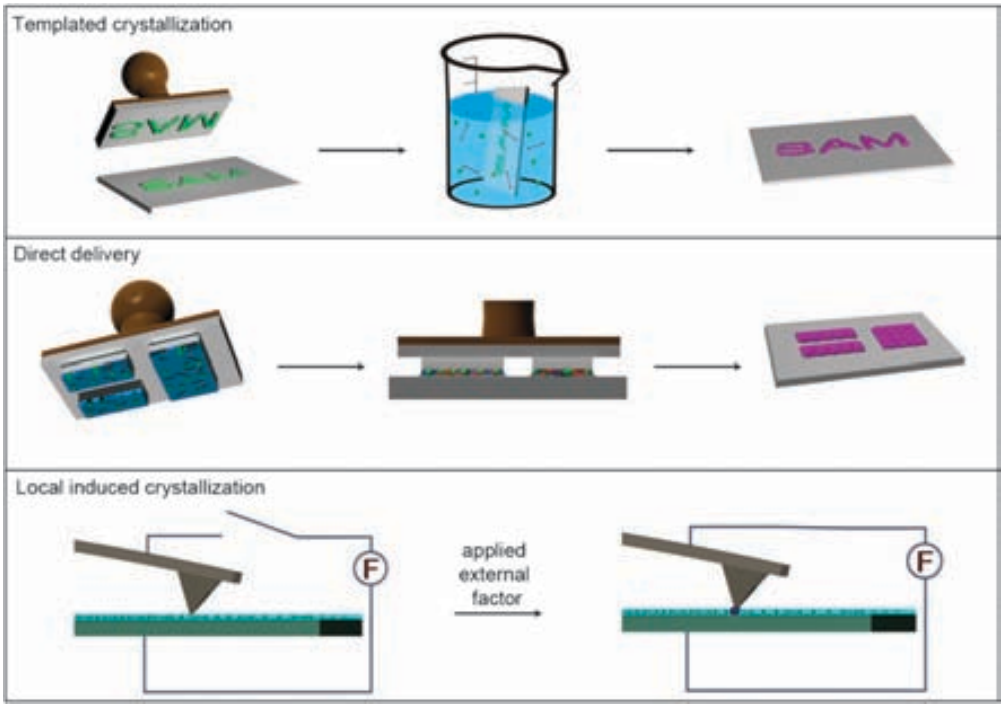

Fig. 9 Schematic illustration of the three principal fabrication strategies used for structuring metal–organic nanostructures on surfaces at the nanometre length scale, including the templated crystallization, the direct delivery and the local induced crystallization.

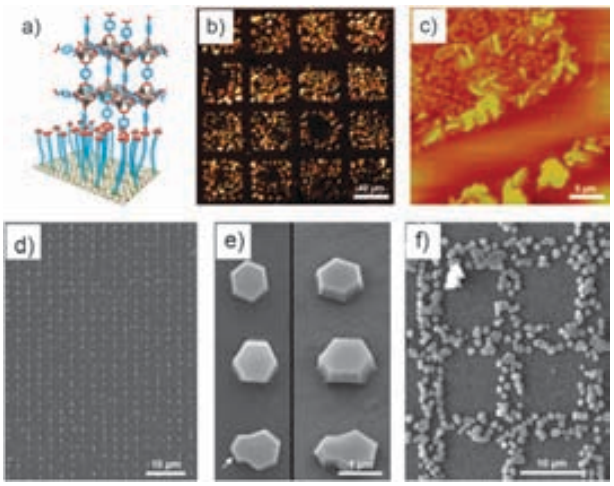

Fig. 10 (a–c) Arrays of MOF-5 crystals. (a) Schematic illustration of the concept of anchoring a typical MOF-5 building unit to a COOH-terminated SAM. (b) Optical microscope and (c) AFM images of a selectively grown film of MOF-5 on a patterned SAM of 16-mercaptohecadecanoic acid on a Au surface. The MOF-5-coated squares are 40 × 40 μm, and the crystals are about 100–500 nm in size. (d–f) Arrays of HKUST-1 crystals fabricated by LCW. (d) Large view and (e) details of individual crystals viewed from above (left) and at a 35° angle (right). The arrow indicates intergrowths caused by a second nucleation. (f) Square-like membrane structure composed of HKUST-1 crystals (© The American Chemical Society and Wiley Interscience, reprinted with permission).

alumina and silica surfaces.[51] In this case, however, the SAM features were patterned with standard photolithographic techniques.

In addition to immersing the pre-structured surface into the precursor solution, the LbL synthesis can also be localized on these SAM templates, thus controlling the positioning of the created metal–organic multilayers. For instance, Wöll *et al.* fabricated HKUST-1 crystalline microarrays on Au surfaces by using the LbL synthesis on COOH-terminated SAM features generated by μCP.[67] Similarly, Boom *et al.* fabricated a metal–organic multilayer pattern by sequentially immersing a glass surface, in which a template consisting of 5 μm OH-terminated SAM lines spaced from each other by 40 μm was created using photopatterning, into solutions of Pt(II) metal ions and 1,4-bis[2-(4-pyridyl)ethenyl]benzene ligands.[68]

Even though the use of SAM features is the most extended approach, recent advances have been made in using lithographic techniques for delivering small volumes of the precursor solution on surfaces, thus directly controlling the location in which the metal–organic structure is positioned or grown. Thus far, precursor solutions have been successfully patterned through different lithographic techniques, including the lithographically controlled wetting (LCW), microtransfer molding (μTM) and micromolding in capillaries (MIMIC). De Vos *et al.* controlled the synthesis of HKUST-1 crystals at the single-crystal level on glass substrates through LCW (Fig. 10d–f).[69] In this method, a polydimethylsiloxane (PDMS) stamp was initially coated with a DMSO solution containing Cu(II) metal ions and BTC ligands. This stamp was then placed in contact with the glass surface; in this manner, capillary forces drove the liquid to distribute only under the protrusions of the stamp. As the solvent evaporated, the nucleation of HKUST-1 crystals took place under these protrusions, and therefore, the grown crystals were formed in a pattern reproducing the motif of the stamp. Similarly,

Vieu *et al.* used μTM to transfer a colloidal solution containing coordination polymer nanoparticles on glass surfaces.[70] It is interesting to note that the resulting nanoparticle structures with dimensions up to 300 nm kept their inherent spin crossover properties. Stamps were also used by Park *et al.* to structure a coordination polymer on glass surfaces using MIMIC.[71] Continuous channels were formed when a PDMS stamp was brought into conformal contact with a solid substrate. These authors used the capillary action to fill the channels with a pyridine solution of a pre-formed coordination polymer composed of Zn(II) metal ions and 4,4′-di(4-pyridyl)cyanostilbene. The selective removal of pyridine by its absorption on the capillary walls drove to the formation while structuration of this coordination polymer.

Conclusions and perspectives

Although at the embryonic stage of their development, the recent advances made on this field, as shown in this review above, assure a brilliant future for this novel type of nanoscale materials. In this review, the advances on the early synthesis of metal–organic nanomaterials up to the initial studies of their properties and potential applications have been discussed. Along the way, there have been a number of achieved "milestones", including the preparation of the first discrete nanostructures with varied compositions, sizes and shapes, the controlled growth of metal–organic thin films and membranes, new fabrication routes for nanostructuring them in pre-designed features on surfaces, the discovery of interesting structural (*e.g.* porosity, encapsulation capabilities, ion-exchange, *etc.*) and physical (*e.g.* electronic, magnetism, *etc.*) properties, and the exploration of promising biological-related applications, including drug delivery, bioimaging, sensing, *etc.*

However, these studies are just the tip of the iceberg. The advantages of metal–organic nanomaterials are their high tailorability in terms of compositions, internal structures, morphologies, dimensions and properties, making possible their rational design for any specific application. A major challenge is then to develop novel methodologies and better understand the existing ones to fully exploit the limitless number of possible formulations, sizes and shapes of these materials. As an example of this issue is the possible local induced crystallization approach that shows promise for fabricating and structuring these materials on surfaces (Fig. 9). This strategy has not yet been explored. There is however no doubt that this route as well as other synthetic methodologies (*e.g.* microfluidics, supercritical conditions, vapour deposition, *etc.*) and lithographic techniques (*e.g.* Dip-Pen Nanolithography, Fountain-Pen Lithography, *etc.*) will be implemented in the next years, expanding the variety of synthesized metal–organic nanomaterials. In the same context, the fundamental understanding of how metal–organic nanomaterials are formed is crucial to begin to conceive of using these methods for controlling the fabrication of nanoscale metal–organic materials with desired properties.

Aside from the development of synthetic routes, there are other challenges which will focus the interest of researchers. One of them is the use of bio-related molecules as new building-blocks. Another direction of development is foreseen in the functionalization of these materials with functional species. Like their inorganic counterparts, this capability is particularly interesting for biological applications because it should allow the biocompatibilization and cell-specific targeting of these nanoscale materials. This future research, which will involve researchers of many different fields, will certainly expand the scope of properties and applications for nanoscale metal–organic materials up to their use for practical applications.

Acknowledgements

This work was supported by projects VALTEC08-2-003 and MAT2009-13977-C03. D. M. and I. I. thank the Ministerio de Ciencia y Tecnología for respective RyC and JdC contracts. A. C. and C. C. thank the Generalitat de Catalunya and the Institut Català de Nanotecnologia (ICN) for research fellowships.

Notes and references

1 Special issue on metal–organic framework materials. *Chem. Soc. Rev.* 2009, **38**, 1201.
2 S. Vaucher, M. Li and S. Mann, *Angew. Chem., Int. Ed.*, 2000, **39**, 1793.
3 G. D. Liang, J. T. Xu and X. S. Wang, *J. Am. Chem. Soc.*, 2009, **131**, 5378.
4 S. F. Hou, C. C. Harrell, L. Trofin, P. Kohli and C. R. Martin, *J. Am. Chem. Soc.*, 2004, **126**, 5674.
5 P. Horcajada, T. Chalati, C. Serre, B. Gillet, C. Sebrie, T. Baati, J. F. Eubank, D. Heurtaux, P. Clayette, C. Kreuz, J.-S. Chang, Y. K. Hwang, V. Marsaud, P.-N. Bories, L. Cynober, S. Gil, G. Férey, P. Couvreur and R. Gref, *Nat. Mater.*, 2010, **9**, 172.
6 Z. Ni and R. I. Masel, *J. Am. Chem. Soc.*, 2006, **128**, 12394.
7 W. J. Son, J. Kim and W. S. Ahn, *Chem. Commun.*, 2008, 6336.
8 S. K. Wu, X. P. Shen, B. S. Cao, L. Lin, K. C. Shen and W. Liu, *J. Mater. Sci.*, 2009, **44**, 6447.
9 X. P. Sun, S. J. Dong and E. K. Wang, *J. Am. Chem. Soc.*, 2005, **127**, 13102.
10 M. Oh and C. A. Mirkin, *Nature*, 2005, **438**, 651.
11 W. Lin, W. J. Rieter and K. M. L. Taylor, *Angew. Chem., Int. Ed.*, 2009, **48**, 650.
12 A. M. Spokoyny, D. Kim, A. Sumrein and C. A. Mirkin, *Chem. Soc. Rev.*, 2009, **38**, 1218.
13 I. Imaz, J. Hernando, D. Ruiz-Molina and D. Maspoch, *Angew. Chem., Int. Ed.*, 2009, **48**, 2325.
14 S. Jung and M. Oh, *Angew. Chem., Int. Ed.*, 2008, **47**, 2049.
15 W. J. Rieter, K. M. L. Taylor, H. Y. An, W. L. Lin and W. Lin, *J. Am. Chem. Soc.*, 2006, **128**, 9024.
16 S. K. Nune, P. K. Thallapally, A. Dohnalkova, C. Wang, J. Liu and G. J. Exarhos, *Chem. Commun.*, 2010, **46**, 4878.
17 W. Cho, H. J. Lee and M. Oh, *J. Am. Chem. Soc.*, 2008, **130**, 16943.
18 J. K.-H. Hui and M. J. Maclachlan, *Coord. Chem. Rev.*, 2010, **254**, 2363.
19 I. Imaz, M. Rubio-Martinez, W. J. Saletra, D. B. Amabilino and D. Maspoch, *J. Am. Chem. Soc.*, 2009, **131**, 18222.
20 K. Liu, H. You, G. Jia, Y. Zheng, Y. Huang, Y. Song, M. Yang, L. Zhang and H. Zhang, *Cryst. Growth Des.*, 2010, **10**, 790.
21 L.-G. Qiu, T. Xu, Z.-Q. Li, W. Wang, Y. Wu, X. Jiang, X.-Y. Tian and L.-D. Zhang, *Angew. Chem., Int. Ed.*, 2008, **47**, 9487.
22 X. H. Yan, P. L. Zhu, J. B. Fei and J. B. Li, *Adv. Mater.*, 2010, **22**, 1283.
23 A. Nisar, Y. Lu and X. Wang, *Chem. Mater.*, 2010, **22**, 3511.
24 Y. Yan, N. A. M. Besseling, A. de Keizer, A. T. M. Marcelis, M. Drechsler and M. A. C. Stuart, *Angew. Chem., Int. Ed.*, 2007, **46**, 1807.
25 W. Lu, V. A. L. Roy and C.-M. Che, *Chem. Commun.*, 2006, 3972.
26 W. J. Rieter, K. M. Pott, K. M. L. Taylor and W. B. Lin, *J. Am. Chem. Soc.*, 2008, **130**, 11584.

27 K. M. L. Taylor-Pashow, J. D. Rocca, Z. Xie, S. Tran and W. Lin, *J. Am. Chem. Soc.*, 2009, **131**, 14261.
28 I. Imaz, M. Rubio, L. García, F. García, D. Ruiz-Molina, J. Hernando, V. Puntes and D. Maspoch, *Chem. Commun.*, 2010, **46**, 4737.
29 R. Nishiyabu, C. Aime, R. Gondo, T. Noguchi and N. Kimizuka, *Angew. Chem., Int. Ed.*, 2009, **48**, 9465.
30 K. M. L. Taylor, A. Jin and W. Lin, *Angew. Chem., Int. Ed.*, 2008, **47**, 7722.
31 K. H. Park, K. Jang, S. U. Son and D. A. Sweigart, *J. Am. Chem. Soc.*, 2006, **128**, 8740.
32 D. Tanaka, A. Henke, K. Albrecht, M. Moeller, K. Nakagawa, S. Kitagawa and J. Groll, *Nat. Chem.*, 2010, **2**, 410.
33 N. Kerbellec, L. Catala, C. Daiguebonne, A. Gloter, O. Stephan, J. C. Bunzli, O. Guillou and T. Mallah, *New J. Chem.*, 2008, **32**, 584.
34 X. Zhang, Z. K. Chen and K. P. Loh, *J. Am. Chem. Soc.*, 2009, **131**, 7210.
35 L. Catala, F. Volatron, D. Brinzel and T. Mallah, *Inorg. Chem.*, 2009, **48**, 3360.
36 E. Coronado, J. R. Galán-Mascaros, M. Monrabal-Capilla, J. García-Martinez and P. Pardo-Ibáñez, *Adv. Mater.*, 2007, **19**, 1359.
37 I. Imaz, D. Maspoch, C. Rodríguez-Blanco, J. M. Pérez-Falcón, J. Campo and D. Ruiz-Molina, *Angew. Chem., Int. Ed.*, 2008, **47**, 1857.
38 I. Boldog, A. B. Gaspar, V. Martínez, P. Pardo-Ibañez, V. Ksenofontov, A. Bhattacharjee, P. Gütlich and J. A. Real, *Angew. Chem., Int. Ed.*, 2008, **47**, 6433.
39 M. Oh and C. A. Mirkin, *Angew. Chem., Int. Ed.*, 2006, **45**, 5492.
40 W. J. Rieter, K. M. L. Taylor and W. Lin, *J. Am. Chem. Soc.*, 2007, **129**, 9852.
41 W. Cho, Y. H. Lee, H. J. Lee and M. Oh, *Chem. Commun.*, 2009, 4756.
42 S. Hermes, M.-K. Scröter, R. Schmid, L. Khodeir, M. Muhler, A. Tissler, R. W. Fischer and R. A. Fischer, *Angew. Chem., Int. Ed.*, 2005, **44**, 6237.
43 M. M. Pires, D. E. Przybyla and J. Chmielewski, *Angew. Chem., Int. Ed.*, 2009, **48**, 7813.
44 D. Zacher, O. Shekhah, C. Wöll and R. A. Fischer, *Chem. Soc. Rev.*, 2009, **38**, 1418.
45 H. Lee, L. J. Kepley, H. G. Hong and T. E. Mallouk, *J. Am. Chem. Soc.*, 1988, **110**, 618.
46 I. Ichinose, H. Tagawa, S. Muzuki, Y. Lvov and T. Kunitake, *Langmuir*, 1998, **14**, 187.
47 J. Nagel and U. Oertel, *Thin Solid Films*, 1998, **327–329**, 495.
48 J. Yuan and M. Liu, *J. Am. Chem. Soc.*, 2003, **125**, 5051.
49 R. Makiura, S. Motoyama, Y. Umemura, H. Yamanaka, O. Sakata and H. Kitagawa, *Nat. Mater.*, 2010, **9**, 565.
50 E. Biemmi, C. Scherb and T. Bein, *J. Am. Chem. Soc.*, 2007, **129**, 8054.
51 D. Zacher, A. Baunemann, S. Hermes and R. A. Fischer, *J. Mater. Chem.*, 2007, **17**, 2785.
52 C. Scherb, A. Schödel and T. Bein, *Angew. Chem., Int. Ed.*, 2008, **47**, 5777.
53 O. Shekhah, H. Wang, M. Paradinas, C. Ocal, B. Schüpbach, A. Terfort, D. Zacher, R. A. Fischer and C. Wöll, *Nat. Mater.*, 2009, **8**, 481.
54 Y.-S. Li, F.-Y. Liang, H. Bux, A. Feldhoff, W.-S. Yang and J. Caro, *Angew. Chem., Int. Ed.*, 2010, **49**, 548.
55 M. Arnold, P. Kortunov, D. J. Jones, Y. Nedellec, J. Kärger and J. Caro, *Eur. J. Inorg. Chem.*, 2007, 60.
56 H. Guo, G. Zhu, I. J. Hewitt and S. Qiu, *J. Am. Chem. Soc.*, 2009, **131**, 1646.
57 R. Ameloot, L. Stappers, J. Fransaer, L. Alaerts, B. F. Sels and D. E. De Vos, *Chem. Mater.*, 2009, **21**, 2580.
58 S. Liu, D. G. Kurth, H. Möhwald and D. Volkmer, *Adv. Mater.*, 2002, **14**, 225.
59 Y. Nishimori, K. Kanaizuka, M. Murata and H. Nishihara, *Chem.–Asian J.*, 2007, **2**, 367.
60 N. Tuccitto, V. Ferri, M. Cavazzini, S. Quici, G. Zhavnerko, A. Licciardello and M. A. Rampi, *Nat. Mater.*, 2009, **8**, 41.
61 Y. Pan, B. Tong, J. Shi, W. Zhao, J. Shen, J. Zhi and Y. Dong, *J. Phys. Chem. C*, 2010, **114**, 8040.
62 Y.-S. Li, H. Bux, A. Feldhoff, G.-L. Li, W.-S. Yang and J. Caro, *Adv. Mater.*, 2010, **22**, 3322.
63 E. Biemmi, A. Darga, N. Stock and T. Bein, *Microporous Mesoporous Mater.*, 2008, **114**, 380.
64 G. Lu and J. T. Hupp, *J. Am. Chem. Soc.*, 2010, **132**, 7832.
65 S. Cobo, G. Molnar, J.-A. Real and A. Bousseksou, *Angew. Chem., Int. Ed.*, 2006, **45**, 5786.
66 S. Hermes, F. Schroder, R. Chelmowski, C. Woll and R. A. Fischer, *J. Am. Chem. Soc.*, 2005, **127**, 13744.
67 O. Shekhah, H. Wang, S. Kowarik, F. Schreiber, M. Paulus, M. Tolan, C. Sternemann, F. Evers, D. Zacher, R. A. Fischer and C. Wöll, *J. Am. Chem. Soc.*, 2007, **129**, 15118.
68 M. Altman, A. D. Shukla, T. Zubkov, G. Evmenenko, P. Dutta and M. E. van der Boom, *J. Am. Chem. Soc.*, 2006, **128**, 7374.
69 R. Ameloot, E. Gobechiya, H. Uji-i, J. A. Martens, J. Hofkens, L. Alaerts, B. F. Sels and D. E. D. Vos, *Adv. Mater.*, 2010, **22**, 2685.
70 C. Thibault, G. Molnár, L. Salmon, A. Bousseksou and C. Vieu, *Langmuir*, 2009, **26**, 1557.
71 Y. You, H. Yang, J. W. Chung, J. H. Kim, Y. Jung and S. Y. Park, *Angew. Chem., Int. Ed.*, 2010, **49**, 3757.

nature chemistry

ARTICLES

PUBLISHED ONLINE: 10 FEBRUARY 2013 | DOI: 10.1038/NCHEM.1569

A spray-drying strategy for synthesis of nanoscale metal–organic frameworks and their assembly into hollow superstructures

Arnau Carné-Sánchez[1], Inhar Imaz[1], Mary Cano-Sarabia[1] and Daniel Maspoch[1,2]*

Metal–organic frameworks (MOFs) are among the most attractive porous materials known today. Their miniaturization to the nanoscale—into nanoMOFs—is expected to serve myriad applications from drug delivery to membranes, to open up novel avenues to more traditional storage and catalysis applications, and to enable the creation of sophisticated superstructures. Here, we report the use of spray-drying as a versatile methodology to assemble nanoMOFs, yielding spherical hollow superstructures with diameters smaller than 5 μm. This strategy conceptually mimics the emulsions used by chemists to confine the synthesis of materials, but does not require secondary immiscible solvents or surfactants. We demonstrate that the resulting spherical, hollow superstructures can be processed into stable colloids, whose disassembly by sonication affords discrete, homogeneous nanoMOFs. This spray-drying strategy enables the construction of multicomponent MOF superstructures, and the encapsulation of guest species within these superstructures. We anticipate that this will provide new routes to capsules, reactors and composite materials.

Metal–organic framework nanoparticles (also known as nanoscale MOFs or nanoMOFs) are the nanosize version of classical MOFs, built from the controlled assembly of metal ions or higher-nuclearity metal clusters with multitopic organic ligands, at the nanometre scale[1–3]. At the nanoscale, MOFs can have size-dependent properties, which, if properly exploited, may expand their scope for numerous practical purposes, including drug delivery[4,5], contrast agents[6], sensor technology[7], functional membranes and thin films[8,9], while also opening up novel avenues to the more traditional storage[10], separation[11] and catalysis[12,13] applications. Discrete nanoMOFs with controlled chemical compositions have already been readily synthesized using solvothermal and microwave conditions as fast precipitation methods[14], and nanoemulsions as confined reaction media[15], but the synthesis of a broad spectrum of nanoMOFs with adjustable composition and homogeneous size distribution remains a difficult and demanding task, as does the large-scale production of nanoMOFs and their assembly into advanced superstructures amenable to practical use. To date, the formation of well-defined MOF superstructures has required the use of sacrificial polymeric templates[16], controlled chemical etching[17] or interfacial synthesis[18], in which the spherical interface between two immiscible solvents, each containing one of the precursors, is used as a template. Because such superstructures can trap guest species, they have been proposed for use as delivery systems, chemical sensors and selective reactors containing molecular catalysts[16,18].

Here, we report a spray-drying technique that can be exploited as a general, low-cost, rapid and scalable method for the synthesis and self-assembly of nanoMOFs. It enables massive production of sub-5 μm hollow, spherical superstructures from the localized crystallization of nanoMOFs on the surfaces of atomized droplets of a MOF precursor solution (containing the metal ions and organic ligands) on heating (Fig. 1). Spray-drying has previously been used to dry suspensions; to encapsulate, micronize and crystallize active species for various applications in the food, drug and construction sectors[19,20]; and to fabricate other materials[21], including silica[22], carbon nanotubes[23], hydroxyapatite[24] and organic crystals[25]. As shown here, the atomized droplets produced in spray-drying can also be used as individual reactors to confine the synthesis and assembly of nanoMOFs at a large scale. The resulting superstructures are robust and, following disassembly by sonication, afford well-dispersed, discrete nanoMOFs. We have demonstrated this principle by producing 14 different discrete nanoMOFs: HKUST-1[26], Cu-bdc[27], NOTT-100[28], MIL-88A[29], MIL-88B[29], MOF-14[30], MOF-74 [M=Zn(II), Ni(II) and Mg(II)][31], UiO-66[32], ZIF-8[33], Cu(II) Prussian blue analogue (Cu-PB)[34], MOF-5[35] and IRMOF-3[36]. These cover most known MOF subfamilies and related hollow superstructures. In all cases, the nanoMOFs retain the excellent sorption properties of the parent material. Moreover, our method enables simultaneous synthesis and assembly of different types of nanoMOFs, opening the way to greater compositional complexity of hollow MOF superstructures.

We envisage that by dissolving or emulsifying a functional component in the precursor solution before spray-drying, we should be able to extend our approach to achieve simultaneous entrapment of guest species inside the cavity of the superstructures. This would enable the confined crystallization of species, the fabrication of functional capsules and reactors, and the development of advanced, three-dimensional, highly complex hybrid materials that combine the properties of the MOF and the guest species, and that show promise for selective pollutant removal and as sensors.

Results and discussion

All methods for the confined synthesis of nanoMOFs demand the generation and stabilization of droplets containing at least one of the corresponding precursors for the duration of the reaction. Typically, this has been achieved by using emulsions created from at least two immiscible solvents and, in most cases, surfactants[1,15]. However, the use of these emulsions to synthesize nanoMOFs is extremely challenging and currently quite limited. This is a result

[1]CIN2 (ICN-CSIC), Catalan Institute of Nanotechnology, Esfera UAB, 08193 Bellaterra, Spain, [2]Institució Catalana de Recerca i Estudis Avançats (ICREA), 08100 Barcelona, Spain. *e-mail: daniel.maspoch@icn.cat

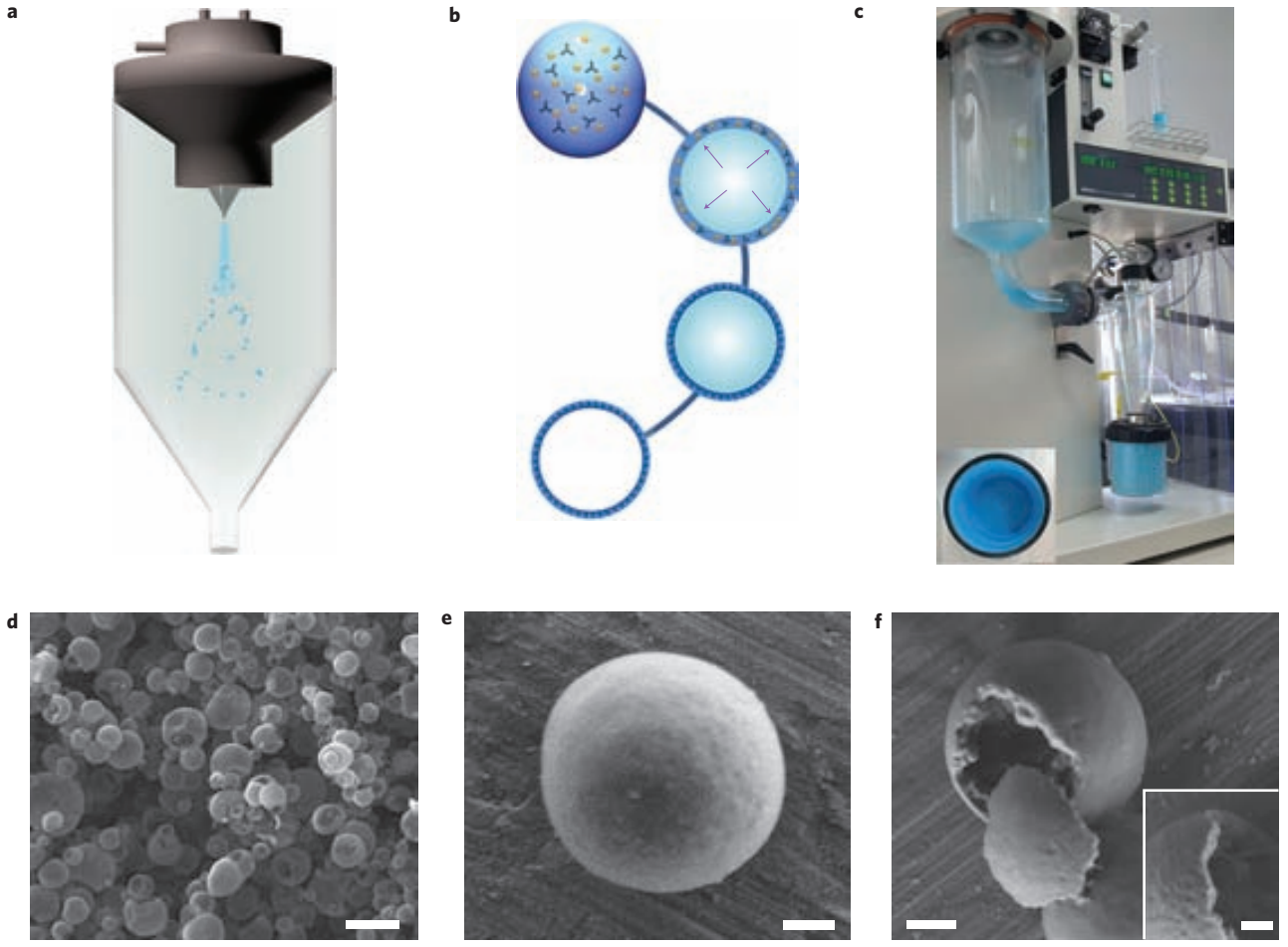

Figure 1 | Spray-drying synthesis of spherical hollow HKUST-1 superstructures. a, Schematic showing the spray-drying process used to synthesize HKUST-1 superstructures. Blue dots, sprayed solution; blue spheres, formed spherical superstructures. **b**, Proposed spherical superstructure formation process (emphasized by purple arrows), which implies the crystallization of nanoMOF crystals. Within a droplet, the MOF precursors (metal ions, orange; spheres and ligands, tri-rods) concentrate and crystallize at the surface into spherical superstructures. **c**, Photograph of the spray-dryer after its use in synthesizing large amounts of blue HKUST-1 superstructures. **d**–**f**, Representative FESEM images showing a general view of the spherical HKUST-1 superstructures (**d**), the wall of a single HKUST-1 superstructure showing the assembly of nanoHKUST-1 crystals (**e**), and a mechanically broken hollow superstructure showing the internal cavity and the thickness of its wall (**f** and inset). Scale bars: 5 μm (**d**), 500 nm (**e**,**f**), 200 nm (**f**, inset).

of several factors, including the complexity of preparing emulsions that mimic the required reaction conditions (for example, solvents, temperature, bases), and solubility problems between the MOF precursors (metal ions and organic ligands) and the constituent polar/nonpolar solvents of the emulsions. Our spray-drying method avoids most of these problems, as it constitutes a general method for forming and homogeneously heating droplets of any desired solvent containing the precursors without the need for any additional immiscible solvents, surfactants, emulsifiers or agitation (for example, stirring or sonication).

The process starts with atomization of a solution of the precursors into a spray of microdroplets using a two-fluid nozzle (Fig. 1a). This step is accomplished by simultaneously injecting the solution at a certain rate (hereafter, 'feed rate') and compressed air or nitrogen gas at another rate (hereafter, 'flow rate'). Thus, each precursor droplet contacts—and is suspended by—a gas stream heated to a certain temperature (hereafter, 'inlet temperature'), causing the solvent to begin evaporating and inducing the precursors to diffuse radially to the droplet surface (Fig. 1b)[20]. As the evaporating droplet shrinks, its receding droplet surface leads to increasing precursor concentrations at the surface, until the critical concentration for reaction is reached, and the nanoMOFs begin crystallizing at the surface. At this moment, the newly formed nanoMOF crystals have very limited mobility, so they accumulate at the surface and merge into a well-packed shell (Fig. 1b).

To benchmark our spray-drying technique, we initially focused on the archetypical compound HKUST-1 (also called MOF-199; $Cu_3(btc)_2$, btc = 1,3,5-benzenetricarboxylate), seeking to confine the synthesis and assembly of nanoHKUST-1 crystals. In a typical experiment, a solution of $Cu(NO_3)_2{\cdot}2.5H_2O$ and btc (molar ratio, 3:2; concentration of the metal salt, 0.0017 M) in a mixture of dimethylformamide (DMF), ethanol and water (1:1:1) was spray-dried at a feed rate of 4.5 ml min^{-1}, a flow rate of 336 ml min^{-1} and an inlet temperature of 180 °C using a Mini Spray Dryer B-290 (BÜCHI Labortechnik). Once the precursor solution had atomized, a dry blue powder instantly appeared in the spray dryer collector (Fig. 1c). This powder (133 mg) was then cleaned with methanol and dichloromethane, and finally suspended in methanol or dried at 130 °C (120 mg; 70% yield; 90% purity, where purity = [weight of purified product]/[weight of crude solid collected in the spray dryer]). Field-emission scanning electron microscopy (FESEM) of the dried powder (Fig. 1d) revealed spherical superstructures (average diameter, 2.5 ± 0.4 μm). As shown in Fig. 1e,f, these superstructures were hollow, and had thin, uniform walls (90–120 nm) created by the close packing of sub-100 nm octahedral nanoparticles, which began to break when exposed to a mechanical

force close to 80 μN (Supplementary Fig. S1). X-ray powder diffraction (XRPD) indicated that the nanoparticles were pure crystalline HKUST-1 (Supplementary Fig. S2). Nitrogen physical adsorption measurements on the hollow HKUST-1 superstructures validated their microporosity. The measured Brunauer–Emmett–Teller (BET) surface area (1,209 $m^2 g^{-1}$) is consistent with previously reported values for HKUST-1[21,37], thereby confirming that our spray-drying process does not affect the quality of the synthesized nanoMOFs.

Importantly, we found that, despite the stability of the hollow HKUST-1 superstructures to solvents and to mechanical stirring, they break down into discrete nanoHKUST-1 crystals on sonication (Fig. 2a). The sonicated (130 W, 20 kHz) methanolic dispersion of HKUST-1 superstructures was readily converted into a stable blue colloid of well-dispersed, discrete octahedral nanoHKUST-1 crystals with mean dimensions of 75 ± 28 nm (Fig. 2b,c). The dimensions of the crystals were confirmed by dynamic light scattering (DLS) measurements, their purity by XRPD (Supplementary Fig. S2) and their microporosity according to their measured BET surface area (1,260 $m^2 g^{-1}$)[21,37].

To fully understand and utilize this methodology, we systematically studied the formation of nanoHKUST-1 crystals and their assembly into hollow superstructures by varying the precursor concentration, inlet temperature and flow rate (Supplementary Table S1). To control the size of the nanoHKUST-1 crystals comprising the walls of the superstructures, three concentrations of the metal salt precursor were tested: 0.0017 M, 0.017 M and 0.17 M (all three with the same 3:2 molar ratio relative to btc). A higher precursor concentration gave larger nanoHKUST-1 crystals. For example, at a constant inlet temperature of 180 °C and a flow rate of 336 ml min^{-1}, a concentration of 0.17 M gave nanoHKUST-1 crystals with an average diameter of up to 160 ± 40 nm (Fig. 2d,e). The flow rate was also critical for size control. For instance, using the same temperature (180 °C) and metal salt precursor concentration (0.17 M) as above but with a higher flow rate (474 ml min^{-1}) gave smaller, discrete nanoHKUST-1 crystals (mean diameter, 107 ± 30 nm). In contrast, when these reactions were performed at a constant metal salt concentration (0.17 M) and flow rate (336 ml min^{-1}) but with a lower inlet temperature (100 °C) no significant size differences were observed in the resulting crystals.

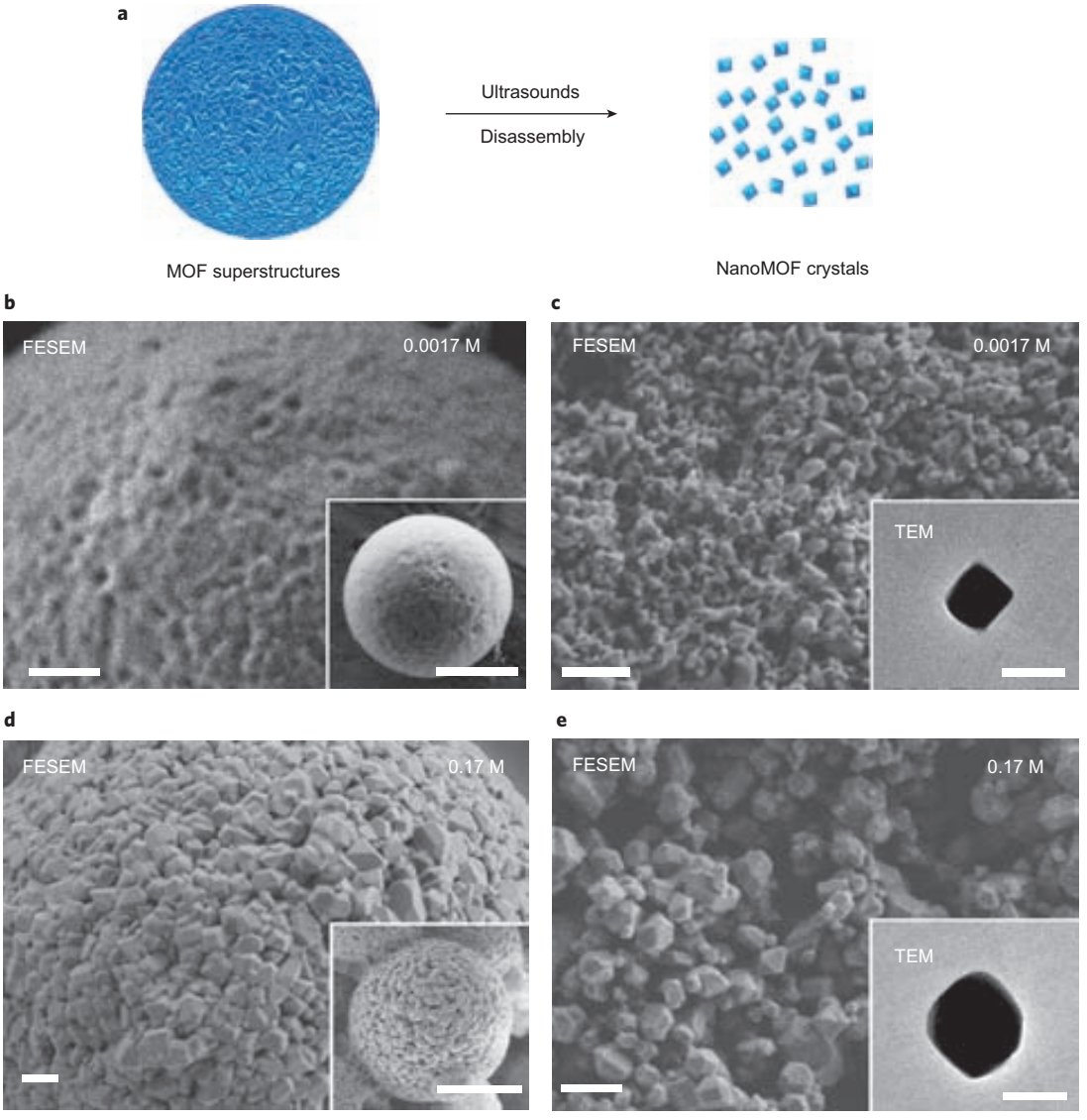

Figure 2 | Size control in spray-drying synthesis of nanoHKUST-1 crystals. a, Schematic showing the disassembly of the HKUST-1 superstructures on sonication to form well-dispersed, discrete nanoHKUST-1 crystals. **b**–**e**, Representative FESEM and TEM (insets) images of the HKUST-1 superstructures (**b**,**d**) and corresponding disassembled nanoHKUST-1 crystals (**c**,**e**, respectively) synthesized using metal salt concentrations of 0.0017 M (**b**,**c**) or 0.17 M (**d**,**e**). Note the larger crystal size at higher concentrations. Scale bars: 500 nm (**b**–**e**), 1 μm (insets to **b**,**d**) and 100 nm (insets to **c**,**e**).

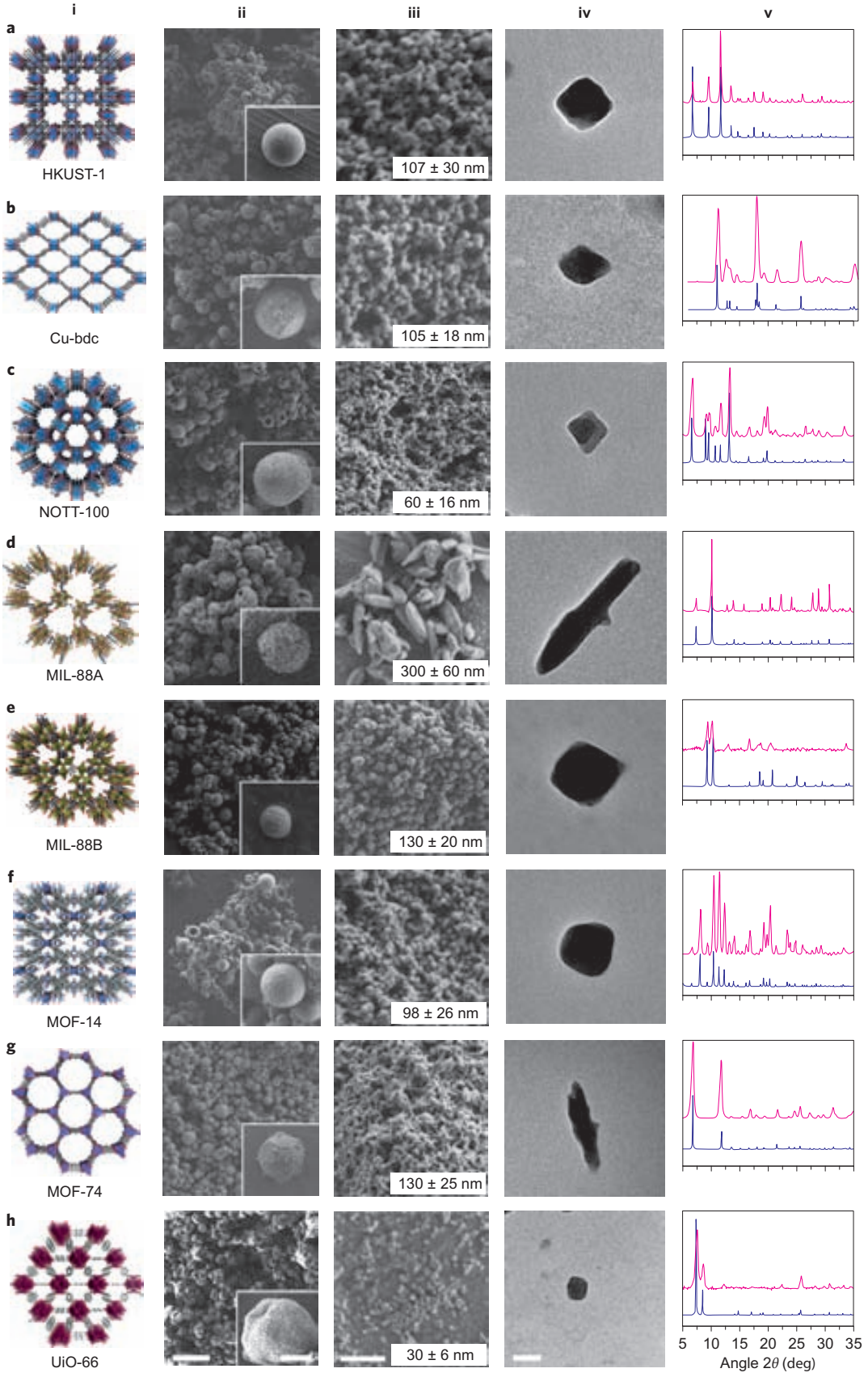

Figure 3 | Series of MOF superstructures and discrete nanoMOF crystals synthesized by spray-drying. Synthesized MOFs: **a**, HKUST-1 (for comparison). **b**, Cu-bdc. **c**, NOTT-100. **d**, MIL-88A. **e**, MIL-88B. **f**, MOF-14. **g**, Zn-MOF-74. **h**, UiO-66. FESEM (**ii**, **ii** inset, **iii**) and TEM (**iv**) images of the synthesized MOF superstructures and discrete nanoMOF crystals, and the corresponding experimental (pink) and simulated (blue) XRPD patterns (**v**, for comparison), are shown for each MOF. Scale bars: 10 μm (**ii**), 2 μm (inset to **ii**), 500 nm (**iii**), 50 nm (**iv**).

Importantly, the yield and purity of the nanoHKUST-1 crystals were also strongly dictated by the precursor concentration, flow rate and inlet temperature (Supplementary Table S1). A higher precursor concentration gave higher HKUST-1 yields but lower purities. Higher inlet temperatures gave higher purities and yields. Finally, a higher flow rate gave higher yields. Thus, by controlling the parameters of the spray-drying method, one can selectively prepare hollow MOF superstructures or discrete nanoMOF crystals with desired dimensions and with optimized purity and yield. For example, using the highest values for all the parameters (flow rate, 474 ml min^{-1}; inlet temperature, 180 °C; metal salt concentration, 0.17 M), we prepared hollow HKUST-1 superstructures and nanoHKUST-1 crystals (~100 nm in size) at a production rate of 140 mg min^{-1} with yields up to 85%. The hollow HKUST-1 superstructures were further miniaturized down to the submicrometre range using a NanoSpray Dryer B-90 (BÜCHI Labortechnik). This instrument reduces the size of the atomized precursor droplets[38], thus providing the ideal conditions for producing HKUST-1 superstructures with average diameters of 950 ± 300 nm (Supplementary Fig. S7).

To demonstrate the scope of our spray-drying technique beyond the archetypical compound HKUST-1, we used it to prepare hollow superstructures and nanocrystals of a series of representative materials from major subfamilies of porous MOFs. The synthesized nanoMOFs comprised the two-dimensional Cu-bdc (Cu(bdc), where bdc is 1,4-benzenedicarboxylate)[27]; the three-dimensional NOTT-100 (also called MOF-505; Cu_2(bptc), where bptc is 3,3′,5,5′-biphenyltetracarboxylic acid)[28]; MIL-88A (Fe_3O(fumarate)$_3$)[29]; MIL-88B ($Fe_3O(NH_2\text{-bdc})_3$)[29]; MOF-14 (Cu_3(btb)$_2$, where btb is 4,4′,4″-benzene-1,3,5-triyl-tribenzoic acid)[30]; MOF-74 (also called CPO-27; M_2(dhbdc), where M is Zn(II), Mg(II) and Ni(II) and dhbdc is 2,5-dihydroxy-1,4-benzenedicarboxylate)[31]; and UiO-66 ($Zr_6O_4(OH)_4$(bdc)$_6$)[32]. Figure 3 presents typical FESEM and transmission electron microscopy (TEM) images of the resulting sub-5 μm hollow superstructures and discrete nanoMOF crystals, in which dimensions down to 150 nm were achieved for most cases. For these, further characterization by DLS (Supplementary Fig. S8) and nitrogen physical adsorption confirmed their sizes and microporosity capacities, and all calculated BET surface areas were similar to previously reported values (Supplementary Table S2).

We implemented our methodology using a three-fluid nozzle to independently atomize the solutions containing the precursors (Fig. 4a), or using additional channels to inject the solutions independently (Fig. 4d). Both approaches enable mixing of the precursor solutions just before they are heated to form atomized droplets. In the first approach, mixing occurs inside the drying chamber owing to the coalescence of the atomized droplets (Fig. 4a). In the second method, mixing occurs in a connector inserted before the two-fluid nozzle. The use of either approach decreases the probability that unwanted species or micrometre-sized MOFs will form in the precursor solution before it is spray-dried. Both methods also allow the use of reagents (for example, bases) to accelerate MOF formation, thus increasing yields and purities and enabling the synthesis of new hollow superstructures and related nanocrystals. To test this possibility, we first synthesized nanoMIL-88A by the independent atomization of two aqueous solutions: one containing the Fe(III) metal salt and one containing fumaric acid that had already been deprotonated with NaOH. We chose MIL-88A because we had previously synthesized it in very poor yield (10%) and purity (8%) by spray-drying a DMF mixture of the Fe(III) metal salt and fumaric acid. It is well known that MIL-88A can be prepared in higher yields when fumarate is used instead of fumaric acid[39]. However, the instantaneous precipitation of an amorphous product when aqueous solutions of fumarate and Fe(III) metal salt are mixed at room temperature prevents its use in spray-drying. To overcome this limitation, we used a three-fluid nozzle to achieve independent atomization of each solution. The atomization ensures that the two reactants only come into contact inside the drying chamber, through coalescence of their droplets. This in turn provides greater yield (40%) and purity (79%) of the resulting hollow MIL-88A superstructures and nanoMIL-88A crystals.

Based on these results, we used the simultaneous atomization to further extend the synthesis of discrete nanocrystals and related hollow superstructures to ZIF-8 ($Zn(Me\text{-}IM)_2$, where Me-IM is 2-methylimidazolate)[33] and Cu-PB ($Cu_3[Fe(CN)_6]_2$)[34] (Fig. 4b,c and Supplementary Figs S11,S12). The variety of MOFs was also increased using the second approach. Thus, it was possible for MOF-5 ($Zn_4O(bdc)_3$; Fig. 4e,f)[35] and IRMOF-3 (Zn_4O(2-amino-bdc)$_3$)[36] to be made in the form of hollow superstructures and sub-100 nm nanocrystals by independently injecting two DMF solutions (one containing Zn(II) acetate and one containing either bdc or 2-amino-bdc) through two channels connected by a T-type connector just before atomization (Supplementary Figs S13,S14).

The spray-drying synthetic method also enables the fabrication of hollow multicomponent MOF superstructures. To explore this possibility, a DMF solution containing a mixture of Zn-MOF-74 and Ni-MOF-74 precursors ($Zn(NO_3)_2{\cdot}6H_2O$, $Ni(NO_3)_2{\cdot}6H_2O$ and dhbdc; molar ratio 3:3:1; concentration of the metal salts, 0.045 M) was spray-dried at a flow rate of 336 ml min^{-1} and an inlet temperature of 180 °C. The collected brownish-green powder was confirmed to comprise hollow MOF-74 superstructures (by XRPD and energy dispersive X-ray (EDX) elemental mapping), each composed of nanoMOF-74 crystals containing both Ni(II) and Zn(II) ions (Supplementary Fig. S15; see also Supplementary Section S1 and Fig. S16 for the synthesis of mixed HKUST-1/NOTT-100 superstructures).

All the data presented here demonstrate that spray-drying enables the formation of nanoMOFs, and hollow MOF superstructures in particular, a capability that could prove important for the entrapment and/or controlled crystallization of active substances within the cavities of these superstructures (Fig. 5a,i). We therefore tested this potential using sodium chloride (NaCl), because it crystallizes easily into cubic crystals, and we reasoned that it would serve as an excellent model. Accordingly, NaCl (0.017 M) was dissolved in a solution of $Cu(NO_3)_2{\cdot}2.5H_2O$ (0.017 M) and btc (0.0011 M) in 50 ml of a 1:1:1 mixture of DMF, ethanol and water. The resulting solution was spray-dried at a flow rate of 336 ml min^{-1} and inlet temperature of 180 °C. Figure 5a,ii presents a FESEM image of the collected blue HKUST-1 superstructures, revealing their golfball-like shape and the absence of any non-entrapped NaCl crystals on the exterior. This observation, combined with XRPD and EDX data, corroborated crystallization of the NaCl inside the HKUST-1 superstructures. Indeed, the XRPD pattern indicated the presence of both crystalline HKUST-1 and NaCl (Supplementary Fig. S17), and EDX mapping of a single superstructure confirmed the presence of both Na and Cl within its interior (Fig. 5a,iii). Interestingly, NaCl entrapment was also confirmed by FESEM analysis of broken NaCl@HKUST-1 superstructures, in which cubic crystals of NaCl were clearly identified within the cavity (Fig. 5a,iv). To further test this encapsulation capability, green fluorescent sodium fluorescein (Fluo) was also entrapped into Zn-MOF-74 superstructures (Fig. 5a,v,vi), and the resulting Fluo@Zn-MOF-74 superstructures were incubated in MeOH for different periods. For each period, the dye content outside and inside the Zn-MOF-74 superstructures was quantified by UV–visible spectroscopy (Supplementary Fig. S18). Notably, dye levels remained constant for up to 8 h, confirming that sodium fluorescein was effectively encapsulated into the Zn-MOF-74 superstructures and that the superstructure walls were indeed impermeable (that is, they lacked any significant structural defects that would have led to fast release)[18].

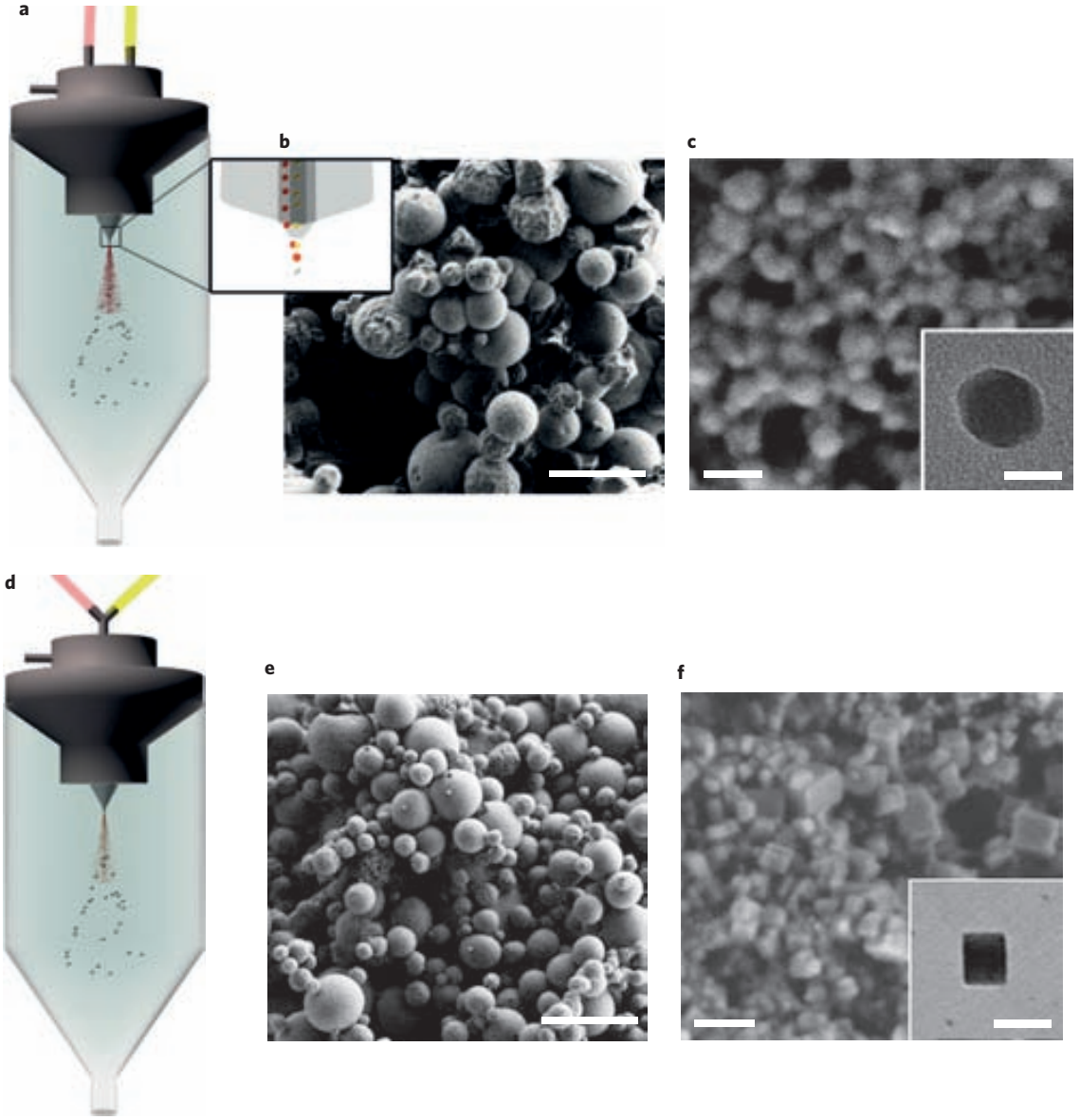

Figure 4 | Synthetic versatility in preparing MOF superstructures and nanoMOFs by spray-drying. a, Schematic showing the independent atomization of two solutions containing MOF precursors (example: metal salt solution, yellow; organic ligand, red). They are mixed within the drying chamber as a result of coalescence of the atomized droplets. **b**,**c**, Representative FESEM and TEM images of the spherical ZIF-8 superstructures (**b**) and discrete nanoZIF-8 crystals (**c**). **d**, Schematic showing the independent injection of two solutions containing precursors (represented in red and yellow) through two channels connected at the entrance of the two-fluid nozzle. **e**,**f**, Representative FESEM and TEM images of the spherical MOF-5 superstructures (**e**) and discrete nanoMOF-5 crystals (**f**). Scale bars: 10 μm (**b**,**e**), 100 nm (**c**,**f**), 50 nm (insets to **c**,**f**).

Another interesting feature of this encapsulation is that species (usually nonpolar ones) that are insoluble in the initial precursor solution (usually in polar solvents) can also be successfully entrapped inside the MOF superstructures. This is achieved by first dispersing or dissolving them in an oil, then creating an emulsion between the resulting oil phase and the precursor solution using a surfactant (Fig. 5b,i). When this emulsion is spray-dried, MOF superstructures that incorporate the guest species in their cavities are formed. For example, we produced fluorescent pyrene@HKUST-1 (Fig. 5b,ii) superstructures by spray-drying an oil-in-MOF precursor solution emulsion comprising Pluronic P-123 surfactant, lemon oil containing dissolved pyrene, and a solution of $Cu(NO_3)_2{\cdot}2.5H_2O$ and btc in a mixture of water and DMF (3:1).

Accordingly, spray-drying can be used not only to create hollow MOF superstructures but also to incorporate functional species within the cavities of these structures, thereby providing a new route to the design of highly sophisticated composites that also have the inherent properties of the entrapped species. For example, we envisage the incorporation of catalysts into these MOF superstructures to create new reactors, or the entrapment of magnetic nanoparticles to allow the MOF superstructures to be guided magnetically. As a first proof of concept, magnetic iron oxide nanoparticles were entrapped in HKUST-1 superstructures, as confirmed by TEM (Fig. 5c,iii), and the resulting iron oxide nanoparticle@HKUST-1 superstructures were used for magnetic solid-phase removal of the organosulfur dibenzothiophene (DBT) fuel contaminant[40,41]. To test this, the superstructures (50 mg), activated under vacuum at 150 °C for 12 h, were dispersed in a solution of 8,700 ppm DBT in isooctane (4 ml) at room temperature (Fig. 5c,i). Following an incubation period, the superstructures

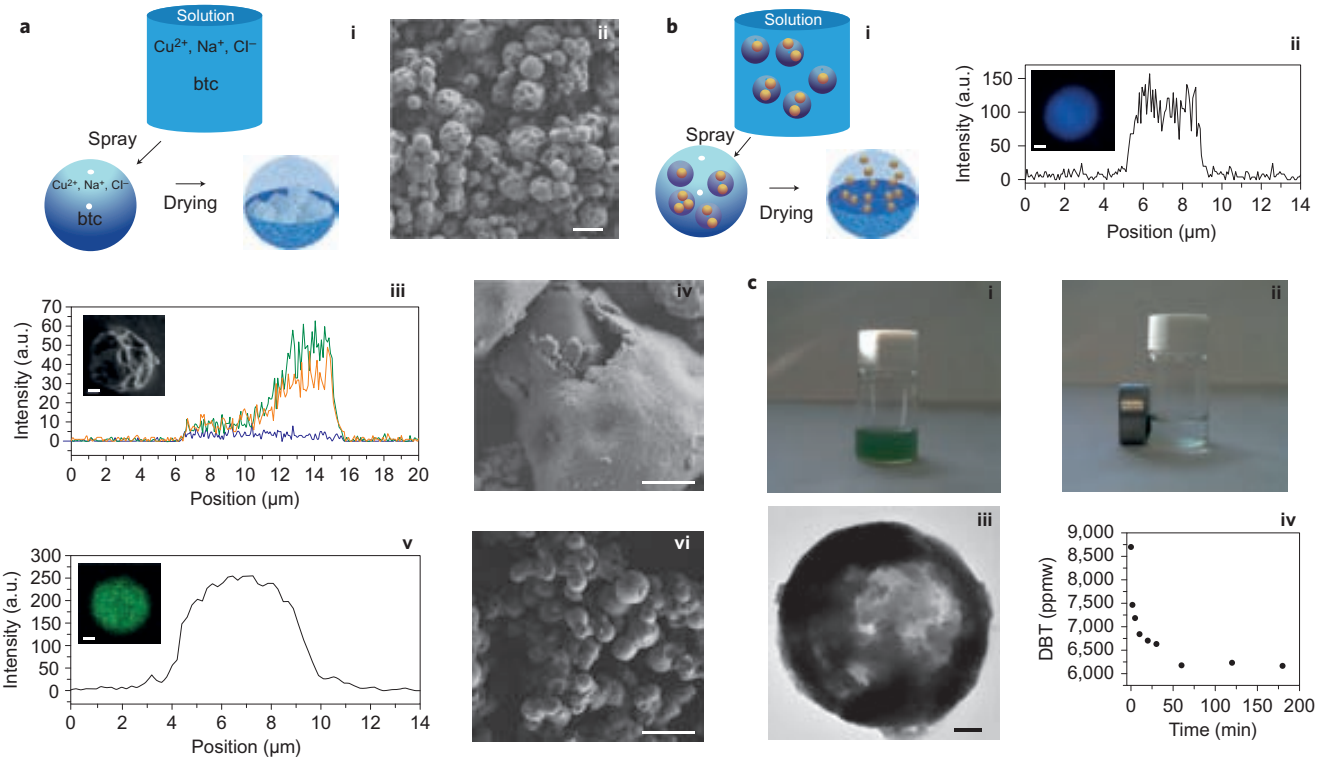

Figure 5 | Introduction of guest species into MOF superstructures by spray-drying. a, Entrapment of guest species (Na^+, Cl^-) that are soluble in the initial precursor solution within the MOF superstructures ($Cu_3(btc)_2$): (**i**) schematic showing the crystallization of NaCl cubic crystals (white) within the enclosed space of MOF superstructures (blue, only partially shown for clarity); (**ii**) representative FESEM image of golfball-shaped NaCl@HKUST-1 superstructures; (**iii**) EDX mapping of a single NaCl@HKUST-1 superstructure showing the Na (yellow), Cl (green) and Cu (blue) distribution, representative of NaCl crystals encapsulated within the MOF superstructures; (**iv**) FESEM image of a mechanically broken NaCl@HKUST-1 superstructure, also illustrating the presence of a single NaCl cubic crystal inside the internal void volume; (**v**) confocal fluorescence image of a single Fluo@Zn-MOF-74 superstructure (inset) and its corresponding fluorescence intensity profile; (**vi**) representative FESEM image of Fluo@Zn-MOF-74 superstructures. **b**, Entrapment of guest species that are not soluble in the initial precursor solution within the MOF superstructures by using emulsions: (**i**) schematic showing the entrapment of pyrene (orange) within the enclosed space of MOF superstructures (blue, only partially shown for clarity), by spray-drying an oil (purple spheres, lemon oil containing dissolved pyrene)-in-MOF precursor solution emulsion; (**ii**) confocal fluorescence image of a single pyrene@HKUST-1 superstructure (inset) and its corresponding fluorescence intensity profile. **c**, Iron oxide nanoparticle@HKUST-1 superstructure for magnetic solid-phase removal of DBT fuel contaminant: (**i**,**ii**) photography composition showing the magnetic attraction of iron oxide nanoparticle@HKUST-1 superstructures dispersed in a solution of DBT in isooctane when they are exposed to a magnet; (**iii**) representative TEM image of a single iron oxide nanoparticle@HKUST-1 superstructure, showing the inclusion of such nanoparticles inside the cavity of the MOF superstructure; (**iv**) time dependence of the removal of DBT. ppmw, parts per million weight. Scale bars: 5 μm (**a**,**ii**), 2 μm (**a**,**iii**), 1 μm (**a**,**iv**), 10 μm (**a**,**vi**), 200 nm (**c**,**iii**).

were collected by a magnet (Fig. 5c,ii), and the DBT content in the isooctane was determined by UV–visible spectroscopy. Redispersing the iron oxide nanoparticle@HKUST-1 superstructures and repeating this process for different incubation periods (up to 3 h) demonstrated the efficient extraction of 200 g DBT (or 35 g sulfur) per kg of superstructure (Fig. 5c,iv)[40], which was then easily removed from the solution by a magnet.

Conclusions

We describe a highly versatile and effective methodology to synthesize either nanoMOFs or hollow MOF superstructures. This strategy is applicable to a broad range of MOFs, drastically reduces their production times and costs, and enables continuous and scalable nanoMOF synthesis as well as solvent recovery. Furthermore, it allows the design of more sophisticated, hollow superstructures comprising multiple nanoMOFs assembled together, thereby opening up new avenues for fine-tuning their porosity. This method also enables simultaneous encapsulation of active species in the cavities of the MOF superstructures. Given the ever-expanding pool of MOFs and the versatile synthetic conditions offered by spray-drying, nanoMOFs can now be prepared readily, rapidly and with control over their composition and size. This, in turn, should facilitate their development and exploitation for numerous applications, including drug delivery, contrast agents, separation, catalysis, storage and sensor technology, capsules, reactors and highly complexity composites.

Methods

Materials. All reactants and solvents were purchased from Sigma-Aldrich, Chemicell and Romil, and were used without any further purification.

Spray-drying synthesis of hollow HKUST-1 superstructures and nanoHKUST-1 crystals using a two-fluid nozzle. A solution of 0.0017 M $Cu(NO_3)_2{\cdot}2.5H_2O$ and 0.0011 M btc in 500 ml of a mixture of DMF, ethanol and water (1:1:1) was spray-dried in a Mini Spray Dryer B-290 (BÜCHI Labortechnik) at a feed rate of 4.5 ml min^{-1}, a flow rate of 336 ml min^{-1} and an inlet temperature of 180 °C, using a spray cap with a 0.5-mm-diameter hole. After 2 h, 133 mg of a blue powder was collected. The powder was then redispersed in 10 ml of methanol and precipitated by centrifugation. This two-step washing process was repeated with dichloromethane. The final product, HKUST-1 superstructures (120 mg; capsule size, 2.5 ± 0.4 μm), was dried under vacuum for 12 h at 130 °C. Yield, 70%; purity, 90%.

Disassembled nanoHKUST-1 crystals were obtained by sonicating a dispersion of the HKUST-1 superstructures in methanol (130 W, 20 kHz). After 5 min of sonication, a stable blue colloid composed of well-dispersed nanoHKUST-1 crystals was formed. The resulting nanocrystals were then collected by centrifugation and redispersed in methanol. This centrifugation/redispersion process was repeated

twice, and the resulting nanocrystals (120 mg; particle size, 75±28 nm) were either redispersed in methanol or dried under vacuum for 12 h at 130 °C. Yield, 70%.

Following this protocol, optimal reaction conditions (solvent mixture, MOF precursor concentrations, inlet temperature, and feed and flow rates) were developed for the spray-drying synthesis of HKUST-1, sub-micrometre spherical HKUST-1 and HKUST-1/NOTT-100 superstructures, and Cu-bdc, NOTT-100, MOF-14, Zn-MOF-74, Ni-MOF-74, Mg-MOF-74, MIL-88A, MIL-88B and UiO-66 superstructures and nanocrystals (Supplementary Section S1).

Spray-drying synthesis of hollow nanoMIL-88A superstructures and nanoMIL-88A crystals using a three-fluid nozzle. A solution of 0.2 M $FeCl_3{\cdot}6H_2O$ in 5 ml of water and a solution of 0.2 M fumaric acid in 5 ml of water (adjusted to pH 7 with 2 M NaOH) were simultaneously spray-dried in a Mini Spray Dryer B-290 using a three-fluid nozzle, a feed rate of 2 ml min^{-1}, a flow rate of 474 ml min^{-1}, an inlet air temperature of 180 °C, and a spray cap with a 0.5 mm hole. A brown powder (76 mg; hollow MIL-88A superstructures) was collected after 5 min. The powder was added to 20 ml of DMF, and the resulting colloid was then sonicated to generate discrete nanoMIL-88A crystals. The crystals were washed using the same centrifugation/redispersion described above, with DMF, ethanol and water. The resulting nanocrystals (55 mg; mean length of each crystal, 300±70 nm) were air-dried for 24 h at room temperature. Yield, 40%; purity, 72%.

The spray-drying synthesis of nanoZIF-8 and nanoCu-PB using the three-fluid nozzle approach is described in Supplementary Section S1.

Spray-drying synthesis of hollow MOF-5 superstructures and nanoMOF-5 crystals using a two-fluid nozzle and two independent channels. A solution of 0.1 M $Zn(acetate)_2$ in DMF and a solution of 0.04 M bdc in DMF were independently pumped to a T-type connector, from which both solutions were mixed and spray-dried in a Mini Spray Dryer B-290 using a feed rate of 4 ml min^{-1}, a flow rate of 336 ml min^{-1}, an inlet temperature of 180 °C and a spray cap with a 0.5 mm hole. A white powder (700 mg; hollow MOF-5 superstructures) was collected after 20 min. The powder was then suspended in 60 ml of DMF, and the resulting suspension was then sonicated to generate discrete nanoMOF-5 crystals. The crystals were then collected and cleaned following the same centrifugation/redispersion described above, with DMF and dichloromethane. The resulting nanocrystals (350 mg; particle size, 60±20 nm) were dried under vacuum for 24 h at 150 °C. Yield, 60%; purity, 50%.

The spray-drying synthesis of nanoscale IRMOF-3 is described in Supplementary Section S1.

Entrapment of guest species inside the cavity of MOF superstructures. A solution or emulsion of the guest species (depending on its solubility) in the initial MOF precursor solution was prepared. For entrapment of NaCl, a solution of $Cu(NO_3)_2{\cdot}2.5H_2O$ (0.017 M), btc (0.011 M) and NaCl (0.017 M) in 50 ml of a 1:1:1 mixture of DMF, ethanol and water was prepared. For entrapment of iron oxide nanoparticles, 500 μl of an aqueous dispersion of iron oxide nanoparticles (concentration, 25 mg ml^{-1}) were added in an identical HKUST-1 precursor solution. For the entrapment of sodium fluorescein, a solution of $Zn(NO_3)_2{\cdot}6H_2O$ (0.017 M), dhbdc (0.056 M) and sodium fluorescein (0.0021 M) in 25 ml of DMF was prepared. For entrapment of pyrene, an emulsion was prepared: 0.1 g of pyrene was dispersed into 7.5 g of lemon oil containing 0.37 g of pluronic surfactant (P-123). This oil phase was then added into 30 ml of a mixture of DMF and water (1:3) containing 0.0017 M $Cu(NO_3)_2{\cdot}2.5H_2O$ and 0.0011 M btc, and the two phases were mixed (mechanical stirring; IKA T18 basic, Ultra–Turrax) for 10 min. The resulting solutions (NaCl and sodium fluorescein), dispersion (iron oxide nanoparticles) and emulsion (pyrene) were spray-dried in a Mini Spray Dryer B-290 using a feed rate of 4.5 ml min^{-1}, a flow rate of 336 ml min^{-1}, an inlet temperature of 180 °C and using a spray cap with a 0.5 mm hole. The resulting powders—comprising NaCl@HKUST-1, Fluo@Zn-MOF-74, iron oxide nanoparticle@HKUST-1 and pyrene@HKUST-1 superstructures, respectively—were collected, and then treated as before.

Received 27 September 2012; accepted 9 January 2013; published online 10 February 2013

References

1. Carné, A., Carbonell, C., Imaz, I. & Maspoch, D. Nanoscale metal–organic materials. *Chem. Soc. Rev.* **40,** 291–305 (2011).
2. Spokoyny, A. M., Kim, D., Sumrein, A. & Mirkin, C. A. Infinite coordination polymer nano- and microparticle structures. *Chem. Soc. Rev.* **38,** 1218–1227 (2009).
3. Lin, W., Rieter, W. J. & Taylor, K. M. L. Modular synthesis of functional nanoscale coordination polymers. *Angew. Chem. Int. Ed.* **48,** 650–658 (2009).
4. Horcajada, P. *et al.* Metal–organic frameworks in biomedicine. *Chem. Rev.* **112,** 1232–1268 (2012).
5. Horcajada, P. *et al.* Porous metal–organic-framework nanoscale carriers as a potential platform for drug delivery and imaging. *Nature Mater.* **9,** 172–178 (2010).
6. Rieter, W. J. *et. al.* Nanoscale metal–organic frameworks as potential multimodal contrast enhancing agents. *J. Am. Chem. Soc.* **128,** 9024–9025 (2006).
7. Kreno, L. E. Metal–organic framework materials as chemical sensors. *Chem. Rev.* **112,** 1105–1125 (2012).
8. Bétard, A. & Fischer, R. A. Metal–organic framework thin films: from fundamentals to applications. *Chem. Rev.* **112,** 1055–1083 (2012).
9. Scherb, C., Schödel, A. & Bein, T. Directing the structure of metal–organic frameworks by oriented surface growth on an organic monolayer. *Angew. Chem. Int. Ed.* **47,** 5777–5779 (2008).
10. Shimomura, S. *et al.* Selective sorption of oxygen and nitric oxide by an electron-donating flexible porous coordination polymer. *Nature Chem.* **2,** 633–637 (2010).
11. Bux, H. *et al.* Oriented zeolitic imidazolate framework-8 membrane with sharp H_2/C_3H_8 molecular sieve separation. *Chem. Mater.* **23,** 2262–2269 (2011).
12. Park, K. H., Jang, K., Son, S. U. & Sweigart, D. A. Self-supported organometallic rhodium quinonoid nanocatalysts for stereoselective polymerization of phenylacetylene. *J. Am. Chem. Soc.* **128,** 8740–8741 (2006).
13. Lu, G. *et al.* Imparting functionality to a metal–organic framework material by controlled nanoparticle encapsulation. *Nature Chem.* **4,** 310–316 (2012).
14. Ni, Z. & Masel, R. I. Rapid production of metal–organic frameworks via microwave-assisted solvothermal synthesis. *J. Am. Chem. Soc.* **128,** 12394–12395 (2006).
15. Vaucher, S. & Mann, S. Synthesis of Prussian blue nanoparticles and nanocrystal superlattices in reverse microemulsions. *Angew. Chem. Int. Ed.* **39,** 1793–1796 (2000).
16. Lee, H. J., Cho, W. & Oh, M. Advanced fabrication of metal–organic frameworks: template-directed formation of polystyrene@ZIF-8 core–shell and hollow ZIF-8 microspheres. *Chem. Commun.* **48,** 221–223 (2012).
17. Hu, M. *et al.* Synthesis of Prussian blue nanoparticles with a hollow interior by controlled chemical etching. *Angew. Chem. Int. Ed.* **51,** 984–988 (2012).
18. Ameloot, R. *et al.* Interfacial synthesis of hollow metal–organic framework capsules demonstrating selective permeability. *Nature Chem.* **3,** 382–387 (2011).
19. Yu, L. Amorphous pharmaceutical solids: preparation, characterization and stabilization. *Adv. Drug Deliv. Rev.* **48,** 27–42 (2001).
20. Reinhard, V. Pharmaceutical particle engineering via spray drying. *Pharm. Res.* **25,** 999–1022 (2008).
21. Boissiere, C. *et al.* Aerosol route to functional nanostructured inorganic and hybrid porous materials. *Adv. Mater.* **23,** 599–623 (2011).
22. Cheow, W. S., Li, S. & Hadinoto, K. Spray drying formulation of hollow spherical aggregates of silica nanoparticles by experimental design. *Chem. Eng. Res. Des.* **88,** 673–685 (2010).
23. Xu, H., Tan, Z., Abe, Z. & Naito, M. Microcapsule assembly of single-walled carbon nanotubes from spray-dried hollow microspheres. *J. Ceram. Soc. Jpn* **119,** 180–184 (2011).
24. Luo, P. & Nieh, T. G. Synthesis of ultrafine hydroxyapatite particles by a spray dry method. *Mater. Sci. Eng. C* **3,** 75–78 (1995).
25. Maas, S. G. The impact of spray drying outlet temperature on the particle morphology of mannitol. *Powder Tech.* **213,** 27–35 (2011).
26. Chui, S. S-Y. *et al.* Chemically functionalizable nanoporous material $[Cu_3(TMA)_2(H_2O)_3]_n$. *Science* **283,** 1148–1150 (1999).
27. Carson, C. G. *et al.* Synthesis and structure characterization of copper terephthalate metal–organic frameworks. *Eur. J. Inorg. Chem.* 2338–2343 (2009).
28. Chen, B. *et al.* High H_2 adsorption in a microporous metal–organic framework with open metal sites. *Angew. Chem. Int. Ed.* **44,** 4745–4749 (2005).
29. Surblé, S. *et al.* A new isoreticular class of metal–organic frameworks with the MIL-88 topology. *Chem. Commun.* 284–286 (2006).
30. Chen, B. *et al.* Interwoven metal–organic framework on a periodic minimal surface with extra-large pores. *Science* **291,** 1021–1023 (2001).
31. Rosi, N. L. *et al.* Rod packings and metal–organic frameworks constructed from rod-shaped secondary building units. *J. Am. Chem. Soc.* **127,** 1504–1518 (2005).
32. Cavka, J. H. *et al.* A new zirconium inorganic building brick forming metal organic frameworks with exceptional stability. *J. Am. Chem. Soc.* **130,** 13850–13851 (2008).
33. Park, K. S. *et al.* Exceptional chemical and thermal stability of zeolitic imidazolate frameworks. *Proc. Natl Acad. Sci. USA* **103,** 10186–10191 (2006).
34. Kaye, S. S. & Long, J. R. Hydrogen storage in the dehydrated Prussian blue analogues $M_3[Co(CN)_6]_2$ (M=Mn, Fe, Co, Ni, Cu, Zn). *J. Am. Chem. Soc.* **127,** 6506–6507 (2006).
35. Li, H., Eddaoudi, M., O'Keeffe, M. & Yaghi, O. M. Design and synthesis of an exceptionally stable and highly porous metal–organic framework. *Nature* **402,** 276–279 (1999).
36. Eddaoudi, M. *et al.* Systematic design of pore size and functionality in isoreticular MOFs and their application in methane storage. *Science* **295,** 469–472 (2002).
37. Lin, X., Jia, J., Hubberstey, P., Schröder M. & Champness, N. R. Hydrogen storage in metal–organic frameworks. *CrystEngComm* **9,** 438–448 (2007).
38. Li, X. A. *et al.* Nanospray drier nanoparticles by spray drying using innovative new technology: the Buchi Nano Spray Drier B-90. *J. Control. Rel.* **147,** 304–310 (2010).

39. Chalati, T., Horcajada, P., Gref, R., Couvreur, P. & Serre, C. Optimisation of the synthesis of MOF nanoparticles made of flexible porous iron fumarate MIL-88[a] *J. Mater. Chem.* **21,** 2220–2227 (2011).
40. Cychosz, K. A., Wong-Foy, A. G. & Matzger, A. J. Liquid phase adsorption by microporous coordination polymers: removal of organosulfur compounds. *J. Am. Chem. Soc.* **130,** 6938–6939 (2008).
41. Cychosz, K. A., Wong-Foy, A. G. & Matzger, A. Enabling cleaner fuels: desulfurization by adsorption to microporous coordination polymers. *J. Am. Chem. Soc.* **131,** 14538–14543 (2009).

Acknowledgements

The authors acknowledge the Servei de Microscopia of the UAB, and Carlos Carbonell for helping with the illustrations. I.I. and M.C.S. thank MICINN and ICN for a Ramón y Cajal grant and a research contract, respectively. A.C. thanks the Generalitat de Catalunya for a FI fellowship.

Author contributions

A.C., I.I. and M.C.S. designed the experiments, performed the syntheses and carried out the characterization, encapsulation and property studies. D.M. conceived the project and drafted the manuscript. All authors discussed the results and commented on the manuscript.

Additional information

Supplementary information is available in the online version of the paper. Reprints and permission information is available online at http://www.nature.com/reprints. Correspondence and requests for materials should be addressed to D.M.

Competing financial interests

The authors have a patent pending on the methods described in this manuscript, filed on 4 October 2011 (European Union application number EP 11183773.8).

ChemPubSoc Europe

DOI: 10.1002/chem.201304529

CHEMISTRY A European Journal Concept

Metal–Organic Frameworks

Metal–Organic Frameworks: From Molecules/Metal Ions to Crystals to Superstructures

Arnau Carné-Sánchez,[a] Inhar Imaz,[a] Kyriakos C. Stylianou,[a] and Daniel Maspoch*[a, b]

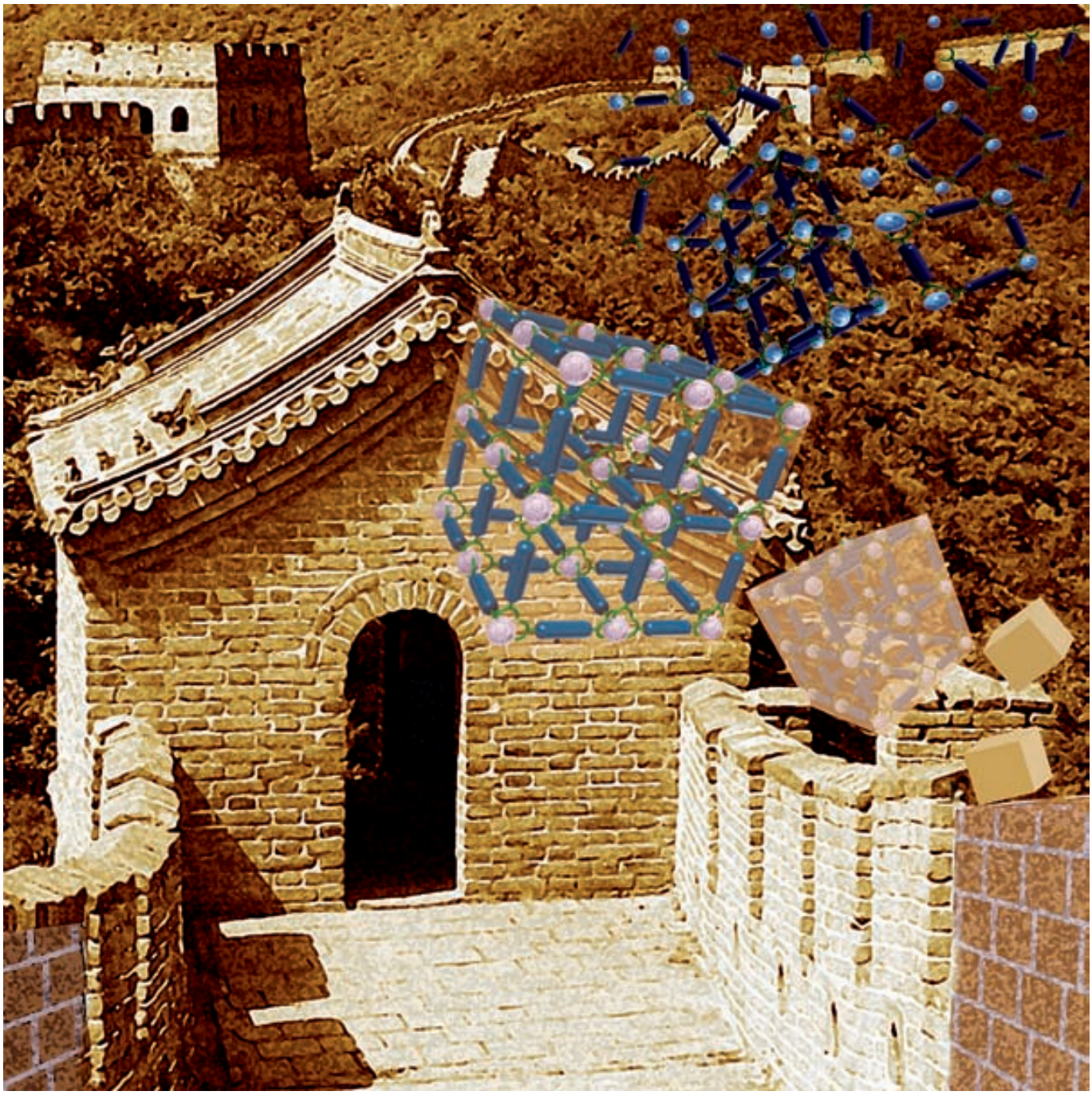

Abstract: Metal–organic frameworks (MOFs) are among the most attractive porous materials known today, exhibiting very high surface areas, tuneable pore sizes and shapes, adjustable surface functionality, and flexible structures. Advances in the formation of MOF crystals, and in their subsequent assembly into more complex and/or composite superstructures, should expand the scope of these materials in many applications (e.g., drug delivery, chemical sensors, selective reactors and removal devices, etc.) and facilitate their integration onto surfaces and into devices. This Concept article aims to showcase recently developed synthetic strategies to control the one-, two- and three-dimensional (1-, 2- and 3D) organisation of MOF crystals.

Introduction

As atoms are used to make molecules, and molecules, to make objects (e.g., crystals, nanoparticles, vesicles, etc.), the resulting objects in turn can be used to make new structures. The self-assembly of discrete objects ranging in size from nanometres to micrometres—and also to millimetres—leads to superstructures (also known as higher-order structures).[1] This type of self-assembly is especially attractive for three reasons: firstly, different objects that are separately fabricated by incompatible processes and that have different functionalities can be combined into a single composite superstructure that incorporates the respective properties of each component; secondly, the resulting superstructures can exhibit collective and/or synergic properties arising from the assembly; and lastly, the self-assembly of objects into 1-, 2- and 3D superstructures is a simple route for shaping and dimensionalising them to facilitate their spatial integration onto or into functional surfaces and devices and enables the use of these composite materials in otherwise inaccessible applications. These characteristics, which transcend the possibilities of molecular self-assembly, make the self-assembly of objects across extended and multiple length scales—basically how nature constructs extremely complex and multifunctional systems—a very powerful strategy to access unique systems and classes of structurally and functionally diverse materials.

MOF Superstructures

We would like to suggest here that making superstructures from the self-assembly of objects—a strategy highly developed for inorganic nanoparticles—can also be applied to metal–organic frameworks (MOFs). MOFs are a fledgling class of crystalline materials comprising one or more metal components and one or more organic components arranged in highly organised porous structures. They have garnered great attention for their potential in areas such as gas storage and catalysis. We believe that the self-assembly of MOF crystals is particularly useful in making advanced MOF-based architectures the characteristics of which (e.g., size, shape, functionality, etc.) would be too complex to obtain by means of traditional chemical synthesis. These novel materials are MOF superstructures: higher-dimensionality structures resulting from the 1-, 2- and 3D organisation of MOF crystals. This definition includes those structures made not only of self-assembled MOF crystals, but also of MOF crystals self-assembled with other materials to make MOF composite superstructures.

In this Concept article, we will discuss recently developed strategies for the self-assembly of MOFs, either alone or together with other components, into superstructures. This work includes methods to control the 1-, 2- and 3D organisation of MOF crystals. Using illustrative examples, we classify the processes leading to MOF superstructures and identify four main approaches: 1) spontaneous higher-order assembly, 2) self-assembly using hard templates, 3) self-assembly using soft templates and 4) self-templated synthesis.

Spontaneous Higher-Order Assembly

Figures 1 and 2 show the self-assembly of MOF crystals in solution without the use of templates. Under these conditions, the self-assembly is governed by the balance of attractive forces (e.g., electrostatic interactions between opposite charges, hydrogen-bonding, van der Waals interactions, etc.) and repulsive forces (e.g., electrostatic interactions between similar charges, steric forces, etc.) among the MOF crystals as well as between these crystals and the solvent. Through spontaneous organisation of MOF crystals without the use of templates, researchers have created a few promising 1-, 2- and 3D extended superstructures and mesocrystals.

Extended superstructures

The formation of extended networks from objects dispersed in a liquid is facilitated by inter-object interactions, such as electrostatic, steric or van der Waals forces, and dipole–dipole interactions.[1c] The fact that these interactions can strongly influence the organisation of MOF crystals, even in solution, was confirmed by Granick and Yanai.[2] They observed that upon addition of sodium nitrate to a solution of colloidal ZIF-8[3] crystals in ethylene glycol, the van der Waals interactions between the flat facets of the crystals were sufficiently strong to drive the self-assembly of the crystals into objects of various shape (e.g., linear, triangular and U-shaped trimmers and linear, rhombic and square tetramers). In this section, we also refer the reader to an excellent recent review article by Granick et al. that addresses the synthesis, stability and assembly of colloidal MOF crystals.[4]

[a] *A. Carné-Sánchez, Dr. I. Imaz, Dr. K. C. Stylianou, Prof. D. Maspoch*
Supramolecular NanoChemistry and Materials Group
ICN2-Institut Catala de Nanociencia i Nanotecnologia, Campus UAB
08193 Bellaterra, Barcelona (Spain)
E-mail: daniel.maspoch@icn.cat

[b] *Prof. D. Maspoch*
Institució Catalana de Recerca i Estudis Avançats (ICREA)
08100 Barcelona (Spain)

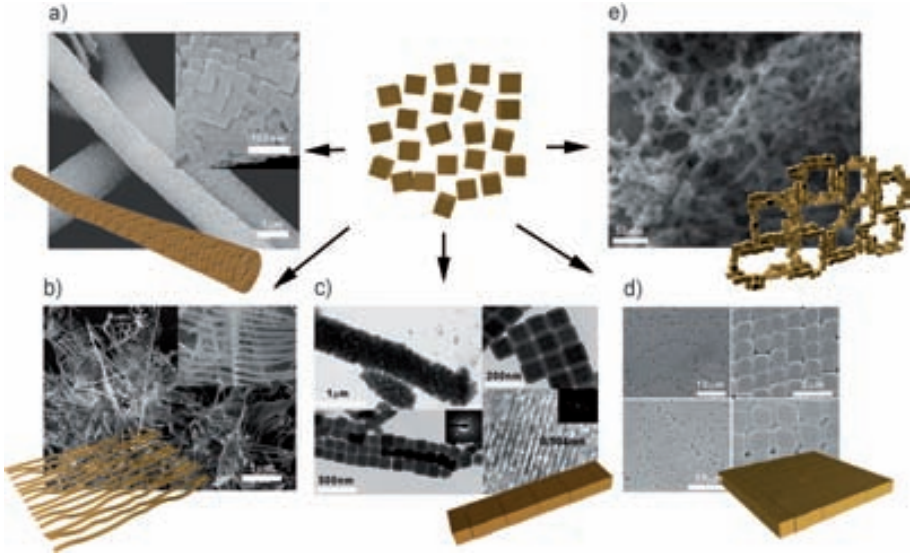

Figure 1. Schematic of the spontaneous organisation of MOF crystals into microrod-like or fishbone-like superstructures, 2D superlattices, or non-ordered hierarchical superstructures. a)–c) Scanning electron microscopy (SEM) and transmission electron microscopy (TEM) images of the self-assembly of Prussian Blue nanocrystals into a) microrod-like and b) fishbone-like superstructures, and c) 2D superlattices. Reproduced with permission of from reference [7]. d) SEM image of M^{III}-soc-MOF microcrystals self-assembled on surfaces in 2D superlattices. Reproduced with permission from reference [9]. e) SEM image of a non-ordered, hierarchical superstructure self-assembled from MOF-74 nanocrystals. Reproduced with permission from reference [11b].

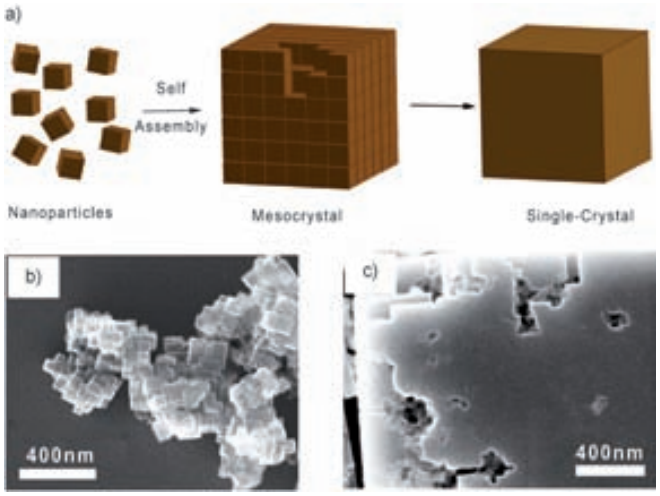

Figure 2. a) Schematic of the formation of mesocrystals built up from the oriented attachment and fusion of nanocrystals. b) SEM image that corresponds to the initial stage of the mesocrystal growth of Prussian Blue. c) SEM image of cubic mesocrystals prepared by the oriented attachment of Prussian Blue nanocrystals. Reproduced with permission from reference [15].

One common method for developing long-range (and also 3D) periodicity involves the evaporation-induced self-assembly of highly monodispersed objects of well-defined shape.[5] For instance, Granick and Yanai obtained tightly packed hexagonal arrangements of the aforementioned colloidal ZIF-8 crystals by drying a suspension of these crystals in *N,N'*-dimethylformamide at 60 °C. In another example, Wu et al. created microrod- and fishbone-like superstructures, and 2D superlattices of Prussian blue by drying an aqueous dispersion of pre-formed cubic Prussian blue[6] nanocrystals (size: 120 nm) under vacuum (see Figure 1 a–c)[7] Significantly, the morphology of the products was highly dependent on the evaporation rate: at higher rates, the rod-like superstructures were favoured, whereas at lower rates, the fishbone-like and 2D superlattices were favoured. The solvent-induced assembly of MOFs is not necessarily restricted to the nanoscale, as exemplified by the creation of large-area, 2D superlattices from the self-assembly of highly monodisperse, cubic microscale (size: 0.9 to 1.5 μm) crystals of M-soc-MOF ($[M_3O(abtc)_{1.5}(H_2O)_3]NO_3 \cdot 3H_2O$;[8] M = In^{III} and Ga^{III}; abtc = 3,3′,5,5′-azobenzenetetracarboxylate; soc = square octahedron) on surfaces (see Figure 1 d).[9]

Interestingly, Granick et al. recently reported that external forces are also important factors to consider for promoting the assembly of MOF crystals.[10] They showed that colloidal ZIF-8 crystals could be aligned "facet-to-facet" into well-defined chains under an external electric field. Once alternating voltages at suitable frequencies were applied to a colloidal solution of ZIF-8 crystals in ethylene glycol, dipoles were induced to bring the crystals close together. This proximity enabled the facet-to-facet adhesion by van der Waals interactions.

In special cases, the formation of amorphous coordination polymers can also induce the spontaneous self-assembly of MOFs into superstructures.[11] For example, simply mixing zinc acetate and 2,5-dihydroxy-1,4-benzenedicarboxylic acid in *N,N'*-dimethylformamide leads to the formation of non-ordered, hierarchical superstructures that comprises an amorphous matrix in which Zn-MOF-74[12] nanocrystals are embedded (see Figure 1 e).[11b] These superstructures show a bimodal pore size distribution: as a result of being formed by microporous Zn-MOF-74 crystals and a mesoporous amorphous matrix, they exhibit both meso- and microporosity.

Mesocrystals

The formation of MOF superstructures can be closely related to crystallisation. In classic crystallisation theory, the process starts from the formation of a stable nucleus, followed by a simple enlargement of the nuclei by unit-cell replication, through growth of the building blocks (atoms, ions, molecules and small clusters) on the nuclei surfaces. The final product is a single crystal, the morphology of which is determined by its intrinsic structure.[1] However, there is a growing number of examples of non-classical crystallisation processes that involve

the oriented attachment and partial fusion of nanoparticles/crystals, which results in the formation of mesocrystals (see Figure 2a). Mesocrystal is an abbreviation of mesoscopically-structured crystal: an ordered superstructure of sub-microscale crystals (size: 1 to 1000 nm). To explain the formation of mesocrystals, one must consider a non-classical (i.e., nanoparticle-based) crystallisation, rather than a classical (i.e., atom, ion, molecule or cluster-based) mechanism. Examples of non-classical processes include the oriented-attachment mechanism proposed by Banfield et al.,[13] and that of grain-growth after grain-rotation and coalescence (in polycrystalline materials). Cölfen and Antonietti recently described a mechanism, which they called the non-classical crystallisation mechanism,[14] that comprises three pathways: 1) oriented attachment of nanoparticles, 2) crystallisation of amorphous or liquid precursors and 3) mesoscale assembly of primary nanoparticles. They attributed this mechanism in the formation of certain biomineral, organic and inorganic superstructures by mesoscale self-assembly of monodispersed nanoparticles.[14]

Recent studies have begun to show that MOFs can crystallise through the oriented attachment and fusion of MOF nanocrystals to create mesocrystals or superstructures. For example, Xie et al., assembled Prussian blue nanoparticles, under hydrothermal conditions and in the presence of glucose, into microscale cubic or frame-like superstructures (see Figure 2b).[15] Time-dependent experiments (40 min, 1.5 h and 2.5 h) confirmed the initial formation of cube-shaped nanoparticles (size: ca. 10 to 20 nm) at short times, and formation of mosaic superstructures with small deviations in orientation at longer times. Interestingly, when Jiang et al. performed similar work with Prussian blue in which they introduced HCl into the reaction, they obtained microscale octahedra.[16]

Self-Assembly Using Hard Templates

The use of physical templates (e.g., polymeric and silica particles, alumina membranes, etc.) as scaffolds is a general, well-known strategy for making superstructures.[1] For MOFs, hard template-directed strategies should exploit templates with active sites on their surfaces that can facilitate the nucleation and growth of MOF crystals. One way to do this is by functionalising the surface of the templates before using them. Interesting functional groups include carboxylic, hydroxyl, sulfonate and phosphonic/phosphate groups, and N-based molecules; basically, those that are currently used to make MOFs. Another way is to use templates comprising metal ions such as metal oxides. In both of these strategies, the idea is to increase the chemical affinity between the MOF precursor (functional group or metal ion) and the surface template at the solid/liquid interface. This enables coordination (and consequently, MOF crystal growth) to be selectively done on the template surface. In fact, this approach has been extensively applied to grow MOFs on large areas[17] (e.g., to create MOF membranes for gas separation) as well as to selectively position MOFs onto functionalised surfaces (e.g., containing $-COOH$, $-OH$ and $-NH_2$).[18]

Based on the aforementioned results, hard-template synthesis offers major potential for the preparation of MOF superstructure composites or freestanding MOF superstructures, whereby the removal of the template triggers the formation of the desired superstructure (e.g., hollow spheres).

MOF composite superstructures

The recent use of particles, membranes and ordered structures containing these active sites as hard templates suggests that this approach might become very important for synthesising MOF superstructure composites of diverse composition and shape:

Organic polymer microparticles

Oh et al. used carboxylate-terminated polystyrene spheres (diameter: ca. 900 nm) as templates to prepare polystyrene@ZIF-8 core-shell composites. They prepared a thin, nanoscale layer of ZIF-8 nanocrystals around the polystyrene spheres by simply exposing the spheres to a methanolic solution of ZIF-8 precursors twice for 10 min at 70 °C.[19]

Mesoporous SiO_2 microparticles

MOF/SiO_2 composites can incorporate the microporosity of MOFs and the mesoporosity of SiO_2 microparticles. For instance, Coronas et al. prepared a uniform ZIF-8 layer (thickness: 700 nm) around mesoporous SiO_2 spheres (diameter: 3 μm).[20] They started by preparing a ZIF-8 seed layer on the surface of silica spheres. Owing to the attractive interactions between the terminal hydroxyl groups of the silica and the Zn^{II} ions, this step simply required stirring the SiO_2 spheres in an aqueous solution of zinc nitrate and 2-methylimidazole for 5 min. The seeded microspheres were then mixed twice in a solution of the same ZIF-8 precursors. Exploiting a similar functionalisation, Zhang et al. employed SiO_2 microparticles as templates: they immobilised Cu^{II} ions onto the microparticles surface, in order to promote the surface synthesis of HKUST-1.[21,22]

Inorganic nanoparticles

Given that inorganic nanoparticles (e.g., gold, silver and iron oxide) can be easily functionalised with surfactants and molecules containing active functional groups, they can serve as excellent templates for MOF crystallisation.[23] For example, Qiu et al. used iron oxide nanoparticles as a template to synthesise HKUST-1 and Fe-MIL-100[24] crystals (Figure 5a and b, later). They synthesised core–shell Fe_3O_4@HKUST-1/MIL-100 composite superstructures by using a stepwise methodology, in which mercaptoacetic acid functionalised iron oxide nanoparticles were alternatively dispersed in solutions of the corresponding metal salt and organic ligand precursors in ethanol.[25] More recently, Kim, Ahn and Moon et al. reported a microfluidic-based technology that enables the solvothermal and hydrothermal synthesis of MOFs and MOF-composite superstructures in microdroplets.[26] Fe_3O_4@ZIF-8 composites were generated by a two-step, continuous process. Firstly, the iron oxide precursor solution and the oil phase were injected and

reacted in a microreactor at 80 °C for 2 min. Then, the resulting iron oxide particles were transported downstream to a second microreactor, to merge and react with a mixture of ZIF-8 precursor (zinc nitrate and 2-methylimidazolate in methanol, and polystyrenesulfonate) at 50 °C. The initial functionalisation of the iron oxide particles with polystyrenesulfonate induced the selective growth of ZIF-8 nanocrystals on the particle surfaces, affording core-shell Fe_3O_4@ZIF-8 composite superstructures (dimensions: 700 ± 50 nm).

Alumina oxide membranes and nanoparticles

Metal oxides can act as the metal source for MOF crystallisation. For instance, alumina oxide is an excellent source of Al^{III} ions. Kitagawa et al. have described a fascinating methodology in which they used a 2D alumina template that acts first as an Al^{III} source, and then as a structural directing agent (see Figure 3 a), in a process that mimics the pseudomorphic mineral replacement observed in geology.[27] The alumina template was first immersed in an aqueous solution of 1,4-naphthalene dicarboxylic acid (H_2ndc), and then heated by microwave irradiation. It initially reacted with the naphthalene dicarboxylic acid ligand to form the 3D MOF [Al(OH)(ndc)],[28] which is composed of infinite 1D chains of $Al(OH)_2O_4$ functionalised with the naphthalene dicarboxylate ligand. Careful design of the template enabled the formation of a 2D superstructure, which combines the mesoporosity of the parent aluminium oxide with the intrinsic microporosity of the 3D porous MOF (see Figure 3 b). The authors then applied the same concept using a 3D alumina template, thereby obtaining a 3D composite superstructure. Interestingly, they investigated the capacity of their 2D and 3D superstructure composites for water/ethanol separation, and found that the 3D superstructure was faster. More recently, the same authors extended this concept to create Au nanorod@alumina@[Al(OH)(ndc)] superstructures (see Figure 4), in which they were able to photothermally control the release of adsorbed species (e.g., anthracene).[29]

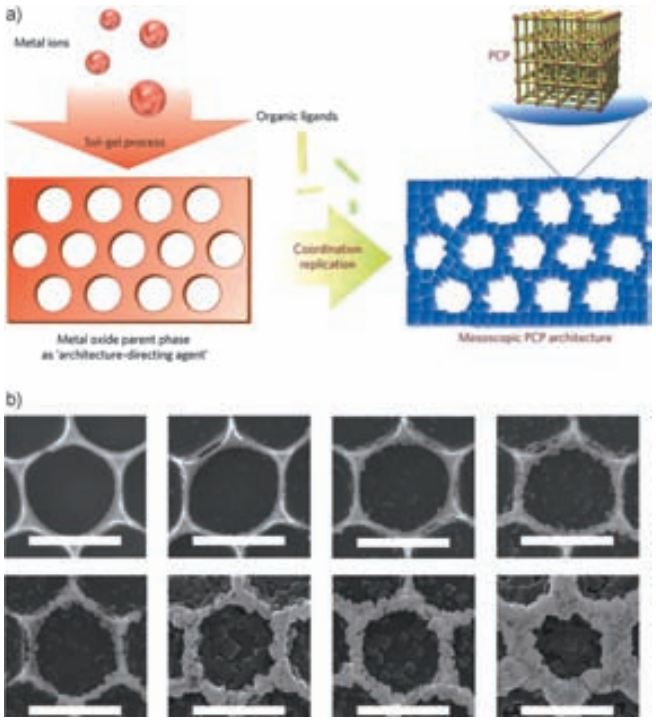

Figure 3. a) Schematic of the preparation of MOF superstructures using a metal oxide membrane that serves as both metal source and structural directing agent. b) SEM images showing the time course of the coordination replication of an alumina oxide template to a 2D superstructure based on [Al(OH)(ndc)] (ndc = 1,4-naphtalene dicarboxylate) crystals. The scale bars correspond to 1 μm. Reproduced with permission from reference [27].

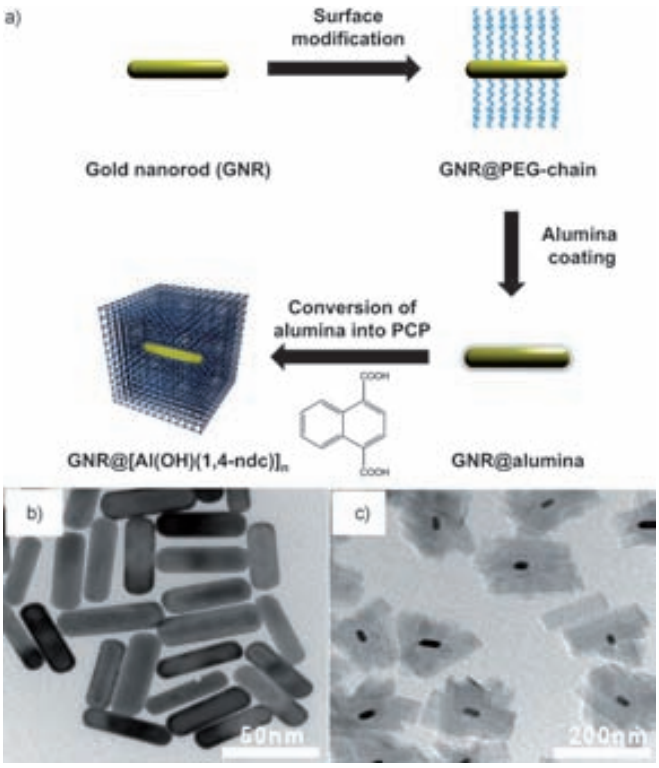

Figure 4. a) Illustration of the protocol developed to synthesise Au nanorod@alumina@[Al(OH)(ndc)] superstructures. b) and c) TEM images showing the Au nanorods used as b) templates and the c) resulting superstructures. Reproduced with permission from reference [29].

3D Ordered macroporous inverse-opal structures

Ordered macroporous MOF superstructures prepared from opaline templates can incorporate the excellent optical properties of these templates—namely, the bright colours generated by diffraction of light. Li et al. first used a 3D-ordered, macroporous polystyrene inverse-opal as a template to synthesise a 3D-ordered, macroporous and photonic HKUST-1 superstructure.[30] They synthesised this superstructure by infiltration of a carboxylic-functionalised polystyrene template with a DMSO solution of the HKUST-1 precursors (copper nitrate and trimesic acid). The solvent was then evaporated off at 90 °C, and the template was subsequently removed with tetrahydrofuran, resulting in the formation of a bright-red colour HKUST-1 superstructure. Importantly, the authors then investigated the optical response of this superstructure upon guest adsorption, and

found that exposure of the superstructure to organic solvents (e.g., ethanol, toluene, cyclohexane, etc.) for 30 min led to a clear shift in the UV/Vis spectrum. They also used this methodology to produce 3D-ordered, macroporous ZIF-8 superstructures, which after exposure to methanol underwent a large blue shift (≈75 nm, as detected by the naked eye), thereby confirming that these superstructures offer high potential for use as label-free sensors.

Freestanding MOF superstructures

As stated above, the formation of freestanding MOF superstructures using hard templates requires removal of the template. Therefore, any MOFs that are to be used in this methodology must be stable to the removal step. A pioneering work that proved the feasibility of this concept—although the product was not a MOF superstructure—was reported by Martin et al., who utilised alumina membranes as sacrificial templates for synthesising metal–organic Zr^{IV}–phosphonate nanotubes.[31] In their methodology, a film of a coordination polymer is initially deposited on the template by means of layer-by-layer deposition. Subsequent removal of the template by thermal or chemical techniques (e.g., using phosphoric acid) leaves behind a tubular structure, the size and shape of which mimic that of the template. Using the same approach, Oh et al. reported the first freestanding MOF superstructures synthesised using sacrificial templates. They dissolved the polystyrene core of the aforementioned polystyrene@ZIF-8 composites[19] by immersing the spherical composites in *N,N′*-dimethylformamide to obtain hollow spherical superstructures, composed of tightly-packed ZIF-8 nanocrystals. They were able to control the thickness of the sphere wall by regulating the number of growth cycles (i.e., the number of times that the template was alternately exposed to either of the two MOF precursor solutions). Interestingly, a minimum thickness of about 50 to 100 nm, corresponding to 2 to 3 growth cycles, was determined to be critical for the stability of the superstructures produced. Using the same strategy, Qiu et al. synthesised hollow HKUST-1 and Fe-MIL-100 superstructures.[33] In this case, polystyrene particles were coated with sulfonate groups, and then alternately exposed to either of the two MOF precursor solutions. The authors confirmed that the thickness of the MOF layer around the particles increased with the number of growth cycles and that a critical thickness (e.g., ca. 40 to 45 nm for a minimum of 50 cycles for Fe-MIL-100; see Figure 5a and b) was required for stability of the final superstructures.

Peng et al. recently published an uncommon, but very promising approach to prepare freestanding 2D MOF superstructures.[34] They demonstrated the use of copper hydroxide nanostrand thin films to grow HKUST-1 crystals on the film surfaces until the films are completely consumed, thereby leading to the formation of free-standing HKUST-1 membranes (see Figure 5c and d). Here, the templates act as an excellent source of Cu^{II} ions as well as a structural directing agent. The authors immersed the copper hydroxide thin films in a solution of trimesic acid, water and ethanol at room temperature for 2 h. In related work, Li et al. produced freestanding HKUST-1 and ZIF-8 membranes by using electrospun fibrous mats as templates, which they then simply removed with organic solvents such as ethanol and tetrahydrofuran.[35]

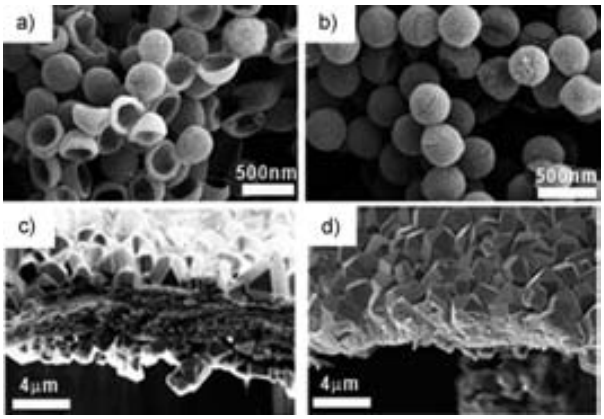

Figure 5. Examples of freestanding MOF superstructures. a) and b) SEM images of hollow, spherical Fe-MIL-100 superstructures synthesised after a) 10 and b) 50 growth cycles. Reproduced with permission from reference [33]. c) and d) SEM images showing the formation of a 2D HKUST-1 superstructure on a copper hydroxide nanostrand thin film after c) 30 min of reaction, and the resulting freestanding HKUST-1 superstructure after d) 2 h of reaction. Reproduced with permission from reference [34].

Self-Assembly Using Soft Templates

Figure 6 illustrates the self-assembly of MOF crystals using soft templates to prepare MOF-based superstructures. MOF synthesis and subsequent self-assembly can be done at the liquid/liquid interface or at the liquid/air interface.

Liquid/liquid interface

This approach, commonly known as interfacial synthesis, is based on first mixing and structuring two non-miscible solvents containing the MOF precursors, and then localising the MOF reaction/crystallisation at the liquid/liquid interface between the two solvents. To date, crystallisation processes at liquid/liquid interfaces have been extensively involved in the preparation of inorganic or polymeric hollow capsules, and have been found to strongly depend on the stabilisation of these interfaces.

A common way to achieve stable liquid/liquid interfaces is through the use of emulsions. The interface between the two liquids can be used to localise the coordination, nucleation and growth of MOFs. This approach usually comprises three steps: 1) dissolving each precursor in the solvent to be dispersed, 2) preparing water-in-oil (w/o) or reverse (o/w) emulsions with a surfactant and 3) reacting the MOF precursors in order to spontaneously induce the coordination and thereby limit the MOF growth to the liquid/liquid interface. The reaction can be driven, for example, by mechanical collision of droplets, or by application of an external stimulus, such as temperature, light or microwave radiation. The precise localisation of the coordination at liquid/liquid interfaces was recently

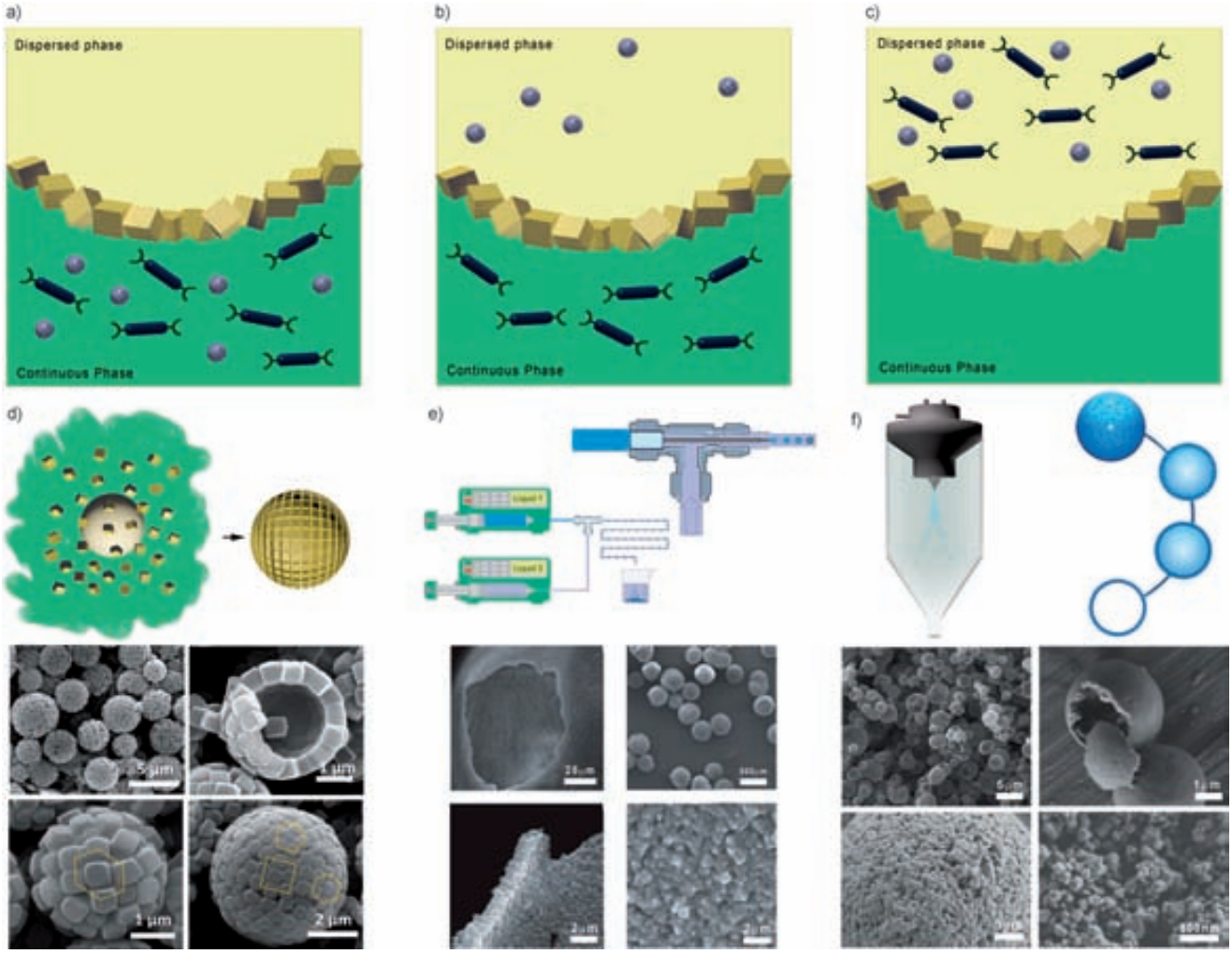

Figure 6. a)–c) Schematics showing the relative position of the MOF precursors in the two phases (liquid or air) in the soft-template strategies used to create MOF superstructures. d) Schematic showing the self-assembly of MOF crystals (formed in the aqueous phase) at the oil/water interface (top). Representative SEM images of spherical superstructures comprising self-assembled Fe-soc-MOF (soc = square octahedron) crystals (bottom). Reproduced with permission from reference [37]. e) Schematic showing the formation of microdroplets of one liquid in another liquid, achieved through microfluidics (top). Representative SEM images of hollow, spherical macroscale HKUST-1 superstructures synthesised using the microfluidics method. Reprinted with permission from reference [42]. f) Schematic showing the spray-drying technique for the growth of hollow, spherical superstructures, and the proposed mechanism of formation (top). SEM image of hollow, spherical, macroscale HKUST-1 superstructures fabricated with the spray-drying technique (bottom). Reproduced with permission from reference [43].

reported by Wang et al., who used an organometallic surfactant terminated with cyanoferrate groups to stabilise an o/w emulsion and localise the coordination of Fe^{III} ions present in the water phase at the boundary of each oil droplet.[36] Following this principle, Eddaoudi et al. prepared very homogeneous Fe-soc-MOF hollow superstructures made of a monolayer shell of assembled microscale cubic crystals (see Figure 6d).[37] They prepared an emulsion containing the MOF precursors (iron nitrate and 3,3′,5,5′-azobenzenetetracarboxylic acid) by stirring a mixture of the precursors and water, dimethylsulfoxide, acetonitrile, *tert*-butylamine and the surfactant polyoxyethylene sorbitan trioleate (Tween-85) at room temperature for 1 h. The resulting emulsion was heated to 120 °C for 2 h with continuous stirring. After heating, highly monodisperse Fe-soc-MOF cubes were formed at the liquid/liquid interface of the droplets, where they self-assembled into spherical hollow superstructures with walls composed of tightly packed MOF crystals. Interestingly, the authors showed that the size of the droplets in the emulsion (and therefore, the diameter of the resulting superstructures) could be controlled by modulating the quantity of surfactant: by using more surfactant, they obtained smaller droplets and consequently, smaller superstructures. For example, at 0.01–0.03 mL of Tween-85, the superstructures had a diameter of about 10 to 20 μm and were composed of 1400 to 2800 crystals, whereas at 0.05 mL of Tween-85, the superstructures had a diameter of about 3 to 5 μm and were composed of only 30 to 200 crystals.

Related work has been done with Pickering emulsions, which are emulsions stabilised by solid particles that adsorb at the liquid/liquid interface, owing to their partial wetting by both phases. Examples of particles used to create these emulsions include those of silica, bacteria, proteins, gold, clay, metal

oxides, carbon black, latex colloids,[38] and more recently, MOFs.[39] Bradshaw et al. exploited the ability of MOF nanocrystals to stabilise Pickering emulsions in order to synthesise hollow, microscale polystyrene capsules containing nanocrystals of two MOFs (ZIF-8 and MIL-101[40]) in the walls.[41] The authors first stabilised o/w Pickering emulsions with pre-synthesised nanocrystals of both MOFs, and then performed controlled polymerisation of the styrene and divinylbenzene contained in the oil phase. In terms of potential applications, the combination of microporous MOF nanocrystals with a hierarchically structured polymer membrane appeared to be effective for the retention of encapsulated dye molecules.

Other researchers have designed more-sophisticated methods for structuring and stabilising liquid droplets of a MOF solution in one solvent added to a MOF solution in a second, immiscible solvent. For example, De Vos et al.[42] have devised a microfluidics-based procedure for the fabrication of hollow, spherical, macroscale MOF superstructures (diameter: ca. 500 μm) containing HKUST-1 nanocrystals (see Figure 6e). The HKUST-1 precursors (copper acetate in water, and trimesic acid in octanol) were dissolved separately, and then each solution was delivered by syringe pump to a T-junction, at which water droplets were generated by breaking the aqueous reagent solution off into the co-flowing organic ligand solution. The HKUST-1 nanocrystals were then assembled at the interface of the two solutions, leading to the formation of hollow HKUST-1 superstructures with defect-free walls (thickness: ca. 2 μm). In terms of potential applications, the authors demonstrated the capacity of these superstructures to encapsulate large dyes, such as Rose Bengal, confirming the absence of any leak except for when the superstructures were mechanically broken. In contrast, encapsulated small molecules were able to diffuse through the MOF pores, proving the selective permeation of the superstructures. Owing to these properties, the authors proposed the use of the HKUST-1 superstructures as new delivery systems, chemical sensors, or selective reactors containing molecular catalysts.

Liquid/air interface

Most of the aforementioned methods for the synthesis of MOF superstructures at liquid/liquid interfaces demand the generation and stabilisation of droplets (e.g., through emulsions) containing at least one of the corresponding MOF precursors for the duration of the reaction. Furthermore, despite the advantages of these methods, they can be extremely challenging and are currently quite limited. This is due to several factors. Firstly, the emulsions that offer the required reaction conditions are difficult to prepare (e.g., the use of specific solvents, high temperatures and certain bases). Secondly, there are often solubility problems between the MOF precursors and the constituent (polar or non-polar) solvents of the emulsions. Lastly, the presence of surfactants can be detrimental to MOF synthesis. These drawbacks could limit the scope of these methods.

One solution to the problems encountered in liquid/liquid MOF synthesis is to perform self-assembly at liquid/air interfaces generated in an aerosol, as one can use the same mixtures as those used in solvothermal synthesis.[43,44] In fact, our group has synthesised a wide range of hollow MOF superstructures by exploiting the special conditions that dictate precipitation and reaction during the drying of an aerosol droplet (see Figure 6f).[43] This spray-drying method does not require any additional immiscible solvents, surfactants, emulsifiers or agitation (e.g., stirring or sonication). It enables atomisation of MOF-precursor solutions into aerosol droplets that are used as individual reactors for MOF synthesis. In the proposed mechanism, the droplets suspended in a hot-air stream start to evaporate, and then the reactants diffuse to the droplet shell, where their concentration increases until reaching a critical level, at which point the MOF crystallises. During crystallisation, the mobility of the MOF nanocrystals is reduced and therefore, they become closely packed within the droplet shell. Interestingly, the resulting hollow MOF superstructures have a single thin layer of uniformly packed MOF nanocrystals, which hold together the structure.

The versatility of this approach was proven by synthesising hollow MOF superstructures that are composed of nanocrystals of HKUST-1, Cu-bdc,[45] NOTT-100,[46] MIL-88A,[47] MIL-88B,[47] MOF-14,[48] MOF-74 [$M = Zn^{II}$, Ni^{II} and Mg^{II}],[12] UiO-66,[49] ZIF-8, a Cu^{II} Prussian blue analogue,[6] MOF-5[50] or IRMOF-3.[51] In all cases, the superstructures retained the excellent sorption properties of the parent MOF. Moreover, it was proved that this method enables partial control of the size of HKUST-1 nanocrystals that form the superstructure walls, through tuning of spray-drying parameters (e.g., concentration and flow rate). Furthermore, it simultaneously enables synthesis and assembly of different types of nanoMOFs, paving the way to hollow MOF superstructures of greater structural complexity. In terms of potential applications, one advantage of the spray-drying approach is that it enables the combined precipitation/crystallisation of different species within a single droplet, which could be exploited to create advanced encapsulation systems in which an active molecule is entrapped within the MOF shell. As a proof of concept, our group entrapped sodium chloride crystals inside the HKUST-1 shell. We then hypothesised that the rate of crystallisation inside the nebulised droplet is related to the relative mobility of the crystals and therefore, to their relative position in the final composite. Thus, sodium chloride crystals would crystallise before having their mobility reduced, whereas HKUST-1 reactants diffuse to the droplet shell, where they then crystallise. We then demonstrated that the hollow HKUST-1 shells could be used to encapsulate functional materials that would confer the final composite with added functionality, such as magnetism (encapsulation of iron oxide nanoparticles) or luminescence (encapsulation of sodium fluorescein). Finally, we confirmed the efficacy of the resulting magnetic MOF composite superstructures for selective magnetic removal of pollutants (e.g., dibenzothiophene).

Self-Templated Synthesis

Among most common literature approaches to prepare hollow inorganic superstructures is that based on self-templating

methods. These methods include Ostwald ripening, the Kirkendall effect, galvanic replacement and surface-protected etching processes. The possibility to extend these methods to create hollow MOF superstructures was explored by Wang et al.,[52] who reported a one-step Ostwald ripening process for the formation of hollow superstructures comprising crystals of a ferrocenyl MOF (see Figure 7a). They synthesised the superstructures by solvothermal reaction of iron chloride with 1,1′-ferrocenedicarboxylic acid in *N,N′*-dimethylformamide at different reaction times. Interestingly, longer reaction times led to larger cavities; at 24 h of reaction, well-defined hollow superstructures were formed (see Figure 7b–e). This observation suggested that the hollow superstructures form by an Ostwald ripening processes, in which the mass diffuses from the interior of solid aggregates (where crystallites are smaller and less compact) to the exterior (where the crystallites are larger and more compact).

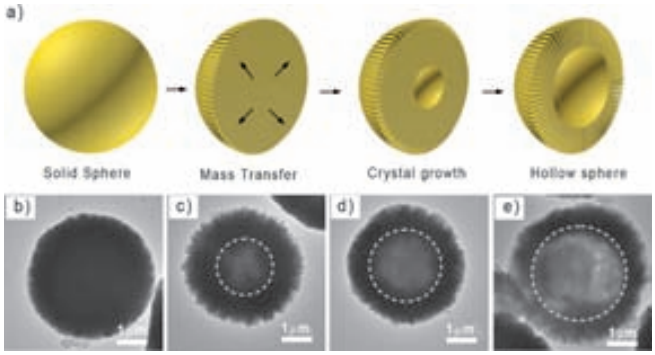

Figure 7. a) Schematic illustration of the Ostwald ripening mechanism. b)–e) TEM images showing the stepwise formation of hollow, spherical, iron-based ferrocenyl MOF superstructures at different times: b) 0, c) 2, d) 6, and e) 10 h. Reproduced with permission from reference [52].

Summary and Outlook

Recent advances in the self-assembly of MOFs into superstructures should ultimately yield a nearly infinite variety of composite superstructures in 1-, 2- and 3D diverse geometries and boasting cumulative and synergic properties. Control over the 1-, 2- and 3D ordering of these superstructures should enable their ready integration into devices and onto surfaces. However, the synthetic accessibility of MOF superstructures remains in its early stage.

We have surveyed the very recently developed approaches to construct the first-ever MOF superstructures, all of which entail control over MOF crystallisation and/or the subsequent spatial layout of the resulting crystals. We have categorised these methods as 1) spontaneous higher-order assembly, 2) self-assembly using hard templates, 3) self-assembly using soft templates and 4) self-templated synthesis.

We strongly believe that the coming years will witness further methodological progress in terms of controlling the composition, size, shape, MOF-crystal packing and interfaces (between MOF crystals and other materials) in MOF superstructures. Given the potential collective and synergistic properties that can arise through assembly of MOF crystals (whether alone or with other materials), we are confident that the forthcoming synthetic advances will ultimately enable the use of MOF superstructures in myriad applications including, for example, sensors (e.g., photonic MOF superstructures),[30] catalysts,[53] systems for magnetic pollutant removal[43] or for triggered delivery (e.g., inorganic nanoparticle@MOF composite superstructures),[29] separation agents (e.g., membrane-like MOF superstructures),[27] sorbents (SiO_2@MOF superstructures),[20] selective reactors and encapsulation systems (e.g., capsule-like MOF superstructures).[42]

Acknowledgements

This work was supported by the Spanish Ministry of Economy and Competitiveness (MINECO), under projects MAT2012-30994 and CTQ2011-16009-E. I.I. and K.C.S. thank MINECO and the EU for a Ramón y Cajal grant and a Marie Curie Fellowship (300390-NanoBioMOFs FP7-PEOPLE-2011-IEF), respectively. The authors also thank Dr. Carlos Carbonell for his assistance in designing some of the graphics.

Keywords: composites · metal-organic frameworks · self-assembly · superstructures · template synthesis

[1] a) M. Boncheva, G. M. Whitesides, *MRS Bull.* **2005**, *30*, 736–742; b) Y. Min, M. Akbulut, K. Kristiansen, Y. Golan, J. Israelachvili, *Nat. Mater.* **2008**, *7*, 527–538; c) S. Mann, *Nat. Mater.* **2009**, *8*, 781–792; d) Z. Nie, A. Petukhova, E. Kumacheva, *Nat. Nanotechnol.* **2010**, *5*, 15–25.
[2] N. Yanai, S. Granick, *Angew. Chem.* **2012**, *124*, 5736–5739; *Angew. Chem. Int. Ed.* **2012**, *51*, 5638–5641.
[3] K. S. Park, Z. Ni, A. P. Côté, J. Y. Choi, R. Huang, F. J. Uribe-Romo, H. K. Chae, M. O'Keeffe, O. M. Yaghi, *Proc. Natl. Acad. Sci. USA* **2006**, *103*, 10186–10191.
[4] M. Sindoro, N. Yanai, A.-Y. Jee, S. Granick, *Acc. Chem. Res.* **2013**.
[5] a) B. Nikoobakht, Z. L. Wang, M. A. El-Sayed, *J. Phys. Chem. B* **2000**, *104*, 8635–8640; b) S. L. Tripp, S. V. Pusztay, A. E. Ribbe, A. Wei, *J. Am. Chem. Soc.* **2002**, *124*, 7914–7915; c) B. G. Prevo, D. M. Kuncicky, O. D. Velev, *Colloids Surf. A* **2007**, *311*, 2–10; d) J. Xu, J. Xia, Z. Lin, *Angew. Chem.* **2007**, *119*, 1892–1895; *Angew. Chem. Int. Ed.* **2007**, *46*, 1860–1863.
[6] S. S. Kaye, J. R. Long, *J. Am. Chem. Soc.* **2005**, *127*, 6506–6507.
[7] S. Wu, X. Shen, Z. Xu, J. Wu, C. Gao, *Appl. Surf. Sci.* **2009**, *255*, 9182–9185.
[8] Y. Liu, J. F. Eubank, A. J. Cairns, J. Eckert, V. C. Kravtsov, R. Luebke, M. Eddaoudi, *Angew. Chem.* **2007**, *119*, 3342–3347; *Angew. Chem. Int. Ed.* **2007**, *46*, 3278–3283.
[9] M. Pang, A. J. Cairns, Y. Liu, Y. Belmabkhout, H. C. Zeng, M. Eddaoudi, *J. Am. Chem. Soc.* **2012**, *134*, 13176–13179.
[10] N. Yanai, M. Sindoro, J. Yan, S. Granick, *J. Am. Chem. Soc.* **2013**, *135*, 34–37.
[11] a) H. Du, J. Bai, C. Zuo, Z. Xin, J. Hu, *CrystEngComm* **2011**, *13*, 3314–3316; b) Y. Yue, Z.-A. Qiao, P. F. Fulvio, A. J. Binder, C. Tian, J. Chen, K. M. Nelson, X. Zhu, S. Dai, *J. Am. Chem. Soc.* **2013**, *135*, 9572–9575.
[12] N. L. Rosi, J. Kim, M. Eddaoudi, B. Chen, M. O'Keeffe, O. M. Yaghi, *J. Am. Chem. Soc.* **2005**, *127*, 1504–1518.
[13] R. L. Penn, J. F. Banfield, *Science* **1998**, *281*, 969–971.
[14] H. Cölfen, M. Antonietti, *Angew. Chem.* **2005**, *117*, 5714–5730; *Angew. Chem. Int. Ed.* **2005**, *44*, 5576–5591.
[15] X.-J. Zheng, Q. Kuang, T. Xu, Z.-Y. Jiang, S.-H. Zhang, Z.-X. Xie, R.-B. Huang, L.-S. Zheng, *J. Phys. Chem. C* **2007**, *111*, 4499–4502.
[16] M. Hu, J.-S. Jiang, R.-P. Ji, Y. Zeng, *CrystEngComm* **2009**, *11*, 2257–2259.

[17] a) H. Bux, F. Liang, Y. Li, J. Cravillon, M. Wiebcke, J. r. Caro, *J. Am. Chem. Soc.* **2009**, *131*, 16000 – 16001; b) D. Zacher, O. Shekhah, C. Woll, R. A. Fischer, *Chem. Soc. Rev.* **2009**, *38*, 1418 – 1429; c) F. Jeremias, S. K. Henninger, C. Janiak, *Chem. Commun.* **2012**, *48*, 9708 – 9710.
[18] C. Carbonell, I. Imaz, D. Maspoch, *J. Am. Chem. Soc.* **2011**, *133*, 2144 – 2147.
[19] H. J. Lee, W. Cho, M. Oh, *Chem. Commun.* **2012**, *48*, 221 – 223.
[20] S. Sorribas, B. Zornoza, C. Tellez, J. Coronas, *Chem. Commun.* **2012**, *48*, 9388 – 9390.
[21] a) S. S.-Y. Chui, S. M.-F. Lo, J. P. H. Charmant, A. G. Orpen, I. D. Williams, *Science* **1999**, *283*, 1148 – 1150.
[22] A. Ahmed, M. Forster, R. Clowes, D. Bradshaw, P. Myers, H. Zhang, *J. Mater. Chem. A* **2013**, *1*, 3276 – 3286.
[23] G. Lu, S. Li, Z. Guo, O. K. Farha, B. G. Hauser, X. Qi, Y. Wang, X. Wang, S. Han, X. Liu, J. S. DuChene, H. Zhang, Q. Zhang, X. Chen, J. Ma, S. C. J. Loo, W. D. Wei, Y. Yang, J. T. Hupp, F. Huo, *Nat. Chem.* **2012**, *4*, 310 – 316.
[24] P. Horcajada, S. Surble, C. Serre, D.-Y. Hong, Y.-K. Seo, J.-S. Chang, J.-M. Greneche, I. Margiolaki, G. Ferey, *Chem. Commun.* **2007**, 2820 – 2822.
[25] F. Ke, L.-G. Qiu, Y.-P. Yuan, X. Jiang, J.-F. Zhu, *J. Mater. Chem.* **2012**, *22*, 9497 – 9500.
[26] M. Faustini, J. Kim, G.-Y. Jeong, J. Y. Kim, H. R. Moon, W.-S. Ahn, D.-P. Kim, *J. Am. Chem. Soc.* **2013**, *135*, 14619 – 14626.
[27] J. Reboul, S. Furukawa, N. Horike, M. Tsotsalas, K. Hirai, H. Uehara, M. Kondo, N. Louvain, O. Sakata, S. Kitagawa, *Nat. Mater.* **2012**, *11*, 717 – 723.
[28] A. Comotti, S. Bracco, P. Sozzani, S. Horike, R. Matsuda, J. Chen, M. Takata, Y. Kubota, S. Kitagawa, *J. Am. Chem. Soc.* **2008**, *130*, 13664 – 13672.
[29] K. Khaletskaya, J. Reboul, M. Meilikhov, M. Nakahama, S. Diring, M. Tsujimoto, S. Isoda, F. Kim, K.-i. Kamei, R. A. Fischer, S. Kitagawa, S. Furukawa, *J. Am. Chem. Soc.* **2013**, *135*, 10998 – 11005.
[30] Y.-n. Wu, F. Li, W. Zhu, J. Cui, C.-a. Tao, C. Lin, P. M. Hannam, G. Li, *Angew. Chem.* **2011**, *123*, 12726 – 12730; *Angew. Chem. Int. Ed.* **2011**, *50*, 12518 – 12522.
[31] S. Hou, C. C. Harrell, L. Trofin, P. Kohli, C. R. Martin, *J. Am. Chem. Soc.* **2004**, *126*, 5674 – 5675.
[32] G. Férey, C. Serre, C. Mellot-Draznieks, F. Millange, S. Surblé, J. Dutour, I. Margiolaki, *Angew. Chem.* **2004**, *116*, 6456 – 6461; *Angew. Chem. Int. Ed.* **2004**, *43*, 6296 – 6301.
[33] A.-L. Li, F. Ke, L.-G. Qiu, X. Jiang, Y.-M. Wang, X.-Y. Tian, *CrystEngComm* **2013**, *15*, 3554 – 3559.
[34] Y. Mao, L. shi, H. Huang, W. Cao, J. Li, L. Sun, X. Jin, X. Peng, *Chem. Commun.* **2013**, *49*, 5666 – 5668.
[35] Y.-n. Wu, F. Li, H. Liu, W. Zhu, M. Teng, Y. Jiang, W. Li, D. Xu, D. He, P. Hannam, G. Li, *J. Mater. Chem.* **2012**, *22*, 16971 – 16978.
[36] G. Liang, J. Xu, X. Wang, *J. Am. Chem. Soc.* **2009**, *131*, 5378 – 5379.
[37] M. Pang, A. J. Cairns, Y. Liu, Y. Belmabkhout, H. C. Zeng, M. Eddaoudi, *J. Am. Chem. Soc.* **2013**, *135*, 10234 – 10237.
[38] a) I. Akartuna, A. R. Studart, E. Tervoort, U. T. Gonzenbach, L. J. Gauckler, *Langmuir* **2008**, *24*, 7161 – 7168; b) A.-C. Baudouin, D. Auhl, F. Tao, J. Devaux, C. Bailly, *Polymer* **2011**, *52*, 149 – 156; c) B. S. Murray, K. Durga, A. Yusoff, S. D. Stoyanov, *Food Hydrocolloids* **2011**, *25*, 627 – 638; d) M. Reger, T. Sekine, H. Hoffmann, *Colloids Surf. A* **2012**, *413*, 25 – 32; e) P. Wongkongkatep, K. Manopwisedjaroen, P. Tiposoth, S. Archakunakorn, T. Pongtharangkul, M. Suphantharika, K. Honda, I. Hamachi, J. Wongkongkatep, *Langmuir* **2012**, *28*, 5729 – 5736; f) V. R. Dugyala, S. V. Daware, M. G. Basavaraj, *Soft Matter* **2013**, *9*, 6711 – 6725.
[39] B. Xiao, Q. Yuan, R. A. Williams, *Chem. Commun.* **2013**, *49*, 8208 – 8210.
[40] G. Férey, C. Mellot-Draznieks, C. Serre, F. Millange, J. Dutour, S. Surblé, I. Margiolaki, *Science* **2005**, *309*, 2040 – 2042.
[41] J. Huo, M. Marcello, A. Garai, D. Bradshaw, *Adv. Mater.* **2013**, *25*, 2717 – 2722.
[42] R. Ameloot, F. Vermoortele, W. Vanhove, M. B. J. Roeffaers, B. F. Sels, D. E. De Vos, *Nat. Chem.* **2011**, *3*, 382 – 387.
[43] A. Carné-Sánchez, I. Imaz, M. Cano-Sarabia, D. Maspoch, *Nat. Chem.* **2013**, *5*, 203 – 211.
[44] A. Garcia Marquez, P. Horcajada, D. Grosso, G. Ferey, C. Serre, C. Sanchez, C. Boissiere, *Chem. Commun.* **2013**, *49*, 3848 – 3850.
[45] C. G. Carson, K. Hardcastle, J. Schwartz, X. Liu, C. Hoffmann, R. A. Gerhardt, R. Tannenbaum, *Eur. J. Inorg. Chem.* **2009**, 2338 – 2343.
[46] B. Chen, N. W. Ockwig, A. R. Millward, D. S. Contreras, O. M. Yaghi, *Angew. Chem.* **2005**, *117*, 4823 – 4827; *Angew. Chem. Int. Ed.* **2005**, *44*, 4745 – 4749.
[47] S. Surble, C. Serre, C. Mellot-Draznieks, F. Millange, G. Ferey, *Chem. Commun.* **2006**, 284 – 286.
[48] B. Chen, M. Eddaoudi, S. T. Hyde, M. O'Keeffe, O. M. Yaghi, *Science* **2001**, *291*, 1021 – 1023.
[49] J. H. Cavka, S. Jakobsen, U. Olsbye, N. Guillou, C. Lamberti, S. Bordiga, K. P. Lillerud, *J. Am. Chem. Soc.* **2008**, *130*, 13850 – 13851.
[50] H. Li, M. Eddaoudi, M. O'Keeffe, O. M. Yaghi, *Nature* **1999**, *402*, 276 – 279.
[51] M. Eddaoudi, J. Kim, N. Rosi, D. Vodak, J. Wachter, M. O'Keeffe, O. M. Yaghi, *Science* **2002**, *295*, 469 – 472.
[52] a) J. Huo, L. Wang, E. Irran, H. Yu, J. Gao, D. Fan, B. Li, J. Wang, W. Ding, A. M. Amin, C. Li, L. Ma, *Angew. Chem.* **2010**, *122*, 9423 – 9427; *Angew. Chem. Int. Ed.* **2010**, *49*, 9237 – 9241; b) J. Huo, L. Wang, E. Irran, H. Yu, L. Ma, J. Gao, D. Fan, W. Ding, A. M. Amin, Y. Tai, *J. Colloid Interface Sci.* **2012**, *367*, 92 – 100.
[53] C.-H. Kuo, Y. Tang, L.-Y. Chou, B. T. Sneed, C. N. Brodsky, Z. Zhao, C.-K. Tsung, *J. Am. Chem. Soc.* **2012**, *134*, 14345 – 14348.

Published online on March 18, 2014

JACS
JOURNAL OF THE AMERICAN CHEMICAL SOCIETY
Communication
pubs.acs.org/JACS

Relaxometry Studies of a Highly Stable Nanoscale Metal–Organic Framework Made of Cu(II), Gd(III), and the Macrocyclic DOTP

Arnau Carné-Sánchez,[†] Célia S. Bonnet,[‡] Inhar Imaz,[†] Julia Lorenzo,[§] Éva Tóth,*[,‡] and Daniel Maspoch*[,†,⊥]

[†]Institut Catala de Nanociencia i Nanotecnologia, Esfera UAB, 08193 Bellaterra, Spain
[‡]Centre de Biophysique Moléculaire, CNRS, Rue Charles Sadron, 45071 Orléans, France
[§]Institut de Biotecnologia i Biomedicina, UAB, 08193 Bellaterra, Spain
[⊥]Institució Catalana de Recerca i Estudis Avançats, 08100 Barcelona, Spain

Supporting Information

ABSTRACT: The macrocyclic ligand DOTP is used to assemble a porous, heterometallic metal–organic framework (MOF). This MOF is miniaturizable down to the nanoscale to form stable colloids, is stable in physiological saline solution and cell culture media, and is not cytotoxic. It shows interesting relaxometric properties with r_1 at high field (500 MHz) of 5 $mM^{-1}\cdot s^{-1}$ and a maximum r_1 = 15 $mM^{-1}\cdot s^{-1}$ at 40 MHz, which remains constant over a wide pH range and increases with temperature.

Magnetic resonance imaging (MRI) is one of the most powerful diagnostic tools in medical science thanks to its noninvasive character and sub-millimeter spatial resolution. Based on the detection of nuclear spin reorientations under a magnetic field, MRI has been demonstrated to be very effective for assessing anatomical changes and monitoring organ functions. However, in many cases, the use of contrast agents (CAs) is necessary to enhance the intrinsic contrast of MR images; 35% of clinical MRI scans are currently performed with the assistance of CAs.[1] These paramagnetic or superparamagnetic substances act by shortening proton longitudinal (T1) and/or transverse (T2) relaxation times of water protons, improving the contrast between diseased and normal tissue. Most of the currently used CAs are stable chelates of the highly paramagnetic Gd(III) ion;[2] however, some limitations persist due to their low sensitivity, lack of selectivity, and low retention time that make them effective only in areas of high accumulation. Nanoparticulate Gd(III)-based CAs can provide increased *in vivo* circulation time and slower rotational tumbling of the agent and contain a high payload of Gd(III) ions per particle, giving rise to superior MRI efficacies.[3] The most common approaches for developing such nanoscale CAs involve the use of Gd(III) oxide nanoparticles[4] and the introduction of Gd(III) chelates in a variety of nanotemplates, such as inorganic nanoparticles,[5] dendrimers,[6] viral capsids,[7] proteins,[8] mesoporous silica,[9] colloidal self-assembled nanoparticles,[10] and zeolites.[11]

Nanoscale metal–organic frameworks (nanoMOFs),[12] which have the advantage of high surface areas and endless possibilities to carry high Gd(III) concentrations per nanocrystal unit, are beginning to be investigated as an alternative class of nanoscale CAs.[13] Primary examples are nanoMOFs assembled from Gd(III) ions and polycarboxylate linkers.[13−15] The biologically viable conception of CAs based on nanoMOFs remains, however, quite challenging. For example, MOFs typically lack stability in water and in body fluids, causing the release of highly toxic free Gd(III) ions and preventing detailed relaxometry studies. This stability is a critical issue toward the potential *in vivo* exploitation of CAs based on MOFs.

Herein we propose to construct a nanoMOF containing Gd(III) by using a macrocyclic ligand with multiple coordination sites in order to limit free Gd(III) leaching. In addition, we present for the first time a temperature- and pH-dependent, variable-field relaxometric study for a nanoMOF to gain insight into the mechanisms that govern the relaxation behavior of these compounds. The Gd(III)-based nanoMOF we have designed features high stability in physiological saline solution and in cell culture media, while it retains an interesting r_1 relaxivity of 15 $mM^{-1}\cdot s^{-1}$ at 40 MHz (25 °C) and r_1 = 5 $mM^{-1}\cdot s^{-1}$ at a higher field (500 MHz, 25 °C). Our concept relies on using the macrocyclic 1,4,7,10-tetraazacyclododecane-1,4,7,10-tetramethylenephosphonic acid (DOTP, Figure 1a) to assemble Gd(III) and Cu(II) ions to form a MOF structure with formula $[GdCu(DOTP)Cl]\cdot 4.5H_2O$ (hereafter called **CAMOF-1**). Cu(II) is chelated inside the cage formed by DOTP, whereas Gd(III) is coordinated by phosphonate groups from different DOTP units, resulting in a porous three-dimensional structure. The choice of DOTP as the organic linker was governed by the following considerations: (1) it belongs to the family of strong chelating ligands capable of forming highly stable complexes with a variety of ligands;[16] (2) it offers a large number of metal binding sites of two distinct types of chemical nature, one at the phosphonate pendant arms and the other within the cyclen ring; (3) phosphonates form stronger bonds than carboxylates do with metal ions,[17] so its four phosphonate groups can be used to form highly stable MOFs in aqueous conditions; and (4) its strong chelating capabilities can be used to sequester the metal ions eventually released upon MOF decomposition, thus further helping to maintain low levels of leached free Gd(III) and Cu(II) ions. Cu(II) ions are also key actors in the formation of the MOF

Received: September 20, 2013
Published: November 11, 2013

   dx.doi.org/10.1021/ja4094378 | J. Am. Chem. Soc. 2013, 135, 17711−17714

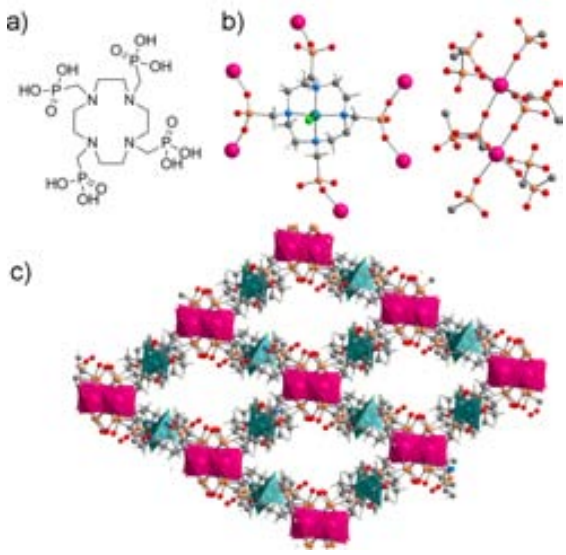

Figure 1. (a) Representation of DOTP ligand. (b) Crystal structure of **CAMOF-1**, showing the coordination of DOTP with one Cu(II) ion and six Gd(III) ions and the coordination geometry of Gd(III) ions. (c) 3D extended structure of **CAMOF-1**, showing the presence of 1D channels. Color code: Gd, pink; C, gray; N, blue; Cu, dark green; Cl, light green; O, red.

structure made of Gd(III) and DOTP: an extended structure is not formed when other secondary metal ions such as Zn(II), Ni(II), Co(II), Mn(II), Fe(III), and Mg(II) are used (Figure S2), likely because they have less preference for nitrogen donors with respect to Cu(II). Gd(III) and Cu(II) are the only ones that have comparably high stability constants with DOTP (28.8[18] and 25.4,[19] respectively). We hypothesize that this similarity makes it possible to disrupt the formation of the very stable mononuclear $[Gd(DOTP)]^{5-}$ species, allowing DOTP to simultaneously coordinate to the two different metal ions and extend the metal–organic structure. In addition to the preference of Cu(II) for nitrogen donors and the preference of lanthanides for oxygen donors, formation kinetic factors might also contribute to yield a structure in which the Cu(II) is in the polyamine cage and the Gd(III) is coordinated by the phosphonates. We discovered that the formation of **CAMOF-1** takes place over a wide pH range (pH = 3–8), and that the crystal size is affected by pH and temperature. Macrocrystals of **CAMOF-1**, suitable for single-crystal X-ray diffraction, have been assembled at low pHs (<4) and at high temperatures, whereas nanocrystals of **CAMOF-1** (hereafter called **nanoCAMOF-1**) have been prepared at high pHs (>6) and at room temperature.

In an initial experiment, macroscopic blue rod-like crystals of **CAMOF-1** were prepared upon reaction of $Gd(NO_3)_3{\cdot}6H_2O$, $CuCl_2$, and DOTP in water at 85 °C for 12 h. Here, square-pyramidal Cu(II) ions are coordinated to the four ring-nitrogen atoms defining the equatorial plane, whereas the axial position is occupied by a chlorine atom. The four deprotonated phosphonate groups of each DOTP are then coordinated to six octahedral Gd(III) ions, which are connected to six DOTP linkers via their phosphonate groups (Figure 1b) to form an extended three-dimensional porous framework with one-dimensional channels (5 × 5 Å; 23% of void space in unit cell)[20] along the (113) direction (Figure 1c). Microporosity of **CAMOF-1** was confirmed by CO_2 gas adsorption studies at 195 K. It showed hysteretic behavior and a BET surface area of 110 $m^2{\cdot}g^{-1}$ (Figure S3).

In order to potentially use **CAMOF-1** as a CA, a requirement is to control its crystal size down to the nanometer length scale. This miniaturization step was done by reproducing the above-mentioned reaction at higher pHs. Subsequent addition of $CuCl_2$ and $Gd(NO_3)_3{\cdot}6H_2O$ to a partially deprotonated form of DOTP in water (pH = 8) at room temperature led to the formation of a very stable blue colloid of **nanoCAMOF-1** (Figure 2a). Transmission electron microscopy (TEM) images

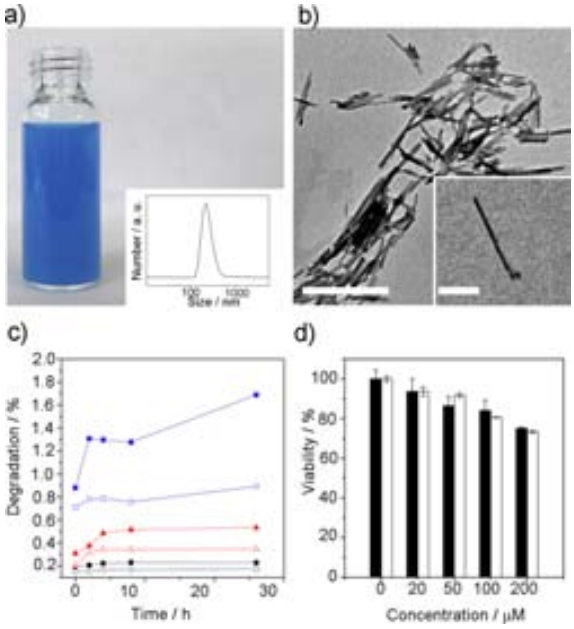

Figure 2. (a) Photograph of **nanoCAMOF-1** colloidal suspension and its size distribution determined by DLS (inset). (b) TEM images of **nanoCAMOF-1**. Scale bars: 500 and 100 nm (inset). (c) Time dependence of the percentage of the total Gd(III) [filled symbols] and the maximum potential free Gd(III) [empty symbols] ions relative to the total Gd(III) content in **nanoCAMOF-1** leached upon incubation in saline solution at pH = 4 (black circles), 7.4 (red triangles), and 9 (blue squares) and at 37.5 °C. (d) Effects of **nanoCAMOF-1** on the viability of HepG2 (filled bars) and MCF7 (empty bars) cells at 24 h. Error bars represent the standard error.

of the colloid demonstrated the formation of uniform nanowires 10 nm in diameter and 200 nm in length (Figure 2b). The average length of these nanowires was further confirmed by dynamic light scattering (DLS) measurements (Figure 2a, inset). Importantly, we were able to control the length of the nanowires by synthesizing them through a diffusion method: we obtained larger nanofibers (up to 100 μm) by diffusing an aqueous solution of $Gd(NO_3)_3{\cdot}6H_2O$ on an aqueous solution of $CuCl_2$ and DOTP (Figure S6). The correspondence between these nanostructures and **CAMOF-1** was confirmed by the positive matching between the elemental analyses, IR spectra, XRPD, and magnetic properties performed on these samples (Figure S5).

The strong Gd(III)–phosphonate bonds and the high connectivity of **nanoCAMOF-1** give it high stability in physiological saline solution (NaCl, 0.9% w/w) and in 4-(2-hydroxyethyl)-1-piperazineethanesulfonic acid (HEPES)-buffered media. To perform these experiments, as-synthesized (200 nm in length) **nanoCAMOF-1** was first centrifuged and redispersed in water three times, and finally redispersed in the

dx.doi.org/10.1021/ja4094378 | J. Am. Chem. Soc. 2013, 135, 17711–17714

studied medium to form a stable colloid, as confirmed by DLS. Exposure of this material to saline solution at pH = 4, 7.4, and 9 and at T = 37.5 °C for 24 h led to the leaching of 0.2%, 0.5%, and 1.6% of the total Gd(III) and 0.2%, 0.4%, and 3.5% of the total Cu(II) content in **nanoCAMOF-1**, respectively, as determined by ICP-OES (Figures 2c and S7a). The maximum concentration of free Gd(III) ions in the incubated samples was also determined by titration with xylenol orange.[21] This study confirmed low maximum concentrations of free Gd(III) ions at all pHs, being 0.2% (11 μM), 0.4% (20 μM), and 0.9% (50 μM) of the total Gd(III) content in **nanoCAMOF-1** at pH = 4, 7.4, and 9, respectively. When exposed to HEPES buffer at pH = 7.4, **nanoCAMOF-1** leached 1.7% of the total Gd(III) and 1.4% of the total Cu(II) content in 24 h (Figure S7b). Further exposure of this material to these media for 1 week did not show a significant increase of leached Gd(III) and Cu(II) ions. In all cases, TEM and DLS analysis after 1 week of exposure confirmed no degradation of **nanoCAMOF-1** (Figures S8 and S9).

It is also important to note here that those differences between total leached Gd(III) and free leached Gd(III) in physiological saline solution at pH = 7.4 and 9 should be attributed to the capacity of DOTP to coordinate metal ions after partial degradation of the MOF. This was confirmed by mass spectrometry analysis of the leached products of the incubated samples. Analysis of the supernatants resulting from the degradation experiments using ESI-MS reveals species corresponding to CuDOTP and CuDOTPGd complexes ($[CuDOTP - 4H + 3Na]^+$ = 675.96, $[CuDOTP - 5H + 4Na]^+$ = 697.94, $[CuGdDOTP - 5H - OH]^+ + 2MeOH$ = 810.96, $[CuGdDOTP - 5H - OH]^+ + 2MeOH + H_2O$ = 828.92, $[CuGdDOTP - 6H - OH + Na]^+ + 2MeOH$ = 832.96; Figures S10 and S11), establishing that certain percentages of Gd(III) and Cu(II) ions are indeed attached to DOTP in solution. These results are in agreement with the cytotoxicity assays conducted with two cell lines, HepG2 and MCF7. After 24 h of incubation, both cells showed good viability (75% for HepG2 and 74% for MCF7) up to 200 μM **nanoCAMOF-1** (Figure 2d). These results demonstrate that **nanoCAMOF-1** does not show significant toxicity resulting from the leakage of free toxic Gd(III) and Cu(II) ions. This lack of noticeable toxicity could be attributed to the capacity of DOTP to chelate a high percentage of the limited quantity of Gd(III) and Cu(II) ions leached upon degradation of **nanoCAMOF-1**.

The efficacy of **nanoCAMOF-1** as a potential CA for MRI was investigated by ^{1}H nuclear magnetic relaxation dispersion (i.e., NMRD relaxometry) profiles in the frequency range 10 kHz ν 500 MHz using a dispersion of these nanowires in saline solution at pH = 4 and 7.4 (Figures 3a and S12). This dispersion was stable throughout the measurement without the addition of any surfactant or thickener to avoid interference. Study of the relaxivity as a function of magnetic field at 25 °C clearly showed an increase at intermediate magnetic fields, reaching a maximum r_1 = 15 $mM^{-1}\cdot s^{-1}$ at 40 MHz, which is more than 3 times higher than the reported relaxivity for $[GdDOTP]^{5-}$ at pH = 7.4.[22] This behavior is characteristic of slow rotational motion, typically observed in nanostructured systems.[23,24] It is important to note that, even at very high field such as 500 MHz, the relaxivity is still >6 $mM^{-1}\cdot s^{-1}$ at 37 °C. In addition, relaxivity increased with temperature, which indicates that the mean proton exchange between the nanowires and the bulk water is limiting relaxivity, as previously observed in other

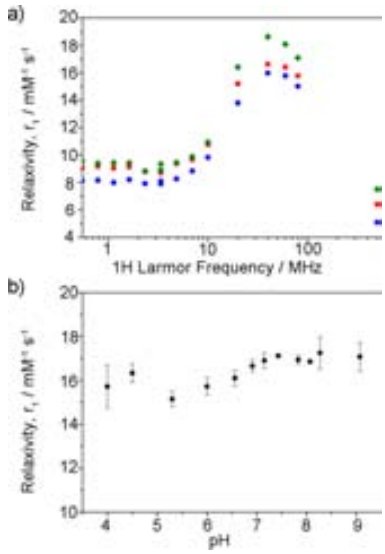

Figure 3. (a) NMRD profile of a colloidal suspension of **nanoCAMOF-1** at pH = 4 at 25 °C (blue dot), 37 °C (red square), and 50 °C (green rhombus). (b) pH dependence of the relaxivity of **nanoCAMOF-1** measured at 40 MHz (25 °C). Error bars represent standard deviation of three replicates.

nanostructured Gd(III)-based CAs.[25] It should be mentioned that we can only obtain information on the "average" value of the proton (or water) exchange rate, as different "sites", likely having different exchange rates, can be found in this MOF. For example, Gd(III) in the porous channels and Gd(III) at the surface of the MOF will behave differently. The crystal structure shows that each Gd(III) ion inside the MOF is coordinated by six phosphonate oxygens, which yields a highly unsaturated coordination sphere for the lanthanide (typical CN = 8 or 9, at least in solution). However, it is impossible to assess the average number of water molecules per Gd(III) that contribute to the relaxivity, their distance from the paramagnetic center, and their exchange rate with bulk water. These parameters all influence the experimental relaxivity, but they cannot be assessed individually by relaxometry. The relaxivity profiles nevertheless unambiguously prove that an inner-sphere type of mechanism based on proton (or water) exchange is the major contributor to the relaxation effect in the case of **nanoCAMOF-1**. This is in contrast to other Gd(III)-containing MOFs, where only an outer-sphere contribution was operating, which yielded very low relaxivities (1 $mM^{-1}\cdot s^{-1}$ at 500 MHz, 298 K).[15] The temperature dependence of the proton relaxivities allows us to draw further conclusions with respect to the mechanism. Previous reports stated that only Gd(III) centers at or near the surface are responsible for the relaxation effect,[13a,15] and those inside do not contribute. Surface Gd(III) ions have an increased hydration number; therefore, they are expected to have a fast water exchange rate.[26] The Gd(III) centers inside might have slower water exchange, or the diffusion of the water molecules through the MOF channels might be limited. The temperature increase will result in an increase of the water (or proton) exchange rate, yielding higher relaxivities.[27] The observation that the relaxivities of **nanoCAMOF-1** increase with increasing temperature therefore provides clear evidence that Gd(III) centers inside the nanoMOF do have a relaxivity contribution.

The pH dependence of the relaxivity of **nanoCAMOF-1** at 40 MHz is shown in Figure 3b. The relaxivity remains relatively

dx.doi.org/10.1021/ja4094378 | J. Am. Chem. Soc. 2013, 135, 17711−17714

constant between pH = 4 and 9, further supporting the structural integrity of **nanoCAMOF-1** over this pH range. The small variation might be related to the protonation of surface DOTP phosphonates. This high stability motivated us to investigate the relaxivity of **nanoCAMOF-1** under physiologically more relevant conditions. To do this, the relaxivity of a dispersion of **nanoCAMOF-1** in DMEM was measured at 40 MHz over time. No significant change of the initial r_1 relaxivity of 13.05 $mM^{-1}{\cdot}s^{-1}$ was observed, even after 24 h (Figure S13). This confirms the stability of **nanoCAMOF-1** under such buffered conditions, with degradation below 10% after 24 h, as confirmed by ICP-OES.

In conclusion, we have reported the use of DOTP, a chelating ligand typically used to generate stable mononuclear lanthanide complexes, to synthesize a bimetallic Cu(II)- and Gd(III)-based MOF with promising relaxometric properties. This MOF is miniaturizable down to the nanometer length scale to form stable colloids; it is stable in water, physiological saline solution, and cell culture media; and it does not show cytotoxicity. It shows a maximum in r_1 relaxivity of 15 $mM^{-1}{\cdot}s^{-1}$ at 40 MHz, which remains constant over a wide pH range and increases with temperature. Importantly, this is the first study of the dependence of the r_1 relaxivity of a MOF as a function of a wide range of temperatures, magnetic fields, and pHs, which allowed us to conclude that an inner-sphere type of mechanism is operating and that Gd(III) centers inside the MOF structure also contribute to the relaxation effect. Synthesizing highly stable MOFs and combining their relaxometric properties and porosities should be feasible, making it possible to also exploit them in theranostics.

■ ASSOCIATED CONTENT

Ⓢ Supporting Information

Experimental details and additional characterization. This material is available free of charge via the Internet at http://pubs.acs.org. Further details on the crystal structure resolution may be obtained from the Cambridge Crystallographic Data Centre, on quoting the depository number CCDC-951712.

■ AUTHOR INFORMATION

Corresponding Authors

eva.jakabtoth@cnrs-orleans.fr
daniel.maspoch@icn.cat

Notes

The authors declare no competing financial interest.

■ ACKNOWLEDGMENTS

We acknowledge financial support from MINECO-Spain under projects MAT2012-30994 and CTQ2011-16009-E. I.I. thanks the MINECO for RyC contracts.

■ REFERENCES

(1) Merbach, A. E.; Helm, L.; Tóth, E. *The Chemistry of Contrast Agents in Medical Magnetic Resonance Imaging*, 2nd ed.; John Wiley and Sons: Chichester, 2013.

(2) (a) Aime, S.; Botta, M.; Terreno, E. *Adv. Inorg. Chem.* **2005**, *57*, 173. (b) Caravan, P.; Ellison, J. J.; McMurry, T. J.; Lauffer, R. B. *Chem. Rev.* **1999**, *99*, 2293.

(3) (a) Botta, M.; Tei, L. *Eur. J. Inorg. Chem.* **2012**, *12*, 1945. (b) Terreno, E.; Castelli, D. D.; Viale, A.; Aime, S. *Chem. Rev.* **2010**, *110*, 3019.

(4) Bridot, J.-L.; Faure, A.-C.; Laurent, S.; Riviere, C.; Billotey, C.; Hiba, B.; Janier, M.; Josserand, V.; Coll, J.-L.; Vander Elst, L.; Muller, R.; Roux, S.; Perriat, P.; Tillement, O. *J. Am. Chem. Soc.* **2007**, *129*, 5076.

(5) (a) Song, Y.; Xu, X.; MacRenaris, K. W.; Zhang, X.-Q.; Mirkin, C. A.; Meade, T. J. *Angew. Chem., Int. Ed.* **2009**, *48*, 9143. (b) Decuzzi, P.; et al. *Nat. Nanotechnol.* **2010**, *5*, 815.

(6) (a) Floyd, W. C.; Klemm, P. J.; Smiles, D. E.; Kohlgruber, A. C.; Pierre, V. C.; Mynar, J. L.; Fréchet, J. M. J.; Raymond, K. N. *J. Am. Chem. Soc.* **2011**, *133*, 2390. (b) Klemm, P. J.; Floyd, W. C.; Andolina, C. M.; Fréchet, J. M. J.; Raymond, K. N. *Eur. J. Inorg. Chem.* **2012**, *12*, 2108.

(7) Ankon, D.; Hooker, J. M.; Botta, M.; Matthew, B. F.; Aime, S.; Raymond, K. N. *J. Am. Chem. Soc.* **2008**, *130*, 2546.

(8) (a) Daldrup-Link, H. E.; Brasch, R. C. *Eur. Radiol.* **2003**, *13*, 354. (b) Liepold, L. O.; Abedin, M. J.; Buckhouse, E. D.; Frank, J. A.; Young, M. J.; Doublas, T. *Nano Lett.* **2009**, *9*, 4520.

(9) (a) Taylor, K. M. L.; Jason, S. K.; William, J. R.; Hongyu, A.; Weili, L.; Lin, W. *J. Am. Chem. Soc.* **2008**, *130*, 2154. (b) Guillet-Nicolas, R.; Bridot, J.-C.; Seo, Y.; Fortin, M.-A.; Kleitz, F. *Adv. Funct. Mater.* **2011**, *21*, 4653. (c) Tse, N. M. K.; Kennedy, D. F.; Kirby, N.; Moffat, B. A.; Muir, B. W.; Caruso, R. A.; Drummond, C. J. *Adv. Healthcare Mater.* **2013**, *2*, 836.

(10) (a) Moghaddam, M. J.; Campo, L.; Waddington, L. J.; Weerawardena, A.; Kirby, N.; Drummond, C. J. *Soft Matter.* **2011**, *7*, 10994. (b) Mulet, X.; Boyd, B. J.; Drummond, C. J. *J. Colloid Interface Sci.* **2013**, *393*, 1.

(11) Csajbók, E.; Banyai, I.; Elst, L. V.; Muller, R. N.; Zhou, W.; Petrs, J. A. *Chem.—Eur. J.* **2005**, *11*, 4799.

(12) (a) Carné, A.; Carbonell, C.; Imaz, I.; Maspoch, D. *Chem. Soc. Rev.* **2011**, *40*, 291. (b) Lin, W.; Rieter, W. J.; Taylor, K. M. L. *Angew. Chem., Int. Ed.* **2009**, *48*, 650.

(13) (a) Rieter, W. J.; Taylor, K. M. L.; An, H.; Lin, W.; Lin, W. *J. Am. Chem. Soc.* **2006**, *128*, 9024. (b) Horcajada, P.; Gref, R.; Baati, T.; Allan, P. K.; Maurin, G.; Couvreur, P.; Férey, G.; Morris, R. E.; Serre, C. *Chem. Rev.* **2012**, *112*, 1232.

(14) Taylor, K. M. L.; Jin, A.; Lin, W. *Angew. Chem., Int. Ed.* **2008**, *120*, 7836.

(15) Pereira, G. A.; Peters, J. A.; Almeida Paz, F. A.; Rocha, J.; Geraldes, C. F. G. C. *Inorg. Chem.* **2010**, *49*, 2969.

(16) Aime, S.; Botta, M.; Terreno, E.; Anelli, P. L.; Uggeri, F. *MRM* **1993**, *30*, 583.

(17) (a) Gagnon, K. J.; Perry, H. P.; Clearfield, A. *Chem. Rev* **2012**, *112*, 1034. (b) Kong, D.; Medvedev, D. G.; Clearfield, A. *Inorg. Chem.* **2004**, *43*, 7308.

(18) Sherry, A. D.; Huskens, J. R.; Brucher, E.; Tóth, E.; Geraldes, F. G. C.; Castro, M. M. C. A.; Cacheris, W. P. *Inorg. Chem.* **1996**, *35*, 4604.

(19) Geraldes, F. G. C.; Marques, M. P.; Castro, B. de; Pereira, E. *Eur. J. Inorg. Chem.* **2000**, *20*, 559.

(20) Spek, A. L. *PLATON*, a Multipurpose Crystallographic Tool; Utrecht University: Utrecht, 1998.

(21) Barge, A.; Cravotto, G.; Gianolio, E.; Fedeli, F. *Contrast Media Mol. Imaging* **2006**, *1*, 184.

(22) Laurent, S.; Vander Elst, L.; Muller, R. N. *Contrast Media Mol. Imaging* **2006**, *1*, 128.

(23) Tsotsalas, M.; Busby, M.; Gianolio, E.; Aime, S.; De Cola, L. *Chem. Mater.* **2008**, *20*, 5888.

(24) Guari, Y.; Larionova, J.; Corti, M.; Lascialfari, A.; Marinone, M.; Poletti, G.; Molvinger, K.; Guérien, C. *Dalton Trans.* **2008**, 3658.

(25) Platas-Iglesias, C.; Elst, L. V.; Zhou, W.; Muller, R. N.; Geraldes, F. G. C.; Maschmeyer, T.; Peters, J. A. *Chem.—Eur. J.* **2002**, *8*, 5124.

(26) Helm, L.; Merbach, A. E. *Chem. Rev.* **2005**, *105*, 1923.

(27) Merbach, A. E.; Helm, L.; Tóth, E. *The Chemistry of Contrast Agents in Medical Magnetic Resonance Imaging*, 2nd ed.; John Wiley and Sons: Chichester, 2013; Chapter 2.